



UCGE Reports

Number 20330

Department of Geomatics Engineering

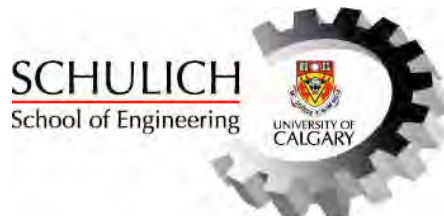
**Use of Earth's Magnetic Field for Pedestrian
Navigation**

(URL: <http://www.geomatics.ucalgary.ca/graduatetheses>)

by

Muhammad Haris Afzal

July 2011



UNIVERSITY OF CALGARY

Use of Earth's Magnetic Field for Pedestrian Navigation

by

Muhammad Haris Afzal

A THESIS

SUBMITTED TO THE FACULTY OF GRADUATE STUDIES
IN PARTIAL FULFILMENT OF THE REQUIREMENTS FOR THE
DEGREE OF DOCTOR OF PHILOSOPHY

DEPARTMENT OF GEOMATICS ENGINEERING

CALGARY, ALBERTA

July, 2011

© Muhammad Haris Afzal 2011

Abstract

With advances in sensor technology and the inclusion of low cost consumer grade sensors in portable systems like smart-phones, pedestrian navigation using such devices has become a reality. With consumer grade sensors comes a Pandora's Box full of errors rendering the unaided navigation solution with these sensors of limited use. A significant contribution to the overall navigation error budget associated with pedestrian navigation is accurate attitude/orientation estimation. This research develops different sensor fusion techniques to utilize the Earth's magnetic field for attitude and rate gyroscope error estimation in pedestrian navigation environments where it is assumed that GNSS is denied.

As the Earth's magnetic field undergoes severe degradation in pedestrian navigation environments, detailed surveys are conducted for characterizing the magnetic field perturbations. A mathematical model of the Earth's magnetic field in presence of perturbation sources is then developed and used for developing different schemes for detecting, mitigating as well as directly using the magnetic perturbations for attitude and gyroscope error estimation.

First, a Multiple Magnetometer Platform (MMP) based perturbation detection and mitigation scheme is developed, which estimates the perturbation free local magnetic field. Second, a Single Magnetometer (SM) based orientation estimator is developed that uses different magnetic field parameters for assessing the accuracy of the estimated

heading. Finally a novel Quasi-Static magnetic Field (QSF) based attitude and angular rate error estimation technique is developed to effectively use magnetic measurements in highly perturbed environments. All of these schemes are used as input measurements for the proposed Extended Kalman Filter (EKF) based attitude estimator.

Results indicate that the combination of QSF and SM is capable of effectively estimating attitude and gyroscope errors, reducing the overall navigation error budget by over 80% in the urban canyons and indoor environments tested.

Acknowledgements

I would first like to thank my supervisor, Professor Gérard Lachapelle. I would have never reached this milestone without your support, guidance and encouragement. I would also like to thank Dr. Valérie Renaudin who provided me with valuable advice throughout my studies. Thank you both for believing in me when I chose this complex but interesting topic and supporting me throughout my research. The valuable advice that I have received from Mr. Vytas Kezys, Research In Motion, is highly appreciated.

I would like to thank Dr. Thomas Williams for helping me with his mechanical skills in designing various non-magnetic fixtures necessary for my research. My thanks also go to the University of Calgary Schulich School of Engineering mechanical shop and Rob Scorey for handling my requests in a timely manner.

This work was sponsored by a Research In Motion grant, matched by a Natural Sciences and Engineering Research Council of Canada Collaborative Research and Development grant, and an Industry Sponsored Collaborative grant from Alberta Advanced Education and Technology.

Finally, I would like to thank my wife Palwasha Hayat. Your support and understanding were crucial for my achievements. Thank you for always being at my side to support and encourage me.

Dedication

I dedicate this thesis to my parents.

Thank you for laying down my foundations and for all that you have done. I can never
repay you.

Table of Contents

Abstract.....	ii
Acknowledgements.....	iv
Dedication.....	v
Table of Contents.....	vi
List of Tables.....	xi
List of Figures and Illustrations.....	xii
List of Symbols and Abbreviations.....	xvii

CHAPTER ONE: INTRODUCTION AND OVERVIEW.....	1
1.1 Background.....	1
1.1.1 Pedestrian Navigation.....	2
1.1.2 Systems/ Techniques for Pedestrian Navigation.....	2
1.2 Earth's Magnetic Field for Orientation Estimation.....	5
1.3 Uses of Magnetic Field.....	7
1.3.1 Non Navigation Applications.....	7
1.3.2 Navigation Applications.....	9
1.3.3 Limitations of Previous Work for Navigation Applications.....	12
1.4 Proposed Research.....	14
1.4.1 Major Objectives and Contributions.....	14
1.5 Thesis Organization.....	16
CHAPTER TWO: THEORY OF THE MAGNETIC FIELD FOR INDOOR ORIENTATION ESTIMATION.....	18
2.1 The Magnetic Field Model.....	18
2.1.1 Ampere's Law.....	18
2.1.2 Biot-Savart Law.....	19
2.1.3 The Vector Potential of the Magnetic Field.....	20
2.1.4 Divergence of Magnetic Field.....	22
2.2 Magnetic Field of a Dipole.....	23
2.2.1 Magnetic Field Along the Z-axis.....	23
2.2.2 Magnetic Field of a Dipole at Arbitrary Locations.....	26
2.2.3 Magnetic Field Components in Cylindrical Coordinate System.....	28
2.2.4 Magnetic Field in Cartesian Coordinate System.....	30
2.3 Vector Potential of Multiple Dipoles.....	31
2.4 The Earth's Magnetic Field.....	35
2.4.1 Heading Estimation Using the Earth's Magnetic Field.....	37

2.5 Effects of Indoor Environment on the Earth’s Magnetic Field	37
2.5.1 Effect of Magnetic Perturbations on Estimated Heading.....	41
CHAPTER THREE: HARDWARE DEVELOPMENTS AND SENSOR ERROR CALIBRATION AND MODELING	43
3.1 Sensor Selection for MSP	44
3.1.1 Magnetic Field Sensors (Magnetometers)	44
3.1.2 Rate Gyroscopes	49
3.1.3 Accelerometers	49
3.1.4 Pressure/ Temperature Sensor.....	50
3.1.5 High Sensitivity GPS Receiver.....	50
3.2 Multiple Magnetometer Platform	50
3.3 Multiple Sensor Platform (MSP) Architecture	52
3.4 Hardware Realization	54
3.5 MSP Sensor Error Modeling.....	55
3.6 Inertial Sensor Errors	55
3.6.1 Biases	56
3.6.2 Axis Misalignments	56
3.6.3 Scale Factor Errors.....	56
3.6.4 Sensor Noise	57
3.7 Inertial Sensor Modeling	57
3.8 Inertial Sensor Calibration Procedure.....	58
3.8.1 Six Position Test for Accelerometer Calibration	58
3.8.2 Rate Test for Gyroscope Calibration	60
3.9 Magnetometer Errors	61
3.9.1 Offset Error	62
3.9.2 Sensitivity Error	63
3.9.3 Non-Orthogonality Errors	64
3.9.4 Cross Axis Sensitivity Error	64
3.9.5 Hard Iron Errors.....	65
3.9.6 Soft Iron Errors	67
3.9.7 Sensor Noise	68
3.10 Magnetometer Calibration Procedure.....	68
3.10.1 Calibration Algorithm.....	70
3.11 Magnetometer Calibration Results	76
3.12 Stochastic Error Modeling.....	78
3.12.1 Allan Variance	78
3.13 MSP Sensors’ Calibration and Noise Parameters.....	86
CHAPTER FOUR: MAGNETIC PERTURBATION DETECTION, ESTIMATION AND MITIGATION TECHNIQUES.....	89
4.1 Factors Affecting the Earth’s Magnetic Field in Different Environments	89
4.2 Assessment of Magnetic Field in Pedestrian Navigation Environments	90

4.2.1 Magnetic Field Surveying Setup.....	90
4.2.2 Selection of Data Collection Environments.....	93
4.3 Statistical Analysis of Indoor Magnetic Field	95
4.4 Detection and Mitigation of Magnetic Field Perturbations Using Multiple Magnetometers.....	100
4.4.1 Detection of Perturbations using Multiple Magnetometers	103
4.4.2 Mitigation of Perturbations using Multiple Magnetometers.....	106
4.5 Detection of Magnetic Field Perturbations Using a Single Magnetometer	108
4.5.1 Perturbation with Strong Horizontal and Strong Vertical Field Components	110
4.5.2 Perturbation with Strong Horizontal and Negligible Vertical Field Components	111
4.5.3 Perturbation with Negligible Horizontal and Strong Vertical Field Components	112
4.5.4 Perturbation with Negligible Horizontal and Negligible Vertical Field Components	112
4.6 Magnetic Field Test Parameters for Perturbation Detection using a Single Magnetometer	112
4.6.1 Single Magnetometer Based Perturbation Detection Techniques.....	113
4.6.2 Realization of Standalone Magnetometer Based Perturbation Detector.....	115
4.6.3 Statistical Analysis of the Detector.....	118
 CHAPTER FIVE: ATTITUDE/ ORIENTATION ESTIMATOR FOR PEDESTRIAN NAVIGATION	 126
5.1 Reference Frames	126
5.1.1 Inertial Frame.....	127
5.1.2 Local Level Frame (LLF)	127
5.1.3 Body Frame.....	127
5.1.4 Sensor Frame (Platform Frame).....	128
5.2 Transformations between the Reference Frames.....	129
5.2.1 Direction Cosine Matrix	129
5.2.2 Euler Angles.....	130
5.2.3 Quaternions	130
5.3 Attitude Computer Realization	132
5.3.1 Vector Measurements	132
5.3.2 Angular Rate Measurements.....	134
5.4 Attitude and Sensor Error Estimator.....	135
5.5 Kalman Filter	136
5.5.1 Kalman Filter Mechanization	137
5.5.2 Extended Kalman Filter (EKF)	139
5.6 EKF Based Attitude and Sensor Error Estimator	141
5.6.1 The State Vector	141
5.6.2 State Initialization	141
5.6.3 System Error Model.....	143

5.6.4 Measurement Error Models	146
5.7 Multiple Magnetometer Based Magnetic Field Measurements	147
5.8 Single Magnetometer based Heading Measurements	148
5.9 Quasi-Static Field (QSF) based Attitude and Angular Rate Measurements.....	149
5.9.1 Quasi-Static Magnetic Field (QSF) Detector Realization.....	150
5.9.2 Statistical Analysis of the QSF Detector	151
5.9.3 Use of QSF Detected Periods for Attitude and Gyroscope Error Estimation	155
5.9.4 QSF Measurement Error Model.....	156
5.10 Overall Scheme for the Proposed Attitude Estimator.....	159
CHAPTER SIX: EXPERIMENTAL ASSESSMENT OF THE PROPOSED ALGORITHMS	161
6.1 Test Setup	161
6.2 Assessment Criterion	163
6.3 Selection of the Test Environments	164
6.3.1 Urban Canyons.....	164
6.3.2 Shopping Malls	166
6.4 Single Magnetometer based Heading Estimator.....	168
6.4.1 Urban Canyon Environment	168
6.4.2 Indoor Shopping Mall	172
6.5 Quasi-Static Field based Attitude and Rate Gyroscope Error Estimator.....	176
6.5.1 Urban Canyon Environment	176
6.5.2 Indoor Shopping Mall	180
6.6 Combined SM and QSF based Attitude Estimator	183
6.6.1 Urban Canyon Environment	184
6.6.2 Indoor Shopping Mall	186
6.7 Multi-Magnetometer Platform based Magnetic Field Measurements	188
6.7.1 Urban Canyon Environment	188
6.7.2 Indoor Shopping Mall	191
6.8 Combined MMP and QSF Based Attitude Estimator.....	194
6.9 Performance of Attitude Estimator in Different Environments.....	195
CHAPTER SEVEN: CONCLUSIONS AND RECOMMENDATIONS	198
7.1 Conclusions.....	198
7.2 Recommendations.....	202
APPENDIX A: DETECTION OF GOOD MAGNETIC FIELD USING TOTAL FIELD MEASUREMENTS	213
APPENDIX B: ATTITUDE DETERMINATION USING GYROSCOPES	216

APPENDIX C: MULTI-MAGNETOMETER PLATFORM BASED LOCAL MAGNETIC FIELD ESTIMATOR	221
APPENDIX D: QUASI-STATIC FILED DETECTOR	223

List of Tables

Table 3-1: Pedestrian navigation system dimensions.	54
Table 3-2: MSP's inertial sensor calibration parameters.....	87
Table 3-3: Magnetometer calibration parameters.	87
Table 3-4: Stochastic modeling of inertial and magnetic field sensors.	88
Table 4-1: High sensitivity magnetic field sensor specifications.	93
Table 4-2: Environments selected for the magnetic field survey.	94
Table 4-3: Test parameter variances for MAD.	119
Table 4-4: Selected thresholds for individual detectors.....	121
Table 4-5: Expected heading error ranges for different detectors.	123
Table 4-6: Design parameters for the output membership functions.....	124
Table 5-1: Parameters selected for the QSF detector.....	153

List of Figures

Figure 2-1: Z-axis magnetic field of a circular current loop.....	24
Figure 2-2: Magnetic field at an arbitrary point.....	26
Figure 2-3: Magnetic field in cylindrical coordinate system. θ is used for resolving the magnetic field from spherical to cylindrical coordinate system.	29
Figure 2-4: Magnetic field generated by a dipole in cylindrical coordinate system.....	30
Figure 2-5: Magnetic field components in cartesian coordinate system.....	31
Figure 2-6: Magnetic field in presence of two dipoles.	33
Figure 2-7: Combined magnetic field of the two dipoles as shown in Figure 2-6.....	33
Figure 2-8: Magnetic field caused by moment M1.....	34
Figure 2-9: Magnetic field caused by moment M2.....	34
Figure 2-10: Earth's magnetic field in cartesian coordinate system.	35
Figure 2-11: Declination angle in degrees over Canada (24Aug10). Colour map shows the declination angle in degrees.	36
Figure 2-12: Earth's magnetic field model in presence of a perturbation source.....	39
Figure 2-13: Earth's magnetic field as sensed in the absence of perturbation.	40
Figure 2-14: Magnetic field of the perturbation source.	40
Figure 2-15: Total magnetic field and its components in the presence of the perturbation source.....	41
Figure 2-16: Heading estimates from clean and perturbed magnetic field.....	42
Figure 3-1: Magnetic field sensors, their sensitivity ranges and possible applications.	45
Figure 3-2: Wheatstone bridge arrangement for sensing the applied magnetic field.	48
Figure 3-3: Geometrical arrangement of six magnetometers in a plane.....	51
Figure 3-4: Multiple Magnetometer Platform (MMP).....	52
Figure 3-5: Embedded navigation system architecture.....	54

Figure 3-6: Multiple Sensor Platform (MSP).	55
Figure 3-7: Inertial sensor calibration setup.	61
Figure 3-8: Use of induction coil to compensate for hysteresis effects.	65
Figure 3-9: Effects of hard iron on sensed magnetic field.	66
Figure 3-10: Effects of soft iron on sensed magnetic field.	67
Figure 3-11: Calibration of MSP's magnetic field sensors. All axes are in Gauss.	77
Figure 3-12: Impact of calibration on measured magnetic field.	78
Figure 3-13: Obtaining the PSD for wide band noise.	80
Figure 3-14: Allan Variance analysis of filtered sensor data for correlated noise.	81
Figure 3-15: AV model for exponentially correlated noise using the rough estimates of PSD and correlation time.	82
Figure 3-16: AV plot for the exponentially correlated noise after tuning the PSD and correlation time.	83
Figure 3-17: Actual versus modeled AV for wide band and exponentially correlated noise.	84
Figure 3-18: Gyroscope Allan Variance, actual versus model.	85
Figure 3-19: Accelerometer Allan Variance, actual versus model.	85
Figure 3-20: Magnetometer Allan Variance, actual versus model.	86
Figure 4-1: Magnetic field data collection setup.	91
Figure 4-2: Calibration of the magnetic field data collection setup.	92
Figure 4-3: Magnetic field data collection indoor.	95
Figure 4-4: Heading error PDFs in different pedestrian navigation environments.	96
Figure 4-5: Total field perturbation PDFs in different pedestrian navigation environments.	97
Figure 4-6: Horizontal field perturbation PDFs in different pedestrian navigation environments.	98

Figure 4-7: Vertical field perturbation PDFs in different pedestrian navigation environments.....	99
Figure 4-8: Inclination angle error PDFs in different pedestrian navigation environments.....	100
Figure 4-9: Dual magnetometer setup at observation point p	101
Figure 4-10: Magnetic field as measured by MAG 1 during a pedestrian walk in a perturbed environment.....	102
Figure 4-11: Magnetic field as measured by MAG 2 during pedestrian's walk in a perturbed environment.....	103
Figure 4-12: Magnetically derived heading in absence and presence of perturbation. ..	105
Figure 4-13: Detection of a destructive perturbation.....	106
Figure 4-14: Gradient analysis of MAG 2 components.....	107
Figure 4-15: Perturbation mitigation using multiple magnetometers.....	108
Figure 4-16: Clean versus perturbed magnetic field parameters.....	110
Figure 4-17: Fuzzy Inference System (FIS) for MAD.....	118
Figure 4-18: ROC curves for individual detectors.....	120
Figure 4-19: Performance of total magnetic field based detector for different window sizes.....	122
Figure 4-20: Relationship between threshold and expected heading errors.....	123
Figure 4-21: Output membership function for FIS.....	124
Figure 5-1: Reference frames used for representing position and attitude.....	129
Figure 5-2: Overall flow of information in a Kalman filter.....	136
Figure 5-3: Information flow in a discrete time Kalman filter.....	139
Figure 5-4: PDF of total field gradient during constant field periods.....	152
Figure 5-5: ROC for different window sizes.....	153
Figure 5-6: Continuous QSF periods and their occurrence.....	155

Figure 5-7: Duration of gaps between QSF periods.	155
Figure 5-8: Attitude estimator using gyroscopes and magnetometers.....	160
Figure 6-1: Test data collection setup by author.....	163
Figure 6-2: Downtown Calgary data collection environment (Google Maps).	165
Figure 6-3: Data collection in downtown Calgary.....	166
Figure 6-4: Market Mall Calgary data collection environment (Google Maps).....	167
Figure 6-5: Data collection in Market Mall Calgary.	168
Figure 6-6: First urban canyon loop with a strong perturbation source – SM.....	169
Figure 6-7: Trajectory for the third loop of urban canyon.....	170
Figure 6-8: Trajectories obtained using SM measurements for error estimation.	171
Figure 6-9: Impact of SM measurements on computed trajectory.	171
Figure 6-10: Continuous trajectory for the urban canyon using SM measurements.	172
Figure 6-11: Trajectory of first loop in shopping mall.	174
Figure 6-12: Trajectory of second loop in shopping mall.....	175
Figure 6-13: Combined trajectory for the two loops in shopping mall.....	176
Figure 6-14: Total field and QSF detections for similar paths in urban canyon.....	177
Figure 6-15: Trajectory obtained using QSF measurements in urban canyon.....	178
Figure 6-16: Trajectories obtained using QSF in urban canyon.	179
Figure 6-17: Continuous trajectory in urban canyon using QSF.	180
Figure 6-18: Total field and QSF detections for similar paths in shopping mall.	181
Figure 6-19: Trajectory obtained using QSF measurements in shopping mall.	182
Figure 6-20: Combined trajectory obtained using QSF in shopping mall.	183
Figure 6-21: Comparison of QSF and QSF+SM measurements.	184
Figure 6-22: Continuous trajectory obtained using QSF+SM in urban canyon.	185

Figure 6-23: Simulated outage of SM measurements for QSF+SM in urban canyon....	186
Figure 6-24: Trajectory estimated in shopping mall using QSF+SM.....	187
Figure 6-25: Combined trajectory estimates for the two loops using QSF+SM in Shopping Mall.....	188
Figure 6-26: Trajectory obtained in urban canyon using MMP measurements.....	189
Figure 6-27: Individual trajectories obtained in urban canyon using MMP.....	190
Figure 6-28: Continuous trajectory obtained using MMP in urban canyon.	191
Figure 6-29: Trajectory obtained using MMP measurements in shopping mall.	192
Figure 6-30: Individual trajectories obtained in shopping mall using MMP.....	193
Figure 6-31: Continuous trajectory obtained in shopping mall using MMP.	193
Figure 6-32: Trajectory obtained using QSF+MMP in shopping mall.....	195
Figure 6-33: Attitude estimation performance in urban canyon.....	196
Figure 6-34: Attitude estimation performance in shopping mall.....	197

List of Symbols and Abbreviations

Symbol	Definition
A	Vector potential of magnetic field
B	Magnetic field
b	Sensor bias
D	Declination angle
F	Magnetic field intensity
f	Specific force vector
g	Acceleration due to gravity
H	Horizontal field
I	Inclination angle
L	Distance between current elements
l	Current loop
M	Magnetic moment
N	Sensor misalignment
q	Quaternion
S	Sensor scale factor
T	Tesla
Z	Vertical field
θ	Pitch angle
λ	LRT ratio
ϕ	Roll angle
ψ	Heading angle
ω	Angular velocity vector
μ_0	Magnetic permeability
∇	Nabla operator
$\tilde{\cdot}$	sensor output (raw)
$\varepsilon.$	Noise vector
$\ \cdot\ $	Norm
τ_c	Correlation time
σ^2	Variance
$\gamma.$	Test statistics threshold
P_f	Probability of false alarm
P_d	Probability of detection
Q_q	Skew symmetric form of quaternion

\bullet^+	Update
\bullet^-	Prediction
\bullet_k	k^{th} epoch
\mathbf{x}_k	State vector
\mathbf{z}_k	Measurement vector
$\mathbf{F}(t)$	Dynamics matrix
$\mathbf{G}(t)$	Shaping matrix
$\mathbf{H}(t)$	Design matrix
$\mathbf{w}(t)$	System noise
$\mathbf{v}(t)$	Measurement noise
$\Phi_{k,k+1}$	State transition matrix
\mathbf{Q}_k	Process noise matrix
\mathbf{P}_k	State covariance matrix
\mathbf{R}_k	Measurement covariance matrix
\mathbf{K}_k	Kalman gain
\bullet^s	Sensor frame
\bullet^n	Navigation frame
\bullet_a^b	Measurements of a frame expressed in b frame
\mathbf{C}_a^b	DCM from a frame to b frame

Abbreviation	Definition
AGPS	Assisted Global Positioning System
ALS	Adaptive Least Squares
AMR	Anisotropic Magneto Resistive
AoA	Angle of Arrival
AV	Allan Variance
BTS	Base transceiver Station
CGRF	Canadian Geomagnetic Reference Frame
CUPT	Coordinate Update
DCM	Direction Cosine Matrix
DoF	Degrees of Freedom
DSC	Digital Signal Controller
ECI	Earth Centred Inertial
EKF	Extended Kalman Filter
FIS	Fuzzy Inference System
GLRT	Generalized Likelihood Ratio Test
GMR	Giant Magneto Resistive
GNSS	Global Navigation Satellite System
GPS	Global Positioning System
HSGPS	High Sensitivity GPS
IC	Integrated Chip
IED	Improvised Explosive Device
IMU	Inertial Measurement Unit
INS	Inertial Navigation System
LEO	Low Earth Orbit
LCD	Liquid Crystal Display
LS	Least Squares
LLF	Local Level Frame
MAD	Magnitude and Angle based Detector
MEMS	Micro Electro Mechanical System
MI	Magneto Impedance
MLE	Maximum Likelihood Estimator
MMP	Multiple Magnetometer Platform
MR	Magneto Resistive
MSP	Multiple Sensor Platform
NED	North East Down
PC	Personal Computer
PDF	Probability Density Function
PDR	Pedestrian Dead Reckoning
PNS	Pedestrian Navigation System
PSD	Power Spectral Density
QSF	Quasi-Static Field
RF	Radio Frequency

RFID	Radio Frequency Identification
ROC	Receiver Operating Characteristics
RSS	Received Signal Strength
SD	Serial Data
SM	Single Magnetometer
TERCOM	Terrain Contour Matching
USB	Universal Serial Bus
WiFi	Wide Fidelity
ZUPT	Zero Velocity Updates
3D	Three Dimensional

Chapter One: **Introduction and Overview**

With the advent of Micro Electro Mechanical Systems (MEMS) and continuing progress in Integrated Chip (IC) fabrication technology, the processing power and sensor elements required for navigation applications can now be incorporated in portable devices (Davidson et al 2009, Ladetto et al 2000). Due to these technological advances, providing a continuous navigation solution to pedestrians in varying urban environments has become a major field of interest for researchers (Inoue et al 2009, Riehle et al 2008). This is not only important from the pedestrians' perspective but is also critical for emergency service providers (Renaudin et al 2007). Due to lack of availability of reliable information sources indoor, not all of the navigation parameters are observable, which causes unbounded error growth in the navigation solution. One of the most critical parameters for indoor navigation is orientation. Magnetic field information can be used for improving the observability and reliability of orientation estimates.

1.1 Background

Navigation is the process of estimating the parameters necessary for describing ones location with respect to some reference frame. These navigation parameters can be classified into two categories. The first category deals with linear displacements and provides information regarding the evolution of position and velocity. The second category deals with angular displacements and describes ones orientation/attitude with respect to a reference frame (Titterton & Weston 2004).

1.1.1 Pedestrian Navigation

The process of providing pedestrians with guidance information, which in some way can be used for simplifying the task of reaching a particular destination, is called pedestrian navigation. It differs from other navigation applications (e.g. land vehicle, sea vessel and aircraft navigation) due to the versatility of environments in which the pedestrian navigation system has to work. Sometimes the pedestrian is strolling in a park outdoors while some other times, the subject is in an urban environment either shopping or going to work. The rest of the time is spent indoors. All of these environmental changes constitute different navigation scenarios for pedestrian navigation. Of all the possible scenarios for pedestrian navigation, the indoor navigation scenario is the most challenging one. These challenges arise from the amount and reliability of information available for estimating the navigation parameters. The challenges and differences, which can be directly identified, correspond to the type of sensors and navigation technologies that can be used (Sternberg & Fessele 2009). Furthermore the environmental versatility for pedestrian navigation imposes the use of self-contained navigation systems that can provide users with navigation parameters irrespective of the availability of external aids.

1.1.2 Systems/ Techniques for Pedestrian Navigation

Pedestrian navigation can be accomplished using either some man-made or planetary/universal information source. Most of the work done so far utilizing manmade information sources revolves around the use of Radio Frequency (RF) signals (Alonso et al 2009, Inoue et al 2009, Luimula et al 2010, Shen et al 2010, Steiner & Wittneben 2010, Su & Jin 2007). Although RF information sources can be used for positioning,

availability in indoor environments becomes the main hurdle for their feasibility. The use of other planetary/universal information sources for estimating navigation parameters is also common. Systems incorporating sensors that can measure planetary/universal forces that can be used for navigation purposes are known as self-contained navigation systems. These systems often integrate a well known navigation methodology, namely an Inertial Navigation System (INS) along with some extra sensors. As the name suggests, INS utilizes inertial sensors that measure the inertial forces/ rates, performs navigation mechanization and provides user with the necessary navigation parameters (Titterton & Weston 2004). These sensors are gyroscopes and accelerometers. Although such systems can be very accurate and reliable depending on the quality of sensors used, in the context of pedestrian navigation where cost, size and power consumption dictate sensor selection, these systems are of the lowest accuracy and reliability (Ramalingam et al 2009). In order to improve the navigation solution of the latter, other aiding sensors/ information sources are utilized, which can be categorized into the use of additional physical measurements or the specificities of the human walk, i.e. its biomechanics.

The first category deals with the use of extra sensors that can measure different physical forces. For example with magnetometers, the measure of the Earth's magnetic field can assist the estimation of the direction of motion, which can further be used for estimating errors associated with gyroscopes (Bekir 2007). On the other hand by measuring atmospheric pressure, it is possible to estimate the altitude which is one of the linear position parameters near the Earth's surface (Tang et al 2005).

The second technique deals with the use of special constraints dictated by the biomechanical description of the user's dynamics (Suh & Park 2009). These include Zero velocity UPdaTes (ZUPT), which can take place whenever the user is stationary. The idea is based on the fact that when the user is not moving, the sensor outputs will be governed only by sensor errors and hence these sensor outputs can be used to estimate the sensor errors.

In addition to these two aiding categories, man-made information sources are also being investigated for pedestrian navigation. Systems capable of utilizing such information sources are known as embedded navigation systems. For example Radio Frequency IDentification (RFID) can be used for re-initializing some of the navigation parameters. This aiding technique is known as Coordinate UPdaTe (CUPT) (Sohne et al 1994). Similar techniques can be used in scenarios where information regarding the proximity to some waypoint is available (Zhou et al 2010). WiFi and Base Transceiver Station (BTS) based triangulation approaches are also becoming common for pedestrian navigation (Tarrío et al 2008), (Hamani et al 2007). In such approaches, the position information regarding WiFi or BTS node along with Received Signal Strength (RSS) or Angle of Arrival (AoA) are utilized to estimate pedestrian's position. The Assisted GPS (AGPS) approach is also becoming popular for aiding GPS signal acquisition and tracking indoor (Karunanayake et al 2004).

The limitations of using man-made information sources for pedestrian navigation are twofold. First they cannot be effectively used for pedestrian navigation because of the above availability constraints. The second limitation of this technique is linked to the fact that not all of the errors associated with navigation parameters can be estimated using these constraints. For example using ZUPT or CUPT, it is impossible to completely estimate the errors associated with the orientation parameters, which may cause an error growth of the third order in position estimates (Farrell & Barth 1999). The same can be said for RF triangulation techniques.

As is evident from the above discussion, a number of approaches can be taken to target pedestrian navigation. All approaches except one depend on some man-made information system, namely self-contained navigation systems. Also it is quite evident that the orientation estimate is the main bottleneck for these systems to be efficient for pedestrian navigation keeping in mind that the availability of ZUPT/CUPT that can be used for compensating for the rest of the errors to some extent (Ladetto & Merminod 2002). Using the Earth's magnetic field for estimating the orientation parameters may solve this problem and improve the overall accuracy and reliability of embedded navigation systems for pedestrians especially in indoor environments.

1.2 Earth's Magnetic Field for Orientation Estimation

The Earth's magnetic field is a naturally occurring planetary phenomenon. It follows the principles of dynamo theory and is created by the constant motion of Earth's outer core

composed mostly of molten iron (Campbell 2001). This field was first discovered in ancient China around 200 B.C. and was first used for spiritual purposes before finally being used for navigation. The Earth's magnetic field can be modeled as a dipole and follows the basic laws of magnetic fields summarized and corrected by Maxwell (Knoepfel 2000, Milsom 2003). In order to fully exploit the Earth's magnetic field, it is necessary to have a complete understanding of Maxwell's equations along with the adaptation of these generic field equations for different combinations of magnetic fields and magnetic substances encountered in indoor environments.

The Earth's magnetic field is a three dimensional vector which originates at the positive pole of the dipole (known as Magnetic South) and ends at the magnetic North pole. For centuries, the Earth's magnetic field has been successfully used for navigation purposes. The effective use of this remarkable information source dates back to around 1600 AD and was well documented by the Europeans at the time. In those days, the property of the magnetic moment (documented in 1800s), which now states that any material with magnetic properties (depends on the magnetic flux alignment at atomic level) experiences a force in the presence of a magnetic field was used (Knoepfel 2000). Thus by using an iron ore, like magnetite, and hanging it in the air or suspending it in some viscous liquid to damp the fluctuations due to ones motion, a reference with respect to the local magnetic field can be found. Later during the exploration age, the anomalies and symmetry issues with the magnetic field were discovered accidentally mostly by explorers (Campbell 2001).

Today with the advancements in sensor technology, this field can be precisely measured with the help of an electronic sensor commonly known as the magnetometer. Based on their application areas, magnetometers can be classified as quantum, coil (fluxgate), magneto-inductive (also known as magneto-impedance) and magneto-resistive sensors (Ripka 2001). Using the sensor measurements with the proper transformation of the field components to the horizontal plane and knowing the declination angle specific to the measurement area and time, a simple trigonometric operation can be used to estimate the geographic heading. It is also possible to estimate the roll and pitch components of orientation parameters using magnetic field data (Steele 2003).

1.3 Uses of Magnetic Field

1.3.1 Non Navigation Applications

Magnetic field information is being used in a number of applications. Here only applications that are to some extent related to orientation estimation as well as to the indoor navigation scenario are discussed.

One of the applications of magnetometers is in medical science where it is being used for studying and analyzing human body limb motion for bio-mechanical applications (Bachmann et al 2003, Sonoda 1995). Here different natural postures of the human body are studied and analyzed using magnetometer networks to design the best artificial replica of different human limbs. Later this study was used to design reliable and effective control systems for artificial limbs thus bringing them as close as possible to reality.

Another application is in industrial/automotive control where magnetometers are used for measuring rotor speeds and angular displacements (Masson et al 2009). This contactless angular displacement technology is gaining popularity in control applications where it is not desirable to have mechanical contacts due to their costly maintenance that results from wear and tear. Here a strong permanent magnet is used as a field source and the magnetic field strength is measured at a fairly close distance to the source. Typically the magnet is mounted on a rotating platform whereas the sensor is fixed on the stationary surface. All changes in the orientation of the local magnetic field are measured by the sensor and then transformed to angular displacements.

Magnetometers are also being used in space applications. Attitude control of micro satellites uses high precision magnetometers for robust space vehicle control (Diaz-Michelena 2009). Here the Earth's magnetic field components are measured and with the help of magneto-torquers, artificial magnetic fields are generated that interact with the Earth's field to produce small magnetic momentums that can be used for manoeuvring these small satellites, which are usually in Low Earth Orbit (LEO).

Magnetometers are also used for traffic control and vehicle detection. In this application the magnetic signature of different vehicles is used for not only detecting the presence of a vehicle but also for categorizing the vehicle according to its size (Cheung et al 2005). This application is proving to be very useful for autonomous and intelligent traffic control. The effects of different ferro-magnetic materials on the Earth's magnetic field

are used here for the detection and classification of vehicles. This phenomenon of the effect of different types/sizes of material on magnetic field is very important from an orientation perspective in indoor environments and requires further investigation.

Airport security gates and other sensitive places provide another example of the use of the magnetic field. Here again magnetic field information is used for detecting metals and disallowed tools being carried by pedestrians/passengers. Now this application has been further improved thanks to advances in magnetic field sensor technology and this same principle is being utilized for detecting Improvised Explosive Devices (IEDs), land mines etc. Even more challenging military applications are also utilizing magnetometers for surveillance purposes. Very sensitive magnetometers are used for submarine as well as under water mine detection (Wiegert et al 2008). Today even the magnetic disturbances caused by submarines at shallow depths can be detected by an airborne magnetometer with decimetre accuracy (Sheinker et al 2009).

1.3.2 Navigation Applications

Another major application of magnetometers is navigation in general and orientation estimation in particular. Magnetic field information has been used for navigation purposes for at least 10 centuries. With improvements and innovations in sensor technology, this source of information can be measured using very small and cost effective instruments. This sensor miniaturization and cost/power reduction has made it possible to use them in portable navigation devices and hence for pedestrian navigation.

Although magnetometers have been successfully used for outdoor navigation applications like aircraft, land and sea vehicles, limited success has been encountered by researchers for all of the pedestrian navigation scenarios. For pedestrian navigation in the outdoors, magnetometers are used to estimate the errors associated with yaw gyroscopes as well as for re-initializing the orientation parameters (Wang et al 2008), but indoor scenarios offer a lot of challenges when using magnetic field information.

One possible processing of magnetometers' data for indoor navigation is inspired by an outdoor application. Here the non-symmetric nature of Earth's magnetic field is exploited to propose a localization method in the vicinity of Earth that uses detailed magnetic field maps/charts and a terrain navigation technique (Goldenberg 2006). A similar solution for indoor localization has been recently presented by Storms & Raquet (2009). A detailed indoor survey of the magnetic field is first performed and then utilized for indoor navigation by adapting a terrain navigation algorithm commonly used in Terrain Contour Matching (TERCOM). In order to improve the accuracy of this algorithm, the authors suggest conducting a very high resolution magnetic mapping of the indoor environment. In this work an indoor magnetic map with a resolution of 40 cm is generated. Results show position accuracies within 10 cm with occasional 60 cm positioning errors. The main cause of such large errors is identified as change in the magnetic signature of specific locations.

Another very interesting approach uses artificial strong magnetic field sources at known locations and sensing this field to capture user's motion (Saber-Sheikh et al 2009). Here the authors have suggested using a strong electromagnet mounted at a fixed location to assess the hip joint movement. Results show a good correlation between this approach and previous studies. This approach could be easily applied for indoor navigation scenarios and could be investigated for its feasibility and effectiveness. Similar studies are also conducted by other researchers (Haverinen & Kemppainen 2009).

Some researchers have tried to process direct magnetic field measurements for orientation estimation by applying special constraints. A robot that executes 360° turns, at high speed, in the horizontal plane at frequent intervals is utilized as a special constraint by Skvortzov et al (2007). Regular sensor calibration is performed based on this manoeuvre.

Finally, another popular approach is to use multiple sensors (gyroscopes, accelerometers) along with magnetometers and perform sensor fusion. Moafipoor et al (2008) has suggested using some quality factors to assess the reliability of magnetic heading in conjunction with tactical grade gyroscopes for indoor environments. Others have utilized MEMS inertial sensors as the primary source for orientation with magnetometers providing measurements for error compensation of these sensors using Kalman filter (Li et al 2008, Xue et al 2009). Most of this work is directed towards outdoor applications where the effects of magnetic field perturbations on orientation estimates are negligible.

1.3.3 Limitations of Previous Work for Navigation Applications

Two major limitations can be identified from the work done so far using magnetic field for navigation, namely

- The magnetometers are not used as standalone sensors for orientation estimation. Researchers have tried to use orientation estimates from magnetic field as extra observations to compensate for the errors associated with other sensors (Li et al 2008, Xue et al 2009). Thus the problem of indoor orientation estimation using magnetometers alone is ignored, which needs to be investigated in order to quantify the impact of magnetic field on estimating the errors associated with the primary orientation sensor, namely the rate gyroscope.
- Secondly pre-existing knowhow of artificial magnetic anomalies is required. Either some man-made infrastructure is being used to generate known magnetic fields or a pre-survey is conducted, which itself translates into a man-made information dependence (Saber-Sheikh et al 2009, Storms & Raquet 2009).

When using known magnetic fields for indoor orientation estimation, similar bottlenecks are encountered as with RF based information sources. Indeed the strength of the magnetic field needs to be sufficient and the magnetometers need to be at a significant distance from perturbation sources in order to distinguish between the earth's magnetic field and the field caused by indoor perturbations (Bachmann et al 2003, Bachmann et al 2004, Sonoda 1995). Using indoor magnetic field maps for navigation also presents limitations. Indeed surveying of any kind is an expensive task. The process for creating a database of such magnetic maps for all indoor environments would be a tedious task not

to mention proper selection of an indoor magnetic field map when one moves from an urban environment to another. Even an error of a few metres can cause one to start using the magnetic map of an adjacent building rather than the one currently occupied. Some extra information might be necessary for this selection. Furthermore indoor magnetic fields are not completely stationary/constant. Changes in the placement and turning on and off of electrical and mechanical equipment can cause the local field to vary. For example, the magnetic field in the vicinity of an elevator will vary depending on which floor the elevator is currently located. Hence the magnetic field generated by the elevator shaft will be different, causing difficulties in using this data to compute a position.

Combining magnetometers with other sensors is interesting but the performance gain depends on the quality of the aiding sensors (Moafipoor et al 2008). For pedestrian navigation, it is desirable to have a very low cost sensor suite and usually such sensors have inherently large errors thus making them useless for magnetic field quality assessment in indoor environments. Such applications make sense only for military or emergency service providers where the critical nature of localizing oneself renders the high grade, high cost sensors useful.

Keeping in mind all of the above mentioned issues regarding magnetic field information in indoor environments, it is desirable to take a deeper look at the factors that contaminate the Earth's magnetic field measurements and establish clearly their limitations for indoor pedestrian navigation. Methods to detect, estimate and reduce the

impact of perturbations on Earth's magnetic field measurements also need to be investigated.

1.4 Proposed Research

In light of the described limitations of existing work for navigation in the indoors, the proposed research investigates the use of magnetic field information for improving the reliability and accuracy of orientation estimates in indoor environments. Indoor magnetic field modeling, magnetic field perturbation detection, estimation and mitigation, optimal sensor error modeling and reliable orientation estimation are the primary focus of this research.

1.4.1 Major Objectives and Contributions

1. Since the primary objective of this work is to investigate new approaches for orientation estimation using indoor magnetic field, existing orientation estimation approaches are reviewed focusing on their possible adaptation for magnetic field information. For this purpose, working principles of different magnetic field sensors are investigated for their usefulness and limitations in indoor environments.
2. As the Earth's magnetic field needs to be reliably measured in order to derive magnetic orientation, the effects of indoor environments on the Earth's magnetic field are assessed. Different indoor environments are surveyed for this analysis.

Measurements from hand-held as well as body fixed locations are considered, which make this research more complex as compared with existing approaches.

3. A detailed theoretical study of the magnetic field and its propagation in different environments is carried out. Magnetic field modeling in the presence of perturbation sources is performed based on the theory of magnetic field. A detailed calibration algorithm for magnetometers is also developed, which has been published in (Renaudin et al 2010).
4. The properties of magnetic field that can be used for assessing the perturbations in indoor environments are identified. Based on these properties, possible methods of detecting perturbations and improving the orientation estimates are investigated.
5. A reliable perturbation mitigation technique is developed in order to use magnetometers in indoor environments. Different techniques and sensor arrangements are investigated to find the best combination for magnetic perturbation mitigation. Some of this work has been published in Afzal et al (2010) while a patent has also been filed targeting one of the novel contributions of this research in the field of pedestrian navigation, namely the QSF detection method described in Section 5.9.
6. An orientation estimator is developed. The results of this estimator are compared with other orientation estimation techniques in use. The impact of the new estimator on pedestrian navigation parameters in indoor environments is analyzed. Finally the effectiveness of the proposed magnetic field based orientation

estimator in identifying and correcting for the errors associated with the primary sensor for orientation estimates (rate gyroscope) is investigated.

1.5 Thesis Organization

In this chapter, a brief introduction to pedestrian navigation is provided. Work done for pedestrian navigation using magnetic field information is the primary agenda of this chapter. Limitations of previous work are identified. A brief overview of how these limitations are addressed in this research is provided including the overall thesis organization. The major contributions of this research in indoor orientation estimation are highlighted.

Chapter 2 addresses the theoretical background of the Earth's magnetic field. Orientation estimation, magnetic field modeling, effects of magnetic anomalies on Earth's magnetic field as well as orientation estimates are described here. This chapter provides all the necessary theoretical knowledge for the subsequent chapters. Based on this theoretical background, the assessment of magnetic field perturbations in indoor environments is conducted keeping in view the properties and models of the magnetic field.

Chapter 3 describes the design and development of a custom hardware platform required to support the presented research. This includes a multiple magnetometer platform as well as the multiple sensor platform. Later, this chapter describes sensor error modeling and calibration procedures, which are necessary for the low cost sensors used in this research.

Chapter 4 starts with the assessment of indoor magnetic perturbations and investigates the impact of related anomalies on heading estimates. Later in this chapter, novel perturbation mitigation techniques are investigated, which are then utilized with magnetic field based orientation estimators.

In Chapter 5, all necessary algorithmic developments are described along with the sensor fusion of magnetometers with rate gyroscopes for a combined orientation estimator, which is utilized for assessing the impact of the proposed algorithms on rate gyroscope error estimation. A novel scheme of utilizing the perturbed magnetic field for estimation of rate gyroscope errors is also described.

Chapter 6 presents the experimental assessments of the proposed algorithms in outdoor urban canyon and indoor shopping mall environments. The reliability and accuracy of the perturbation mitigation and the final orientation estimation are evaluated in the position domain. A repeatability criterion is utilized for assessing the accuracy and reliability of the proposed algorithms.

Finally in Chapter 7, all of the results achieved along with the novel contributions of this research are summarized and possible future research directions are identified.

Chapter Two: **Theory of the Magnetic Field for Indoor Orientation Estimation**

Before utilizing the magnetic field measurements for pedestrian navigation applications in indoor environments, its detailed modeling is necessary. This chapter starts with modeling the magnetic field generated by a single dipole and then extends these relationships to take into account the field generated by multitude of dipoles, which is used for the development of perturbation detection and mitigation techniques described in the later chapters.

2.1 The Magnetic Field Model

Before going into the details of magnetic field modeling, some important laws need to be recalled in order to lay the foundations for its mathematical modeling.

2.1.1 Ampere's Law

In the early nineteenth century, André-Marie Ampère (1775-1836) observed that if currents are flowing in two circuits (a wire connected to a current source), they interact with each other, i.e. some sort of mechanical force acts on them (Kaufman et al 2009). This force depends on the magnitude of currents, the direction of charge movement, the shape and dimension of circuits and their relative positions. Based on his experiments, he formulated a relationship between this mechanical force and the above mentioned parameters, now called Ampère's Law and written as

$$\mathbf{F}_p = \frac{\mu_0}{4\pi} I_p I_q \oint_{L_1} \oint_{L_2} \frac{d\mathbf{l}_p \times [d\mathbf{l}_q \times \mathbf{L}_{qp}]}{L_{qp}^3}, \quad (2.1)$$

where I_p and I_q are the magnitudes of current in circuit elements $d\mathbf{l}_p$ and $d\mathbf{l}_q$ respectively, L_{qp} is the distance between these elements and μ_0 is the magnetic permeability. L_1 and L_2 are the closed loop lengths of the two circuits.

2.1.2 Biot-Savart Law

The force F_p experienced by the current element p is caused by a field, which itself is created by the flow of currents. This field is known as the magnetic field and it is introduced through Ampère's law as

$$d\mathbf{F}_p = I_p d\mathbf{l}_p \times d\mathbf{B}_p, \quad (2.2)$$

where

$$d\mathbf{B}_p = \frac{\mu_0}{4\pi} I_q \frac{d\mathbf{l}_q \times \mathbf{L}_{qp}}{L_{qp}^3}. \quad (2.3)$$

Equation (2.3) establishes a relationship between the elementary currents in circuit elements and the field caused by these elements. This equation is known as the Biot-Savart law. The magnitude of the magnetic field is given by

$$dB_p = \frac{\mu_0}{4\pi} I_q \frac{dl}{L_{qp}^2} \sin(\mathbf{L}_{qp}, d\mathbf{l}), \quad (2.4)$$

where $(\mathbf{L}_{qp}, d\mathbf{l})$ is the angle between \mathbf{L}_{qp} and $d\mathbf{l}$ respectively. $d\mathbf{B}_p$ is perpendicular to these vectors. The unit vector characterizing the direction of the magnetic field is given by

$$\mathbf{b}_0 = \frac{d\mathbf{l} \times \mathbf{L}_{qp}}{|d\mathbf{l} \times \mathbf{L}_{qp}|}. \quad (2.5)$$

Equation (2.4) establishes a relation between the magnetic field and linear currents, but in reality, volume currents should be considered. Linear and volume currents are related by

$$I dl = \mathbf{j} dS dl = \mathbf{j} dV. \quad (2.6)$$

Here \mathbf{j} is the current density vector, dS is the elementary surface and dV is the elementary volume enclosing the elementary currents. Substituting for the elementary volume in Equation (2.3), the Biot-Savart law becomes

$$d\mathbf{B}_p = \frac{\mu_0}{4\pi} \frac{\mathbf{j}_q \times \mathbf{L}_{qp}}{L_{qp}^3} dV. \quad (2.7)$$

Integrating Equation (2.7) yields

$$\mathbf{B}_p = \frac{\mu_0}{4\pi} \int_V \frac{\mathbf{j}_q \times \mathbf{L}_{qp}}{L_{qp}^3} dV. \quad (2.8)$$

From Equation (2.8), it can be observed that current is the sole generator of a magnetic field. Also as by the definition of the current density, \mathbf{j}_q is always closed (currents going out of the element are equal to currents entering it), therefore the field generated is also of a closed nature, i.e. a vortex field (Kaufman et al 2009).

2.1.3 The Vector Potential of the Magnetic Field

The relationship between current and magnetic field given by Biot-Savart law is somewhat complex for modeling. In order to simplify this law, a fictitious vector is introduced here. It is known as the vector potential of the magnetic field, which is derived herein.

Expanding the term $\mathbf{L}_{qp}L_{qp}^{-3}$ in Equation (2.8), one gets

$$\frac{\mathbf{L}_{qp}}{\|\mathbf{L}_{qp}\|^3} = \left(\frac{x_q - x_p}{\|\mathbf{L}_{qp}\|^3}, \frac{y_q - y_p}{\|\mathbf{L}_{qp}\|^3}, \frac{z_q - z_p}{\|\mathbf{L}_{qp}\|^3} \right), \quad (2.9)$$

where $\|\mathbf{L}_{qp}\| = \sqrt{(x_q - x_p)^2 + (y_q - y_p)^2 + (z_q - z_p)^2}$.

Upon further simplification, it can be shown that

$$\frac{\mathbf{L}_{qp}}{\|\mathbf{L}_{qp}\|^3} = \overset{q}{\nabla} \frac{1}{\|\mathbf{L}_{qp}\|} = -\overset{p}{\nabla} \frac{1}{\|\mathbf{L}_{qp}\|}, \quad (2.10)$$

where $\overset{q}{\nabla} = \left(\frac{\partial}{\partial x_q}, \frac{\partial}{\partial y_q}, \frac{\partial}{\partial z_q} \right)$, also known as the nabla operator or the gradient.

Substituting Equation (2.10) in Equation (2.8), one gets

$$\mathbf{B}_p = \frac{\mu_0}{4\pi} \int_V \mathbf{j}_q \times \overset{q}{\nabla} \frac{1}{\|\mathbf{L}_{qp}\|} dV = \frac{\mu_0}{4\pi} \int_V \overset{p}{\nabla} \frac{1}{\|\mathbf{L}_{qp}\|} \times \mathbf{j}_q dV. \quad (2.11)$$

Using the vector identity for curl operation ($\nabla \times$),

$$\nabla \times (\phi \mathbf{a}) = \nabla \phi \times \mathbf{a} + \phi (\nabla \times \mathbf{a}), \quad (2.12)$$

Equation (2.11) becomes

$$\mathbf{B}_p = \frac{\mu_0}{4\pi} \int_V \overset{p}{\nabla} \times \frac{\mathbf{j}_q}{\|\mathbf{L}_{qp}\|} dV - \frac{\mu_0}{4\pi} \int_V \frac{\overset{p}{\nabla} \times \mathbf{j}_q}{\|\mathbf{L}_{qp}\|} dV. \quad (2.13)$$

As \mathbf{j}_q depends only on q , its curl with respect to point p is zero. Therefore, Equation

(2.13) reduces to

$$\mathbf{B}_p = \frac{\mu_0}{4\pi} \int_V \overset{p}{\nabla} \times \frac{\mathbf{j}_q}{\|\mathbf{L}_{qp}\|} dV. \quad (2.14)$$

Here the differentiation (curl operation) is performed with respect to the point p whereas the integration is performed with respect to point q , enclosed in the elementary volume dV , thus allowing one to interchange these two operations. Equation (2.14) becomes

$$\mathbf{B}_p = \nabla_p \times \frac{\mu_0}{4\pi} \int_V \frac{\mathbf{j}_q}{\|\mathbf{L}_{qp}\|} dV. \quad (2.15)$$

In Equation (2.15), the vector potential for magnetic field is given by

$$\mathbf{A} = \frac{\mu_0}{4\pi} \int_V \frac{\mathbf{j}_q}{\|\mathbf{L}_{qp}\|} dV. \quad (2.16)$$

Therefore the Biot-Savart law now becomes

$$\begin{aligned} \mathbf{B}_p &= \nabla_p \times \mathbf{A} \\ \text{or} \\ \mathbf{B}_p &= \text{curl } \mathbf{A}_p. \end{aligned} \quad (2.17)$$

It can be observed from Equation (2.16) that the vector potential for magnetic field is directly related to the current density. This helps in modeling and visualizing the magnetic fields as well as coming up with a relationship for magnetic moments, which provides a better insight into how magnetic fields generated by different dipoles react with each other.

2.1.4 Divergence of Magnetic Field

As the vector potential for the magnetic field depends on the current density vector, it can be implied that the divergence of this vector potential is zero because the current density vector is always closed:

$$\begin{aligned} \operatorname{div} \mathbf{A} &= 0 \\ \text{or} & \\ \nabla \cdot \mathbf{A} &= 0 \end{aligned} \tag{2.18}$$

Based on Equation (2.17), this further implies that

$$\nabla \cdot \mathbf{B} = 0. \tag{2.19}$$

Equation (2.19) belongs to the set of Maxwell's equations and states that the magnetic field is a closed field (a vortex field) forming the basis for the magnetic field of a dipole.

2.2 Magnetic Field of a Dipole

Using the relationships developed in the preceding section, the magnetic field generated by a dipole can now be mathematically modeled.

2.2.1 Magnetic Field Along the Z-axis

Assume we have a circular current loop as shown in Figure 2-1. The observation point p is on the z-axis, which passes through the center of the current loop.

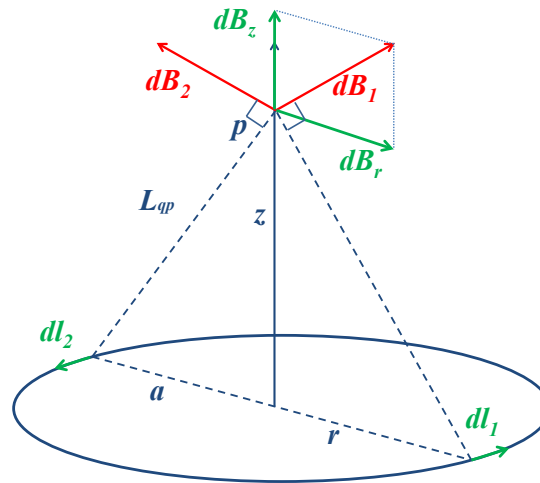


Figure 2-1: Z-axis magnetic field of a circular current loop.

In this case the vector potential of the magnetic field is given by

$$A_p = \frac{\mu_0}{4\pi} I \oint_L \frac{dl}{\|L_{qp}\|}. \quad (2.20)$$

As the distances from elementary currents to the observation point are the same for all currents,

$$A_p = \frac{\mu_0}{4\pi} \frac{I}{\|L_{qp}\|} \oint_L dl. \quad (2.21)$$

As this is a closed path, the integral is equal to zero. Therefore the vector potential of the magnetic field vanishes along the z-axis in this case.

According to Biot-Savart law, the current elements $I dl_i$ create a field composed of two components: dB_z and dB_r along the z and r axes of the cylindrical coordinate system.

It can be observed in Figure 2-1 that the horizontal (r axis) components are all paired.

This causes the total horizontal field component to vanish leaving only the vertical field components. The magnitude of this vertical field component is given by

$$dB_{zp} = \frac{\mu_0}{4\pi} I \frac{dl}{\|\mathbf{L}_{qp}\|^3} \|\mathbf{L}_{qp}\| \sin 90^\circ \frac{a}{\|\mathbf{L}_{qp}\|}, \quad (2.22)$$

where a is the radius of the current loop as shown in Figure 2-1. Integrating Equation (2.22), the magnetic field along the z-axis becomes

$$B_z = \frac{\mu_0 I \pi a^2}{2\pi (a^2 + z^2)^{3/2}}. \quad (2.23)$$

The magnetic moment of a dipole is the measure of its tendency to align with a magnetic field (Kaufman et al 2009). Mathematically, it is given by

$$M = I \pi a^2. \quad (2.24)$$

Substituting I from Equation (2.24) into Equation (2.23), the latter becomes

$$B_z = \frac{\mu_0 M}{2\pi (a^2 + z^2)^{3/2}}. \quad (2.25)$$

From Equation (2.25), it can be observed that the intensity of the magnetic field does not solely depend upon current or loop radius, but rather on the product $M = I \pi a^2 = IS$ where S is the area enclosed by the current loop.

When the distance z is much greater than the radius a , one gets

$$B_z = \frac{\mu_0 M}{2\pi z^3}. \quad (2.26)$$

An example of interest of this particular case is the Earth's magnetic field.

2.2.2 Magnetic Field of a Dipole at Arbitrary Locations

Assuming that the observation point is located arbitrarily in the new cylindrical coordinate system (r, z, ϕ) , as shown in Figure 2-2, there exists a pair of vector potentials along the closed loop where the current carrying elements have opposite x-axis components which cancel out.

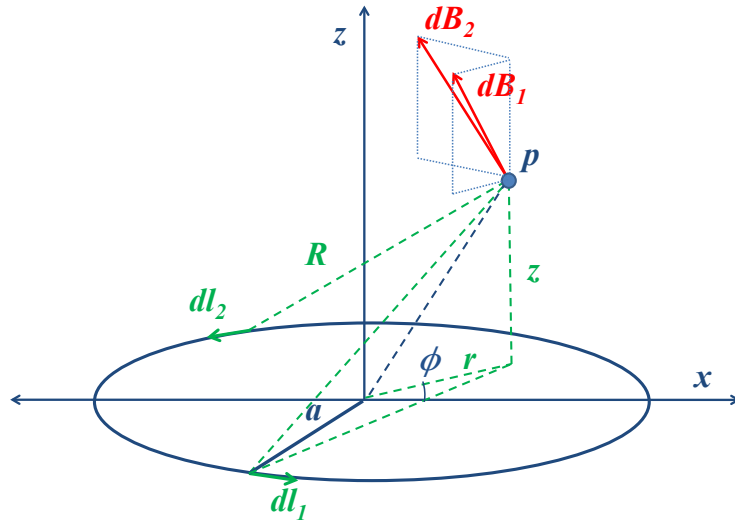


Figure 2-2: Magnetic field at an arbitrary point.

This leaves only the vector potential components along ϕ . Therefore the vector potential is in a plane perpendicular to the z-axis and has only the ϕ component:

$$A_{\phi} = \frac{\mu_0 I}{4\pi} \oint_L \frac{dl_{\phi}}{R}, \quad (2.27)$$

where $dl_{\phi} = a \cos \phi d\phi$ and $R = (a^2 + r^2 - 2 a r \cos \phi)^{1/2}$. Substituting these quantities in Equation (2.27), one gets

$$A_{\phi} = \frac{\mu_0 I}{2\pi} \int_0^{\pi} \frac{a \cos \phi d\phi}{(a^2 + r^2 - 2 a r \cos \phi)^{1/2}}. \quad (2.28)$$

Using Equation (2.17) for the components of magnetic field, one can write

$$\begin{aligned} \mathbf{B} &= \nabla \times \mathbf{A} \\ B_r &= \frac{-\partial A_\phi}{\partial z}, B_\phi = 0 \text{ and } B_z = \frac{1}{r} \frac{\partial}{\partial r} (rA_\phi). \end{aligned} \quad (2.29)$$

From Equation (2.29) it can be observed that the magnetic field vectors form closed loops in the vertical plane. If the observation distance is very large as compared with the loop radius, R can be approximated as:

$$R = (r^2 + z^2)^{1/2}. \quad (2.30)$$

In this case the magnitude of the vector potential becomes

$$A_\phi = \frac{\mu_0 I a^2 r}{4R^3}. \quad (2.31)$$

Multiplying Equation (2.31) with the linear current density vector \mathbf{i}_ϕ , the vector potential becomes

$$\mathbf{A} = A_\phi \mathbf{i}_\phi = \frac{\mu_0 I S r}{4\pi R^3} \mathbf{i}_\phi. \quad (2.32)$$

In a spherical coordinate system (R, θ, ϕ) with origin at the centre of the current loop and z-axis directed perpendicular to the loop, the direction of the current is seen counter clockwise when z is strictly positive. In this case the vector potential is given by

$$\mathbf{A} = \frac{\mu_0 I S}{4\pi R^2} \mathbf{i}_\phi \sin \theta. \quad (2.33)$$

The moment of current loop is directed along the z-axis and has its magnitude equal to the current in the loop and the loop area

$$\mathbf{M} = I S \mathbf{z}_0, \quad (2.34)$$

where \mathbf{z}_0 is the unit vector in z-axis direction. Substituting for the loop moment in Equation (2.33), one gets

$$\begin{aligned} \mathbf{A} &= \frac{\mu_0 M}{4\pi R^2} \mathbf{i}_\phi \sin \theta = \frac{\mu_0 \mathbf{M} \times \mathbf{R}}{4\pi R^3} \\ \text{since } \mathbf{M} \times \mathbf{R} &= MR \mathbf{i}_\phi \sin \phi. \end{aligned} \quad (2.35)$$

Using Equation (2.17) for the magnetic field vector components results in

$$B_R = \frac{\mu_0}{R \sin \theta} \frac{\partial (A_\phi \sin \theta)}{\partial \theta}, \quad B_\theta = -\frac{\mu_0}{R} \frac{\partial (RA_\phi)}{\partial R} \quad \text{and } B_\phi = 0, \quad (2.36)$$

which leads to

$$B_R = \frac{2\mu_0 M}{4\pi R^3} \cos \theta, \quad B_\theta = \frac{\mu_0 M}{4\pi R^3} \sin \theta, \quad B_\phi = 0. \quad (2.37)$$

Equation (2.37) is the governing equation for modeling the magnetic field generated by a dipole with moment \mathbf{M} in a spherical coordinate system.

2.2.3 Magnetic Field Components in Cylindrical Coordinate System

Transforming the magnetic field from the spherical coordinate system of Equation (2.37) to a cylindrical system (r, z, ϕ) , one gets

$$\begin{aligned} B_r &= B_R \sin \theta + B_\theta \cos \theta \\ B_z &= B_R \cos \theta - B_\theta \sin \theta \\ B_\phi &= 0. \end{aligned} \quad (2.38)$$

Now in order to visualize the effects of distance on magnetic field, Equation (2.38) needs to be expressed as a function of the separation R . B_r can then be written as

$$B_r = \frac{3\mu_0 M}{4\pi R^3} \sin \theta \cos \theta, \quad (2.39)$$

where $R = \sqrt{r^2 + z^2}$ is as shown in Figure 2-3. From the same figure, it can be observed that

$$\begin{aligned} z &= R \cos \theta \\ r &= R \sin \theta \end{aligned} \quad (2.40)$$

Inserting Equation (2.40) in Equation (2.39) and expanding R results in

$$B_r = \frac{3\mu_0 M r z}{4\pi (r^2 + z^2)^{5/2}}. \quad (2.41)$$

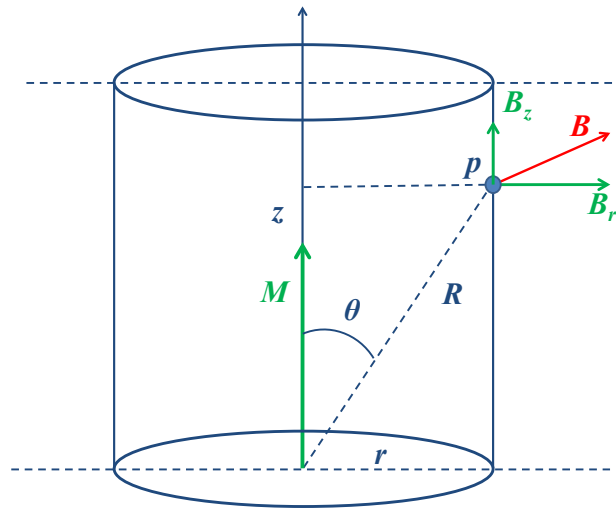


Figure 2-3: Magnetic field in cylindrical coordinate system. θ is used for resolving the magnetic field from spherical to cylindrical coordinate system.

Similarly B_z can also be written as a function of distance:

$$B_z = \frac{\mu_0 M}{4\pi (r^2 + z^2)^{5/2}} (2z^2 - r^2). \quad (2.42)$$

Using equations (2.41) and (2.42), the magnetic field can be visualized as a function of r and z . Figure 2-4 shows the magnetic field profile with radius r constant for the dipole arrangement of Figure 2-3. It can be observed that with changes in the separation from

the source (magnetic dipole), the components of magnetic field and hence the total magnetic field vary.

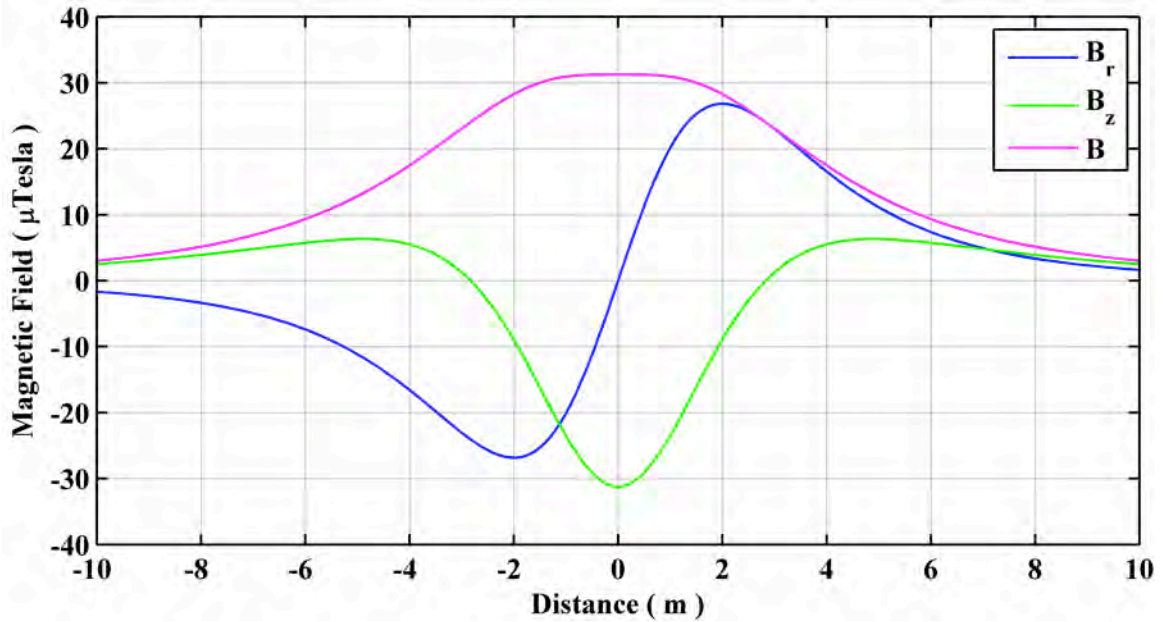


Figure 2-4: Magnetic field generated by a dipole in cylindrical coordinate system.

2.2.4 Magnetic Field in Cartesian Coordinate System

In order to derive a relationship between the magnetic field and the observation point p with respect to a frame similar to the one used for navigation, the governing equations for magnetic field intensity need to be transformed into the cartesian coordinate system as

$$\begin{aligned} B_x &= B_r \sin \phi \\ B_y &= B_r \cos \phi, \\ B_z &= B_{z_cyl} \end{aligned} \quad (2.43)$$

where B_{z_cyl} is the z-axis component of the magnetic field in the cylindrical coordinate system. These components in a cartesian coordinate system are further elaborated in Figure 2-5.

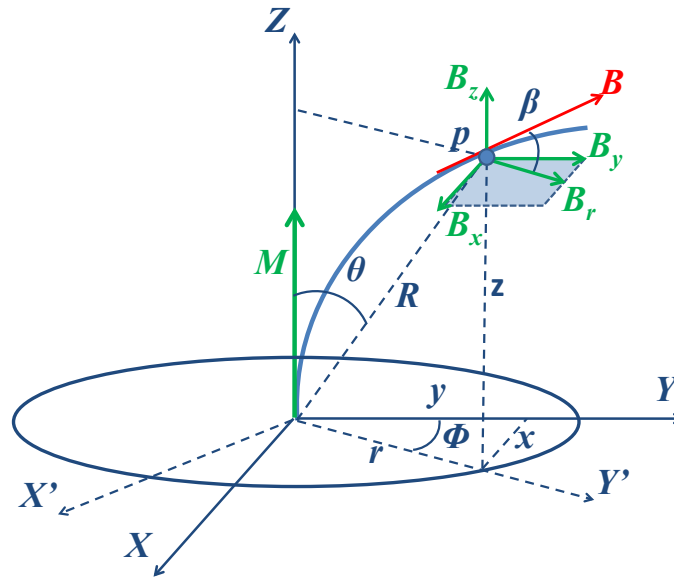


Figure 2-5: Magnetic field components in cartesian coordinate system.

2.3 Vector Potential of Multiple Dipoles

Assuming an arbitrary number of dipoles oriented in a random fashion, each of these dipoles is characterized by its magnetic moment M_i . By the law of superposition, the combined moment is described by

$$M = \sum M_i. \quad (2.44)$$

In other words, all of these dipoles can be associated with a single dipole and a combined moment M (Kaufman et al 2009). Defining the density of moments at the observation point p as

$$P = \frac{dM}{dV}, \quad (2.45)$$

the combined moment due to all magnetic moments enclosed in an elementary volume is given by

$$\mathbf{M} = \int_V \mathbf{P} dV, \quad (2.46)$$

and the vector potential due to the density of moments is given by

$$\mathbf{A} = \frac{\mu_0}{4\pi} \int_V \frac{\mathbf{P} \times \mathbf{L}_{qp}}{\|\mathbf{L}_{qp}\|^3} dV. \quad (2.47)$$

Equation (2.47) defines the magnetic vector potential for cases where more than one magnetic dipole are producing the local magnetic field. Indoor environments are typical examples of such cases.

The combined magnetic field in the presence of two dipoles arbitrarily oriented with each other is depicted in Figure 2-6. Here the orientation of the combined field has changed from the case of a single dipole. This change in the orientation of the local field is the main cause of heading errors. The magnetic field components of the combined moment are depicted in Figure 2-7. To further explain the impact of two dipoles on the sensed magnetic field, individual magnetic profiles of the two dipoles are portrayed in Figure 2-8 and Figure 2-9 respectively.

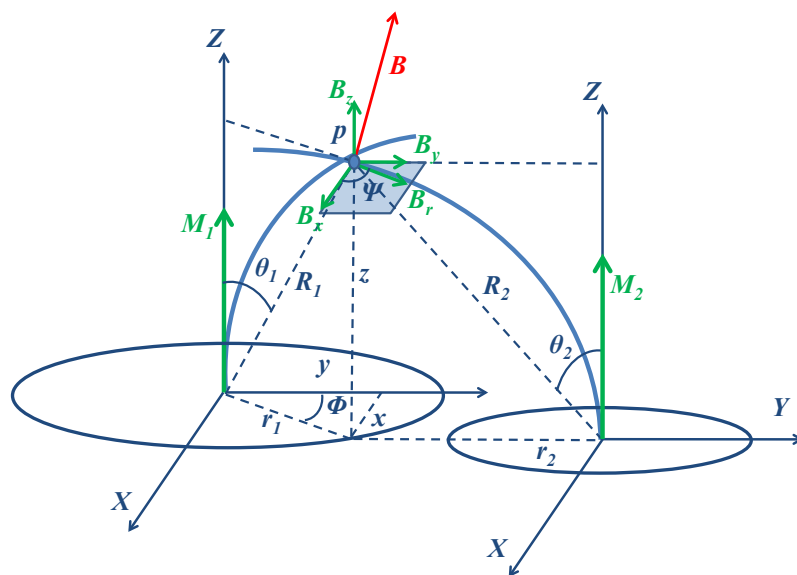


Figure 2-6: Magnetic field in presence of two dipoles.

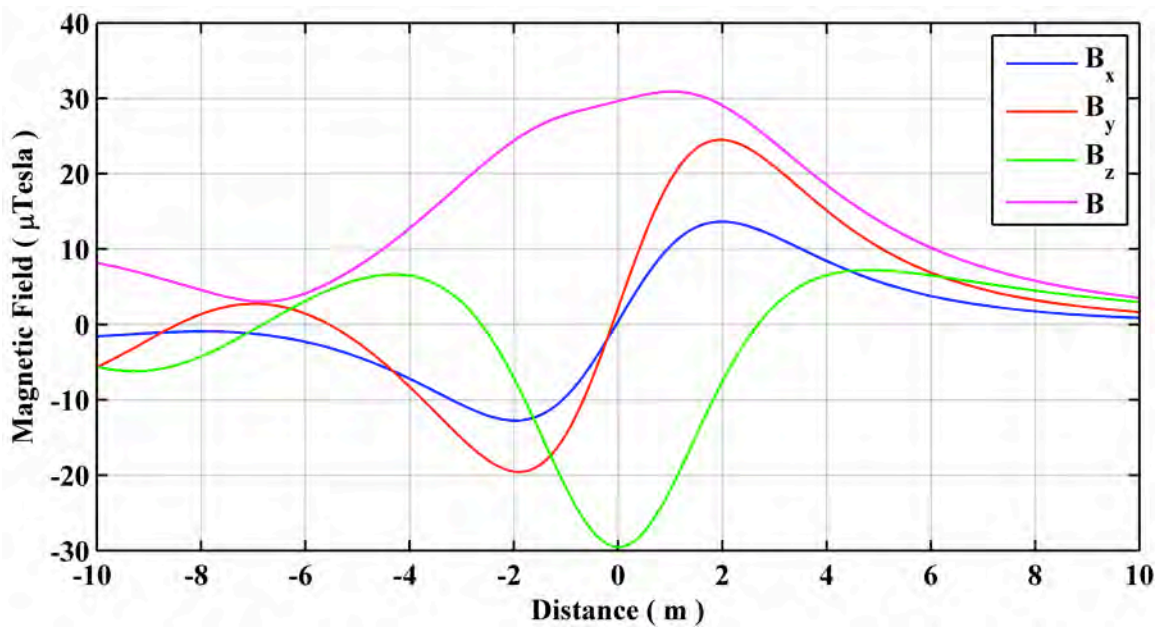


Figure 2-7: Combined magnetic field of the two dipoles as shown in Figure 2-6.

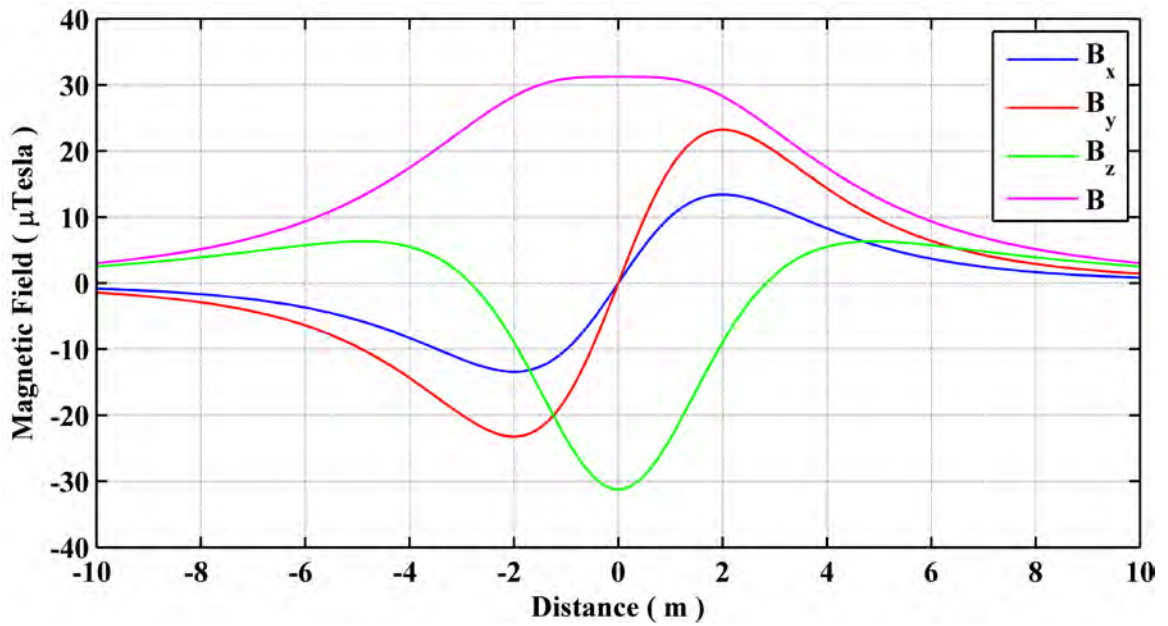


Figure 2-8: Magnetic field caused by moment M1.

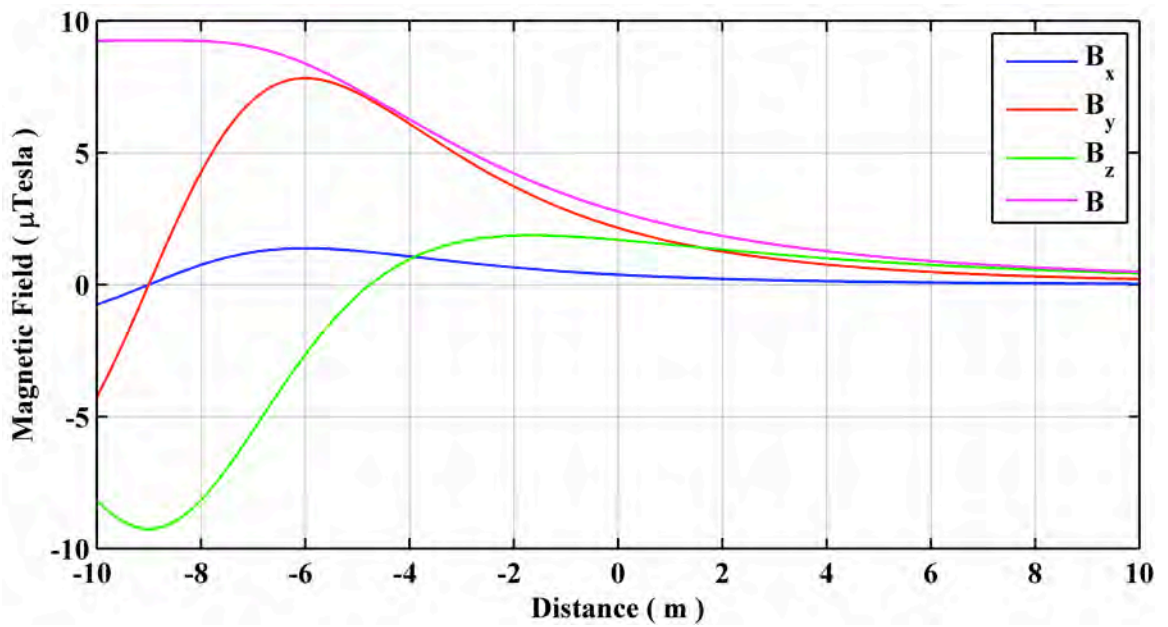


Figure 2-9: Magnetic field caused by moment M2.

2.4 The Earth's Magnetic Field

It has been known for centuries that there exists a magnetic field everywhere on the surface of the Earth. The Earth's magnetic field is associated with one dipole (Knoepfel 2000). Hence all the relations developed in the preceding sections hold for this field as well. In fact all the magnetic fields generated around us are those of dipoles. In a cartesian coordinates system (i, j, k) , the Earth's magnetic field is given by

$$\mathbf{B} = B_x \mathbf{i} + B_y \mathbf{j} + B_z \mathbf{k} . \quad (2.48)$$

The x-axis is oriented along the geographical meridian and is positive in the North direction. The y-axis is aligned with the geographic parallel with East in the positive direction and z-axis is directed downwards. The magnetic field vector is further elaborated in Figure 2-10. Here \mathbf{H} is the horizontal field component. The angle between the True North and \mathbf{H} is called the declination angle D whereas the angle between the magnetic field \mathbf{B} and horizontal plane is called the inclination angle I .

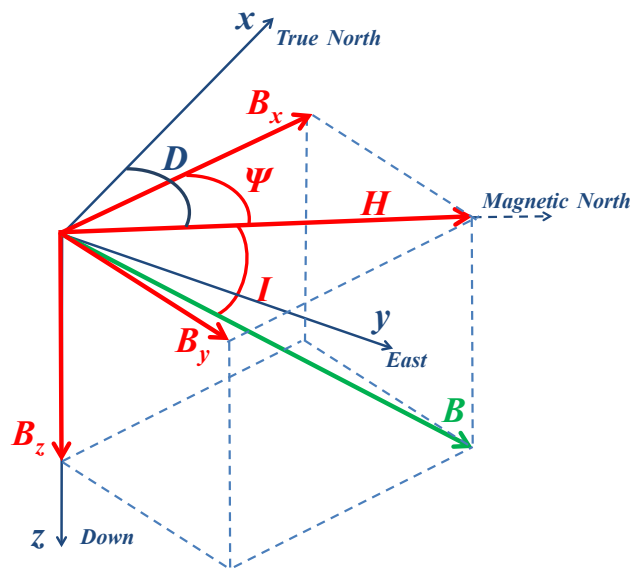


Figure 2-10: Earth's magnetic field in cartesian coordinate system.

The horizontal field magnitude is given by

$$H = (B_x^2 + B_y^2)^{1/2}. \quad (2.49)$$

From Figure 2-10 and by using trigonometric identities, it is possible to derive the relationships for inclination angle as

$$I = \tan^{-1} \left(\frac{B_z}{(B_x^2 + B_y^2)^{1/2}} \right). \quad (2.50)$$

Due to non symmetric and time varying nature of the Earth's outer core, the Earth's magnetic field changes temporally as well as spatially. This is further elaborated in Figure 2-11 where the variation in the declination angle over Canada is depicted for a particular day.

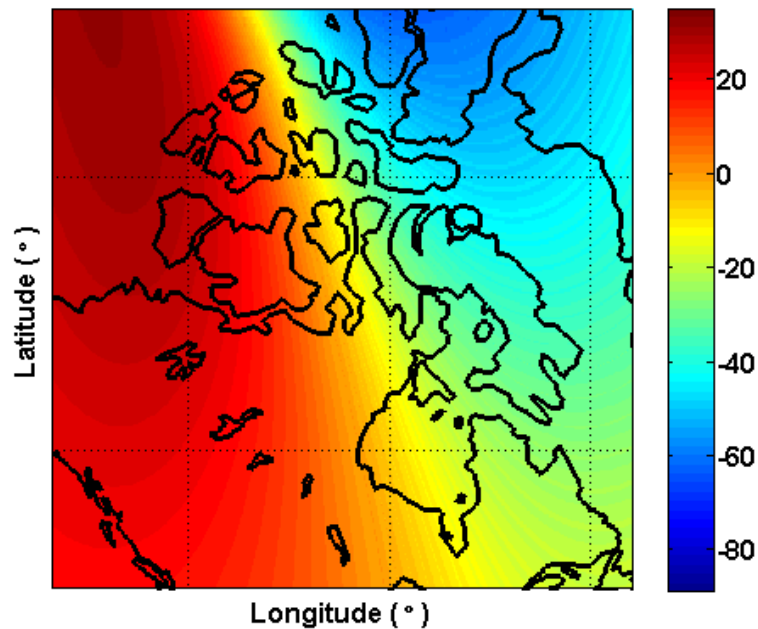


Figure 2-11: Declination angle in degrees over Canada (24Aug10). Colour map shows the declination angle in degrees.

Thus location and time dependent modeling of the Earth's magnetic field is necessary to accurately compute the local declination and inclination angles. A number of Earth's magnetic field models are available (Milsom 2003). For this work, the Canadian Geomagnetic Reference Field (CGRF) model is utilized as it offers the most accurate Earth's magnetic field model for the Canadian region.

2.4.1 Heading Estimation Using the Earth's Magnetic Field

Heading is estimated using the orthogonal components of the horizontal magnetic field. Thus the local level must be known in order to find the horizontal field component of the measured Earth's magnetic field. In order to estimate the heading with respect to true North instead of the magnetic North, the declination angle also needs to be predicted using one of the Earth's magnetic field models. After resolving the magnetic field to the local level and estimating the declination angle, a simple trigonometric relationship is used for estimating the heading from the measured Earth's magnetic field:

$$\psi = \tan^{-1}\left(\frac{B_y}{B_x}\right) \pm D, \quad (2.51)$$

where B_x and B_y are the orthogonal components of the horizontal magnetic field and D is the declination angle as depicted in Figure 2-10.

2.5 Effects of Indoor Environment on the Earth's Magnetic Field

Analogous to the scenario modeled in Section 2.3, the Earth's magnetic field can be modeled in an indoor environment in the presence of magnetic dipoles known as

magnetic perturbations. These perturbations are due either to electromagnetic devices or magnetization of man-made structures in the presence of an external magnetic field, which is mostly constituted of the Earth's magnetic field.

As the distance between the observation point and the Earth's dipole is very large, it can be assumed that any small displacements (e.g. inside a building) on the Earth's surface have no impact on the measured magnetic field. Mathematically, this gives

$$R = \sqrt{r^2 + z^2} \approx \sqrt{r^2} \quad (2.52)$$

as $z \ll r$

Therefore, while the observation point moves in the indoors, a magnetic dipole moves with it thus keeping the separation's length constant. This dipole reflects the Earth's magnetic dipole. Other dipoles keep on appearing and disappearing in the sensitivity range of the magnetic field sensors. This is graphically depicted in Figure 2-12. \mathbf{M}_E is the magnetic moment creating the Earth's magnetic field whereas \mathbf{M}_P is that of a perturbation source.

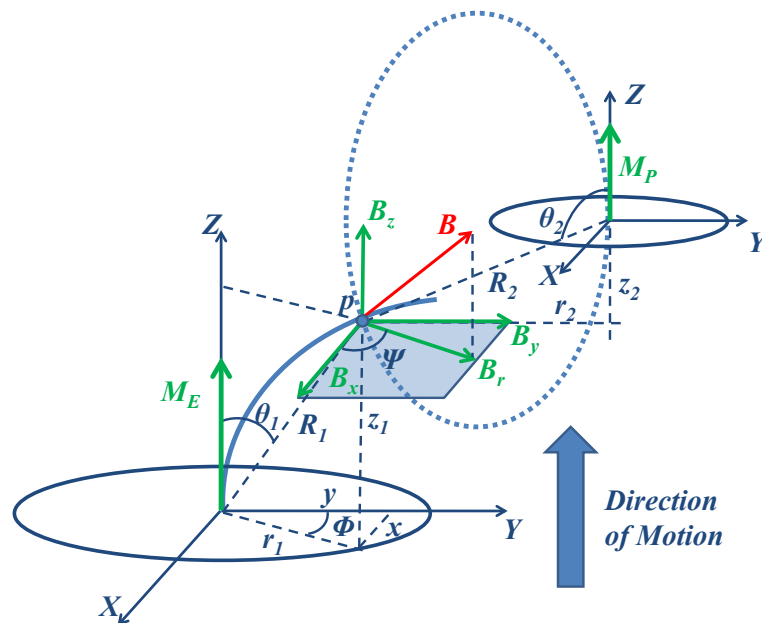


Figure 2-12: Earth's magnetic field model in presence of a perturbation source.

The magnetic field generated by the perturbation source increases in magnitude as one moves in a direction such that the separation R_2 reduces as shown in Figure 2-12. This causes the magnetic field components measured in the cartesian coordinate system to undergo a magnitude change, which causes the field vector to change its overall orientation. This phenomenon is further illustrated in Figure 2-13, Figure 2-14 and Figure 2-15. Figure 2-13 depicts the magnetic field components as one moves in the absence of any perturbation source. These components are those of the Earth's magnetic field. Figure 2-14 depicts the magnetic field of a perturbation source as one walks towards and away from it. Finally, Figure 2-15 portrays the magnetic field profile of the combined magnetic fields. It can be observed that at the beginning and at the end, the magnetic field components are dominated by the Earth's magnetic field, because the separation R_2 is very large, whereas in the middle of this magnetic profile, the magnetic field components

undergo changes in magnitude. Also it can be seen that the magnetic field vector B changes its magnitude in the presence of a perturbation source.

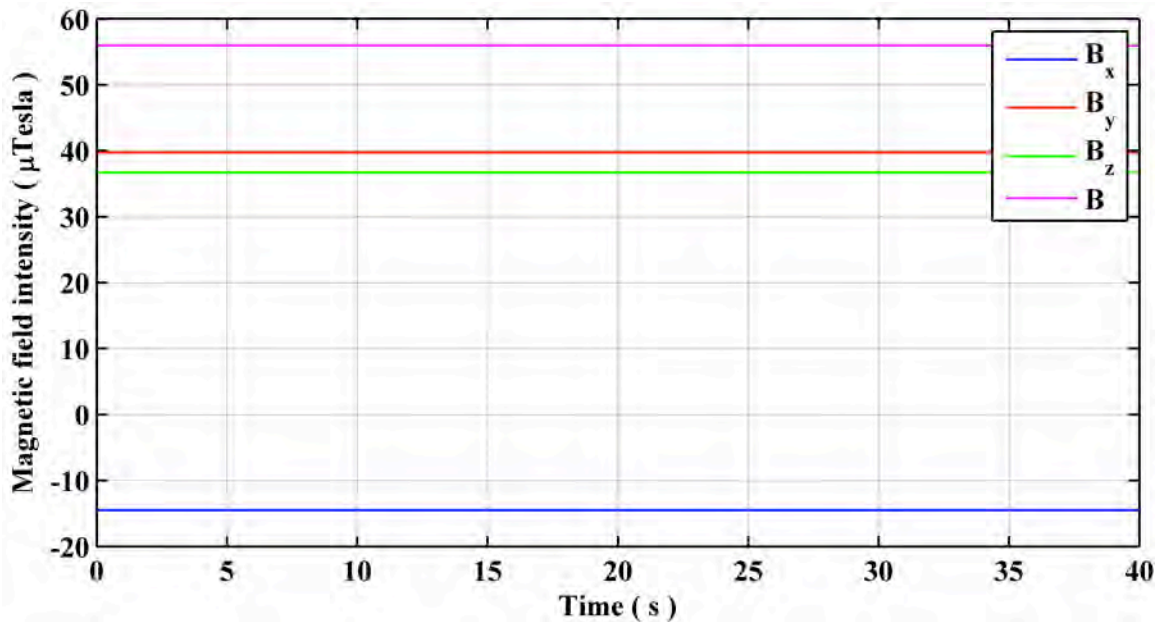


Figure 2-13: Earth's magnetic field as sensed in the absence of perturbation.

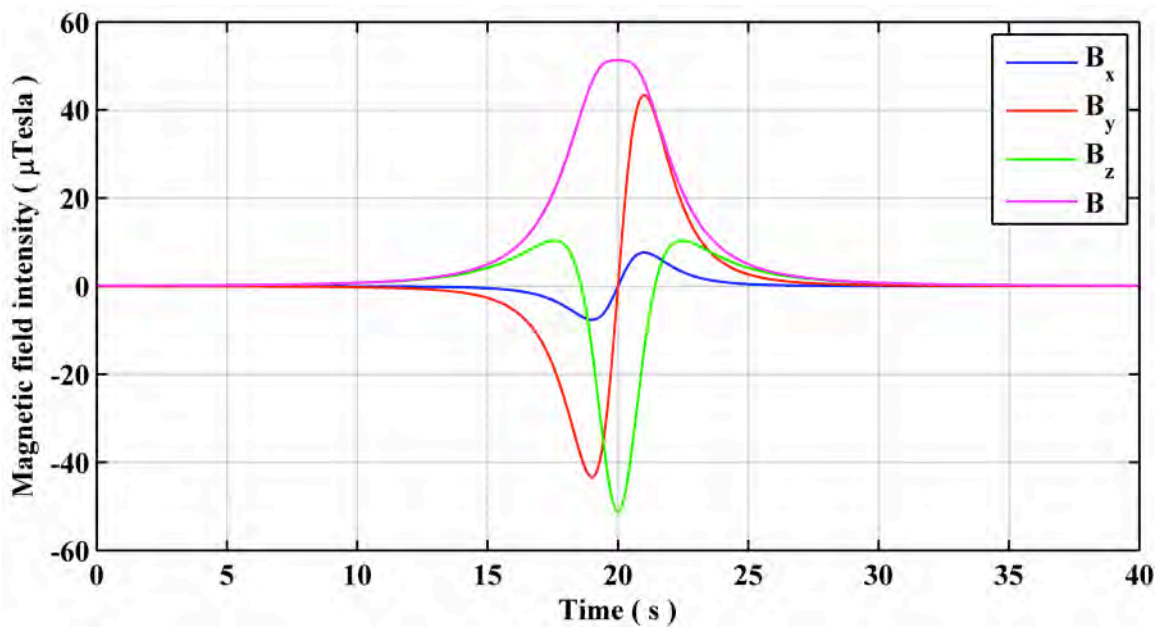


Figure 2-14: Magnetic field of the perturbation source.

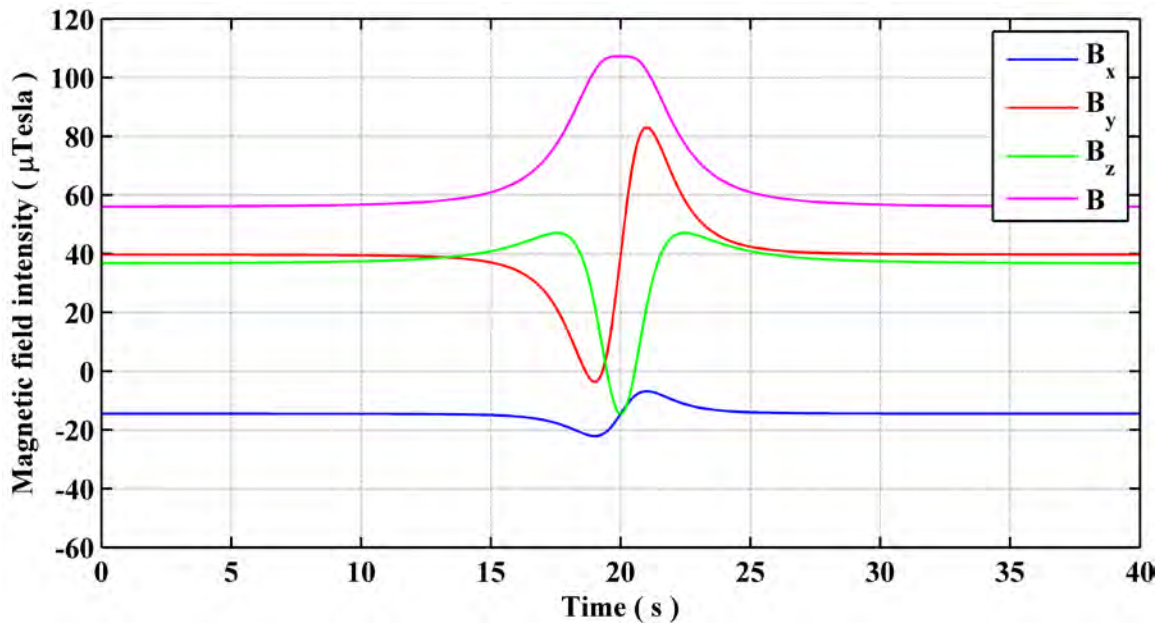


Figure 2-15: Total magnetic field and its components in the presence of the perturbation source.

2.5.1 Effect of Magnetic Perturbations on Estimated Heading

Figure 2-16 depicts the heading estimates for the scenario introduced in the preceding section. Here it can be observed that in the close vicinity of a perturbation source, the heading estimate deviates from the nominal heading with respect to the Earth's magnetic field. This results from the change in the local magnetic field components due to the perturbation source. In order to estimate the magnetically derived heading, the perturbation sources need to be mitigated. Furthermore it is important to qualify the magnetic field measurements, e.g. with covariance matrices, prior to performing any sensor fusion using some estimation technique.

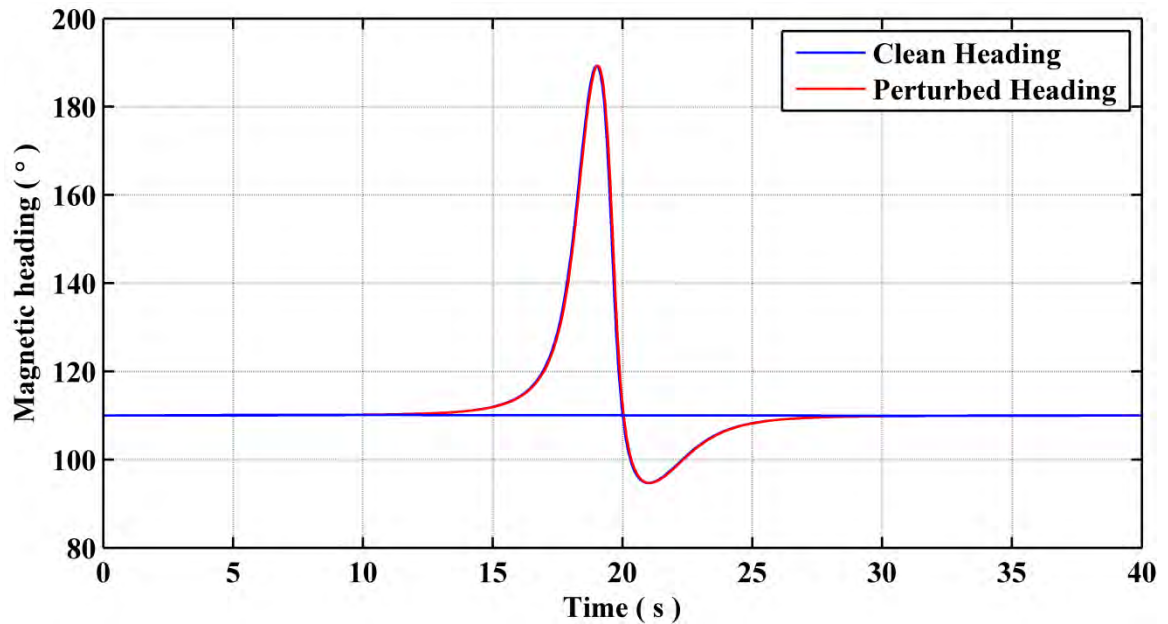


Figure 2-16: Heading estimates from clean and perturbed magnetic field.

The magnetic field model developed in this chapter to analyze the effects of magnetic field perturbations on the Earth's magnetic field can be utilized to investigate different perturbation mitigation techniques, which can be used for detecting the presence of such fields and then estimating their effects on the Earth's magnetic field. This is described in Chapter 4 following the detailed description of the sensors required for sensing the magnetic field along with other parameters necessary for this research, which constitutes Chapter 3.

Chapter Three: **Hardware Developments and Sensor Error Calibration and Modeling**

As this research investigates attitude estimation in general and orientation estimation in particular for pedestrian navigation applications, a hardware platform equipped with all the necessary sensors for these investigations is required. Keeping in mind the future requirements for this research, which involves extension of the attitude estimator to a complete pedestrian navigation system, some additional sensors not currently being utilized are also incorporated in the hardware. A Pedestrian Navigation System (PNS) referred to here as a Multiple Sensor Platform (MSP) is realized, which is described in this chapter. As the sensors selected for the MSP are of consumer grade, detailed sensor error modeling as well as their calibration is performed and detailed here.

The MSP with the following specifications was envisioned for this research:

1. Interface with consumer grade MEMS gyroscopes and accelerometer
2. Interface with multiple magnetic field sensors
3. Interface with a pressure sensor
4. Interface with a high sensitivity GPS (HSGPS)
5. Capability of logging all sensor data
6. Interface with SD card and USB thumb drives for sensor data logging
7. Small size to be carried in hand or in pocket

From these specifications, it is quite evident that the hardware platform being sought should be very versatile and cover all aspects of a PNS. Such systems are not available off-the-shelf for conducting research in the field of pedestrian navigation, which justifies the development efforts undertaken here. All of the hardware developments and sensor error modeling are described in the following sections.

3.1 Sensor Selection for MSP

Successful estimation of the desired parameters not only depends on the algorithms but also on the optimal selection of the sensors required for measurement of the necessary information sources for navigation. Therefore the first step in designing the MSP is the selection of sensors based on the application requirements. As this research deals with pedestrian navigation, the sensors must meet the following constraints:

1. Low cost
2. Small size
3. Low power consumption

Based on these constraints, the sensors described below were selected for the MSP.

3.1.1 Magnetic Field Sensors (Magnetometers)

From Figure 3-1, it can be seen that different types of magnetic field sensors can be used for pedestrian navigation purposes.

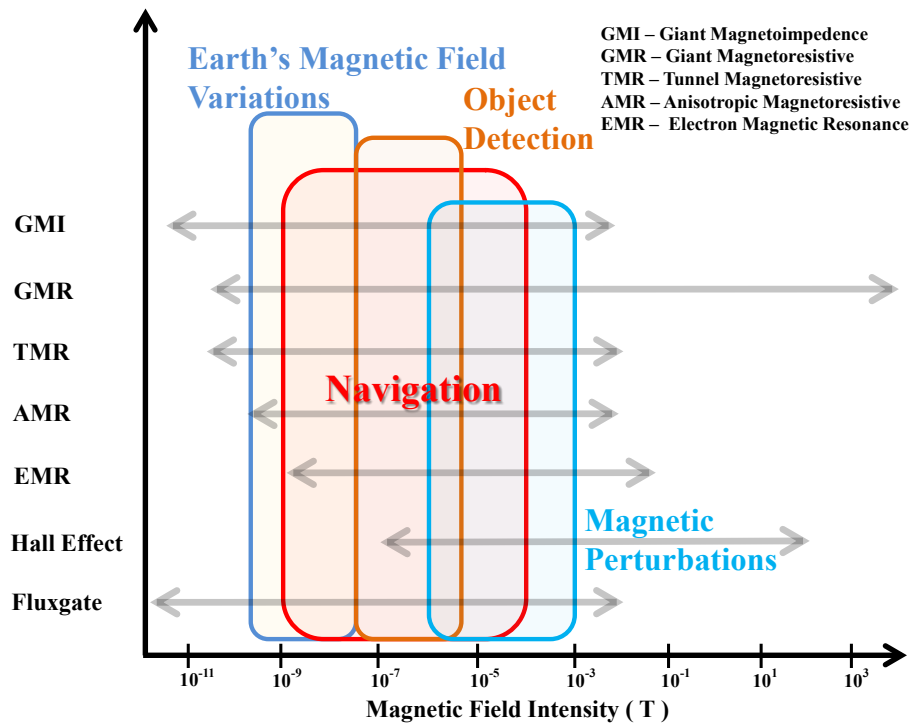


Figure 3-1: Magnetic field sensors, their sensitivity ranges and possible applications.

Based on the sensor selection constraints, three types of magnetic field sensors can be used for pedestrian navigation. These types are commonly known as Magneto-Resistive (MR), Magneto-Impedance (MI) and Hall Effect respectively. An MR sensor has different sub-categories based on the properties of MR substances used for their fabrication. These categories are:

1. Giant Magneto-Resistive (GMR)
2. Anisotropic Magneto-Resistive (AMR)

Some other categories are also coming into use but are in research phases and hence are not discussed here. The GMR sensors have very high sensitivity to small amplitude changes and are very useful for sensing weak magnetic fields. Furthermore this sensor

does not become saturated in the presence of very strong fields (Caruso & Smith 2007). This sensor seems to be a good candidate for pedestrian navigation but current fabrication technology is not able to make it direction sensitive. That is, although very weak fields can be sensed, their direction cannot be accurately identified. Another issue with this sensor is the requirement of a bias field (a strong magnetic field) in its vicinity to make it operate in its linear region. These limitations leave little hope for this sensor to be used for orientation estimation at this time. This could change in the future with advances in fabrication technology.

The Anisotropic Magneto-Resistive (AMR) sensors are not capable of sensing very weak fields and they get saturated in the presence of strong fields, but they can be very effectively used for field direction measurements (Caruso & Smith 2007). Also by utilizing an inductive coil in close proximity of the sensing element, the effects of saturation can be effectively removed from the sensor in the presence of strong magnetic fields.

The Magneto-Impedance sensors are capable of both sensing very weak magnetic fields as well as direction. They also consume far less power as compared with AMR making them ideal for embedding them in smart phones and hand held devices.

The Hall Effect sensors are widely used for contactless switching applications. In the past, these sensor elements suffered from sensitivity issues requiring very strong magnetic fields for them to operate. This was the main reason for them to be candidate

sensors for automotive applications where a strong magnetic field is used for measurements. Now with advancements in fabrication technology, the sensitivity of this sensor has improved and researchers have started using it for orientation estimation by sensing the Earth's magnetic field (AKM 2010). This sensor can also be considered as a candidate for indoor orientation estimation in the near future.

For this research, Honeywell's HMC5843 tri-axis AMR sensor was selected as the primary candidate for magnetic field sensing (Honeywell 2010b). Although GMI sensors are superior from a sensitivity and power consumption point of view, due to their unavailability in a reasonable IC package for hand soldering, they could not be considered for this research.

3.1.1.1 Anisotropic Magneto-Resistive (AMR) Sensor

AMR sensors belong to the family of miniaturized magnetic field sensors well suited for pedestrian navigation applications. AMR elements change their effective resistance when they pass through a magnetic field. As the name suggests (anisotropy means direction dependent), their sensitivity to incident magnetic field also depends on the angle of incidence. This property makes them useful for sensing magnetic field vector components for orientation estimation. Inside the sensor module, AMR elements are used as the four primary components of a Wheatstone bridge. If no magnetic field exists, the voltage out of the Wheatstone bridge will be half of the actual voltage applied. In the presence of a uniform magnetic field, the AMR elements will have different resistances changing the

output voltage of the Wheatstone bridge from its nominal value (1/2 of the applied voltage). This is further elaborated in Figure 3-2.

Thus a simple relationship between changes in voltage to the applied magnetic field can be used for calculating the magnetic field strength. In case of three orthogonal magnetic field sensors, which are required for sensing the magnetic field in three dimensions, three Wheatstone bridges are fabricated in a sensor module.

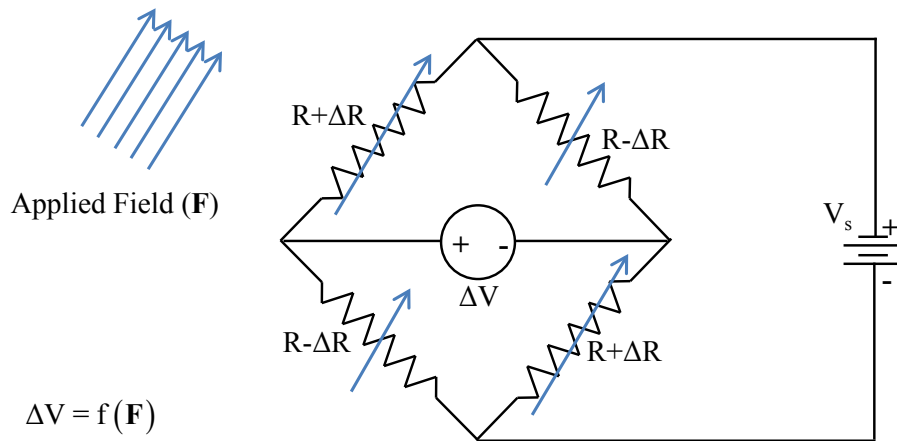


Figure 3-2: Wheatstone bridge arrangement for sensing the applied magnetic field.

The operating principle of AMR sensors, as explained in the preceding paragraph, is possible only if all four resistances of the Wheatstone bridge have the same values in the ideal condition (absence of magnetic field). Although the manufacturers try to fabricate identical AMR sensor elements, the difficulty of depositing perm-alloy (NiFe) evenly and of same density causes these magneto-resistive elements to have slightly different values. These slight errors in AMR elements cause an offset on the voltage output of the

Wheatstone bridge. This voltage offset is read as a magnetic field, which does not exist in reality, thus contributing to the sensor bias errors. Hence calibrating the AMR sensors for this offset voltage is necessary. Other issues associated with AMR sensors are caused by the non-linearity and hysteresis properties of the perm-alloy. All of the instrumentation errors associated with AMR sensors are discussed in Section 3.9.

3.1.2 Rate Gyroscopes

For measuring the angular rates as well as investigating the impact of the proposed algorithms on gyroscope error estimation, an orthogonal arrangement of rate gyroscopes is necessary. For roll and pitch angular rates, ST Microelectronics' LPR530AL dual-axis MEMS rate gyroscope is selected (ST 2010a). For yaw angular rates, the LY530ALH single-axis yaw gyroscope from the same manufacturer is selected (ST 2010b). This arrangement makes it possible to have all three gyroscope axes in a single plane as the IC internally has an orthogonally arranged sensor elements, thus reducing circuit complexity.

3.1.3 Accelerometers

Accelerometers are also a vital part of navigation systems for pedestrian applications. These sensors are not only utilized for INS mechanization, but also serve as an information source for identifying user dynamics constraints as explained in Section 1.1.2. Another application of these sensors is partial estimation of attitude in the absence of user accelerations (Farrell 2008, Pahadia 2010). For this MSP, Analog Devices' ADXL335 tri-axis accelerometer is selected (Analog 2010). As all the three axes are

incorporated in a single IC, this eases the circuit implementation and resolves the problem of aligning the sensors on to the Printed Circuit Boards (PCBs) in an orthogonal arrangement.

3.1.4 Pressure/ Temperature Sensor

For pedestrian navigation application, pressure sensors are utilized for estimating the altitude using atmospheric pressure and temperature. Although this sensor is not utilized in this research, it has been incorporated for the sake of completeness and future use of the PNS. For this work, VTI Technologies' SCP1000 absolute pressure sensor is selected (VTI 2010). With this sensor, an altitude resolution of about 10 cm is possible in indoor environments.

3.1.5 High Sensitivity GPS Receiver

Although GPS suffers from signal degradations indoors and in dense urban areas, still due to versatility of environments for pedestrian navigation, a High Sensitivity GPS (HSGPS) receiver VENUS634FLPx by SkyTraq is incorporated into the MSP (SkyTraq 2010). As the performance of the proposed algorithms can be evaluated against a reference system, GPS time will help time synchronizing the two systems for a better comparison.

3.2 Multiple Magnetometer Platform

In order to investigate the dependence of sensed magnetic field on the AMR sensors' orientation, a Multiple Magnetometer Platform (MMP) was developed. It is composed of

twelve tri-axis magnetometers arranged on two planes (6 magnetometers per plane) in the geometrical configuration portrayed in Figure 3-3.

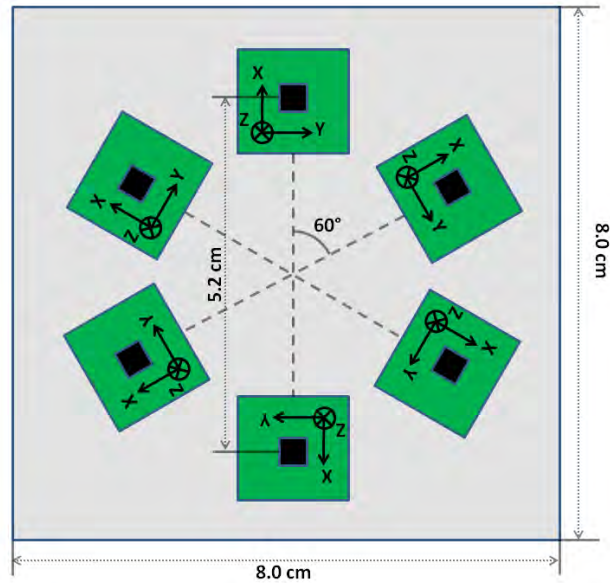


Figure 3-3: Geometrical arrangement of six magnetometers in a plane.

Figure 3-4 depicts the MMP designed and utilized for this research. Notice the two orthogonal planes carrying six magnetometers each. The magnetometers selected for MMP are the same as for MSP.

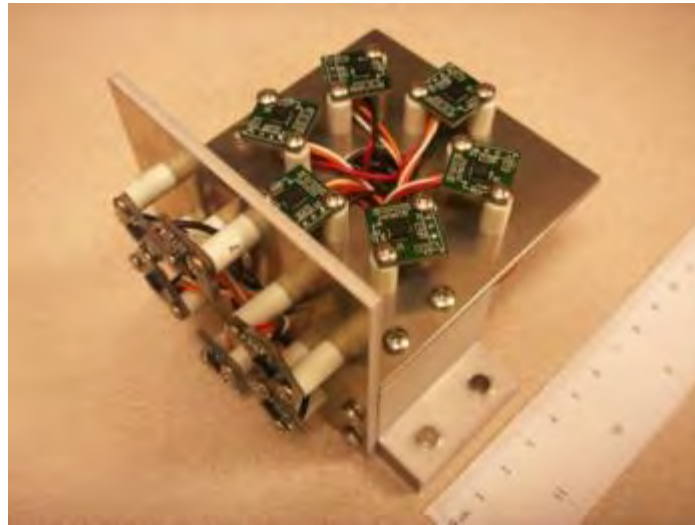


Figure 3-4: Multiple Magnetometer Platform (MMP).

Detailed utilization of the MMP is explained in Chapter 4. Although the multiple magnetometer arrangement is not suitable for hand held applications, it is investigated here because of its potential for detecting and mitigating magnetic perturbations. May be in the near future, fabrication of multiple magnetometers (more than three) in a single package will become a reality, thus allowing for this approach to be effectively used for pedestrian navigation applications.

3.3 Multiple Sensor Platform (MSP) Architecture

MSP is built around a 16-bit Digital Signal Controller (DSC). All sensors described in Section 3.1 are interfaced with the DSC, which acts as the main data acquisition module. Microchip's dsPIC30F6012A is selected for this purpose. The MMP is interfaced to a 32-bit microcontroller hosting Microsoft .NET micro framework, which acts as the processing module. The data acquisition module is also interfaced to the processing module where all the sensor data is compiled into a single packet. The latter can either be

transmitted to a PC via a USB interface, logged on SD card or a USB drive. The sensor data can also be processed in real time using algorithms implemented on the processing module. Results are displayed on a Liquid Crystal Display (LCD) screen. Figure 3-5 depicts the overall architecture of the system. The firmware for the data acquisition module is written using assembly and C languages whereas that for the processing module is in C#. The gyroscopes and accelerometers are sampled at 100 Hz while the magnetometer and pressure sensors are sampled at 50 Hz. All of these sensors are then down sampled to 25 Hz by performing integration. Although this procedure reduces the processing burden as well as the sensor noise, it may cause errors in estimated attitude using gyroscopes due to presence of coning motion (Titterton & Weston 2004). Such errors are considered negligible herein as updates from aiding sensors will compensate for them. Thus the effective data update rate for this system is 25 Hz, which is considered sufficient for the present purpose.

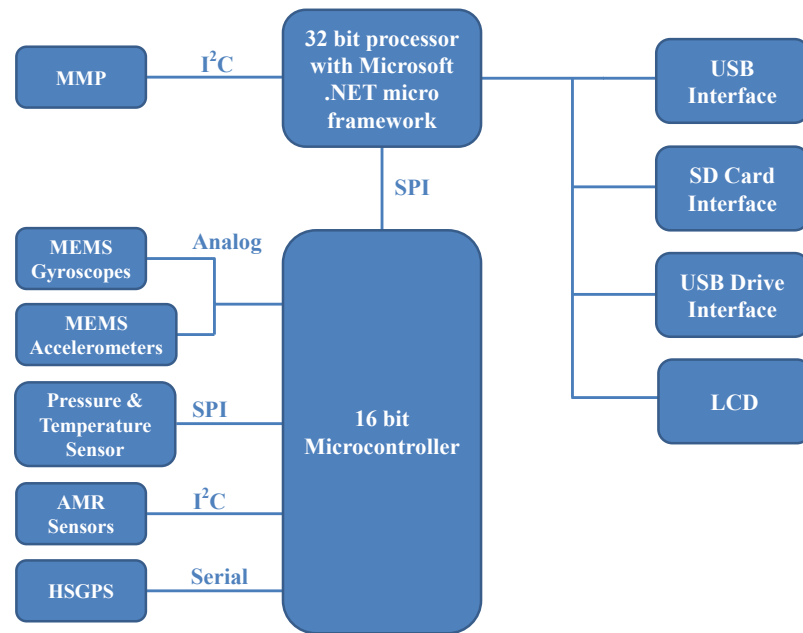


Figure 3-5: Embedded navigation system architecture.

3.4 Hardware Realization

Figure 3-6 shows MSP designed and developed for this research. Table 3-1 summarizes the system dimensions, which suggest that the system is small enough to be held in hand or carried in a side pocket or purse. These sensor locations are of utmost importance for pedestrian navigation scenarios. Most of the research done so far for pedestrian navigation deals with body-fixed sensors. This research considers hand-held as well as body fixed (pocket) locations, which makes it complete and more complex than existing approaches.

Table 3-1: Pedestrian navigation system dimensions.

Parameter	Dimensions (cm)
Length	10.5
Width	7.5
Height	4.0

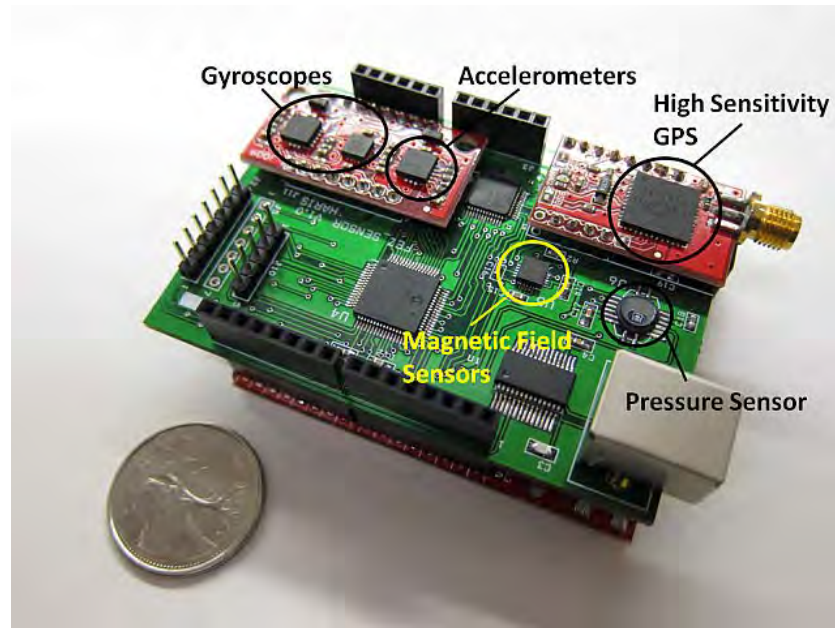


Figure 3-6: Multiple Sensor Platform (MSP).

3.5 MSP Sensor Error Modeling

As the sensors selected for this research are of consumer grade that can be easily incorporated in smart phones, proper calibration of the deterministic errors and modeling of the time varying ones is necessary. Sections 3.6 and 3.9 give details of the errors associated with the inertial sensors (gyroscope and accelerometers) and magnetometers while Sections 3.8 and 3.10 detail their calibration and modeling techniques.

3.6 Inertial Sensor Errors

With consumer grade inertial sensors comes a Pandora's Box full of errors, which require pre-calibration as well as error modeling. Although there are a number of errors contaminating inertial sensor measurements (Lawrence 1993), only the most dominant ones are addressed for this research as the consumer grade inertial sensors are too noisy to observe the rest (Park & Gao 2008).

3.6.1 Biases

The inertial sensor biases are the offsets in the measurements. Inertial sensor biases are composed of both deterministic as well as time varying components (Zhiqiang & Gebre-Egziabher 2008). The deterministic part is normally calibrated out of the sensor measurements by using some calibration techniques while the time varying part is modeled as a stochastic process.

3.6.2 Axis Misalignments

These are the errors that arise from imperfect mounting/ alignment of the sensor with the chosen sensor frame and cause non-orthogonality issues (Aggarwal et al 2006). As the sensors selected for this research are single chip implementations of multiple axes, the axis misalignment errors will also be affected by sensor fabrication imperfections. The sensor axes are not aligned with the sensor frame in this case, which results in each axis measurements being affected by the inertial forces applied on the other two axes of the sensor frame. This error is deterministic and can be calibrated out of the sensor measurements.

3.6.3 Scale Factor Errors

A scale factor is defined as the ratio of the sensor's output to input. Ideally the sensor should measure only the forces applied to it resulting in a scale factor of one. But due to sensor fabrication limitations, the scale factor deviates from its ideal value causing artificial amplification/attenuation effects on the measurements. Scale factor errors associated with inertial sensors can be of two types: linear and non-linear. In the case of

consumer grade MEMS sensors, this error can be modeled as linear as the higher order errors are overshadowed by sensor noise (Aggarwal et al 2006). Scale factor errors are deterministic and can be calibrated out of the sensor measurements. Similar to sensor bias, scale factor errors also vary with temperature but these variations are not substantial (Aggarwal et al 2007).

3.6.4 Sensor Noise

Noise plays a vital role in consumer grade inertial sensors' imperfections and needs to be properly modeled as a stochastic process. Careful analysis of the sensor noise is necessary for its modeling. How detailed the model should be depends upon the navigation application/ scenario (Zhiqiang & Gebre-Egziabher 2008). Inertial sensor noise modeling is discussed in Section 3.12 whereas the noise modeling parameters are summarized in Section 3.13.

3.7 Inertial Sensor Modeling

Based on the sensor errors discussed in the preceding section, the sensor error models for inertial sensors in light of this research are given by

$$\tilde{\mathbf{f}} = \mathbf{f} + \mathbf{b}_f + \mathbf{S}\mathbf{f} + \mathbf{N}\mathbf{f} + \boldsymbol{\varepsilon}_f \quad \text{and} \quad (3.1)$$

$$\tilde{\boldsymbol{\omega}} = \boldsymbol{\omega} + \mathbf{b}_\omega + \mathbf{S}\boldsymbol{\omega} + \mathbf{N}\boldsymbol{\omega} + \boldsymbol{\varepsilon}_\omega, \quad (3.2)$$

where $\{\mathbf{f}, \boldsymbol{\omega}\}$ are the true accelerometer and rate gyroscope measurement vectors, \sim is used to indicate the sensor outputs, \mathbf{b} designates the inertial sensor bias, \mathbf{S} is the scale factor error matrix, \mathbf{N} is the misalignment error matrix and $\boldsymbol{\varepsilon}$ is the sensor noise vector.

These error models although not representing all of the errors encountered by inertial sensors are used for this research work considering the quality of the sensors used. The calibration procedure selected for this research targets these errors and allows for in lab calibration with minimal dedicated apparatus making the overall calibration process affordable, yet effective.

3.8 Inertial Sensor Calibration Procedure

For consumer grade inertial sensors, the six position test and the rate test are most commonly used for calibration of accelerometers and rate gyroscopes, respectively (Titterton & Weston 2004), and are detailed in the following sections.

3.8.1 Six Position Test for Accelerometer Calibration

This test requires the sensor platform (MSP in this case) to be rigidly mounted on a levelled surface. Ideally, the accelerometer axis pointing downwards will sense the g vector (1 g) while the other two axes will read out 0 g . But due to sensor misalignments, scale factor errors and biases, the sensor measurements will vary from the expected ones. This information is used for estimating the accelerometer errors. Excluding the noise term for now, Equation (3.1) can be written in matrix form as

$$\begin{bmatrix} \tilde{f}_x \\ \tilde{f}_y \\ \tilde{f}_z \end{bmatrix} = \begin{bmatrix} m_{xx} & m_{xy} & m_{xz} \\ m_{yx} & m_{yy} & m_{yz} \\ m_{zx} & m_{zy} & m_{zz} \end{bmatrix} \begin{bmatrix} f_x \\ f_y \\ f_z \end{bmatrix} + \begin{bmatrix} b_{f_x} \\ b_{f_y} \\ b_{f_z} \end{bmatrix} \quad (3.3)$$

where m_{ij} with $i \in \{x, y, z\}$ and $j \in \{x, y, z\}$ are the elements of a matrix reflecting the combined effects of the scale factor and misalignment errors. Here the diagonal elements

represent the scale factor errors while the off diagonal elements are for the sensor misalignments. Equation (3.3) can be further simplified to

$$\begin{bmatrix} \tilde{f}_x \\ \tilde{f}_y \\ \tilde{f}_z \end{bmatrix} = \underbrace{\begin{bmatrix} m_{xx} & m_{xy} & m_{xz} & b_{f_x} \\ m_{yx} & m_{yy} & m_{yz} & b_{f_y} \\ m_{zx} & m_{zy} & m_{zz} & b_{f_z} \end{bmatrix}}_{\mathbf{M}} \begin{bmatrix} f_x \\ f_y \\ f_z \\ 1 \end{bmatrix}. \quad (3.4)$$

Using the six position test, the expected three axis accelerometer measurements are given by

$$\mathbf{f}_1 = \begin{bmatrix} g \\ 0 \\ 0 \end{bmatrix}, \mathbf{f}_2 = \begin{bmatrix} -g \\ 0 \\ 0 \end{bmatrix}, \mathbf{f}_3 = \begin{bmatrix} 0 \\ g \\ 0 \end{bmatrix}, \mathbf{f}_4 = \begin{bmatrix} 0 \\ -g \\ 0 \end{bmatrix}, \mathbf{f}_5 = \begin{bmatrix} 0 \\ 0 \\ g \end{bmatrix}, \mathbf{f}_6 = \begin{bmatrix} 0 \\ 0 \\ -g \end{bmatrix}, \quad (3.5)$$

where \mathbf{f}_1 is the expected accelerometer measurements with x-axis facing upward and \mathbf{f}_2 with x-axis facing downward. These measurements can be used for estimating the calibration matrix \mathbf{M} using least squares (LS) adjustment (Aggarwal et al 2006). In this case, the design matrix for LS is given by

$$\mathbf{A} = \begin{bmatrix} \mathbf{f}_1 & \mathbf{f}_2 & \mathbf{f}_3 & \mathbf{f}_4 & \mathbf{f}_5 & \mathbf{f}_6 \\ 1 & 1 & 1 & 1 & 1 & 1 \end{bmatrix}. \quad (3.6)$$

The raw accelerometer measurements constitute the matrix \mathbf{U} given by

$$\mathbf{U} = \begin{bmatrix} \tilde{\mathbf{f}}_1 & \tilde{\mathbf{f}}_2 & \tilde{\mathbf{f}}_3 & \tilde{\mathbf{f}}_4 & \tilde{\mathbf{f}}_5 & \tilde{\mathbf{f}}_6 \end{bmatrix}, \quad (3.7)$$

$$\text{where } \tilde{\mathbf{f}}_1 = \begin{bmatrix} \tilde{f}_x \\ \tilde{f}_y \\ \tilde{f}_z \end{bmatrix}_{x_up} \text{ and } \tilde{\mathbf{f}}_2 = \begin{bmatrix} \tilde{f}_x \\ \tilde{f}_y \\ \tilde{f}_z \end{bmatrix}_{x_down}.$$

The calibration parameters' matrix \mathbf{M} can be extracted from the above system of equations using the solution for LS given by

$$\mathbf{M} = \mathbf{U}\mathbf{A}^T (\mathbf{A}\mathbf{A}^T)^{-1}. \quad (3.8)$$

The overall calibration data collection setup for accelerometers is shown in Figure 3-7(a) while the calibration parameters are summarized in Section 3.13.

3.8.2 Rate Test for Gyroscope Calibration

Similar to the six position test for accelerometers, rate tests can be used for gyroscope calibration. As consumer grade MEMS rate gyroscopes have high noise levels, which render them insensitive to Earth's rotation, high angular rates need to be artificially generated in order to calibrate them. For this purpose a 1 Degree of Freedom (DoF) turntable is used. A constant angular rate of 200 °/s is generated using the turntable both in clockwise and counter clockwise directions. The MSP is rigidly mounted on the turntable with each gyroscope axis pointing upwards once. This procedure gives six expected measurements similar to accelerometer calibration. The LS adjustment method is then utilized to extract the calibration parameters for gyroscopes as described in Section 3.8.1. Figure 3-7(b) shows the gyroscope calibration setup and the calibration parameters are summarized in Section 3.13.

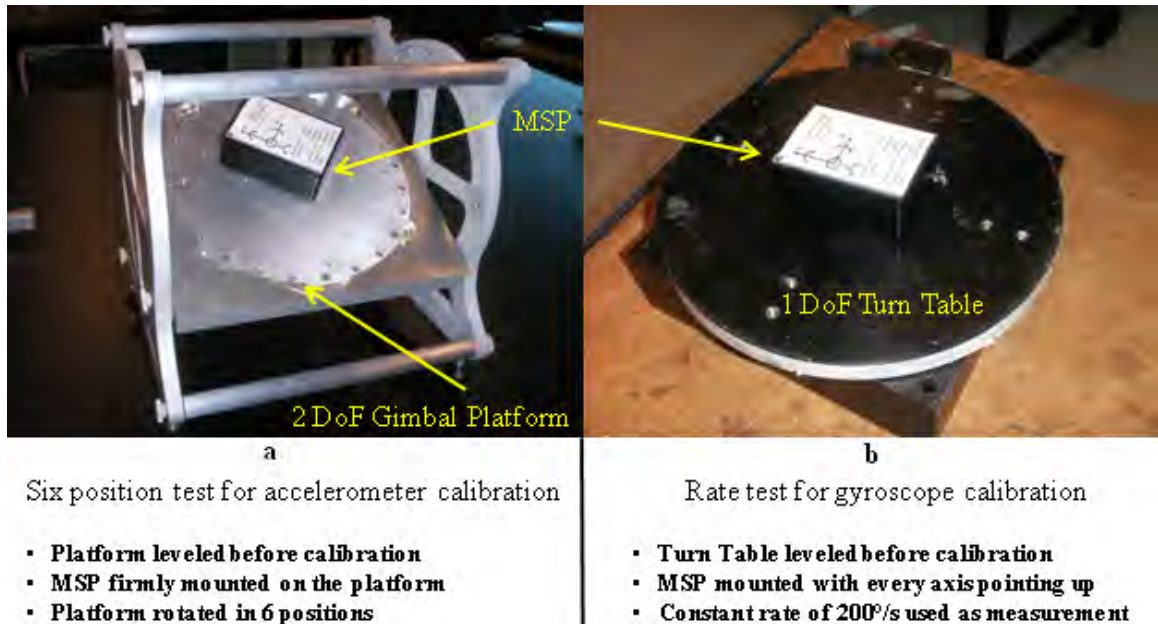


Figure 3-7: Inertial sensor calibration setup.

3.9 Magnetometer Errors

In addition to the instrumentation errors similar to those encountered by the inertial sensors, the magnetic field sensors also suffer from errors due to magnetic perturbations. The presence of ferro-magnetic materials and electro-magnetic systems in the vicinity of the sensor are the main cause of these perturbations, i.e. the host platform itself may be responsible for them. Even with proper compensation of instrumentation errors, these perturbations cause artificial bias, scale factor as well as non-orthogonality errors in the sensor measurements. One part of these errors is qualified as artificial because the instrument itself is not introducing it, rather it's the host platform that generates the magnetic fields that is causing these errors. These artificial errors can be categorized as hard and soft iron errors and are now described.

The overall magnetic field sensor model used for this research is given by

$$\tilde{\mathbf{B}} = \boldsymbol{\varepsilon}_{ni} (\boldsymbol{\varepsilon}_{nm} \mathbf{B} + \boldsymbol{\varepsilon}_{lm}) + \boldsymbol{\varepsilon}_{li} + \boldsymbol{\varepsilon}_w. \quad (3.9)$$

Here $\tilde{\mathbf{B}}$ is the measured magnetic field vector composed of the three field components given by

$$\tilde{\mathbf{B}} = [\tilde{B}_x \quad \tilde{B}_y \quad \tilde{B}_z]^T. \quad (3.10)$$

\mathbf{B} is the true magnetic field vector given by

$$\mathbf{B} = [B_x \quad B_y \quad B_z]^T. \quad (3.11)$$

$\boldsymbol{\varepsilon}_{ni}$ is a 3x3 matrix composed of non-linear instrumentation errors. $\boldsymbol{\varepsilon}_{nm}$ is a 3x3 matrix composed of non-linear errors caused by magnetic perturbations. $\boldsymbol{\varepsilon}_{lm}$ is a vector composed of linear errors caused by magnetic perturbations. $\boldsymbol{\varepsilon}_{li}$ is a vector of linear instrumentation errors and $\boldsymbol{\varepsilon}_w$ is the sensor noise vector. These error terms are caused by combinations of different error types, which are explained in the following sections.

3.9.1 Offset Error

The bridge offset of a particular AMR sensor remains constant for the entire lifespan of the sensor (Honeywell 2010a). Thus one needs to compensate for bridge offset just once. This offset is not like the bias associated with accelerometers and gyroscopes that vary with time as well as with turn on/off although substantial temperature variations may cause this error to have a varying component. The primary means to calculate this bridge offset is accurate calibration. Often Helmholtz coils are used for offset computation (Lassahn & Trenkler 1995), which provides very accurate information regarding the

applied field. Usually an Helmholtz coil is used to cancel the Earth's field (nullify the total magnetic field in the test region) and then analyze the sensor output, which will be the offset itself. An alternate method for offset compensation is to measure the sensor output at different orientations assuming that the applied field is constant (a good assumption is an outdoor open environment like a park), and use the least squares approach to solve for the offset with multiple observations.

Let the sensor offset errors be represented by a vector given by

$$\boldsymbol{\varepsilon}_{os} = \begin{bmatrix} \varepsilon_{osx} & \varepsilon_{osy} & \varepsilon_{osz} \end{bmatrix}^T \quad (3.12)$$

This error contributes to the linear instrumentation errors ($\boldsymbol{\varepsilon}_l$) of Equation (3.9).

3.9.2 Sensitivity Error

The AMR elements are non-linear by nature. This means that the sensitivity of the AMR sensors varies with the variations in the magnitude of the sensed magnetic field. This non-linearity results in a scale factor error. In order to compensate for this error, proper calibration of AMR sensors is necessary. For this purpose, an external field is generated with known magnitudes and a function relating the scale factor to the input is estimated. The generated magnetic field needs to be strong enough to cover the complete range of expected magnetic field strengths. Again in this case, the Earth's magnetic field is chosen as the source of measurements, which are taken at different orientations ranging from no sensed magnetic field (perpendicular to the field vector) to maximum field strength (parallel to the field vector). Care must be taken as this calibration is valid only if the expected field strengths are within the calibration region.

Let the magnetic field sensor's sensitivity errors be given by

$$\boldsymbol{\varepsilon}_s = \begin{bmatrix} \varepsilon_{sx} & 0 & 0 \\ 0 & \varepsilon_{sy} & 0 \\ 0 & 0 & \varepsilon_{sz} \end{bmatrix} \quad (3.13)$$

These errors contribute to the non-linear instrumentation errors ($\boldsymbol{\varepsilon}_{ni}$) as given in Equation (3.9).

3.9.3 Non-Orthogonality Errors

The magnetic field sensor utilized for this research is a combined three-axis one. There will be some non-orthogonality errors due to improper fabrication of the sensor as well as soldering and housing in the host system. These errors contribute to the non-linear instrumentation errors ($\boldsymbol{\varepsilon}_{ni}$) of the sensor model given by Equation (3.9).

Let the non-orthogonality errors be represented by a 3x3 matrix as

$$\boldsymbol{\varepsilon}_{no} = \begin{bmatrix} \varepsilon_{nox} & \varepsilon_{noxy} & \varepsilon_{noxz} \\ \varepsilon_{noyx} & \varepsilon_{noyy} & \varepsilon_{noyz} \\ \varepsilon_{noz} & \varepsilon_{nozy} & \varepsilon_{nozz} \end{bmatrix}, \quad (3.14)$$

where each element gives the angular direction of the sensor axes in the body frame.

3.9.4 Cross Axis Sensitivity Error

With time, the AMR sensors attain uneven magnetization, which changes their sensitivity axis' orientation. This phenomenon acts as a misalignment error for a tri-axis magnetic field sensor. In order to remedy for this error, an inductor/coil is utilized to create a magnetic field in opposite directions that demagnetizes the AMR sensor as shown in

Figure 3-8. This method is similar to the one performed for erasing the memory of magnetic tapes. The coil is usually fabricated along with the sensor elements. Frequent use of this coil rectifies any error due to hysteresis. As the cross-axis sensitivity errors are periodically compensated for by utilizing the coil, which is also known as the set/reset strap, they are compensated and hence do not contribute to any of the error terms of Equation (3.9).

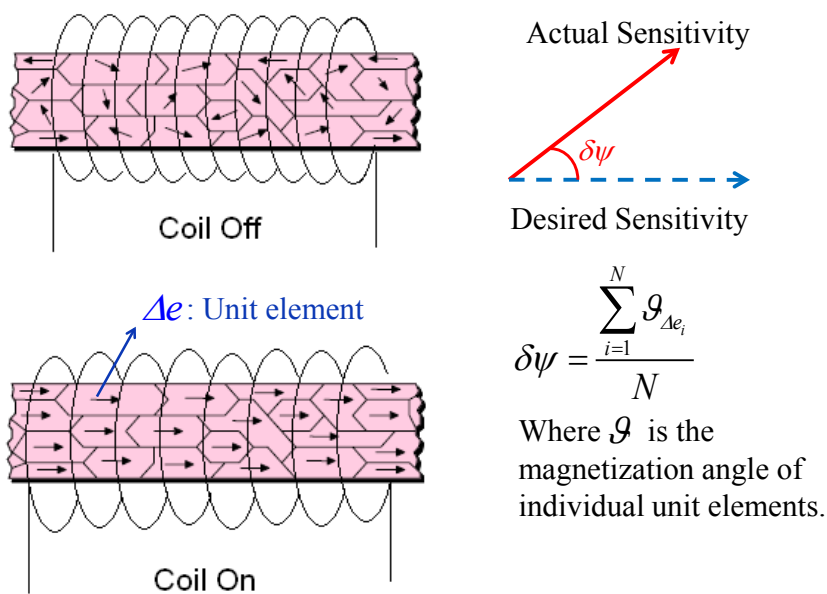


Figure 3-8: Use of induction coil to compensate for hysteresis effects.

3.9.5 Hard Iron Errors

Hard iron errors on the platform are caused by a magnetic source, which generates permanent field irrespective of the platform's orientation with respect to Earth's magnetic field. In other words, magnetic fields generated due to different electronic sub-systems in the vicinity of the sensor and that do not have any or have negligible dependence on the

Earth's magnetic field are called hard iron magnetic sources. These magnetic fields cause a bias in the sensed magnetic field as shown in Figure 3-9. Here the effects of hard iron are expressed in two dimensions only. This is done to ease the visualization of these effects. Indeed there will be a three dimensional impact of hard iron errors on the sensed magnetic field, which may cause biases in all three axes.

With the presence of hard iron on the three axes, the locus of the magnetic field intensity sensed by a magnetometer triad will be a sphere with a shifted origin. This can be visualized in the right part of Figure 3-9 in two dimensions.

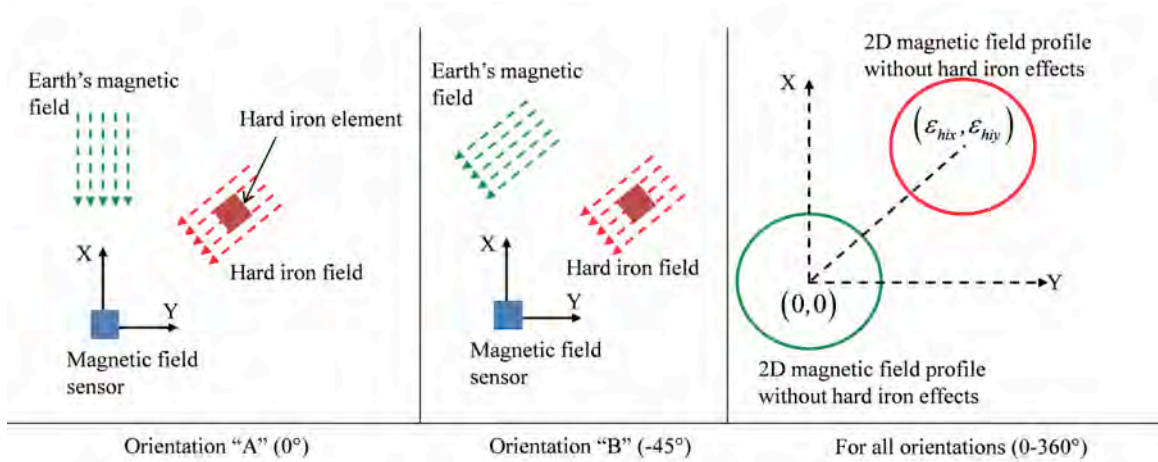


Figure 3-9: Effects of hard iron on sensed magnetic field.

As is evident from Figure 3-9, the hard iron errors act as biases, which contribute to the linear errors caused by magnetic perturbations (ϵ_{lm}) of the magnetic field sensor model given by Equation (3.9). The hard iron errors can be represented by a vector given by

$$\epsilon_{hi} = [\epsilon_{hix} \quad \epsilon_{hiy} \quad \epsilon_{hiz}]^T. \quad (3.15)$$

3.9.6 Soft Iron Errors

Soft iron errors are caused by much complex magnetic fields that are generated by ferro-magnetic materials. These magnetic fields have a direct interaction with the Earth's magnetic field. Their magnitudes depend on the incident angle of the Earth's magnetic field on the material. Hence it changes as the host platform changes its orientation with respect to the Earth's magnetic field. The general trend of this phenomenon can be observed in Figure 3-10.

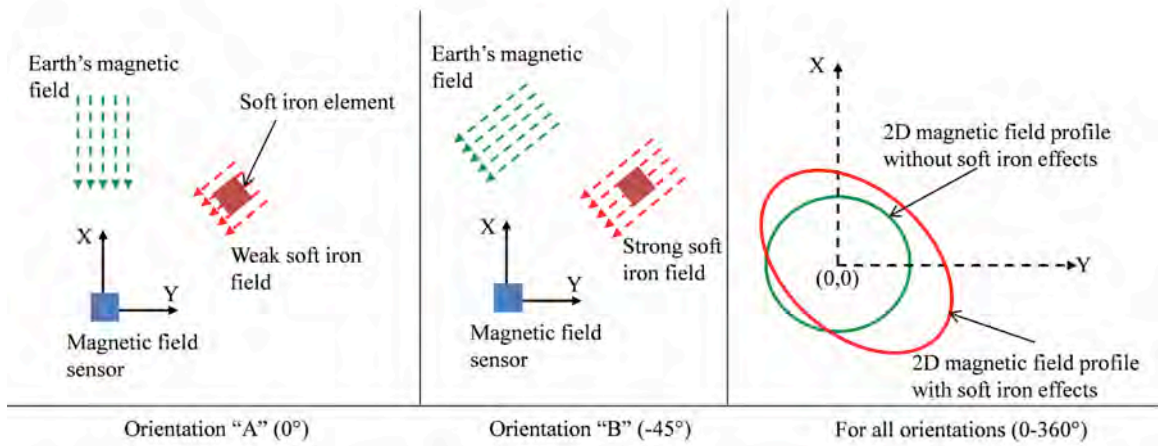


Figure 3-10: Effects of soft iron on sensed magnetic field.

It is quite evident that the errors caused by soft iron effects are complex and non-linear as compared with hard iron effects. These errors contribute to the non-linear errors caused by magnetic field perturbations (ϵ_{nm}) of the magnetic field sensor model given in Equation (3.9). The soft iron errors change the magnitude as well as the direction of the sensed field and can be expressed by a 3x3 matrix given by

$$\epsilon_{si} = \begin{bmatrix} \epsilon_{sixx} & \epsilon_{sixy} & \epsilon_{sixz} \\ \epsilon_{siyx} & \epsilon_{siyy} & \epsilon_{siyz} \\ \epsilon_{sizx} & \epsilon_{sizy} & \epsilon_{sizz} \end{bmatrix}, \quad (3.16)$$

where ε_{sijk} for $j \in \{x, y, z\}$ and $k \in \{x, y, z\}$ are the effects of soft iron on j and k axis combinations.

3.9.7 Sensor Noise

The last error source in magnetic field sensors is the sensor noise. Similar to inertial sensors, this error cannot be calibrated. The sufficient information to model this error as a stochastic process can be obtained using an Allan Variance analysis as discussed in Section 3.12.

3.10 Magnetometer Calibration Procedure

After identifying and explaining different errors associated with magnetometers, calibration is required for estimating the deterministic errors. These can then be removed from successive sensor measurements to bring them as close to true measurements as possible. There are a number of calibration algorithms that have been published for estimating the errors associated with magnetic field sensors. At the beginning of the 19th century, the navigator Nathaniel Bowditch published a guide dedicated to celestial navigation. It contains the well-known swinging calibration technique (Bowditch 1977) that requires levelling the instrument and rotating it in a series of known azimuths. The need for external heading information and the constraint of levelling the platform are the main limitations of this method. Using measurements collected during a full rotation of the levelled sensor in the horizontal plane, (Caruso 1997) exploits the minimum and maximum values to estimate the scale factors and biases of the compass. This compensation technique is very practical but ignores several sensor errors.

A more complete approach in the magnetic field domain was proposed by Gebre-Egziabher et al (2006). This approach is dedicated to sensors sensing a known linear field that remains constant. During the procedure, the device rotates and an iterative batch least squares technique estimates the deviation and the combined scale factors of the sensor. Initial conditions are provided by a non-linear two step LS using a change of variables technique. The limitations of this calibration lay in the hypothesis that misalignments can be neglected and that the soft iron deteriorates only the measurements on the sensor's axis aligned with the induced magnetic field. In (Vasconcelos et al 2008), a geometric method based on an iterative Maximum Likelihood Estimator (MLE) best fits the device's measurements to an ellipsoid manifold; a separate closed-form optimal algorithm computes the misalignment matrix.

Instead of using software based calibrations in the magnetic domain, some techniques consist in using non-magnetic platforms dedicated to the calibration of magnetometer. A system based on piezoelectric motors mounted on a platform made of aluminum, brass, plastic, and glass is proposed by Petrucha et al (2009). The equipment has three axes of rotation and uses motors and optical encoders to control the motion and improve the calibration outputs.

Keeping under consideration the limitations of previously developed calibration algorithms, a new calibration algorithm is developed, which does not simplify the effects of soft iron on magnetic field measurements, thus providing better calibration parameters (Renaudin et al 2010).

3.10.1 Calibration Algorithm

Rewriting Equation (3.9)

$$\tilde{\mathbf{B}} = \boldsymbol{\varepsilon}_{ni} (\boldsymbol{\varepsilon}_{nm} \mathbf{B} + \boldsymbol{\varepsilon}_{lm}) + \boldsymbol{\varepsilon}_{li} + \boldsymbol{\varepsilon}_w, \quad (3.17)$$

it can be observed that all but the last error term are deterministic, in which case the later can be modelled as a stochastic process as explained in the sequel. Expanding Equation (3.17) and combining linear and non-linear error terms, the magnetometer error model becomes

$$\tilde{\mathbf{B}} = \mathbf{A}\mathbf{B} + \mathbf{b} + \boldsymbol{\varepsilon}_w, \quad (3.18)$$

where $\mathbf{A} = \boldsymbol{\varepsilon}_{ni} \boldsymbol{\varepsilon}_{nm}$ is the combination of the errors due to misalignments, scale factors and soft iron, $\mathbf{b} = \boldsymbol{\varepsilon}_{ni} \boldsymbol{\varepsilon}_{lm} + \boldsymbol{\varepsilon}_{li}$ is the combined bias caused by the combination of misalignments, hard iron and sensor offset. This simplified model will now be utilized for development of a calibration algorithm.

3.10.1.1 Constraint on the Magnitude of the Measured Field

In a perturbation free environment, the total magnetic field (norm) of the magnetometer vector measurement should be equal to the magnitude of the Earth's magnetic field. Consequently while rotating the sensor in space, the locus described by its readings should describe a sphere with a radius equal to the magnitude of the local Earth's magnetic field (Gebre-Egziabher et al 2006). This norm $\|\mathbf{F}\|$ can be extracted from a specific geomagnetic model (Haines & Newitt 1997). Following equation constraints the measurements of a perfect magnetometer in a perturbation free environment:

$$\|\mathbf{F}\|^2 - \|\mathbf{B}\|^2 = \|\mathbf{F}\|^2 - \mathbf{B}^T \mathbf{B} = 0. \quad (3.19)$$

If the square transformation matrix \mathbf{A} and the combined bias \mathbf{b} are known, then Equation (3.18) can be rewritten as

$$\mathbf{B} = \mathbf{A}^{-1}(\tilde{\mathbf{B}} - \mathbf{b} - \boldsymbol{\varepsilon}_w). \quad (3.20)$$

Substituting Equation (3.20) in Equation (3.19) and omitting the stochastic error term gives

$$(\tilde{\mathbf{B}} - \mathbf{b})^T (\mathbf{A}^{-1})^T \mathbf{A}^{-1} (\tilde{\mathbf{B}} - \mathbf{b}) - \|\mathbf{F}\|^2 = 0. \quad (3.21)$$

Introducing the following intermediate parameter

$$\mathbf{Q} = (\mathbf{A}^{-1})^T \mathbf{A}^{-1}, \quad (3.22)$$

Equation (3.21) becomes

$$(\tilde{\mathbf{B}} - \mathbf{b})^T \mathbf{Q} (\tilde{\mathbf{B}} - \mathbf{b}) = \|\mathbf{F}\|^2. \quad (3.23)$$

Expanding Equation (3.23) the following quadratic equation is obtained

$$\tilde{\mathbf{B}}^T \mathbf{Q} \tilde{\mathbf{B}} + \mathbf{u}^T \tilde{\mathbf{B}} + k = 0, \quad (3.24)$$

where

$$\mathbf{u} = -2\mathbf{Q}^T \mathbf{b}, \quad (3.25)$$

$$k = \mathbf{b}^T \mathbf{Q} \mathbf{b} - \|\mathbf{F}\|^2. \quad (3.26)$$

This equation represents a general plane of the second order and describes a surface, e.g. a hyperboloid, a cone or an ellipsoid. Because \mathbf{Q} is a positive definite matrix inherited from its definition, if the following condition holds then Equation (3.24) is an ellipsoid (Markovsky et al 2004):

$$\mathbf{u}^T \mathbf{Q}^{-1} \mathbf{u} > 4k. \quad (3.27)$$

Differencing the terms on the left and right sides of the inequality gives

$$\mathbf{u}^T \mathbf{Q}^{-1} \mathbf{u} - 4k = \|\mathbf{F}\|^2. \quad (3.28)$$

The square of the amplitude of the Earth Magnetic field is strictly positive, thus Equation (3.27) holds. This implies that Equation (3.24) is the general equation of an ellipsoid. Consequently, calibrating a tri-axis magnetometer corresponds to estimating the unknown parameters of Equation (3.24), knowing that this second order equation describes an ellipsoid.

Using magnetic field measurements collected in a perturbation free environment along several orientations that best describe the ellipsoid, it is possible to use the constraint on the norm of the field vector given by Equation (3.19) to calibrate the magnetometers for the sensor errors and the host platform effect.

The proposed calibration algorithm comprises two steps. First the parameters of the ellipsoid equation are estimated and then the calibration elements \mathbf{A} and \mathbf{b} in Equation (3.20) are derived. The novelty of this calibration algorithm can be explained by the following two reasons. It does not require any assumption on the magnetic deviation and it calibrates directly the magnetic readings without estimating the geometrical properties of the ellipsoid (rotation, translation and lengths of the semi-axes).

3.10.1.2 Limitations of Classical Ellipsoid Fitting Algorithms

The first step consists in finding the parameters \mathbf{b} and \mathbf{Q} that satisfy Equation (3.24), which is an ellipsoid fitting problem with magnetic field measurements collected along different orientations.

Several methods have been developed. Algebraic fitting methods try to solve an optimization problem using least squares techniques (Fitzgibbon et al 1999, Li & Griffiths 2004). Geometric fitting approaches try to minimize the Euclidian distance from a point to the dataset using an orthogonal regression method (Cheng & Van Ness 1999). However due to the quadratic form in the measurement in Equation (3.19), these techniques are statistically inconsistent. Indeed analyzing the derivation of the noise term $\boldsymbol{\varepsilon}_w$ in Equation (3.19), it is shown that the algorithm's solution may be biased.

Introducing Equation (3.20) in the quadratic equation yields

$$\begin{aligned} \left\| \mathbf{A}^{-1}(\tilde{\mathbf{B}} - \mathbf{b}) \right\|^2 &= \left\| \mathbf{B} + \mathbf{A}^{-1} \boldsymbol{\varepsilon}_w \right\|^2 \\ &= \left\| \mathbf{B} \right\|^2 + 2\mathbf{B}^T \mathbf{A}^{-1} \boldsymbol{\varepsilon}_w + \boldsymbol{\varepsilon}_w^T \mathbf{Q} \boldsymbol{\varepsilon}_w \\ &= \left\| \mathbf{B} \right\|^2 + \boldsymbol{\delta}. \end{aligned} \quad (3.29)$$

With the variable \mathbf{B} and the noise term $\boldsymbol{\varepsilon}_w$ being independent and having zero mean, the new noise term $\boldsymbol{\delta}$ has still undesirable proprieties as its expectation can be strictly positive:

$$E(\boldsymbol{\delta}) = 2E(\mathbf{B}^T \mathbf{A}^{-1} \boldsymbol{\varepsilon}_w) + E(\boldsymbol{\varepsilon}_w^T \mathbf{Q} \boldsymbol{\varepsilon}_w) \geq 0. \quad (3.30)$$

If the assumption that the noise term $\boldsymbol{\varepsilon}_w$ tends to be null holds for the magnetometer measurements, then the previous estimation techniques will provide the exact parameters. However, low grade AMR sensors that have relatively high noise level are considered

here. Consequently an unbiased ellipsoid fitting algorithm that treats the noise as an additional parameter in the estimation process is considered.

3.10.1.3 Calibration Parameters

The next step consists in extracting the elements \mathbf{A} and \mathbf{b} defined in Equation (3.18) and required to calibrate the magnetometers readings.

The adaptive least squares (ALS) method, described in Markovsky et al (2004) estimates the solution $(\mathbf{Q}, \mathbf{u}, k)$ from Equation (3.24) along with the measurement error variance $\sigma_{\varepsilon_w}^2$. Correcting for the quadratic nature of the constraint on the norm of the magnetic field measurements in the LS, the ALS algorithm provides a consistent solution to the ellipsoid fitting problem. Therefore it is adapted here for the calibration of low cost magnetometers.

The combined bias \mathbf{b} , corresponding to the translation of the ellipsoid coordinate system, is computed from Equation (3.25) as

$$\mathbf{b} = \frac{-1}{2} \mathbf{Q}^{-1} \mathbf{u}. \quad (3.31)$$

Knowing the ALS estimate of \mathbf{Q} , the matrix \mathbf{A} can be derived from Equation (3.22).

Because \mathbf{Q} is a positive definite matrix, an eigen-decomposition can be applied as

$$\mathbf{Q} = \alpha \mathbf{V} \mathbf{D} \mathbf{V}^T \quad (3.32)$$

where $\alpha \in \mathbb{R}$, V corresponds to the eigenvectors of QQ^T and D is a 3x3 diagonal matrix containing the eigenvalues λ_i , $i \in \{1,2,3\}$. The columns of V form the basis vector directions for Q . Let us define

$$\sqrt{D} = \begin{bmatrix} \sqrt{\lambda_1} & 0 & 0 \\ 0 & \sqrt{\lambda_2} & 0 \\ 0 & 0 & \sqrt{\lambda_3} \end{bmatrix} \quad (3.33)$$

and

$$M = V\sqrt{\alpha D}V^T. \quad (3.34)$$

One can then write

$$M^T M = V\sqrt{\alpha D}V^T V\sqrt{\alpha D}V^T = \alpha V D V^T \quad (3.35)$$

where M corresponds to the matrix square root of Q and gives the solution for A^{-1} . To find α , one applies the constraint Equation (3.26) on the norm of the magnetic field measurement. Expanding Equation (3.24) while considering Equation (3.32) gives

$$\tilde{B}^T V \alpha D V^T \tilde{B} - 2b^T V \alpha D V^T \tilde{B} + b^T V \alpha D V^T b - \|F\|^2 = 0 \quad (3.36)$$

The introduction of α changes the definition of k , which becomes

$$k = b^T V D V^T b - \frac{\|F\|^2}{\alpha}. \quad (3.37)$$

Expanding Equation (3.37), α can be computed as

$$\alpha = \frac{4\|F\|^2}{4k - (V^T u)^T D^{-1} (V^T u)} \quad (3.38)$$

Finally Equation (3.20) can be applied on the magnetic field measurements to calibrate the host platform influence. Calibrated magnetic field measurements are given by

$$\mathbf{B} = \mathbf{V} \sqrt{\alpha \mathbf{D}} \mathbf{V}^T (\tilde{\mathbf{B}} - \mathbf{b} - \boldsymbol{\varepsilon}_w). \quad (3.39)$$

3.11 Magnetometer Calibration Results

In order to calibrate the magnetic field sensors, the data collection environment needs to be free from magnetic field perturbations. Also the total magnetic field in the vicinity of the data collection environment must be known, which is used as the calibration constraint. Thus an open field with no manmade ferrous infrastructure is selected for calibrating the magnetic field sensors. Three-dimensional orientation manoeuvres are performed to obtain enough information for ellipsoidal fitting as well as proper calibration of the three orthogonal axes. The expected total magnetic field in the data collection region is obtained from the CGRF model (Haines & Newitt 1997), which is utilized as the calibration constraint given by Equation (3.19). Figure 3-11 shows the calibration results for the magnetic field sensors where both the un-calibrated as well as the calibrated magnetic fields are plotted in 3D. The mesh globe shows the expected 3D magnetic field, which differs much from the measured one in the un-calibrated case. After calibration, the measured field components are coincident with the expected ones, thus showing calibration success.

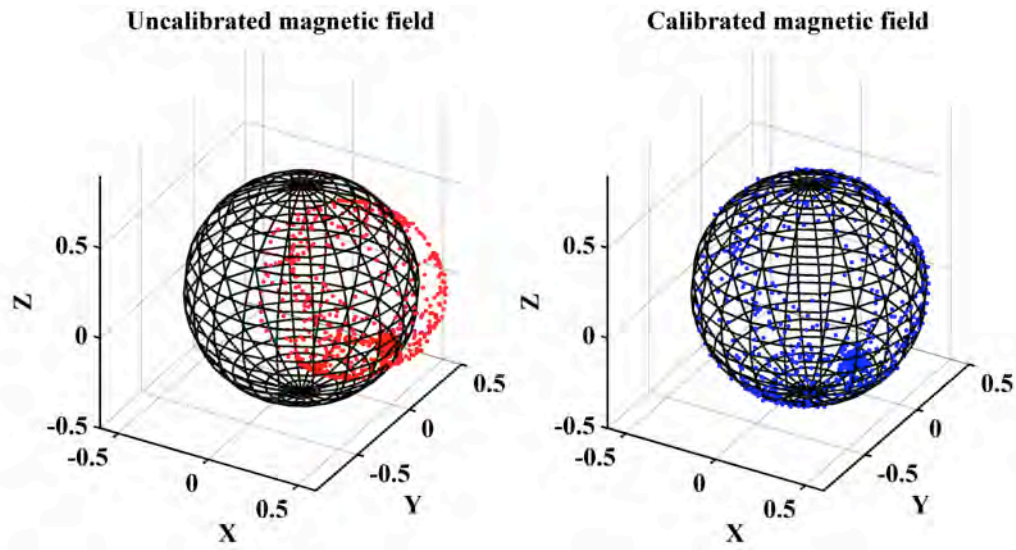


Figure 3-11: Calibration of MSP's magnetic field sensors. All axes are in Gauss.

Figure 3-12 shows the total magnetic field before and after calibration. Due to presence of instrumentation and magnetic field errors, the measured magnetic field is erroneously varying with changes in the orientation of the MSP before calibration. After estimation of the deterministic errors using the calibration algorithm, the magnetic field measured is consistent at different orientations and is very close to the expected magnetic field in that region. The only errors remaining are those caused by sensor noise, to be dealt with using stochastic error modeling. The calibration parameters for a three-axis magnetic field sensor are summarized in Section 3.13.

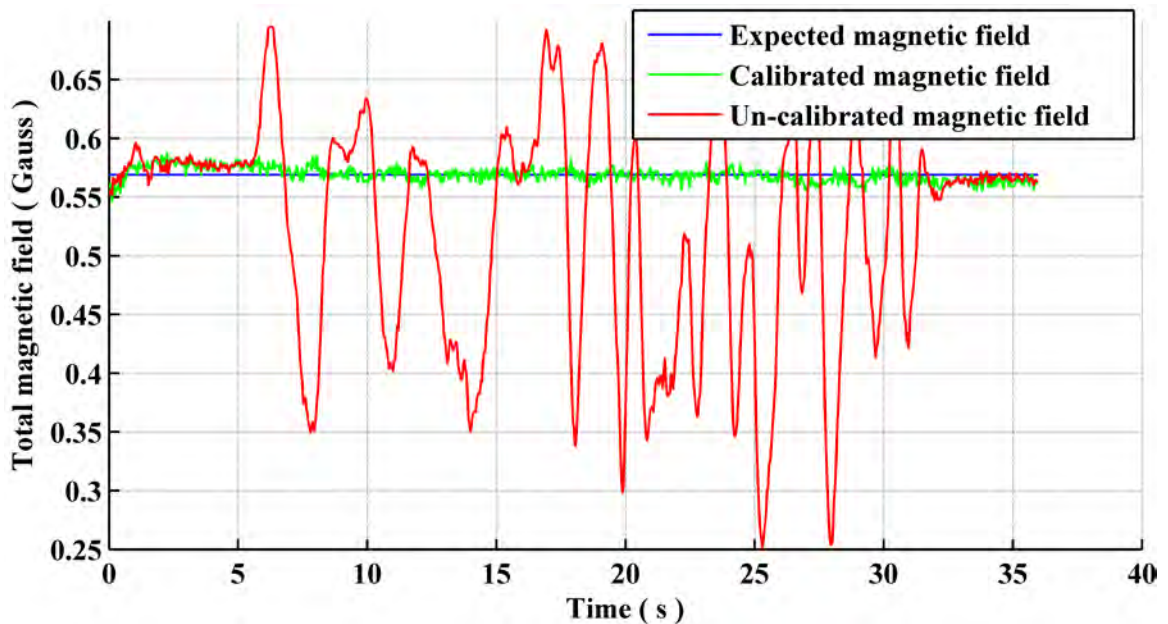


Figure 3-12: Impact of calibration on measured magnetic field.

3.12 Stochastic Error Modeling

After calibrating for the deterministic errors associated with the inertial as well as magnetic field sensors, it is desirable to have sufficient information regarding the noise terms associated with these sensors for stochastic modeling. A common procedure used for modeling the effects of sensor noise is the Allan variance analysis (Xing & Gebre-Egziabher 2008).

3.12.1 Allan Variance

The Allan Variance (AV) is a time domain sensor noise characterization method developed by David Allan (Allan 1987). It identifies the dominant noise components with respect to correlation times and is a well-known method for stochastic modeling of inertial sensors. For this research and in order to properly model the effects of sensors'

noise, 72 hours of static data was collected in an environment that encounters very little temperature variations. Although detailed stochastic modeling is possible with AV analysis, for this research, only the most dominant noise parameters are modeled here. These include the wide band noise and the exponentially correlated noise.

3.12.1.1 Model Parameters for Wide Band Noise

Wide band noise is a high frequency component of the sensor noise, which is a dominant noise parameter for smaller averaging times in an Allan Variance plot. The Power Spectral Density (PSD) for wide band noise is obtained by fitting a -1 slope ($-\frac{1}{2}$ slope in case of Allan deviation) line to the beginning of an AV plot and reading the AV value at 1 s averaging times as shown in Figure 3-13. Here the Z-axis gyroscope data is used for developing the procedure of extracting the PSDs. The PSD for wide band noise can then be converted to the noise variance by taking into account the sensor sampling time used for mechanization of the estimator.

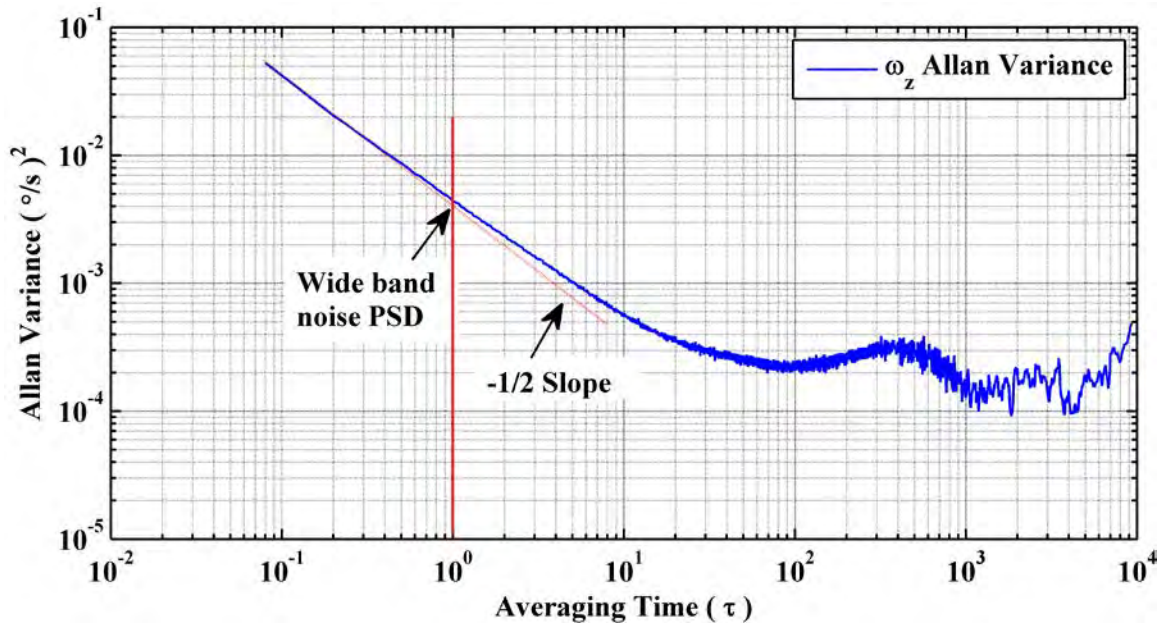


Figure 3-13: Obtaining the PSD for wide band noise.

3.12.1.2 Model Parameters for Exponentially Correlated Noise

Correlated noise is a medium frequency component of the sensor noise. It is caused by the slow variations in the sensor bias, thus can be used for modeling the time varying part of it. Being medium frequency, the AV plot for medium to higher averaging times is dominated by this noise parameter. To get a better estimate of modeling parameters for correlated noise, the sensor data was first filtered using a low pass filter to attenuate the effects of wide band noise. In this case, a low pass filter is realized using a moving average technique with a cut off frequency of 1 Hz. The low pass filtering technique effectively implements the subtraction of wide band noise AV from the total AV given by

$$\sigma^2(\tau) - \sigma_w^2(\tau) = \sigma_c^2(\tau), \quad (3.40)$$

where $\sigma^2(\tau)$ is the total AV, τ is the averaging time, $\sigma_w^2(\tau)$ is the wide band noise AV and $\sigma_c^2(\tau)$ is the exponentially correlated noise AV.

The filtered sensor data is then subjected to AV analysis, which now shows the exponentially correlated noise as a dominant noise parameter. This is depicted in Figure 3-14. The procedure for obtaining the PSD for correlated noise is not straight forward as compared with the one for wide band noise. First a line with $+1/2$ slope is fitted to the AV plot such that it intersects the 1 s averaging time.

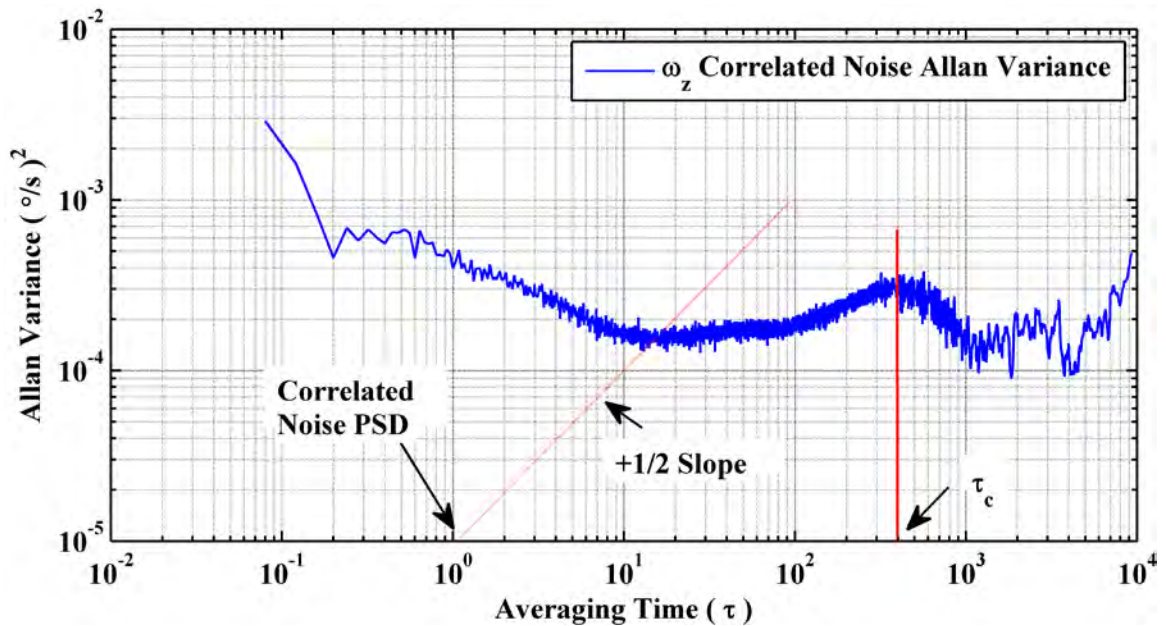


Figure 3-14: Allan Variance analysis of filtered sensor data for correlated noise.

Also a line with one slope is fitted to the averaging time where the AV plot changes from a positive slope to negative one. This is shown in Figure 3-14. The point where the $+1/2$ slope intersects the AV plot gives a rough estimate of the PSD for exponentially correlated noise whereas the rough estimate for the correlation time τ_c is obtained from the intersection of $+1/2$ and $-1/2$ slopes. These estimates are then utilized to assess the exponentially correlated noise model given by

$$\sigma_c^2(\tau) = \frac{(Q_c \tau_c)^2}{\tau} \left[1 - \frac{\tau_c}{2\tau} \left(3 - 4e^{-\frac{\tau}{\tau_c}} + e^{-\frac{2\tau}{\tau_c}} \right) \right], \quad (3.41)$$

where τ_c is the rough estimate of correlation time and Q_c is the rough estimate of the exponentially correlated noise PSD. Utilizing Equation (3.41), the AV for exponentially correlated noise is obtained, which is considered as the model and plotted with its actual AV in Figure 3-15.

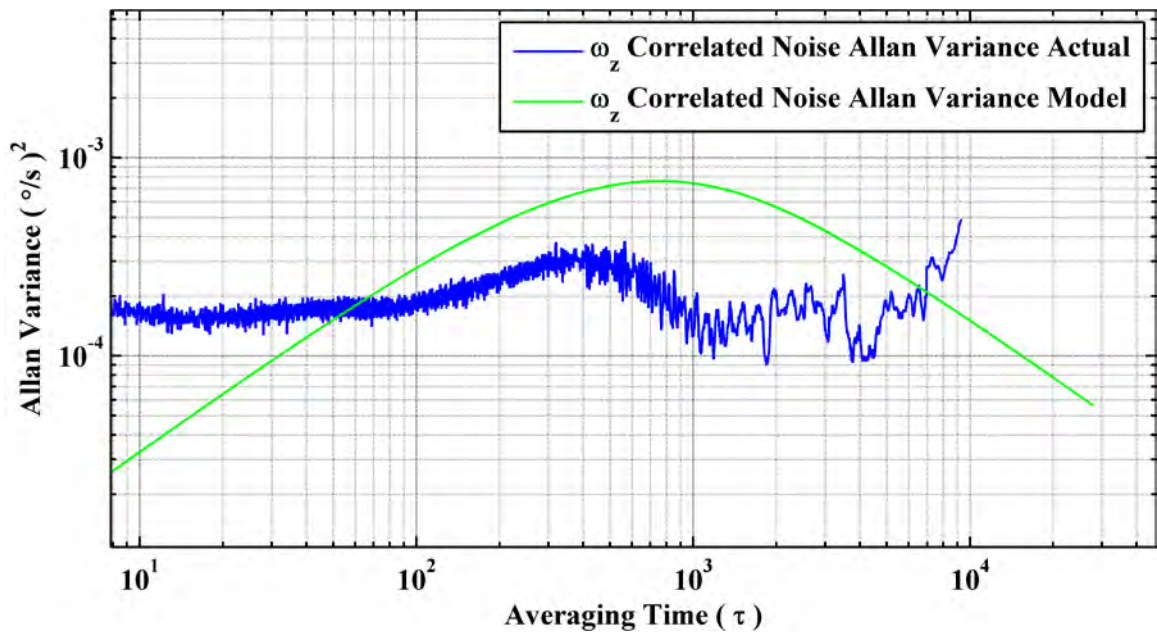


Figure 3-15: AV model for exponentially correlated noise using the rough estimates of PSD and correlation time.

Here it can be observed that the AV model is not following the actual one for exponentially correlated noise. The peak for the model is lagging the actual one and the PSD is higher in case of the model. These two parameters are iteratively adjusted so that the AV model closely follows the actual one. As the actual AV plot, which is composed of a number of noise components, is not completely modeled (only the most influential

noise components are modeled), various researchers suggest to slightly over-bound the exponentially correlated noise AV (Xing & Gebre-Egziabher 2008). The final AV model for the exponentially correlated noise is shown in Figure 3-16.

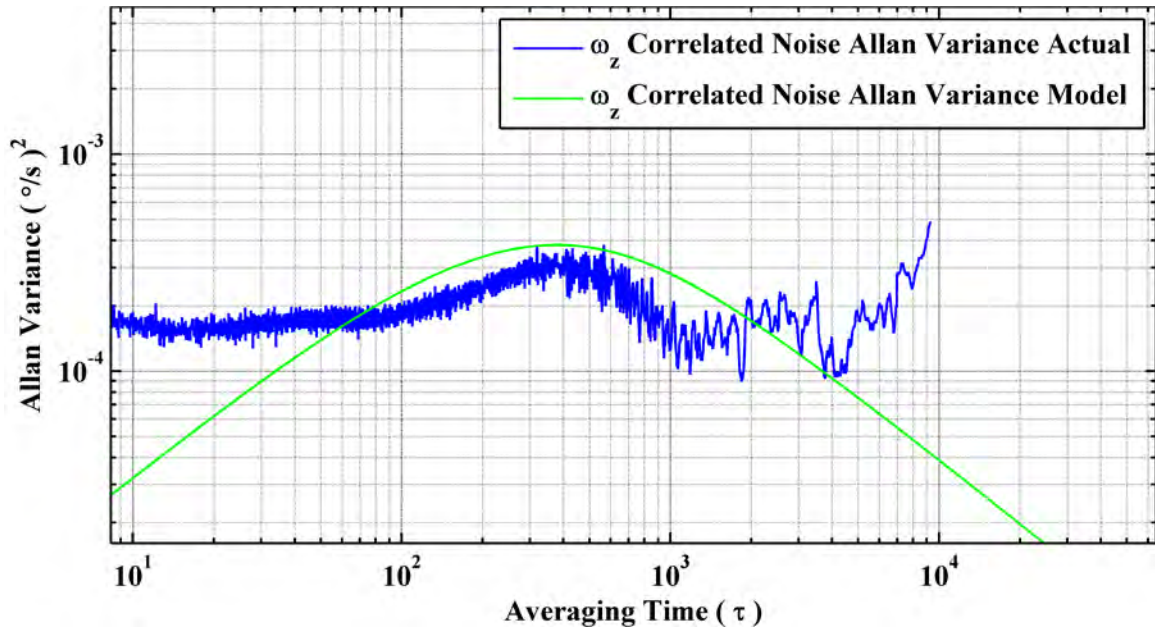


Figure 3-16: AV plot for the exponentially correlated noise after tuning the PSD and correlation time.

3.12.1.3 Complete Allan Variance Model

After obtaining the necessary modeling parameters for wide band noise and exponentially correlated noise, the combined noise model is assessed against the actual AV plot using the relationship governing the complete AV given by

$$\sigma^2(\tau) = \sigma_w^2(\tau) + \sigma_c^2(\tau). \quad (3.42)$$

Figure 3-17 depicts the AV plot for the modeled noise parameters. It can be observed that the model closely follows the actual AV for wide band (smaller averaging times) and exponentially correlated noise (medium averaging times). For larger averaging times, the

model deviates from the actual one as the noise components affecting the sensor at very low frequencies are not modeled for this research.

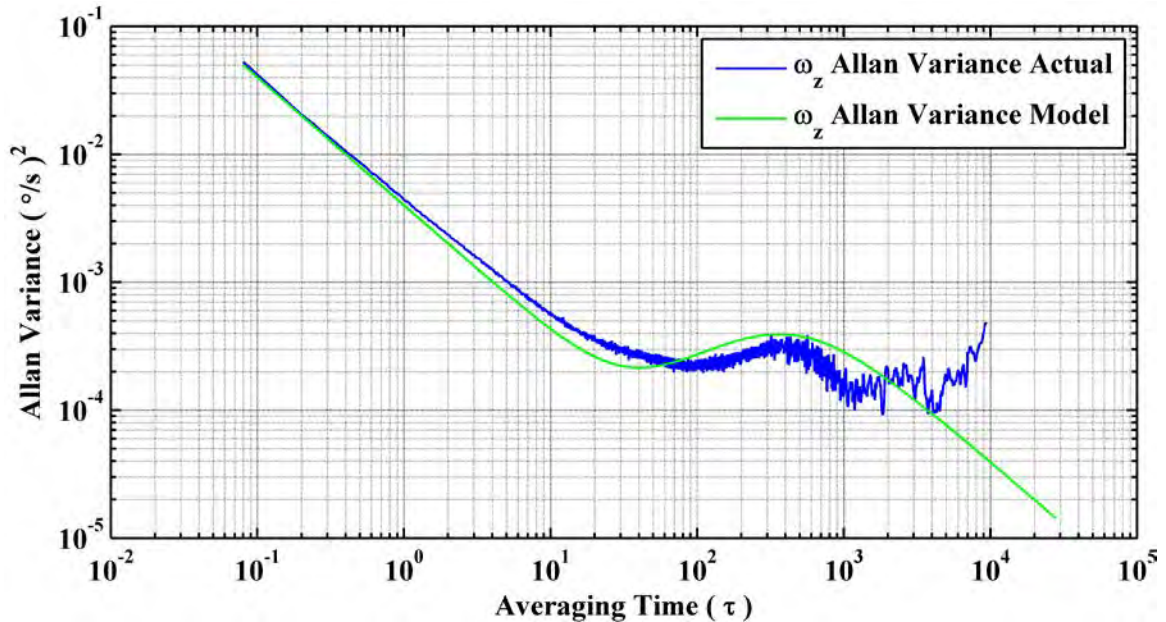


Figure 3-17: Actual versus modeled AV for wide band and exponentially correlated noise.

3.12.1.4 AV Analysis for the MSP Sensors

Figure 3-18 shows the Allan variance plot for the rate gyroscopes. The Allan Variances obtained using only the modeled noise parameters are also shown here. It can be observed that the modeled noise components are closely following the actual ones for averaging times of 1000 s and less, which constitutes the wide band noise and the exponentially correlated noise components. Thus the stochastic error modeling achieved using the Allan Variance is sufficient for the sensor error model being used for this research. Similar observations can be made from Figure 3-19 and Figure 3-20, which show AV plots for accelerometers and magnetometers respectively.

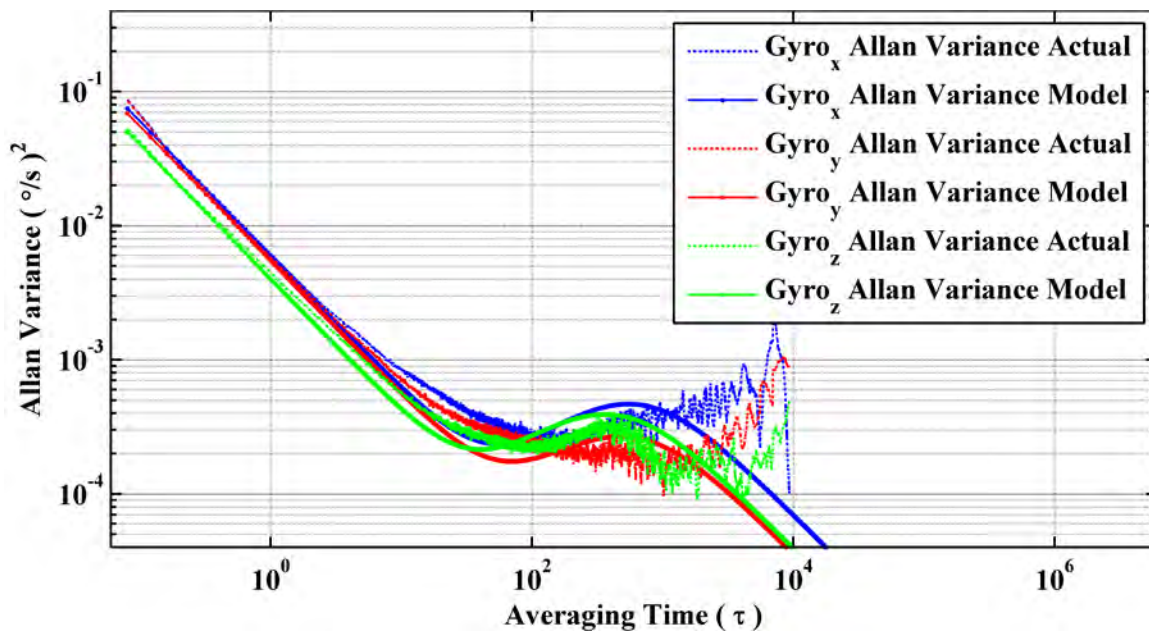


Figure 3-18: Gyroscope Allan Variance, actual versus model.

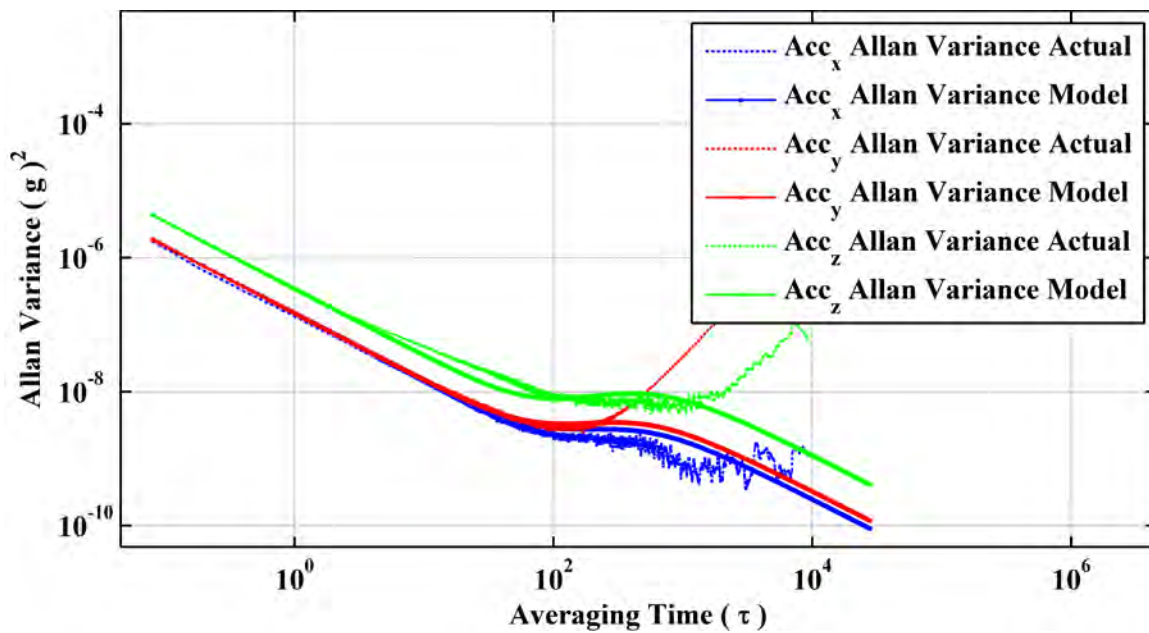


Figure 3-19: Accelerometer Allan Variance, actual versus model.

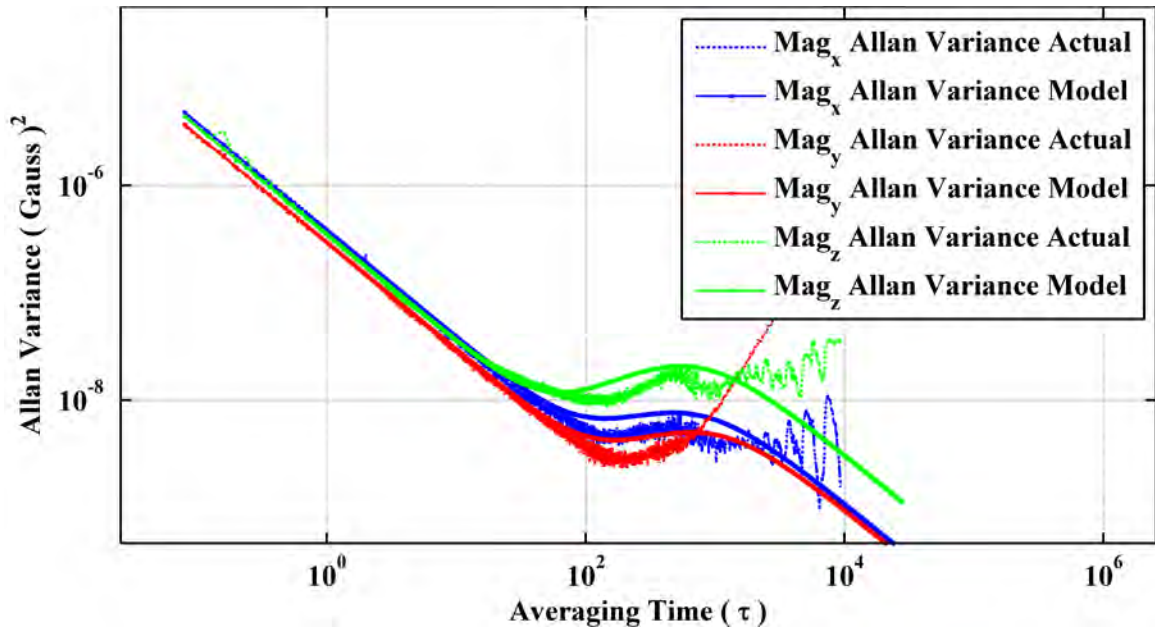


Figure 3-20: Magnetometer Allan Variance, actual versus model.

3.13 MSP Sensors' Calibration and Noise Parameters

Following Equation (3.3), the calibrated accelerometer triad data is obtained using

$$\begin{bmatrix} f_x \\ f_y \\ f_z \end{bmatrix} = \underbrace{\begin{bmatrix} m_{xx} & m_{xy} & m_{xz} \\ m_{yx} & m_{yy} & m_{yz} \\ m_{zx} & m_{zy} & m_{zz} \end{bmatrix}}_{A^{-1}} \left\{ \begin{bmatrix} \tilde{f}_x \\ \tilde{f}_y \\ \tilde{f}_z \end{bmatrix} - \underbrace{\begin{bmatrix} b_{f_x} \\ b_{f_y} \\ b_{f_z} \end{bmatrix}}_b \right\}. \quad (3.43)$$

Similarly, the calibrated gyroscope triad data is obtained using

$$\begin{bmatrix} \omega_x \\ \omega_y \\ \omega_z \end{bmatrix} = \underbrace{\begin{bmatrix} m_{xx} & m_{xy} & m_{xz} \\ m_{yx} & m_{yy} & m_{yz} \\ m_{zx} & m_{zy} & m_{zz} \end{bmatrix}}_{A^{-1}} \left\{ \begin{bmatrix} \tilde{\omega}_x \\ \tilde{\omega}_y \\ \tilde{\omega}_z \end{bmatrix} - \underbrace{\begin{bmatrix} b_{\omega_x} \\ b_{\omega_y} \\ b_{\omega_z} \end{bmatrix}}_b \right\}. \quad (3.44)$$

These calibration parameters are obtained by using the calibration algorithms discussed in Sections 3.8.1 and 3.8.2. Table 3-2 summarizes the inertial sensor calibration results.

In case of magnetometers, the combined effect of non linear instrumentation and magnetic field errors along with the linear instrumentation and magnetic field errors are estimated using the calibration algorithm detailed in Section 3.10. These calibration parameters are summarized in Table 3-3.

The stochastic modeling parameters associated with inertial and magnetic field sensors are obtained using the AV method and are summarized in Table 3-4.

Table 3-2: MSP's inertial sensor calibration parameters.

Sensor Triad	Scale factor and misalignment error matrix (A)	Biases (b)
Gyroscopes	$\begin{bmatrix} 1.0072 & -0.0044 & -0.0165 \\ 0.0248 & 1.0030 & 0.0117 \\ 0.0024 & -0.0075 & 0.9941 \end{bmatrix}$	$\begin{bmatrix} 0.0140 \\ -0.1004 \\ -0.0421 \end{bmatrix} \text{ } \frac{\circ}{s}$
Accelerometers	$\begin{bmatrix} 1.0502 & 0.0356 & -0.0027 \\ -0.0039 & 1.0427 & -0.0144 \\ -0.0096 & 0.0239 & 1.0319 \end{bmatrix}$	$\begin{bmatrix} 0.0140 \\ -0.1004 \\ -0.0421 \end{bmatrix} \text{ } g$

Table 3-3: Magnetometer calibration parameters.

Sensor Triad	Non linear and linear errors' matrix (A)	Biases (b)
Magnetometers	$\begin{bmatrix} 0.9475 & -0.0178 & 0.0195 \\ -0.0178 & 0.9283 & 0.0096 \\ 0.0195 & 0.0096 & 1.0097 \end{bmatrix}$	$\begin{bmatrix} 0.0209 \\ -0.0130 \\ 0.0162 \end{bmatrix} \text{ } \text{Gauss}$

Table 3-4: Stochastic modeling of inertial and magnetic field sensors.

Sensor	Axis	Stochastic Modeling Parameters @ 25Hz		
		Wide Band Noise	Exponentially Correlated Noise	
		σ_w	τ_c	σ_c
Gyroscopes	X	0.387 °/s	300 s	0.035 °/s
	Y	0.370 °/s	270 s	0.026 °/s
	Z	0.316 °/s	200 s	0.031 °/s
Accelerometers	X	2.00 mg	200 s	77 µg
	Y	1.92 mg	200 s	89 µg
	Z	2.93 mg	250 s	150 µg
Magnetometers	X	3.10 mG	300 s	134 µG
	Y	2.72 mG	400 s	109 µG
	Z	2.95 mG	300 s	229 µG

Chapter Four: **Magnetic Perturbation Detection, Estimation and Mitigation Techniques**

Chapter 2 described the theoretical modeling of the magnetic field generated by a dipole and then extended it to take into account the effects of multiple dipoles. This chapter first assesses the impact of magnetic field perturbations on the Earth's magnetic field in different pedestrian navigation environments and then analyzes different magnetic field parameters to mitigate the effects of these perturbations. These are achieved by detailed magnetic field surveying of various pedestrian navigation environments using the hardware developed in Chapter 3. Investigation of the use of various magnetic field parameters in lieu of the detailed modeling conducted in Chapter 2 is then carried out, which utilizes the outcome of the magnetic field survey. The factors affecting the Earth's magnetic field in different pedestrian navigation environments are also discussed. It is worth mentioning that the detailed magnetic field survey conducted for this research as discussed in this chapter becomes the backbone for assessing the effects of perturbations and development of the different mitigation techniques that follow (Afzal et al 2010).

4.1 Factors Affecting the Earth's Magnetic Field in Different Environments

Urban canyons and indoor environments are the ones most used by pedestrians. Unlike outdoor environments, these are overtaken by different infrastructures most of which are composed of metallic structures and electrical/ electronic systems. These generate artificial magnetic fields, which alter the Earth's magnetic field's magnitude as well as direction. In order to analyze the effects of these perturbations and mitigate them,

assessment and statistical characterization of the magnetic field perturbations is necessary in pedestrian navigation environments.

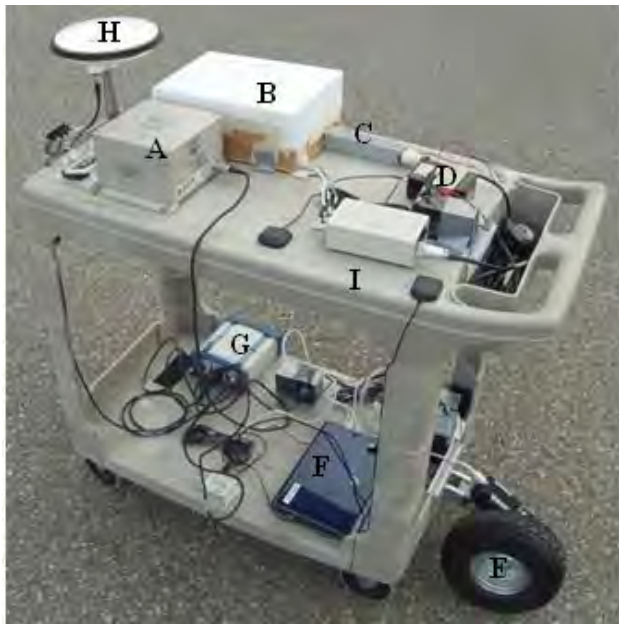
4.2 Assessment of Magnetic Field in Pedestrian Navigation Environments

Assessment of the magnetic field is conducted by surveying different indoor and outdoor environments using the MSP, MMP as well as a high sensitivity magnetic field sensor. A high accuracy reference system along with an optical wheel encoder is also used for comparative analysis as well as qualitative assessment of the developed mitigation and estimation techniques. Assessment and characterization of the effects of perturbations is conducted for the following magnetic field parameters:

1. Horizontal field
2. Vertical field
3. Total field (norm)
4. Angle of inclination
5. Magnetometer's orientation with respect to the perturbation field.

4.2.1 Magnetic Field Surveying Setup

Figure 4-1 shows the overall hardware setup for the magnetic field survey. All of the sub-systems are identified. The MMP is enclosed in a box to protect it from the elements.



- A: Tactical grade IMU
- B: MMP (enclosed)
- C: Fluxgate magnetic field sensor
- D: MSP
- E: Optical wheel encoder
- F: Data logging laptop
- G: Dual frequency GNSS receiver
- H: Dual frequency GNSS antenna
- I: Plastic cart

Figure 4-1: Magnetic field data collection setup.

Before conducting any magnetic field survey, all of the magnetic field sensors need to be calibrated so that the measurements are dominated by the environmental perturbations rather than the sensor errors described in Section 3.9. The magnetic field sensors' calibration algorithm is described in Section 3.10. As the magnetic field perturbations can also be generated by the data collection platform (cables, batteries, electronics etc.), calibration is performed for the entire test setup. This is depicted in Figure 4-2 where the complete data collection setup is being rotated in 3 dimensions. An open field is selected for the calibration of magnetic field sensors so as to only calibrate for the instrumentation and platform's magnetic field induced errors.



Figure 4-2: Calibration of the magnetic field data collection setup.

To assess the impact of magnetic field perturbations on the Earth's magnetic field in general and magnetic heading estimates in particular, reference information regarding the expected Earth's magnetic field as well as heading is required. The true heading is computed using the SPAN-CPT HG1700 and SPAN-SE LCI GNSS/INS System from NovAtel. It is composed of a tactical grade Inertial Measurement Unit (IMU) capable of estimating the heading with a 1° accuracy. Knowledge of the Earth's magnetic field at and around the vicinity of the data collection site is necessary to distinguish between the fields due to local perturbations and that caused by the Earth's dipole. The latter is predicted using the Canadian Geomagnetic Reference Field (CGRF) that continuously observes and models the Earth's magnetic field parameters in the Canadian region as described in the previous chapter. This field is transformed to the sensor frame by utilizing the attitude estimates from the reference system. To get an accurate measurement of the magnetic field, a high resolution and sensitivity fluxgate magnetic

field sensor is utilized. This type of magnetic field sensor falls in the medium grade category and is suitable for sensing very low to high magnetic fields encountered in the indoors (Ripka 2001). The main specifications of this sensor are summarized in Table 4-1.

Table 4-1: High sensitivity magnetic field sensor specifications.

Parameter	Details
Type	Fluxgate
Manufacturer	Bartington
Axis	Three
Measuring range	$\pm 100 \mu\text{T}$
ADC Resolution	12 bits
Sensitivity	48 nT

4.2.2 Selection of Data Collection Environments

The effect of perturbations on the Earth's magnetic field depends on the frequency of occurrence and the magnitude of the local magnetic perturbations. Thus the infrastructure type as well as its usage will govern the amount of perturbations expected in a particular indoor/ outdoor environment. Consequently the magnetic field survey is conducted in a diverse set of buildings including old and new office constructions, schools, a student center and a shopping mall so as to reflect the diversity of indoor environments. An urban area (downtown) is also surveyed to complete the pedestrian navigation environments' set. Table 4-2 summarizes the environmental characteristics for the magnetic field data collection. A total of 2.5 hours (7 km) of magnetic field data was collected at a walking speed of 1 m/s, which is maintained on average to keep the survey as realistic as possible from a pedestrian navigation perspective.

Table 4-2: Environments selected for the magnetic field survey.

Name	Construction		Open Space	I.T. Hardware	Shops (S)/ Offices (O)
	Old	New			
CCIT-UofC		X		X	O
Engg.-UofC	X			X	O
ICT-UofC		X	X	X	O
MacEwan-UofC	X	X	X		S
Mall		X	X		S
Downtown	X	X	X		S

The first four environments selected for the assessment of magnetic field are located on the main campus of the University of Calgary. These are Calgary Centre for Innovative Technologies (CCIT), Engineering building (Engg.), Information and Communications Technology (ICT) and MacEwan student centre. CCIT is a new building hosting graduate student offices. It has narrow corridors and is equipped with office equipment (photocopiers, computers etc.). This building is selected for magnetic field data collection as it portrays a modern office setup. The Engineering building is an old construction and hosts lecture halls, departmental offices and labs. It has wide corridors and can be considered a typical school building. ICT is also a new construction with wide corridors, lecture halls and students' sitting area. It offers a lot of ferrous infrastructure, which justifies its selection for the data collection. MacEwan is the student centre of the University of Calgary and has the food court as well as halls for student related activities. It offers an arrangement common to different public places like hospitals (waiting areas), ports etc. A North American shopping mall is also targeted for the data collection. As pedestrian navigation has a lot of commercial impact in such buildings, the shopping mall provides a critical magnetic field data set for this research. Finally an urban canyon (downtown Calgary) is also targeted for the magnetic field survey as it also offers a

commercially important area for pedestrian navigation. Figure 4-3 shows magnetic field data collection being carried out in CCIT and Engineering buildings. The same setup is used for data collection in all of the remaining environments as well.



Figure 4-3: Magnetic field data collection indoor.

4.3 Statistical Analysis of Indoor Magnetic Field

After collecting magnetic field data in different pedestrian navigation environments, its characterization was carried out (Afzal et al 2010). This is necessary to attain the statistical information regarding the perturbations in different environments. The distribution that best fits the magnetic field parameter being investigated is identified by its detailed statistical analysis. Figure 4-4 depicts the Probability Density Functions (PDFs) for heading estimates in different environments. It can be observed that the outdoor urban canyon environment (Downtown) is providing the best heading estimates whereas the office buildings are the worst with a few errors even exceeding 130° .

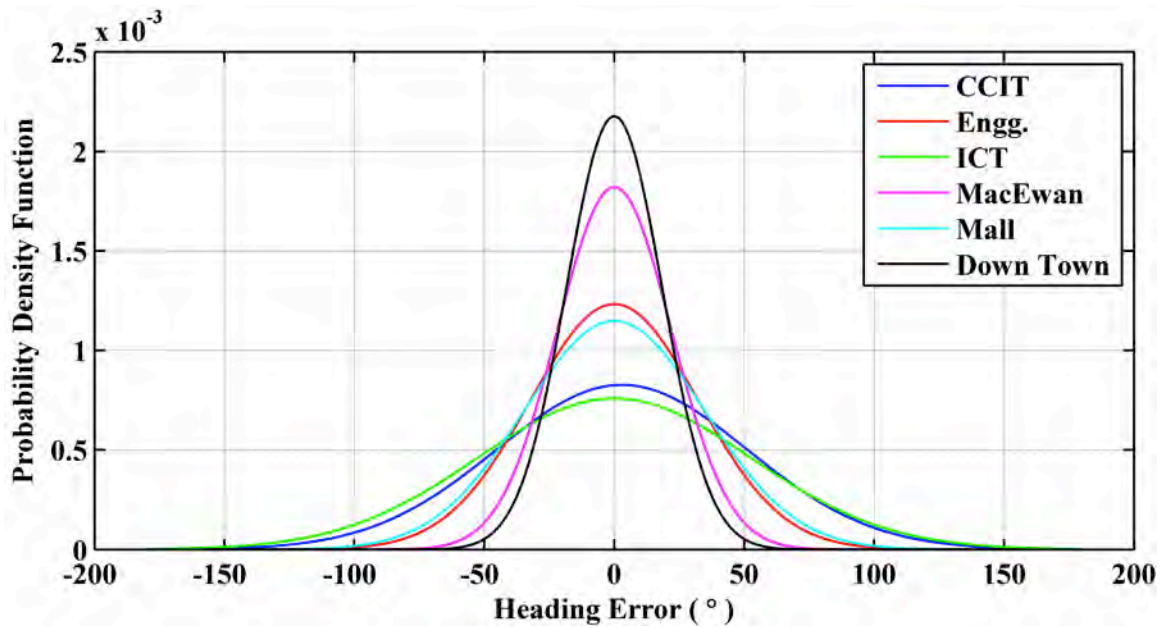


Figure 4-4: Heading error PDFs in different pedestrian navigation environments.

Figure 4-5 shows the total field perturbation PDFs for different environments. The urban outdoor environment is showing the least perturbations in this case, which suggests good heading estimates. But if one compares the heading and total field perturbation PDFs for the Engineering building, it can be observed that although the heading estimates in this environment are the third best overall, the total field perturbations are the worst. This means that one cannot just observe the total field magnitude and decide upon the goodness of the heading estimates. More parameters need to be examined.

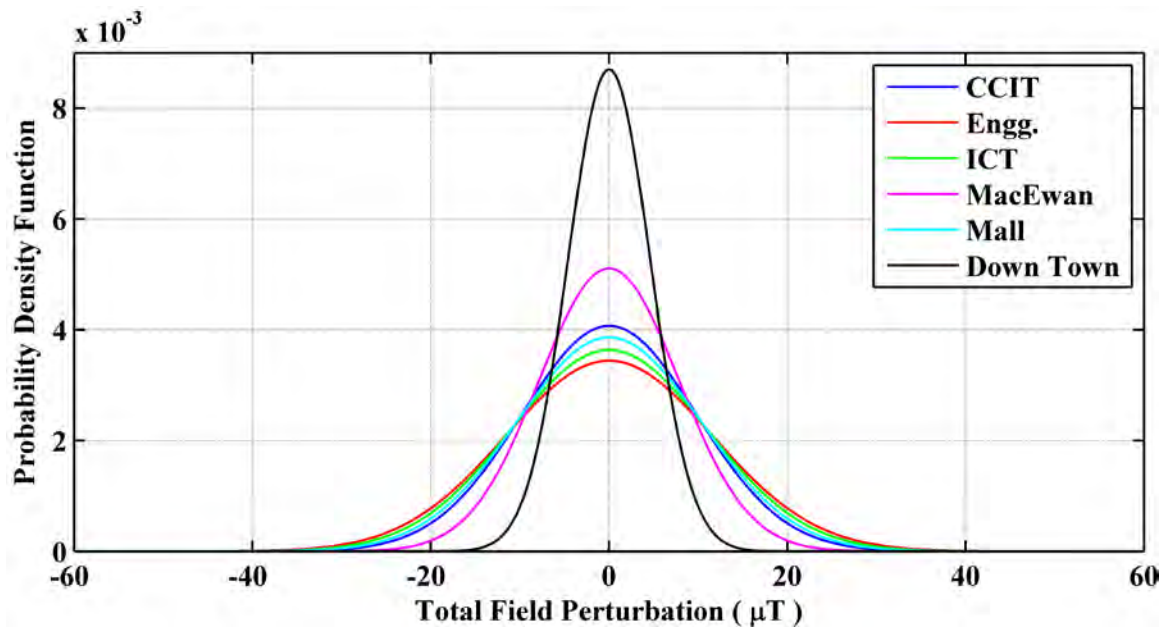


Figure 4-5: Total field perturbation PDFs in different pedestrian navigation environments.

Figure 4-6 shows the horizontal field perturbation PDFs. Again the urban outdoor environment is the cleanest followed by the engineering building that has the worst total field perturbations as depicted in Figure 4-5. This suggests that it is the horizontal field rather than the total field that gives a better insight into the accuracy of heading estimates.

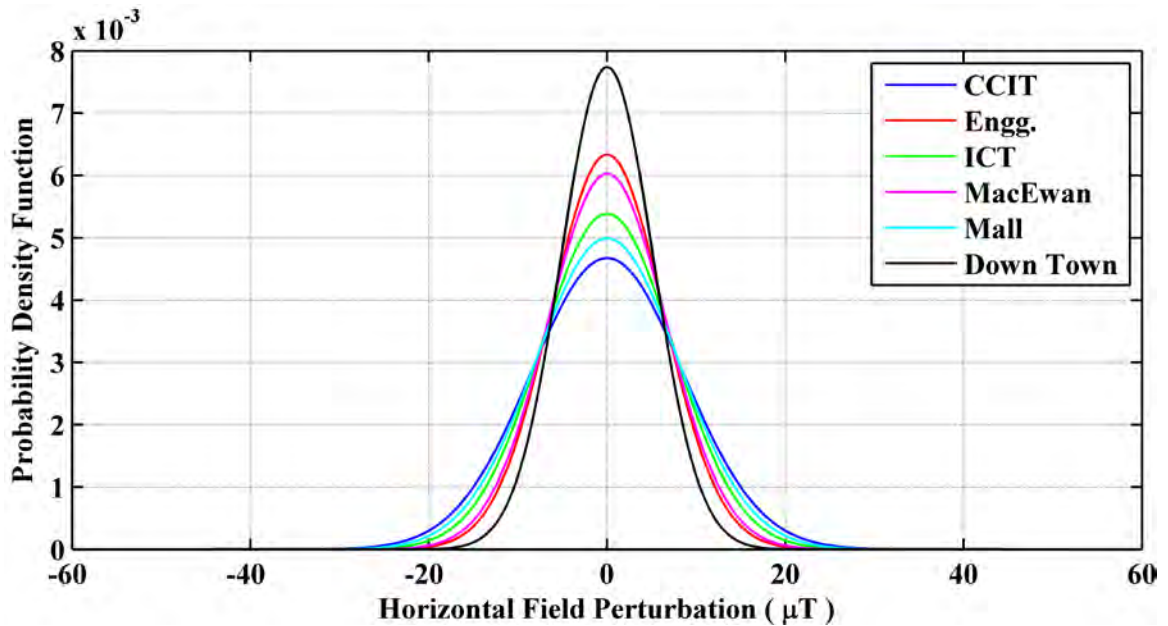


Figure 4-6: Horizontal field perturbation PDFs in different pedestrian navigation environments.

Figure 4-7 shows the vertical field perturbation PDFs for the different pedestrian navigation environments. Upon comparing these PDFs with Figure 4-5, it can be observed that there is a direct relationship between total field and vertical field perturbations. This is a critical observation identifying strong vertical field perturbations in pedestrian navigation environments, which suggests that good heading estimates are possible even if the total field magnitude is strongly perturbed. Equation (2.51) suggests that the vertical field perturbations play no role in the heading estimates. Therefore one can give a lower weight to the vertical field perturbations while assessing the accuracy of the heading estimates.

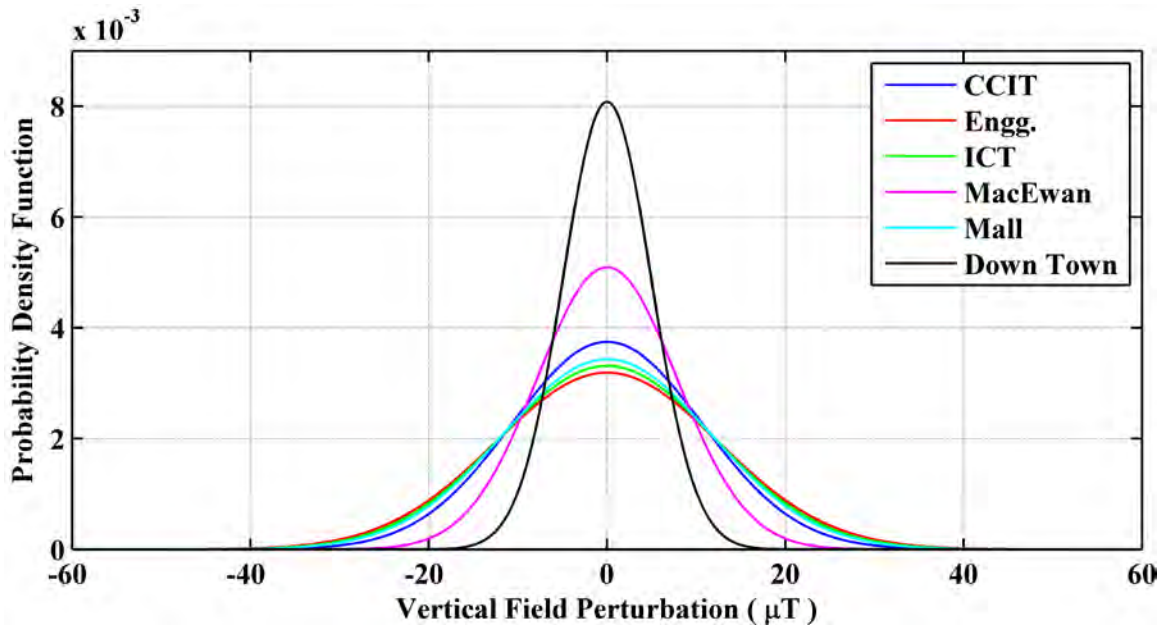


Figure 4-7: Vertical field perturbation PDFs in different pedestrian navigation environments.

Similar to the total and vertical field perturbation distributions, inclination angle error distributions for the selected environments suggest that the decision to accept heading estimates cannot be solely made by observing the inclination angle errors as shown in Figure 4-8.

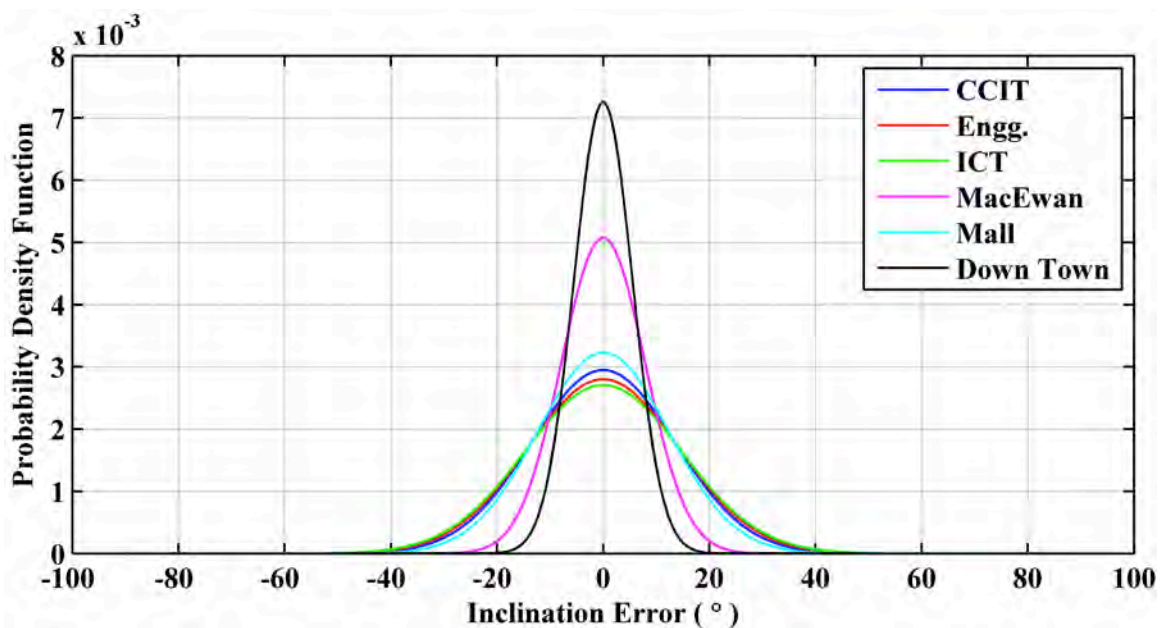


Figure 4-8: Inclination angle error PDFs in different pedestrian navigation environments.

The characterization of different magnetic field parameters suggests that these follow a Gaussian distribution. The statistical knowledge attained from this analysis is used for detection, mitigation and estimation of magnetic field perturbations in different environments.

4.4 Detection and Mitigation of Magnetic Field Perturbations Using Multiple Magnetometers

Section 2.5 described the Earth's magnetic field modeling in the presence of a perturbation source. Assume another tri-axis magnetic field sensor at the observation point p , which is oriented at 30° with respect to the first one as shown in Figure 4-9.

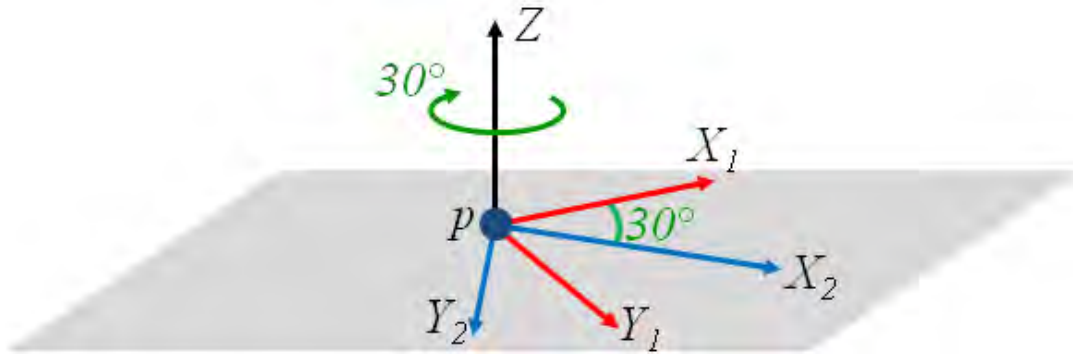


Figure 4-9: Dual magnetometer setup at observation point p .

By simulating a pedestrian's walk towards and away from the perturbation dipole as shown in Figure 2-6, the magnetic field profile for first magnetometer (MAG 1) is shown in Figure 4-10. It can be observed from the magnetic field profile that the sensor measures only the Earth's magnetic field at the beginning and at the end. When the pedestrian comes close to the perturbation source in the middle of the profile, the total magnetic field as well as the individual magnetic field components become perturbed.

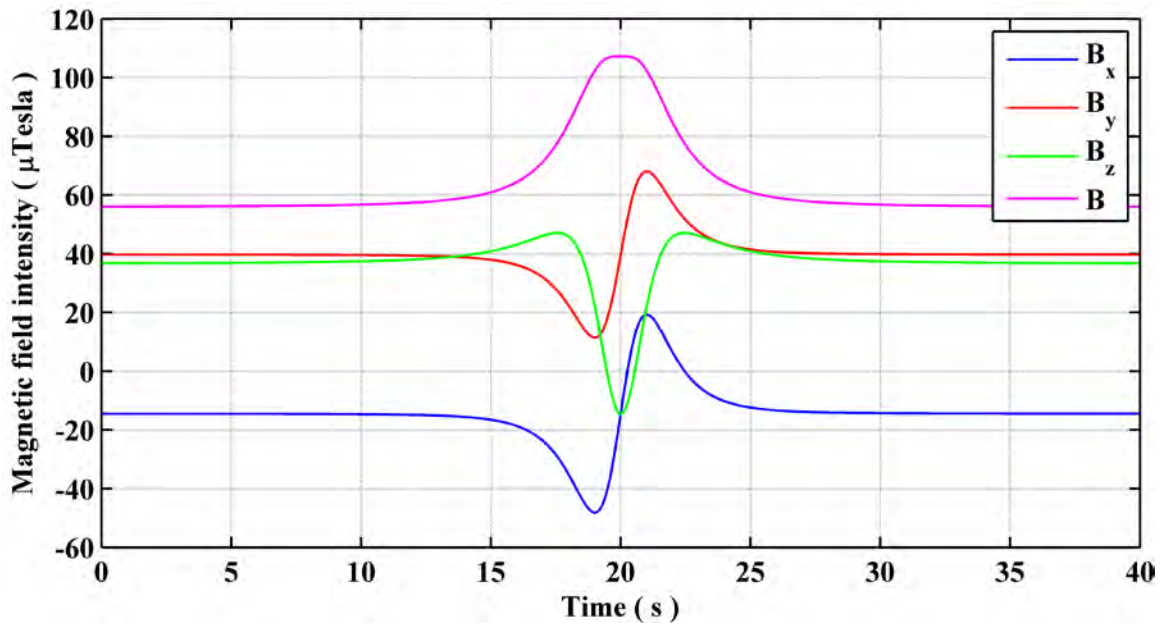


Figure 4-10: Magnetic field as measured by MAG 1 during a pedestrian walk in a perturbed environment.

However, although the total magnetic field as measured by the second magnetometer (MAG 2) is also perturbed, the individual magnetic field components are different as shown in Figure 4-11. It is also observed that the X-axis component of the measured magnetic field is constant, which means that the magnetometer is oriented in such a way that one of its components is insensitive to the magnetic field generated by the perturbation source. This is a critical observation that plays an important role in the development of a multiple magnetometer based perturbation mitigation technique. From this theoretical analysis, it can be concluded that: *“there exists information regarding the presence or the absence of magnetic perturbations in the three dimensional magnetic field components sensed by magnetic field sensors placed very close to each other but arranged in different orientations in space”*.

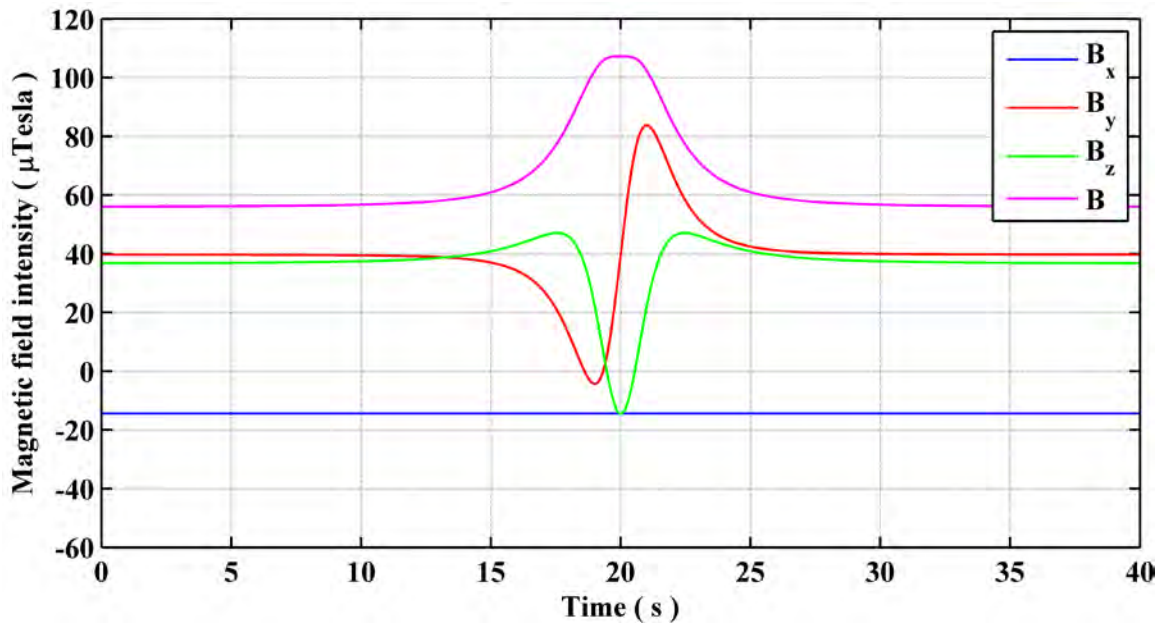


Figure 4-11: Magnetic field as measured by MAG 2 during pedestrian's walk in a perturbed environment.

4.4.1 Detection of Perturbations using Multiple Magnetometers

The above concluded that multiple magnetometers can be utilized for detecting and reducing the effects of magnetic perturbations on heading estimates. But before using multiple magnetometers, it is necessary to find out whether the perturbation exists or not. This section investigates different sources of information contained in the magnetic field data acquired using multiple magnetometers for detecting the perturbations. To keep the investigation simple, two magnetometer triads with their Z-axes aligned and with a 30° rotation angle around the Z-axis are considered as shown in Figure 4-9. In the presence of a perturbation source, as depicted in Figure 4-10, it can be seen that the total magnetic field (norm) varies from its nominal value. Thus some information about the presence and strength of the perturbation is contained in the norm itself. However it is quite possible that the magnetic moment, which results from the combination of the Earth's

magnetic field and the perturbation sources, changes its magnitude but not its orientation. This can be derived from Equation (2.47). Such perturbation sources can be considered as constructive as they amplify the magnetic field without any effect on its orientation hence not causing any errors in the heading estimates. On the other hand, if the perturbation sources change not only the magnitude of the Earth's magnetic moment but also its direction, they are considered destructive as the heading estimates using this combination will not be oriented with respect to the magnetic North.

In order to distinguish between constructive and destructive perturbations, additional information is required along with the magnetic field intensity. Figure 4-12 depicts the magnetically derived heading estimates in the absence and in the presence of a magnetic perturbation. Here it can be observed that the presence of a perturbation source causes an abrupt change in the estimated heading for both magnetometers having a 30° orientation difference. Thus observing a change in the norm of the magnetic field as well as a change in the estimated heading can be utilized for detecting a destructive perturbation source.

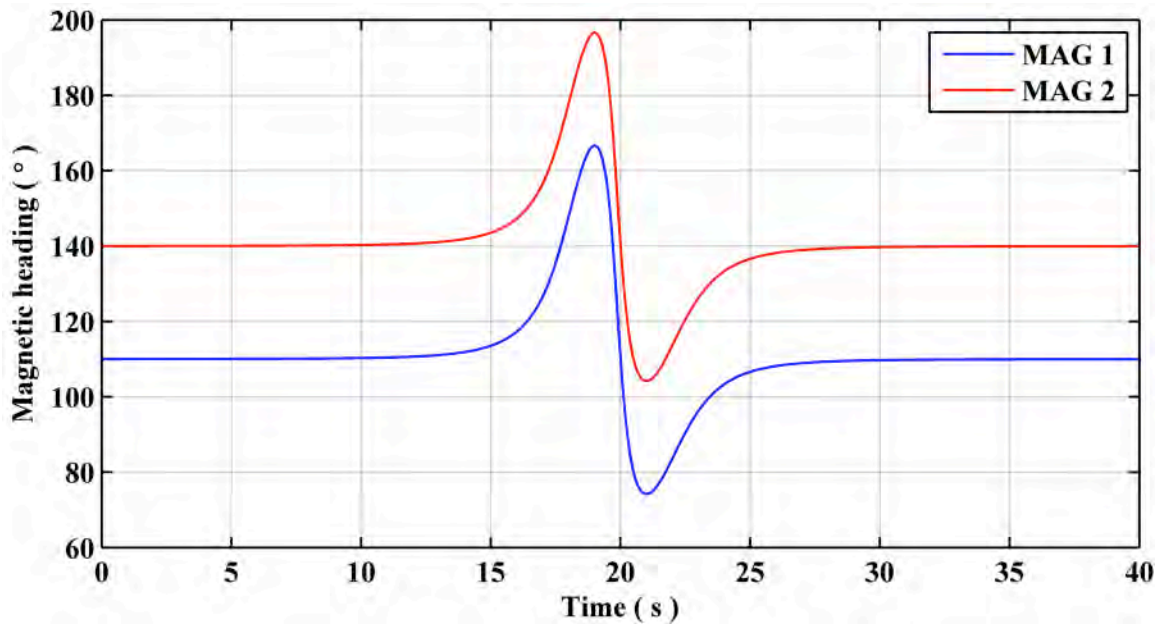


Figure 4-12: Magnetically derived heading in absence and presence of perturbation.

Figure 4-13 shows the number of possible magnetic field combinations in a pedestrian navigation scenario. From this flowchart, it can be concluded that the detection of a destructive perturbation and its impact on the magnetic field depends on the magnitude of the magnetic field and the orientation rate of change.

Based on these observations, the proposed perturbation detector is given by

$$\varepsilon_F = |F - F_E| \dot{\psi}, \quad (4.1)$$

where ε_F is the perturbation indicator, F_E is the expected local Earth's magnetic field, F is the local magnetic field and $\dot{\psi}$ is the orientation rate of change.

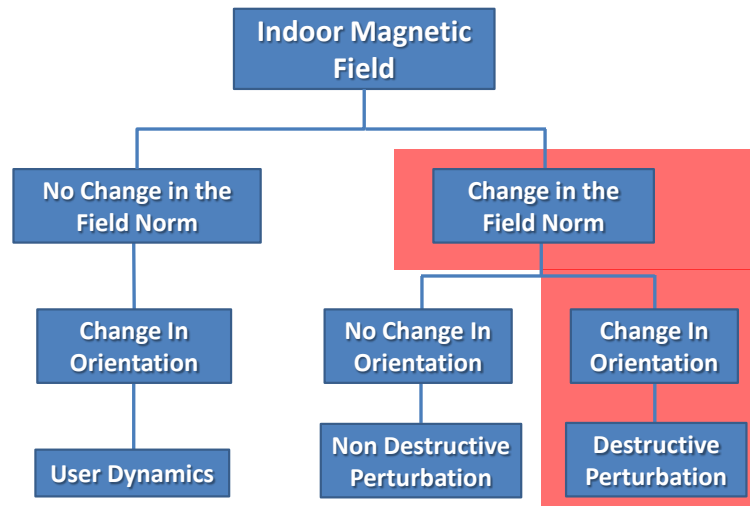


Figure 4-13: Detection of a destructive perturbation.

4.4.2 Mitigation of Perturbations using Multiple Magnetometers

From Equation (2.35), the general form of Biot-Savart law is given by

$$d\mathbf{B}(p) = \frac{\mu_0}{4\pi} \frac{\mathbf{M} \times \mathbf{R}}{\|\mathbf{R}\|^3}. \quad (4.2)$$

It can be observed from this equation that a change in the magnetic field vector depends on two main terms:

1. the distance between the origin of the magnetic dipole and the observation point p , namely the separation and
2. the angle between \mathbf{M} and the sensor orientation given by a unit vector $\frac{\mathbf{R}}{\|\mathbf{R}\|}$.

The variation in the total magnetic field can only result from a change in the separation.

This is possible only due to the presence of an artificial perturbation source as the Earth's

magnetic dipole is too far to be affected by pedestrian's motion. But the change in orientation can be either due to user dynamics or a perturbation.

Because the perturbation detector is able to distinguish between a change in orientation due to either user dynamics or perturbation, a variation in the magnetic field components, i.e. computing the field gradient, can be used to identify which magnetometer's measurement senses the least perturbed Earth's magnetic field component as shown in Figure 4-14.

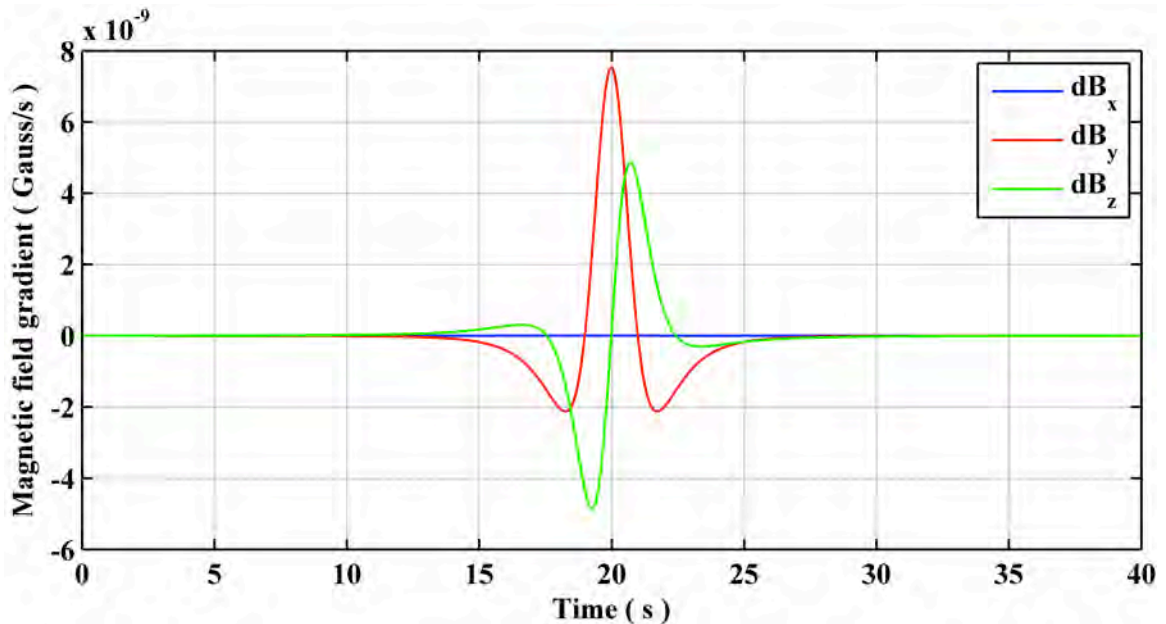


Figure 4-14: Gradient analysis of MAG 2 components.

Once the components of magnetic field measurements with least perturbation effects are identified using the field gradients, the remaining component can be estimated by propagating the good estimates of Earth's magnetic field from the previous epoch to the present one. This approach is shown in Figure 4-15. Chapter 5 will describe the estimator

for mitigating the effects of perturbations using multiple magnetometers and estimating heading (Afzal et al 2010).

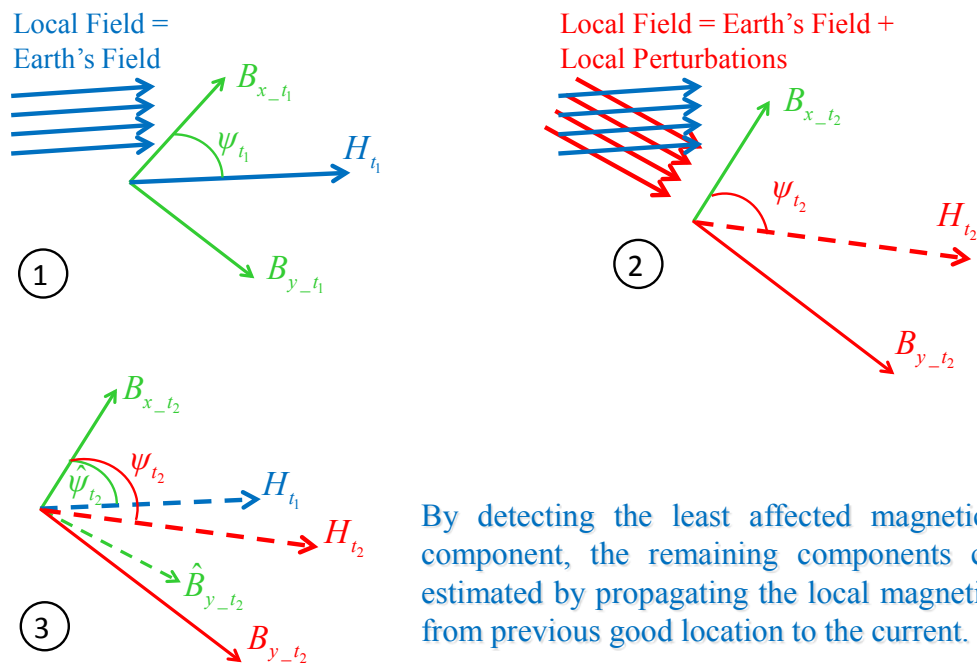


Figure 4-15: Perturbation mitigation using multiple magnetometers.

4.5 Detection of Magnetic Field Perturbations Using a Single Magnetometer

Because specific applications, e.g. smart-phone based navigation, cannot afford the implementation of multiple magnetometers, detection of good magnetic field measurements using only a single tri-axis sensor has been further studied.

The Earth generates a three dimensional magnetic field. This field can be sensed by an orthogonal arrangement of magnetometers. Using the X and Y-axis components of this field measurement, which constitute the horizontal field, the magnetically derived heading with respect to the true North as given by Equation (2.51) is rewritten here for convenience

$$\psi = \tan^{-1}\left(\frac{B_y}{B_x}\right) \pm D. \quad (4.3)$$

From Equation (4.3), it can be observed that perturbations in any of the horizontal field components will cause the heading estimates to be erroneous. Therefore the individual components of the perturbation field govern the impact of that perturbation on heading estimates. Figure 4-16 shows the Earth's magnetic field components in the absence and the presence of perturbations. It can be observed that the perturbations can cause errors in estimated heading based on their effects on one or a combination of the following four magnetic field parameters:

1. Total magnetic field $F = \|B_x + B_y + B_z\|$
2. Horizontal field $H = \|B_x + B_y\|$
3. Vertical field $Z = B_z$
4. Inclination angle $I = \tan^{-1}\left(\frac{Z}{H}\right)$

The effects of perturbations on these four magnetic field parameters are further elaborated in the following subsections.

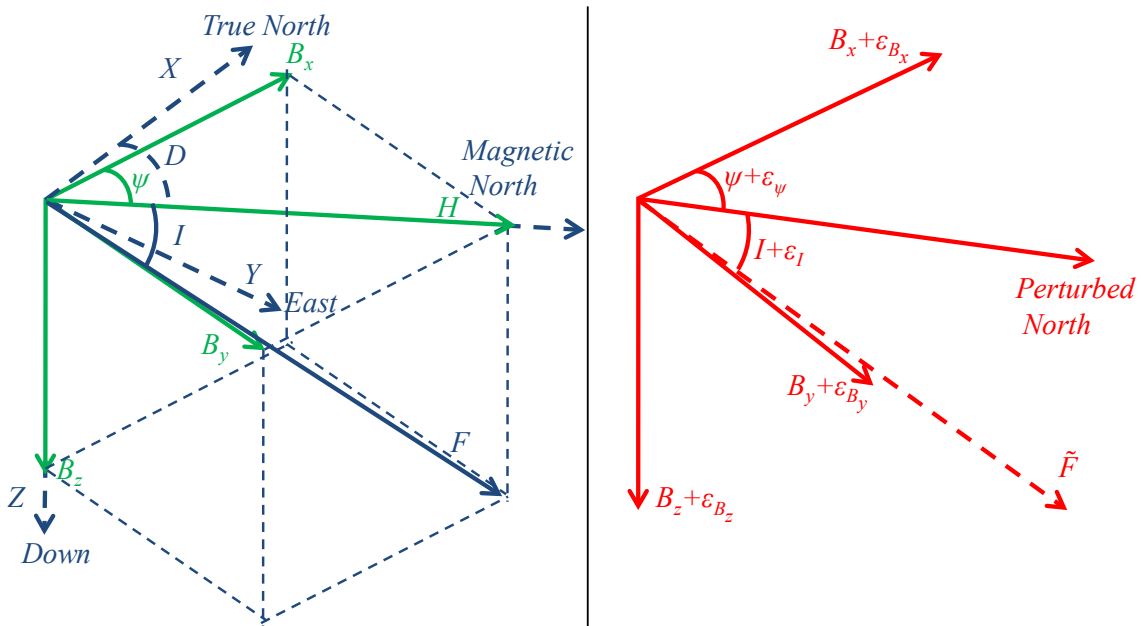


Figure 4-16: Clean versus perturbed magnetic field parameters.

4.5.1 Perturbation with Strong Horizontal and Strong Vertical Field Components

In case of a strong perturbation in both horizontal and vertical, a number of combinations are possible, namely:

1. Magnitude changes along the Earth's field axis with the same ratio.
2. Magnitude changes along the Earth's field axis with a different ratio.
3. Magnitude changes at different axes than the Earth's field one with the same ratio.
4. Magnitude changes at different axes than the Earth's field one with a different ratio.

In the first case, the perturbation is considered constructive as it will not cause any change in heading estimates, which is evident from Equation (4.3). But the total field magnitude will be different from the reference (CGRF). Thus if one utilizes the total field magnitude as means of detecting good heading estimates, such constructive perturbation scenarios will be missed. On the other hand, if one uses the inclination angle as means of

detection, this constructive perturbation can be identified. In the remaining three cases, the impact of perturbation will be destructive causing substantial errors in heading estimates. Neither field magnitude nor inclination angle will be free of errors. Hence a combination of total field magnitude and inclination angle can be used for detecting good field measurements if the perturbations fall in this category.

4.5.2 Perturbation with Strong Horizontal and Negligible Vertical Field Components

In this case, the perturbation along the horizontal field axis can have two possible combinations.

1. Both X and Y field components become affected by perturbations with the same ratio.
2. Both X and Y field components become affected by perturbation with a different ratio.

In the first case, the perturbation has no effect on heading estimates. Again the effects of perturbations can be considered constructive. But in the second case, the perturbation will cause errors. It is worth mentioning that the total magnetic field will change for this category of perturbation and hence by looking at the field magnitude only, one will miss the constructive perturbation periods. The same can be said for the inclination angle as it will vary in this case from the reference one. The magnitude of horizontal and vertical fields can be used for detecting this perturbation category.

4.5.3 Perturbation with Negligible Horizontal and Strong Vertical Field Components

In this case, the heading estimates will not have any substantial error due to the perturbation. Both the total field magnitude as well as the inclination angle will vary from the reference (CGRF). Similar to previous category, by looking at the magnitude of horizontal and vertical field components, this perturbation category can be identified.

4.5.4 Perturbation with Negligible Horizontal and Negligible Vertical Field Components

This type of perturbation will give the most reliable heading estimates. In this case, the magnitude of the total field, horizontal field and vertical field will be comparable to the reference. Also the inclination angle will correspond to the expected one.

4.6 Magnetic Field Test Parameters for Perturbation Detection using a Single Magnetometer

The observations of the preceding sections lead to the following magnetic field test parameters that can be utilized for detecting the presence of perturbations.

1. Magnitude of total magnetic field.
2. Magnitude of horizontal magnetic field.
3. Magnitude of vertical magnetic field.
4. Inclination angle

As the impact of magnetic field perturbations in these test parameters on heading estimates depends on the perturbation characterization and statistical analysis of the individual parameters in different pedestrian navigation environments as discussed in

Section 4.3, a detection and weighting scheme is needed to estimate the accuracy of estimated heading in the presence of these perturbations.

4.6.1 Single Magnetometer Based Perturbation Detection Techniques

Some work for detecting perturbations has already been done by researchers, which utilizes some of the above mentioned test parameters. Most of the work done so far utilizes multiple sensors (gyroscopes and magnetometers) to detect good heading estimates. Few researchers have investigated the magnetic field alone for identifying good measurements. Some promising approaches are reviewed and their limitations identified here.

4.6.1.1 Multi-Stage Compass Filter

In this approach, the authors suggest using a multi-stage filter to reject magnetic field measurements that are affected by perturbations (Faulkner et al 2010). The primary parameter that acts as a perturbation detector in this case is the magnitude of the total magnetic field. If the difference between the measured magnetic field and a known reference (e.g. CGRF) is within a predefined threshold, then the second stage of the filter is triggered. In this second stage, the gradients of magnetic field based heading estimates are compared with those of the inertial sensors (gyroscopes) for a predefined sliding window. If the difference between these two gradients falls within a threshold, the magnetic heading estimates are considered free of perturbations.

The main limitation of this approach is its dependence on the magnitude of the total field alone, which is the primary trigger for the second stage of this filter. As described in the previous section, there are both destructive as well as constructive perturbations present in pedestrian navigation environments. This approach will reject the constructive perturbations as they do cause changes in the magnitude of the field. Thus the probability of missing good heading estimates will be high. The second limitation is the requirement for heading estimates from inertial sensors (rate gyroscopes). It is quite possible to have a Pedestrian Dead Reckoning (PDR) approach using magnetometers and accelerometers only (Jimenez et al 2009).

4.6.1.2 Magnetic Field Magnitude and Inclination Angle

In this approach, the authors suggest utilizing not only the magnitude of the total field, but also the inclination angle, which is formed between the horizontal and vertical field components (Roetenberg et al 2003). The horizontal and vertical field components of the magnetic field are measured by the magnetic field sensors as well as estimated using gyroscopes and accelerometers. Magnetic field data is considered usable as long as the difference between measurements and estimates is within a predefined threshold.

The primary limitation of this approach is its dependence on the magnitudes of horizontal and vertical fields as this can lead to rejecting good heading estimates in case of constructive perturbations as described in the previous section. Dependence on using other sensors for estimating the magnetic field components for comparison purposes results in limitations similar to those of the previous approach.

4.6.2 Realization of Standalone Magnetometer Based Perturbation Detector

In light of the above mentioned limitations, it is desirable to investigate a magnetic field perturbation detector that relies only on the information contained within the magnetic field itself. Also the statistical information regarding the heading estimates is not available using the approaches described in Section 4.6.1.1 and 4.6.1.2. This information is necessary to assess the reliability of the heading estimates.

The effects of different magnetic field parameters on heading estimates, as described in Section 4.6, suggest that in order to improve the detection of good heading estimates based solely on magnetic field, all of the four magnetic field test parameters need to be simultaneously considered. They are the three magnitudes (F, H, Z) and an angle (I).

A detector is developed herein that utilizes Generalized Likelihood Ratio Test (GLRT) for individual magnetic field parameters. The test statistics of these parameters are later combined using fuzzy logic. This detector is hereby referred to as Magnitude and Angle based Detector (MAD).

4.6.2.1 Development of Individual Detectors

For a window size of N samples, let the test parameter for total field detector be given by

$$\{F_k\}_{k=n}^{n+N-1} = \{F_M - F_R\}_{k=n}^{n+N-1}, \quad (4.4)$$

where the subscripts M and R stand for the measurements (ideal) and reference respectively. Using the statistical signal detection technique, known as Likelihood Ratio Test (LRT), the following test statistic for total field detector is formulated:

$$\frac{I}{\sqrt{N}} \left(\sum_{k=n}^{n+N-1} y_k^F \right) < \gamma_F. \quad (4.5)$$

Where γ_F is the test statistics threshold given by

$$\gamma_F = \left(2 \sigma_F^2 \ln(\lambda) \right)^{1/2}. \quad (4.6)$$

Here σ_F^2 is the total field variance and λ the LRT ratio. A detailed derivation of the proposed total field based detector can be found in Appendix A, which utilizes Equation (4.4).

By utilizing Equation (4.5) and comparing it against a predefined threshold, one can robustly detect the total magnetic field measurements y_k^F adequate for good heading estimates. Similar detectors can be realized for the remaining three magnetic field parameters, which are summarized as follows:

$$\begin{aligned} \frac{I}{\sqrt{N}} \left(\sum_{k=n}^{n+N-1} y_k^H \right) < \gamma_H \quad \text{where } \gamma_H &= \sqrt{2 \sigma_H^2 \ln(\lambda_H)}, \\ \frac{I}{\sqrt{N}} \left(\sum_{k=n}^{n+N-1} y_k^Z \right) < \gamma_Z \quad \text{where } \gamma_Z &= \sqrt{2 \sigma_Z^2 \ln(\lambda_Z)}, \\ \frac{I}{\sqrt{N}} \left(\sum_{k=n}^{n+N-1} y_k^I \right) < \gamma_I \quad \text{where } \gamma_I &= \sqrt{2 \sigma_I^2 \ln(\lambda_I)}. \end{aligned} \quad (4.7)$$

4.6.2.2 Combining the Individual Detectors

One way of realizing a detector that takes into account all of the four parameters is by deriving the joint probability distributions while considering the dependence of different parameters on each other. Another approach is to utilize the knowledge about the possible perturbations encountered in pedestrian navigation environments, as described in Section 4.6, for defining detection rules. These rules can then be utilized with a Fuzzy Inference System (FIS) to evaluate the combined impact of all four parameters on the accuracy of heading estimates. Figure 4-17 shows the overall architecture of the fuzzy combiner for MAD. It is quite evident from Equations (4.5), (4.6), (4.7) and Figure 4-17 that a number of factors need to be investigated in order to completely describe the proposed detector.

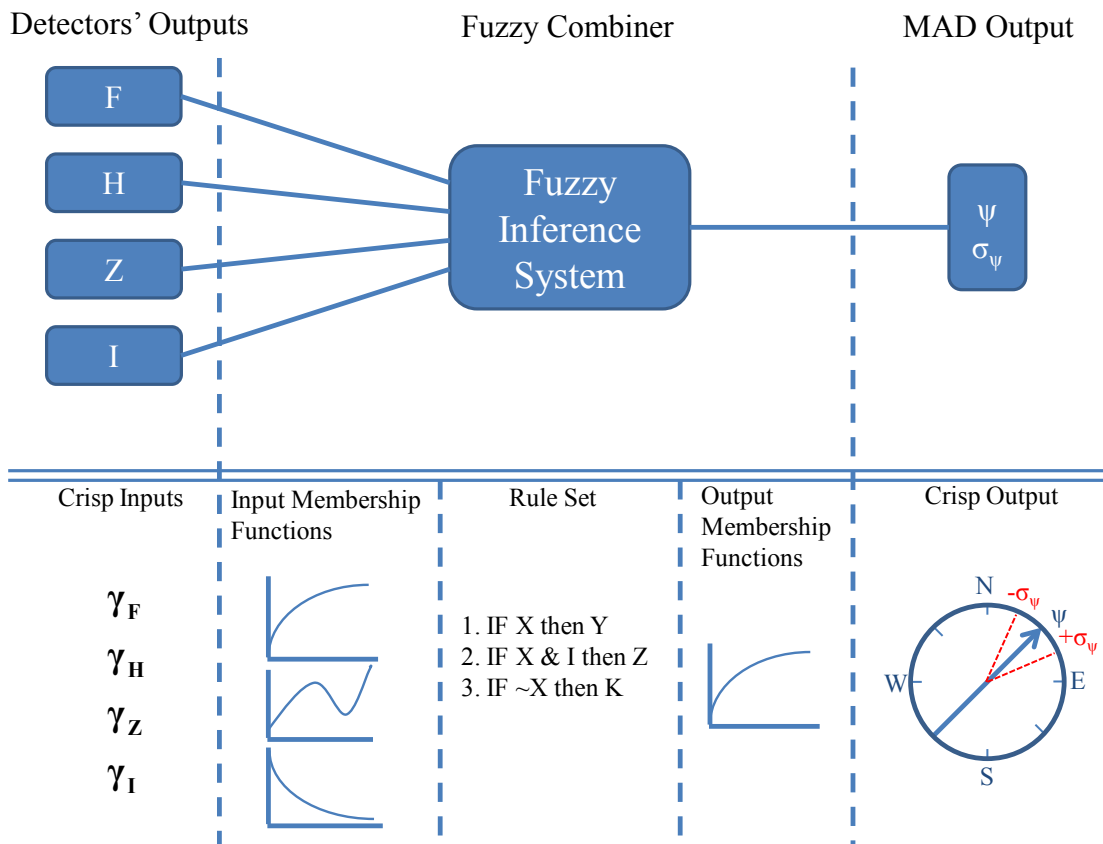


Figure 4-17: Fuzzy Inference System (FIS) for MAD.

4.6.3 Statistical Analysis of the Detector

The tuning parameters in the proposed detector can be divided into two categories, one for the individual detectors and the second for FIS. The parameters required for the individual detectors are the measurement variances, the test statistics' threshold and the sample window size whereas for FIS, the input membership functions (fuzzification), the rule set and the output membership functions (defuzzification) are required.

4.6.3.1 Selection of Measurement Variances for Individual Detectors

Selection of measurement variances requires a detailed insight into the perturbations that one can expect in different pedestrian navigation environments and their impact on the heading estimates. A magnetic field survey was conducted in such environments as described in Section 4.3. The measurement variances required for individual detectors are selected from the combined distributions of all the four magnetic field parameters, the latter being obtained from a statistical analysis of the magnetic field data. These are summarized in Table 4-3.

Table 4-3: Test parameter variances for MAD.

Parameter	Variance
Total field (F)	84 μT^2
Horizontal Field (H)	49 μT^2
Vertical Field (Z)	99 μT^2
Inclination Angle (I)	129.4 $^{\circ 2}$

4.6.3.2 Selection of the Test Statistics' Threshold for Individual Detectors

The threshold can be selected based on the relationship between the probability of detection P_d and the acceptable probability of false alarms P_f . The Receiver Operating Characteristics (ROC) curve is utilized for this (Hippenstiel 2002), which also defines the performance of the detector. Figure 4-18 depicts the relationship between the probability of detection and the probability of false alarms for the four detectors.

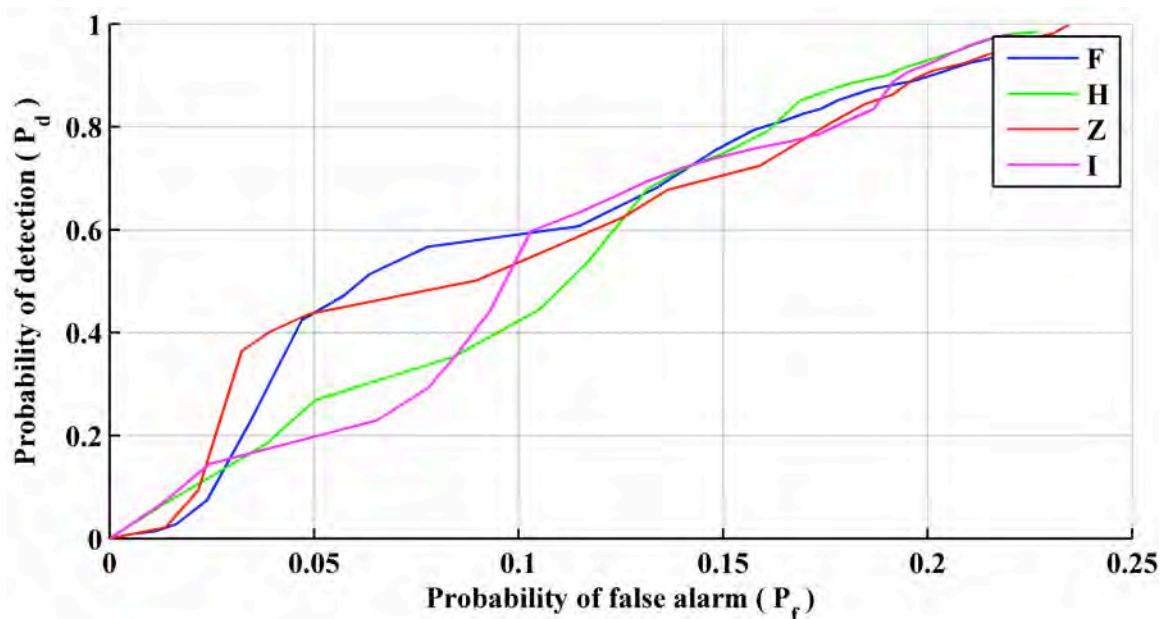


Figure 4-18: ROC curves for individual detectors.

It is quite evident that the detectors based on individual magnetic field parameters have different performance for smaller thresholds. This is a very important observation and signifies that even if some of the magnetic field parameters are very close to the reference ones (smaller threshold means a better agreement between reference and measured parameters), still these detectors will end up producing more false alarms. For example, the inclination angle based detector has the highest P_f for a P_d of 0.2. This observation further signifies the importance of combining the outcome of individual detectors for robust heading estimates.

For this research, the P_f of approximately 16% is selected as acceptable false alarms, which leads to different thresholds and P_d for the individual detectors as summarized in Table 4-4.

Table 4-4: Selected thresholds for individual detectors.

Detector	Threshold	P_d	P_f
F	9.3	0.81	0.16
H	8.0	0.85	0.16
Z	11.0	0.81	0.17
I	10.7	0.81	0.18

4.6.3.3 Selection of the Sliding Window Size

The last parameter required for tuning the individual detectors' performance is the sliding window's size. Figure 4-19 shows the ROCs for the total magnetic field based detector with different window sizes. The sensor sampling rate in this case is 40 ms, which gives the smallest window size of 40 ms ($N = 1$) and the largest window size of 600 ms ($N = 15$) tested for this analysis. As can be observed in the figure, the window size changes do not cause substantial changes in the detector's performance. This can be related to the pedestrian's walking speed, which is 1 m/s on average. Even for window sizes of 600 ms, this speed was not enough to cause substantial changes in the magnetic field test parameter. Therefore it can be concluded that for normal pedestrian walking speed, the effect of the investigated window sizes on detector's performance is negligible. The same is also found for the remaining three detectors.

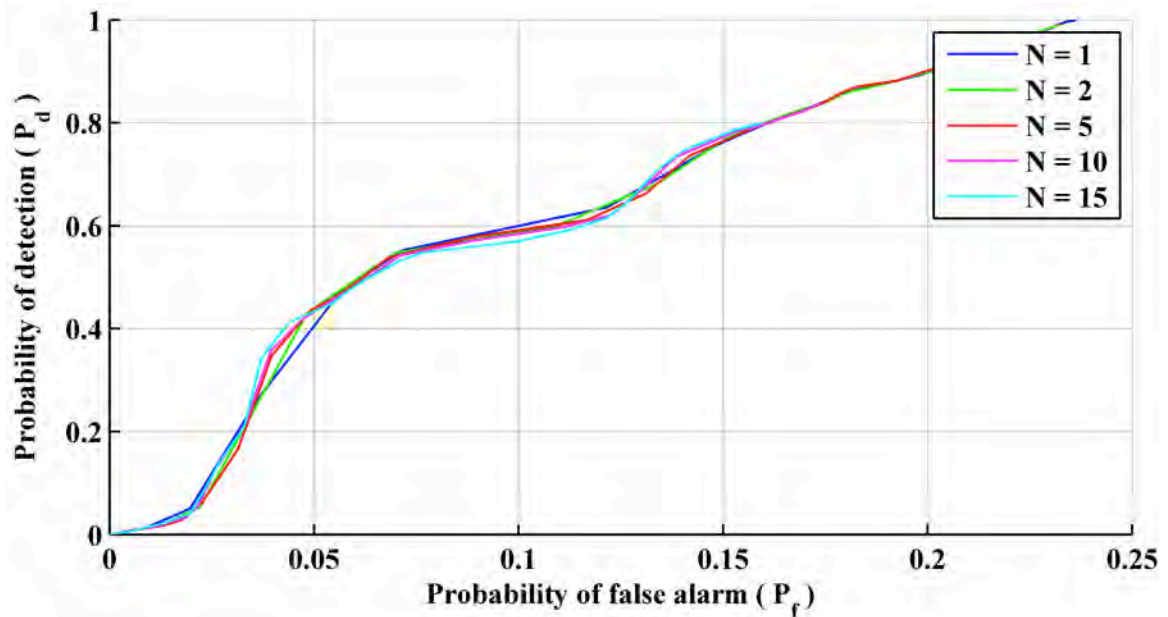


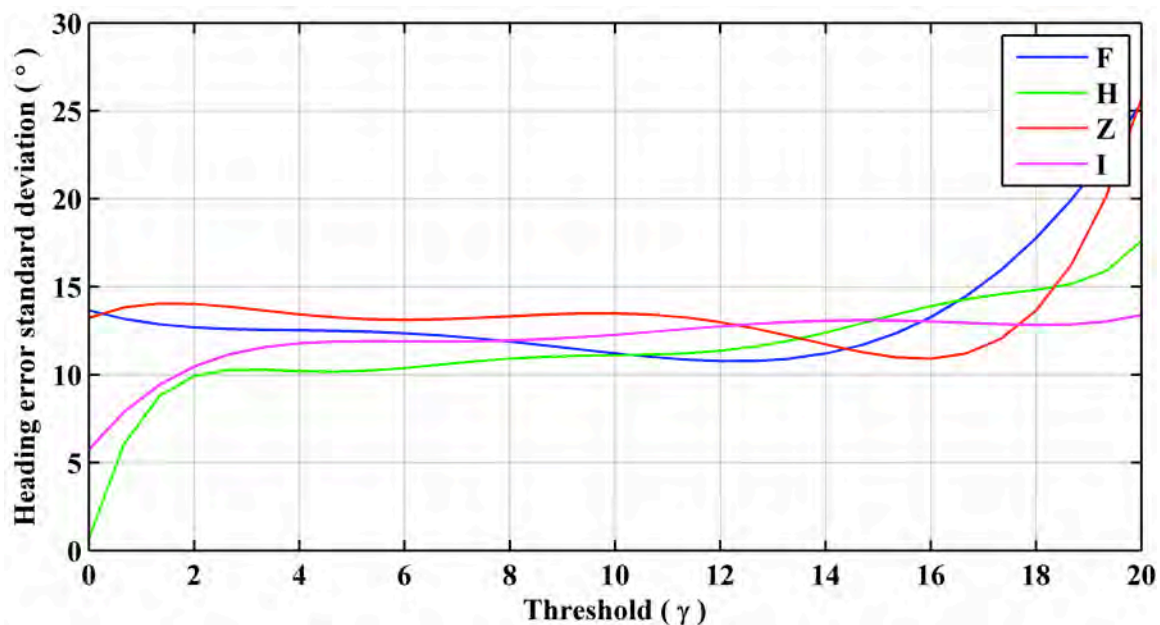
Figure 4-19: Performance of total magnetic field based detector for different window sizes.

4.6.3.4 Relationship Between Test Statistics' Output and Expected Heading Errors

Figure 4-20 shows the relationship between the estimated heading errors and the test statistics' outputs for individual detectors, which are compared with a predefined threshold depending upon the acceptable false alarms as summarized in Table 4-5. A critical observation here is that there exists a relationship between the outcome of the test statistics and the accuracy of the heading estimates for individual detectors. Thus these relationships can be utilized for the formulation of membership functions for FIS. The latter are required for fuzzification of the crisp test statistics' outputs. Table 4-5 summarizes the heading error standard deviations that are achievable with different detectors. These are used later for mapping each membership function (spanning values from 0 to 1) to their corresponding weight in the rule sets.

Table 4-5: Expected heading error ranges for different detectors.

Detector	Min. σ	Max. σ
F	11.0°	25.0°
H	1.0°	17.3°
Z	11.0°	25.0°
I	5.8°	13.0°

**Figure 4-20: Relationship between threshold and expected heading errors.**

4.6.3.5 FIS Output Membership Functions

The selection of output membership functions depends on the application requirements. Here it is assumed that categorizing the heading estimates into good, bad and worse is sufficient. In order to find a relationship between these three fuzzy outputs and expected heading errors, the thresholds of individual detectors are divided into three equal sets. The output membership functions' distributions are then evaluated by keeping under consideration the actual errors encountered in heading estimates for the respective

threshold sets. For this purpose, the entire data set except for the shopping mall is considered. The latter is used for evaluating the performance of this detector on a data set not used for tuning purposes. The output membership functions' distributions are summarized in Table 4-6 and shown in Figure 4-21.

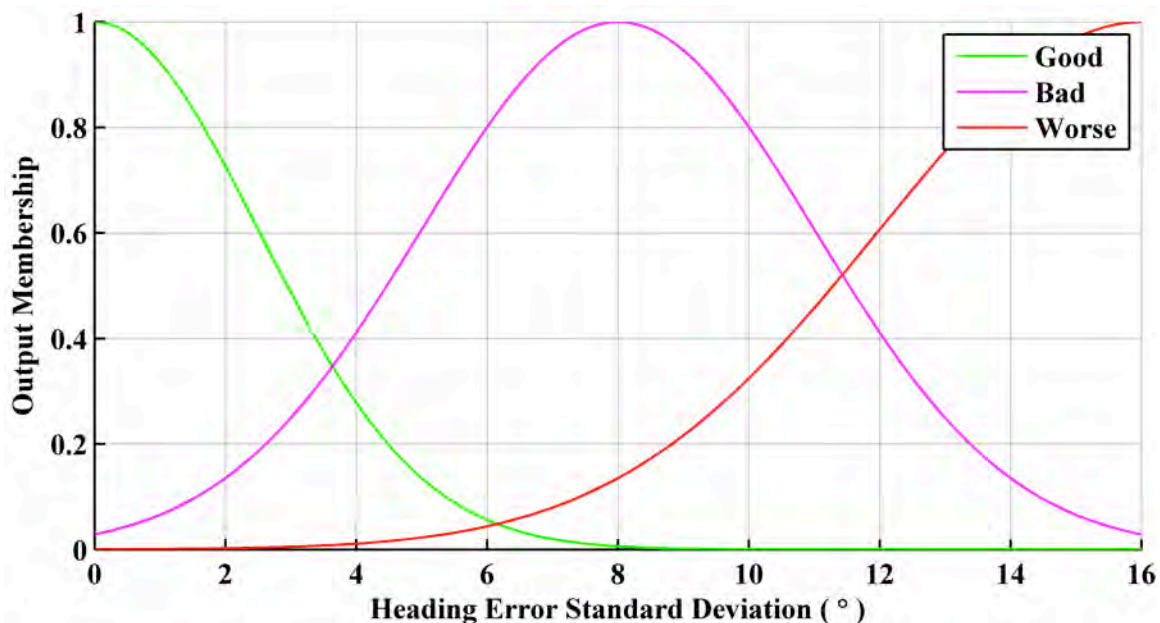


Figure 4-21: Output membership function for FIS.

Table 4-6: Design parameters for the output membership functions.

Output MF	Mean (°)	Std. deviation (°)
Good	0	2.5
Bad	8	3
Worse	16	4

4.6.3.6 FIS Rule Set

In order to combine the information contained in individual detectors, a set of rules is required for weighing each detector and mapping the final outcome to one of the output membership functions. As described in Section 4.5, the impact of different perturbation

sources on magnetic field parameters are utilized for this. This leads to the definition of the following fuzzy rules:

1. If F is good and I is good then the heading is good.
2. If F is good and H is good then the heading is good.
3. If F is bad and H is good and Z is bad then the heading is bad.
4. If F is bad and I is good then the heading is bad.
5. If F is good and H is bad then the heading is worse.

By utilizing the detectors developed in Section 4.6.2.1 for assessing the impact of magnetic field perturbations on the individual test parameters, the above mentioned rules can be used for translating the effects of perturbations to heading errors. Thus the quality of magnetic field based heading estimates can be evaluated using the proposed single magnetometer based approach, which can be used as a measurement for estimating the errors associated with orientation in general and gyroscopes in particular. Chapter 5 describes the measurement error model utilizing the outcome of a single magnetometer based perturbation detector and heading estimator.

Chapter Five: **Attitude/ Orientation Estimator for Pedestrian Navigation**

The main focus of this research is to achieve the reliable estimation of pedestrian's attitude in general and orientation/ heading in particular. As the pedestrian navigation environments hinder the use of most of the sensors/ systems for estimating the attitude, use of inertial sensors is the primary means for this purpose. Angular rate sensors, namely rate gyroscopes, are the primary sensors for estimating the pedestrian's attitude with respect to a reference frame. In light of the nature of consumer grade rate gyroscopes selected for this research and the associated errors, which were described in Section 3.6, additional measurements are required to mitigate these errors. The use of the Earth's magnetic field and its related parameters as potential measurements for attitude and rate gyroscope error corrections has been discussed in the preceding chapters. This chapter's primary focus is the development of an attitude estimator using rate gyroscopes as primary sensors and magnetometers as aiding ones, due to their complementary nature. First, different reference frames, which can be used for pedestrian navigation, are introduced. The attitude computer mechanization techniques are then presented and the one selected for this research is detailed. Finally an estimator is developed, which models the errors associated with the gyroscopes and utilizes the potential measurements for estimating these in pedestrian navigation environments.

5.1 Reference Frames

This section defines the reference frames that are commonly used for pedestrian navigation applications. Figure 5-1 shows all the reference frames detailed in this section.

5.1.1 Inertial Frame

Inertial frame is the one in which the inertial sensors (rate gyroscopes and accelerometers) operate and hence is always encountered when Inertial Navigation Systems (INS) are used. For navigation in the vicinity of the Earth, the origin of the three mutually perpendicular axes of the inertial frame is taken to be at the center of the Earth's mass (Titterton & Weston 2004). In this case, the inertial frame is referred to as Earth Centered Inertial (ECI) frame.

5.1.2 Local Level Frame (LLF)

LLF is the most commonly used frame for navigation and attitude representation (Farrell 2008), which is referred to as the navigation frame herein. This frame moves with the point of interest and is tangent to the geodetic reference ellipsoid. The axes of the LLF can be defined in numerous ways. For this research, LLF is defined as North East Down (NED) frame, i.e. the X-axis is pointing North, Z is pointing orthogonally to the ellipsoid downward and Y is pointing East, completing a right handed orthogonal triad.

5.1.3 Body Frame

For pedestrian navigation, the objective is to find an estimate of the position and the attitude angles of the subject with respect to a navigation frame. The body frame is associated with the pedestrian and has its origin and orientation fixed. As the pedestrian can be oriented arbitrarily with respect to the navigation frame, it is the attitude/orientation of the body frame with respect to the navigation frame that needs to be estimated. Here the body frame is chosen to have its X-axis pointing forward (along the

walking direction), Z-axis pointing down and Y-axis completing a right handed orthogonal triad.

5.1.4 Sensor Frame (Platform Frame)

The sensor/ platform frame is fixed to the sensor block being used for navigation and is aligned with the sensing axis of the inertial sensors' triad. In case of pedestrian navigation, the sensor block can be located anywhere on the subject, either in the pocket, in a hand or in a purse, even mounted rigidly to the shoe (used for some special applications). Thus there exists an orientation ambiguity between the sensor and body frames. As the sensor block is held by the pedestrian in such a way so as to have the X-axis pointing in the walking direction, this ambiguity was assumed to be zero for orientation estimation herein. For real world applications, this ambiguity has to be resolved, otherwise a bias will exist between sensor and body frame, resulting in errors in the derived position updates. Accelerometers can be used for resolving this ambiguity by either transforming the accelerations from the sensor frame to the navigation frame and estimating the direction of acceleration vector or by utilizing human gait modeling (Steinhoff & Schiele 2010). This is outside the scope of this thesis. However, the sensor block (MSP), developed for this research is equipped with accelerometers, which will be used later for investigating different direction of motion estimation techniques.

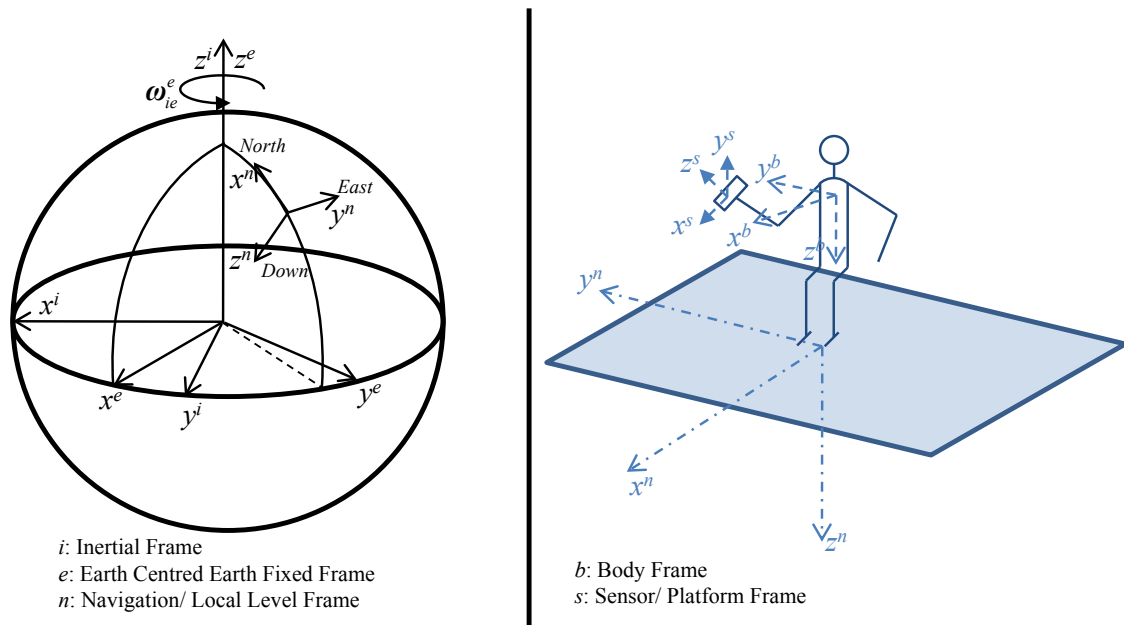


Figure 5-1: Reference frames used for representing position and attitude.

5.2 Transformations between the Reference Frames

As is evident from Figure 5-1, there exist rotation vectors between different frames. Thus in order to express the same vector in frame *a* or in frame *b*, a transformation is required. This section describes the methods used for transforming vectors between two frames, which are right handed and whose coordinate axes follow an orthogonal arrangement.

5.2.1 Direction Cosine Matrix

The Direction Cosine Matrix (DCM) is a 3x3 matrix whose columns represent the rotations from the axes of one frame into the three axes of another frame (Titterton & Weston 2004). Commonly the capital letter “*C*” is used for representing the DCM. Let the DCM representing rotations from frame *a* to frame *b* be given by

$$\mathbf{C}_a^b = \begin{bmatrix} c_{11} & c_{12} & c_{13} \\ c_{21} & c_{22} & c_{23} \\ c_{31} & c_{32} & c_{33} \end{bmatrix}, \quad (5.1)$$

where $c_{ij}, i \in \{1,2,3\}$ and $j \in \{1,2,3\}$ are the individual components of the DCM.

Let a vector \mathbf{v} expressed in the reference frame a be defined as \mathbf{v}^a . In order to express this vector in the reference frame b by utilizing the DCM \mathbf{C}_a^b , the following relationship can be used:

$$\mathbf{v}^b = \mathbf{C}_a^b \mathbf{v}^a. \quad (5.2)$$

5.2.2 Euler Angles

As the reference frames are defined by three orthogonal rectangular coordinate axes, it is possible to rotate/ transform from one frame to another by successively performing three rotations about the three axes. These three rotation angles are referred to as the Euler angles (Titterton & Weston 2004). The standard notations for the three Euler angles are ψ about the Z-axis, θ about the Y-axis, and ϕ about the X-axis. The Euler angles are the most common representation of the rotation angles as they give a direct measure of the actual angles that are formed between two different reference frames. Hence the final outcome of an attitude estimator for pedestrian applications is usually represented by Euler angles.

5.2.3 Quaternions

After coming up with the relationship for transforming a vector from one reference frame to another using Euler angles, it was found that by utilizing these Euler angles, a

relationship can be obtained that requires a single rotation about a three dimensional vector to transform between two frames (Grubin 1970). This vector is called a quaternion and is defined by four parameters. One of these parameters is a scalar, which represents the magnitude of the quaternion vector while the other three are the direction components. In vector notation form, a quaternion \mathbf{q} is represented as

$$\begin{aligned}\mathbf{q} &= q_1 + \bar{\mathbf{q}} \\ \bar{\mathbf{q}} &= [q_2 \quad q_3 \quad q_4]\end{aligned}\quad (5.3)$$

Manipulation of quaternions is carried out using quaternion algebra, details of which can be found in numerous books on navigation (Farrell 2008, Lawrence 1993, Titterton & Weston 2004). In order to rotate a vector \mathbf{v} from frame a to frame b using the rotation quaternion \mathbf{q} , first the vector needs to be represented in its quaternion form given by

$$\mathbf{q}_v^a = [0 \quad \mathbf{v}]^T. \quad (5.4)$$

Then using quaternion algebra, the rotation of a vector from one frame to another using quaternion can be achieved:

$$\mathbf{q}_v^b = \mathbf{q} \circ \mathbf{q}_v^a \circ \bar{\mathbf{q}} = \mathbf{Q}_q \bar{\mathbf{Q}}_{\bar{\mathbf{q}}} \mathbf{q}_v^a. \quad (5.5)$$

5.2.3.1 Advantages of Using Quaternions

Although performing a three dimensional vector transformation using a single rotation about a vector sounds complex, quaternion representation of the coordinate rotation has a number of advantages over DCM and Euler representations:

1. The quaternion differential equation is linear. This property is very important as the attitude computer implementation requires propagation of rotation matrix representation in time.
2. Quaternions do not suffer from singularity issues when approaching a 90° pitch angle. This is a common issue with Euler angles and is also referred to as a gimbal lock (being a mathematical representation of the mechanical gimbals).
3. Fewer computational complexities are involved when using quaternions for representing and propagating the rotation vector as compared with DCM and Euler angles. This makes them attractive for real time attitude computation.

5.3 Attitude Computer Realization

Attitude computer is the digital implementation of the mathematical equations governing the attitude of a body with respect to a reference frame (Wertz 1990). There are two ways to compute the attitude in three dimensions:

1. Using two or more vector measurements
2. Propagation of attitude using angular rate measurements.

5.3.1 Vector Measurements

The general principle of using vector measurements for attitude estimation is finding a common transformation matrix that maps the vector measurements in body frame to those in a reference frame by minimizing the cost function known as the Wahba problem (Wahba 1965) given by

$$J = \frac{1}{2} \sum_{i=1}^N (\mathbf{u}_i^b - \mathbf{C}_n^b \mathbf{u}_i^n)^T (\mathbf{u}_i^b - \mathbf{C}_n^b \mathbf{u}_i^n), \quad (5.6)$$

where \mathbf{u}_i^b is the i^{th} vector measurement in the body frame, \mathbf{u}_i^n is the i^{th} reference vector in the navigation frame and \mathbf{C}_n^b is the transformation matrix that minimizes the cost function J . Once this transformation matrix is obtained, the Euler angles can be extracted from it. In this approach, vector measurements of at least two non collinear vectors are needed (Shuster & S.D 1981). Vector measurements based attitude computation is a well addressed technique (Cohen 1992), which is mostly used for spacecraft attitude estimation (Wertz 1978).

5.3.1.1 Vector Measurements for Pedestrian Navigation

A number of vector measurements can be utilized for solving the Wahba problem (Wertz 1978). From a pedestrian navigation perspective, mainly two vector measurements are available for this. They are the Earth's magnetic field vector and the Earth's gravity vector. These vectors are non collinear and their reference values in the navigation frame are also available. The Earth's magnetic field has already been discussed in Section 2.4. Similarly, Earth's gravity models are also available (Britting 1971).

5.3.1.2 Problems with Using the Vector Measurements for Pedestrian Navigation

Although two non collinear vectors are available for solving the Wahba problem in the pedestrian navigation domain, the navigation environments and user dynamics limit the use of these vectors for estimating the attitude. Indeed indoor environments are contaminated with magnetic field perturbations causing errors in the vector

measurements. Also, due to the walking dynamics of a pedestrian, the specific forces measured by the accelerometers will not correspond to those of the g vector resolved in the sensor frame.

All of these limitations cause discontinuities in attitude estimation using simultaneously the magnetic field and g vector measurements as not all of the measurements are useful for estimation. Therefore the approach of using only non collinear vector measurements for attitude estimation is not feasible for pedestrian navigation.

5.3.2 Angular Rate Measurements

As the vector measurements are not available for estimating the attitude at every epoch, propagation of the attitude in time is necessary. For this purpose, an inertial sensor providing angular rate measurements, namely the rate gyroscope, can be used (Farrell 2008). The derivative relating the representation of rotation (DCM, Euler or quaternion) to the angular rates is utilized for attitude propagation. Although any of the three representations of the rotation matrix can be utilized for attitude propagation in time, considering the advantages of representing the rotations using a quaternion as described in Section 5.2.3, the quaternion derivative is used for estimating the attitude using angular rate measurements herein, which is given by

$$\dot{\mathbf{q}} = \frac{1}{2} \begin{bmatrix} -q_2 & -q_3 & -q_4 \\ q_1 & q_4 & -q_3 \\ -q_4 & q_1 & q_2 \\ q_3 & -q_2 & q_1 \end{bmatrix} \begin{bmatrix} -\omega_x^s \\ -\omega_y^s \\ -\omega_z^s \end{bmatrix}, \quad (5.7)$$

where ω_x^s, ω_y^s and ω_z^s are the three angular rate measurements in the sensor frame obtained using the rate gyroscopes. Readers are referred to Appendix B for detailed derivation of Equation (5.7).

5.3.2.1 Errors Caused in Attitude Computations using Angular Rates

As the angular rates required for computing the quaternion derivative are provided by the MEMS rate gyroscopes, the errors associated with them, as detailed in Section 3.6, introduce errors in the estimated attitude. The gyroscope errors as well as the attitude errors need to be estimated and mitigated for estimating reliable attitude in pedestrian navigation environments.

5.4 Attitude and Sensor Error Estimator

Attitude and its error estimation is a non linear problem (Bak 1999). Although a number of estimation approaches are available to solve non linear problems, in this research an extension of a Kalman filter based estimator is used, namely an Extended Kalman Filter (EKF) (Brown & Hwang 1997). The main purpose of this estimator is to model the effects of the gyroscope errors on attitude estimates and use the magnetic field information as corrective measurements to estimate the attitude errors in general and gyroscope errors in particular, which can then be compensated from the present epoch and remodelled for the proceeding ones until new measurements are available. Detailed derivation of said estimator can be found in a number of books (Bak 1999, Bekir 2007, Britting 1971, Brown & Hwang 1997, Cohen 1992, Farrell 2008, Grewal et al 2001). Only the working principles and the governing equations of an EKF are addressed herein.

5.5 Kalman Filter

Figure 5-2 shows the overall flow of the Kalman filter. The first stage is the initialization of the state vector \mathbf{x} along with its uncertainties. Next comes the prediction stage, where the state vector is propagated in time based on the system model. The epochs are defined by the subscripts k whereas the superscripts identify whether the state (or some other parameter required for Kalman filter mechanization) is updated (+) or predicted (-). Once the observations z_k are available, the update stage is used for estimating the state vector at the current epoch based on the present predictions \mathbf{x}_k^- and the uncertainties associated with both the predictions and observations. The same is temporally illustrated on the right hand side of Figure 5-2.

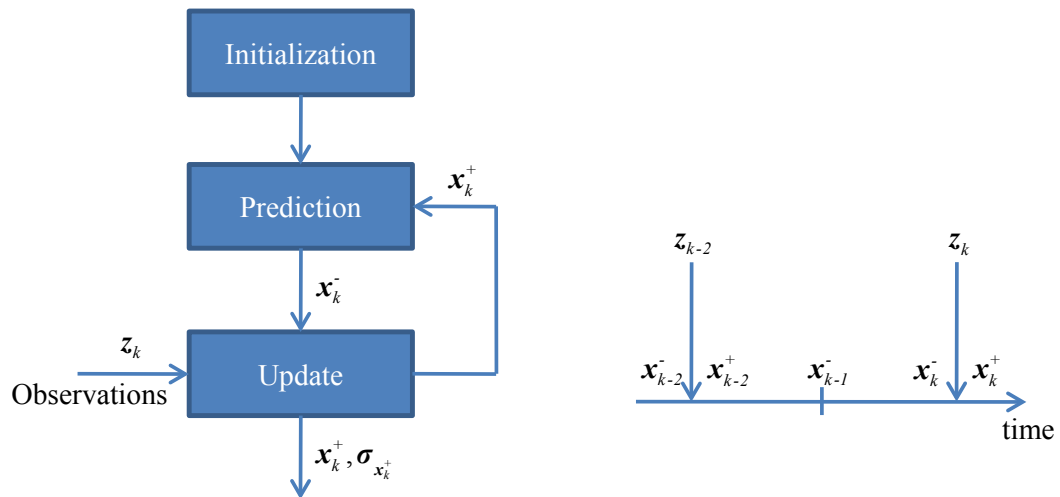


Figure 5-2: Overall flow of information in a Kalman filter.

5.5.1 Kalman Filter Mechanization

The system model for a Kalman filter is usually expressed in state-space form, which is a convenient way for developing and understanding it (Brown & Hwang 1997). This system model for navigation applications in general and attitude estimators in particular is represented by a first order differential equation given by

$$\dot{\mathbf{x}}(t) = \mathbf{F}(t)\mathbf{x}(t) + \mathbf{G}(t)\mathbf{w}(t), \quad (5.8)$$

where \mathbf{x} is the state vector, the first term on the right hand side represents the dynamics model and the last term the stochastic model. The dynamics model defines how the states propagate in time. \mathbf{F} is the dynamics matrix, which is obtained based on the physics defining the relationship between different states. As the system dynamics can only be modeled to a certain extent, the uncertainties are represented by the stochastic model. \mathbf{G} is the shaping matrix and \mathbf{w} is the vector of zero mean white Gaussian noise.

The measurement model is given by

$$\mathbf{z}(t) = \mathbf{H}(t)\mathbf{x}(t) + \mathbf{v}(t), \quad (5.9)$$

where \mathbf{H} is the design matrix relating the measurements with the states and \mathbf{v} represent the measurement noise vector.

As the navigation sensors provide digital equivalents of analog (continuous) data at usually periodic discrete times, it is desirable to convert the Kalman filter's governing equations from continuous to discrete time. Equations (5.8) and (5.9) in discrete time are given by

$$\mathbf{x}_k = \Phi_{k-1,k}\mathbf{x}_{k-1} + \mathbf{w}_{k-1}, \quad (5.10)$$

$$\mathbf{z}_k = \mathbf{H}_k\mathbf{x}_k + \mathbf{v}_k. \quad (5.11)$$

Here, Φ is the transition matrix, which is the discrete time equivalent of the dynamics matrix and is obtained using the Taylor series expansion as

$$\Phi_{t_0,t} = \Phi(t-t_0) = e^{F(t-t_0)} = \mathbf{I} + \mathbf{F}(t-t_0) + \frac{(\mathbf{F}(t-t_0))^2}{2!} + \frac{(\mathbf{F}(t-t_0))^3}{3!} + \dots \quad (5.12)$$

As the Kalman filter propagates the states, their respective uncertainties are also propagated in time. Let $\mathbf{Q}(t)$ define the Power Spectral Density (PSD) matrix for the noise terms. The sensor noise PSDs, obtained using the Allan Variance (AV) analysis as detailed in Section 3.12 are utilized for this purpose. The covariance of \mathbf{w}_k , also known as the process noise covariance matrix, is given by

$$\mathbf{Q}_k = \int_{t_k}^{t_{k+1}} \Phi_{\tau,t_{k+1}} \mathbf{G}(\tau) \mathbf{Q}(\tau) \mathbf{G}^T(\tau) \Phi_{\tau,t_{k+1}}^T d\tau. \quad (5.13)$$

The corresponding covariance matrix for \mathbf{v}_k is represented by \mathbf{R} and is called the measurement noise covariance matrix.

Now, the variance-covariance matrix \mathbf{P} of the state vector is propagated in the prediction stage of the Kalman filter by

$$\mathbf{P}_{k+1}^- = \Phi_{k,k+1} \mathbf{P}_k^+ \Phi_{k,k+1}^T + \mathbf{Q}_k. \quad (5.14)$$

Whenever measurements are available, the Kalman filter uses these in combination with the predicted states to come up with a better estimate of the states along with their covariance matrix. For this blending purpose, a gain \mathbf{K} is used that weighs the predicted states and the new measurements while updating the states. The Kalman gain is computed using

$$\mathbf{K}_k = \mathbf{P}_k^- \mathbf{H}_k^T (\mathbf{H}_k \mathbf{P}_k^- \mathbf{H}_k^T + \mathbf{R}_k)^{-1}. \quad (5.15)$$

Once the Kalman gain is computed, the state vector is updated using

$$\mathbf{x}_k^+ = \mathbf{x}_k^- + \mathbf{K}_k (\mathbf{z}_k - \mathbf{H}_k \mathbf{x}_k^-), \quad (5.16)$$

and the covariance matrix for the new states is given by

$$\mathbf{P}_k^+ = (\mathbf{I} + \mathbf{K}_k \mathbf{H}_k) \mathbf{P}_k^-. \quad (5.17)$$

Equations (5.10) through (5.17) constitute the overall mechanization of the Kalman Filter. Figure 5-3 depicts the flow of the discrete time Kalman filter using the above equations.

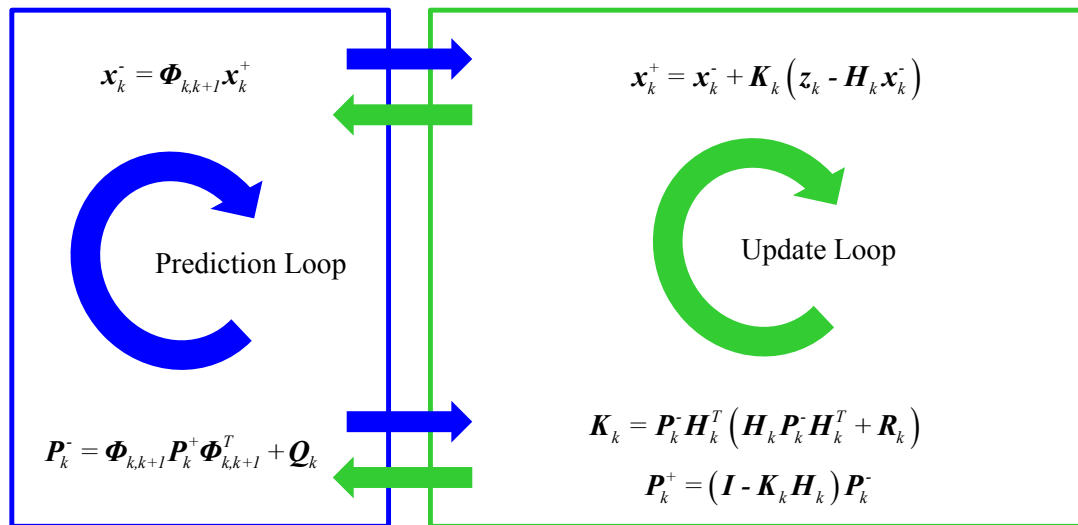


Figure 5-3: Information flow in a discrete time Kalman filter.

5.5.2 Extended Kalman Filter (EKF)

In case of navigation applications, usually both the system as well as measurement models are non-linear (Brown & Hwang 1997, Farrell 2008). Thus these models need to be linearized in order to be used with the Kalman filter. For this purpose, a linearization

point is necessary, which represents the nominal states $\mathbf{x}^{nom}(t)$. In EKF, the linearization point is obtained by utilizing the most recent state estimates. For example, in case of an attitude computer, the most recent state estimates are obtained from the derivative of the rotation vector using the angular rates, as detailed in Section 5.3.2. As the nominal states are known before hand, the state vector can now be modeled as

$$\mathbf{x}_k = \mathbf{x}_k^{nom} + \delta\mathbf{x}_k, \quad (5.18)$$

where $\delta\mathbf{x}_k$ are the errors in the nominal state, which need to be estimated and compensated. Now the Kalman filter is required to estimate the errors in the states rather than the states themselves and the system and measurement models become:

$$\begin{aligned} \delta\mathbf{x}_k &= \Phi_{k-1,k} \delta\mathbf{x}_{k-1} + \mathbf{w}_{k-1} \\ \delta\mathbf{z}_k &= \mathbf{H}_k \delta\mathbf{x}_k + \mathbf{v}_k \end{aligned} \quad (5.19)$$

Every time the state errors $\delta\mathbf{x}_k$ are updated, these are applied to the most recent state estimates. Hence after every Kalman filter update, the error state vector is reset. Thus in case of EKF, the state predictions achieved by Equation (5.10) are no longer required. Also the state vector updates, as given by Equation (5.16), reduce to

$$\begin{aligned} \delta\mathbf{x}_k^+ &= \delta\mathbf{x}_k^- + \mathbf{K}_k \delta\mathbf{z}_k \\ &= 0 + \mathbf{K}_k \delta\mathbf{z}_k, \\ \delta\mathbf{x}_k^+ &= \mathbf{K}_k \delta\mathbf{z}_k \end{aligned} \quad (5.20)$$

and the actual state is updated as

$$\begin{aligned} \mathbf{x}_k^+ &= \mathbf{x}_k^- + \delta\mathbf{x}_k^+ \\ \mathbf{x}_k^+ &= \mathbf{x}_k^- + \mathbf{K}_k \delta\mathbf{z}_k \end{aligned} \quad (5.21)$$

5.6 EKF Based Attitude and Sensor Error Estimator

In order to use the EKF based estimator for attitude estimation of a sensor block carried by a pedestrian, appropriate states, measurements and their respective system and measurement error models are required, which are detailed in this section.

5.6.1 The State Vector

As this research only targets attitude/orientation estimation for pedestrian navigation, the main states to be estimated are the three attitude angles given by

$$\boldsymbol{\Gamma} = [\phi \quad \theta \quad \psi]^T, \quad (5.22)$$

where ϕ is the roll angle, θ is the pitch angle and ψ is the heading angle as defined in Section 5.2.2. The attitude is primarily determined using the angular rates obtained using the rate gyroscopes. The deterministic errors associated with this sensor are already compensated for using the calibration procedure described in Section 3.8. The residual errors are the time varying biases, which are given by

$$\mathbf{x}_\omega = [b_{\omega_x} \quad b_{\omega_y} \quad b_{\omega_z}]^T. \quad (5.23)$$

Thus the complete state vector is given by

$$\mathbf{x} = [\phi \quad \theta \quad \psi \quad b_{\omega_x} \quad b_{\omega_y} \quad b_{\omega_z}]^T = [\boldsymbol{\Gamma} \quad \mathbf{x}_\omega]^T. \quad (5.24)$$

5.6.2 State Initialization

As the EKF is one of the linearization techniques used for Kalman filter with non-linear systems, a fairly good linearization point along with the measure of uncertainties is needed. For this purpose, the state vector is initialized using the best possible nominal

estimates. There exist numerous ways to initialize the state vector (Farrell 2008), the one utilized for this research is described here.

5.6.2.1 Initialization of the Bias States

The rate gyroscope measurements are first compensated for the deterministic errors using the calibration parameters summarized in Section 3.13 before using them in any mechanization equation. Thus the bias states are initialized as zeros and the uncertainties in these states are represented by the sensor noise.

5.6.2.2 Initialization of the Attitude States

Once the sensor measurements are compensated for the errors using the calibration parameters, these measurements can be used for estimating the initial attitude angles. For attitude initialization, the calibrated accelerometer measurements are used for estimating the roll and pitch angles during a stationary period using the following relationships (Luinge & Veltink 2005):

$$\begin{aligned}\phi &= \operatorname{atan}\left(\frac{f_y}{\sqrt{f_x^2 + f_z^2}}\right) \\ \theta &= \operatorname{atan}\left(\frac{\sqrt{f_x^2 + f_y^2}}{f_z}\right).\end{aligned}\tag{5.25}$$

The roll and pitch estimates are then used for rotating the magnetic field vector from sensor frame to the navigation frame, which is then used for estimating the heading angle given by

$$\mathbf{B}^n = \begin{bmatrix} \cos\theta & \sin\theta\sin\phi & \sin\theta\cos\phi \\ 0 & \cos\phi & -\sin\phi \\ -\sin\theta & \cos\theta\sin\phi & \cos\theta\cos\phi \end{bmatrix} \mathbf{B}^s \quad (5.26)$$

$$\psi = \text{atan2}(B_y^n, B_x^n)$$

It is assumed that the state initialization is carried out at a location that is free from magnetic perturbations.

5.6.3 System Error Model

The perturbed state vector in this case is given by

$$\delta\mathbf{x} = [\boldsymbol{\rho} \quad \delta\mathbf{x}_\omega]^T, \quad (5.27)$$

where $\boldsymbol{\rho} = [\varepsilon_\phi \quad \varepsilon_\theta \quad \varepsilon_\psi]^T$ is the attitude error vector, which defines the small angle rotations to align the estimated local level frame to the actual one. $\delta\mathbf{x}_\omega$ are the errors in the inertial sensor bias estimates. As the attitude errors are periodically updated using the measurement vectors, the components of $\boldsymbol{\rho}$ give the small angle representation of the attitude errors (Farrell 2008). A small angle transformation matrix $(\mathbf{I} - \mathbf{E})$ can then be used for compensating for the attitude errors from the predicted rotation matrix given by

$$\hat{\mathbf{C}}_s^n = (\mathbf{I} - \mathbf{E}) \mathbf{C}_s^n, \quad (5.28)$$

where $\mathbf{E} = [\boldsymbol{\rho} \times] = \begin{bmatrix} 0 & -\varepsilon_\psi & \varepsilon_\theta \\ \varepsilon_\psi & 0 & -\varepsilon_\phi \\ -\varepsilon_\theta & \varepsilon_\phi & 0 \end{bmatrix}$ is the skew symmetric matrix for the vector $\boldsymbol{\rho}$ and

the circumflex accent on the rotation matrix means that it has been compensated for the attitude errors.

5.6.3.1 Dynamics Matrix

From Equation (5.28), it can be shown that

$$\mathbf{C}_s^n = (\mathbf{I} + \mathbf{E}) \hat{\mathbf{C}}_s^n. \quad (5.29)$$

The derivative of Equation (5.29) is

$$\dot{\mathbf{C}}_s^n = (\mathbf{I} + \mathbf{E}) \dot{\hat{\mathbf{C}}}_s^n + \dot{\mathbf{E}} \hat{\mathbf{C}}_s^n. \quad (5.30)$$

The differential equation for the rotation matrix is given by

$$\dot{\mathbf{C}}_s^n = \mathbf{C}_s^n \boldsymbol{\Omega}_{is}^s \quad (5.31)$$

where $\boldsymbol{\Omega}_{is}^s = [\boldsymbol{\omega}_{is}^s \times]$ is the skew symmetric matrix of the angular rate vector obtained from the rate gyroscopes. Substituting Equation (5.31) in Equation (5.30) and simplifying gives

$$\begin{aligned} \mathbf{C}_s^n \boldsymbol{\Omega}_{is}^s &= (\mathbf{I} + \mathbf{E}) \dot{\hat{\mathbf{C}}}_s^n + \dot{\mathbf{E}} \hat{\mathbf{C}}_s^n, \\ (\mathbf{I} + \mathbf{E}) \hat{\mathbf{C}}_s^n \boldsymbol{\Omega}_{is}^s &= (\mathbf{I} + \mathbf{E}) \dot{\hat{\mathbf{C}}}_s^n + \dot{\mathbf{E}} \hat{\mathbf{C}}_s^n. \end{aligned} \quad (5.32)$$

The matrix $\boldsymbol{\Omega}_{is}^s$ is defined by the uncompensated gyroscope measurements. Let $\delta\boldsymbol{\Omega}_{is}^s$ be the skew symmetric matrix for the gyroscope measurement errors. $\boldsymbol{\Omega}_{is}^s$ can now be written as

$$\boldsymbol{\Omega}_{is}^s = \hat{\boldsymbol{\Omega}}_{is}^s + \delta\boldsymbol{\Omega}_{is}^s. \quad (5.33)$$

Substituting Equation (5.33) in Equation (5.32) and simplifying to get a relationship for $\dot{\mathbf{E}}$ yields

$$\begin{aligned} (\mathbf{I} + \mathbf{E}) \hat{\mathbf{C}}_s^n (\hat{\boldsymbol{\Omega}}_{is}^s + \delta\boldsymbol{\Omega}_{is}^s) &= (\mathbf{I} + \mathbf{E}) \dot{\hat{\mathbf{C}}}_s^n + \dot{\mathbf{E}} \hat{\mathbf{C}}_s^n, \\ (\mathbf{I} + \mathbf{E}) \hat{\mathbf{C}}_s^n + (\mathbf{I} + \mathbf{E}) \hat{\mathbf{C}}_s^n \delta\boldsymbol{\Omega}_{is}^s &= (\mathbf{I} + \mathbf{E}) \dot{\hat{\mathbf{C}}}_s^n + \dot{\mathbf{E}} \hat{\mathbf{C}}_s^n, \end{aligned}$$

$$\dot{E}\hat{C}_s^n = \hat{C}_s^n \delta\Omega_{is}^s + E\hat{C}_s^n \delta\Omega_{is}^s. \quad (5.34)$$

Neglecting the last term as it is of second order in the error terms gives

$$\dot{E} = \hat{C}_s^n \delta\Omega_{is}^s \hat{C}_n^s, \quad (5.35)$$

which, in vector form, becomes

$$\dot{\rho} = \hat{C}_s^n \delta\omega_{is}^s. \quad (5.36)$$

In Equation (5.36)

$$\delta\omega_{is}^s = \omega_{is}^s - \hat{\omega}_{is}^s, \quad (5.37)$$

where ω_{is}^s is the true angular rate vector and $\hat{\omega}_{is}^s$ is the angular rate estimates obtained after compensating for the sensor errors, which are estimated using calibration as well as stochastic modeling. The estimated angular rate vector can be written as

$$\hat{\omega}_{is}^s = \tilde{\omega}_{is}^s - \hat{\mathbf{x}}_\omega, \quad (5.38)$$

where $\tilde{\omega}_{is}^s$ is the raw angular rate measurement vector and $\hat{\mathbf{x}}_\omega$ is the estimate of the time varying bias vector obtained from the estimator (EKF). Substituting for the gyroscope model and Equation (5.38) in Equation (5.37), one gets

$$\delta\omega_{is}^s = \tilde{\omega}_{is}^s - \mathbf{x}_\omega - \boldsymbol{\varepsilon}_\omega - \tilde{\omega}_{is}^s + \hat{\mathbf{x}}_\omega, \quad (5.39)$$

which after simplification becomes

$$\delta\omega_{is}^s = -\delta\mathbf{x}_\omega - \boldsymbol{\varepsilon}_\omega, \quad (5.40)$$

where $\delta\mathbf{x}_\omega = \mathbf{x}_\omega - \hat{\mathbf{x}}_\omega$ is the perturbation in the time varying gyroscope biases. Equation (5.36) now becomes

$$\dot{\rho} = -\hat{C}_s^n \delta\mathbf{x}_\omega - \hat{C}_s^n \boldsymbol{\varepsilon}_\omega. \quad (5.41)$$

The time varying gyroscope bias is modeled as an exponentially correlated noise term as detailed in Section 3.12, and the derivative of perturbations in the time varying gyroscope bias $\delta\mathbf{x}_\omega$ is given by (Farrell 2008)

$$\delta\dot{\mathbf{x}}_\omega = -\frac{1}{\underbrace{\beta_\omega}_{F_\omega}}\delta\mathbf{x}_\omega + \boldsymbol{\varepsilon}_{x_\omega}, \quad (5.42)$$

where β_ω is the correlation time and $\boldsymbol{\varepsilon}_{x_\omega}$ is the noise vector for the stochastic modeling of the time varying gyroscopes' biases. Equations (5.41) and (5.42) lead to the following system dynamics model:

$$\underbrace{\begin{bmatrix} \dot{\boldsymbol{\rho}} \\ \delta\dot{\mathbf{x}}_\omega \end{bmatrix}}_{\delta\dot{\mathbf{x}}} = \underbrace{\begin{bmatrix} 0 & -\hat{\mathbf{C}}_s^n \\ 0 & \mathbf{F}_\omega \end{bmatrix}}_F \underbrace{\begin{bmatrix} \boldsymbol{\rho} \\ \delta\mathbf{x}_\omega \end{bmatrix}}_{\delta\mathbf{x}} + \underbrace{\begin{bmatrix} -\hat{\mathbf{C}}_s^n & 0 \\ 0 & \mathbf{I} \end{bmatrix}}_G \underbrace{\begin{bmatrix} \boldsymbol{\varepsilon}_\omega \\ \boldsymbol{\varepsilon}_{x_\omega} \end{bmatrix}}_w \quad (5.43)$$

Utilizing the Equations presented in Section 5.5, the discrete time state transition matrix and the process noise covariance matrix can be obtained.

5.6.4 Measurement Error Models

The measurements used for compensating the errors associated with the attitude vector in general and gyroscope biases in particular are herein solely based on the magnetic field vector measurements. The perturbation detection and mitigation techniques developed for compensation and statistical evaluation of the magnetic field measurements in pedestrian navigation environments, which are detailed in Chapter 4, can be utilized for the development of measurement error models. In addition to these, a technique for estimating the sensor frame's angular rates using a tri-axis magnetometer is also detailed

here, which constitutes the third set of measurement models for attitude and rate gyroscope error estimation.

5.7 Multiple Magnetometer Based Magnetic Field Measurements

Once the least perturbed magnetic field components using the algorithm detailed in Section 4.4 has been detected, the next step is to estimate the remaining magnetic field component. For this purpose, an EKF based estimator was developed (Afzal et al 2010). Details of this estimator can be found in Appendix C. The final outcome of the multiple magnetometer based magnetic field estimator is the best estimate of the unperturbed local magnetic field vector in sensor frame, which is given by

$$\mathbf{B}^s = \begin{bmatrix} B_x^s & B_y^s & B_z^s \end{bmatrix}^T. \quad (5.44)$$

The measurement noise vector, which represents the uncertainties in the estimated magnetic field as detailed in Appendix C, is represented by $\boldsymbol{\varepsilon}_{MMP}$. This gives the complete model of multiple magnetometer-based magnetic field measurements to be $\mathbf{B}^s + \boldsymbol{\varepsilon}_{MMP}$.

The magnetic field measurement of Equation (5.44) can be rotated to the navigation frame as

$$\hat{\mathbf{B}}^n = \hat{\mathbf{C}}_s^n \mathbf{B}^s. \quad (5.45)$$

Using the local magnetic field model, the measurement error is obtained as

$$\delta \mathbf{B}^n = \mathbf{B}^n - \hat{\mathbf{B}}^n, \quad (5.46)$$

where \mathbf{B}^n is the local magnetic field vector obtained from the CGRF model in this case.

Substituting Equation (5.45) into Equation (5.46) and simplifying, one obtains

$$\begin{aligned}\delta \mathbf{B}^n &= \mathbf{B}^n - \hat{\mathbf{C}}_s^n (\mathbf{B}^s + \boldsymbol{\varepsilon}_{MMP}) \\ \delta \mathbf{B}^n &= \mathbf{B}^n - (\mathbf{I} - \mathbf{E}) \mathbf{C}_s^n (\mathbf{B}^s + \boldsymbol{\varepsilon}_{MMP}) \\ \delta \mathbf{B}^n &= \mathbf{E} \mathbf{B}^n - \mathbf{C}_s^n \boldsymbol{\varepsilon}_{MMP},\end{aligned}\tag{5.47}$$

which in terms of the error state vector becomes

$$\delta \mathbf{B}^n = \left[\left[\mathbf{B}^n \times \right] \right] \boldsymbol{\rho} - \mathbf{C}_s^n \boldsymbol{\varepsilon}_{MMP}.\tag{5.48}$$

From Equation (5.48), the measurement error model for the multiple magnetometer-based magnetic field estimator becomes

$$\underbrace{\delta \mathbf{B}^n}_{\delta \mathbf{z}} = \underbrace{\left[\left[\mathbf{B}^n \times \right] \quad \mathbf{0}_{3 \times 3} \right]}_{\mathbf{H}_B} \underbrace{\begin{bmatrix} \boldsymbol{\rho} \\ \delta \mathbf{x}_\omega \end{bmatrix}}_{\delta \mathbf{x}} - \mathbf{C}_s^n \boldsymbol{\varepsilon}_{MMP},\tag{5.49}$$

where $\left[\mathbf{B}^n \times \right] = \begin{bmatrix} 0 & -B_z^n & B_y^n \\ B_z^n & 0 & -B_x^n \\ -B_y^n & B_x^n & 0 \end{bmatrix}$ and \mathbf{H}_B is the design matrix for multiple

magnetometer based magnetic field measurements.

The computation of the measurement noise covariance for these measurements is given in Appendix C, and is represented by \mathbf{R}_{MMP} .

5.8 Single Magnetometer based Heading Measurements

After testing the magnetometer's output for possible perturbations, it is possible to use another measurement, available from clean magnetic field information, that is the heading estimate. The heading estimates along with necessary statistics are available using the perturbation detection and heading estimation technique as detailed in Section

4.5. The heading estimates are given by ψ_{ns}^n whereas the measurement covariance matrix in this case is represented by R_ψ . This leads to the following measurement error:

$$\delta\psi = \psi_{ns}^n - \hat{\psi}, \quad (5.50)$$

where $\hat{\psi}$ is the heading estimate obtained using the EKF, which is given by

$$\hat{\psi} = \psi_{ns}^n - \varepsilon_\psi. \quad (5.51)$$

Substituting Equation (5.51) in Equation (5.50) and simplifying, one gets

$$\delta\psi = \varepsilon_\psi, \quad (5.52)$$

which leads to the following measurement error model for heading measurements:

$$\underbrace{\delta\psi}_{\delta z} = \underbrace{\begin{bmatrix} 0 & 0 & 1 & \mathbf{0}_{1 \times 3} \end{bmatrix}}_{H_\psi} \underbrace{\begin{bmatrix} \boldsymbol{\rho} \\ \delta \mathbf{x}_\omega \end{bmatrix}}_{\delta x}. \quad (5.53)$$

5.9 Quasi-Static Field (QSF) based Attitude and Angular Rate Measurements¹

Because previous measurement updates are only possible if the perturbations have successfully been mitigated from the sensed data and because it was exhaustively demonstrated that indoor environments are full of perturbations, novel work was conducted by the author to develop a new approach for mitigating these errors. Consequently a novel idea for estimating attitude and gyroscope errors using magnetic field measurements for pedestrian navigation environments is detailed here. It mainly involves detection of static (constant) total magnetic field periods during pedestrian motion, which are then utilized as measurements for estimating attitude and gyroscope errors. The quasi-static magnetic field (QSF) detector is developed using statistical signal

¹ Patent Pending.

processing techniques. The magnetic field measurements detected as quasi-static are then utilized to estimate the errors associated with attitude and rate gyroscopes, which make up for the final measurement error model used herein. Contrary to existing solutions, this technique is working in magnetically perturbed environments as long as the field is identified as constant over a selective period of time.

5.9.1 Quasi-Static Magnetic Field (QSF) Detector Realization

The Earth's magnetic field, though a good source of information for estimating heading outdoor, suffers severe degradations in the indoors caused by magnetic field perturbations as shown in Section 4.3. These perturbations are of changing magnitudes and directions, which induce random variations in the total magnetic field. These variations render the magnetic field information useless for orientation estimation indoor with respect to the magnetic North. Although the magnetic field indoor is not spatially constant due to changing perturbation sources, depending on the pedestrian's speed and surroundings, it is possible to have locations as well as short periods (user not moving) when the perturbed magnetic field is constant in magnitude as well as direction. The rate of change of the total magnetic field in such situations will be ideally zero. It is possible to have very slight changes in the magnitude and direction of the total magnetic field (due to sensor noise) that can be considered quasi-static.

The information to be considered for detecting a QSF is the rate of change of the total magnetic field $\|\dot{\mathbf{F}}\|$, which is referred to as the field gradient and is computed using

$$\|\dot{\mathbf{F}}\| = \left\| \frac{\mathbf{F}_k - \mathbf{F}_{k-1}}{\Delta t} \right\|, \quad (5.54)$$

where \mathbf{F}_k is the total magnetic field at the current epoch, \mathbf{F}_{k-1} is the total magnetic field at the previous epoch and Δt is the measurement update rate. For a window of size N , a QSF detector will detect a static field if

$$\left\{ \left\| \dot{\mathbf{F}}_k \right\| \right\}_{k=n}^{n+N-1} \approx 0. \quad (5.55)$$

Utilizing a statistical signal detection technique known as Likelihood Ratio Test (LRT), the QSF detector is given by

$$\left| \frac{I}{\sqrt{N}} \left(\sum_{k=n}^{n+N-1} y_k \right) \right| < \gamma_{\|\dot{\mathbf{F}}_k\|}, \quad (5.56)$$

where $\gamma_{\|\dot{\mathbf{F}}_k\|}$ is the threshold for QSF detection. Readers are referred to Appendix D for a detailed derivation of the QSF detector.

5.9.2 Statistical Analysis of the QSF Detector

In order to quantify the performance of the proposed detector, statistical analysis was conducted. From Equation (5.56), it can be observed that there are a number of tuning parameters that need to be evaluated for effectively using the QSF detector. These are the threshold, noise variance and the number of samples (window size) required for the detection test statistics.

5.9.2.1 Measurement Noise Variance

This factor is taken to be the variance of the total field gradient when the field itself is not changing. This gives a measure of the gradient noise that one will encounter during

quasi-static field periods. Figure 5-4 depicts the field gradient noise distribution, which is used for estimating the noise variance at 1σ . This comes out to be $0.057 \mu\text{T}^2$.

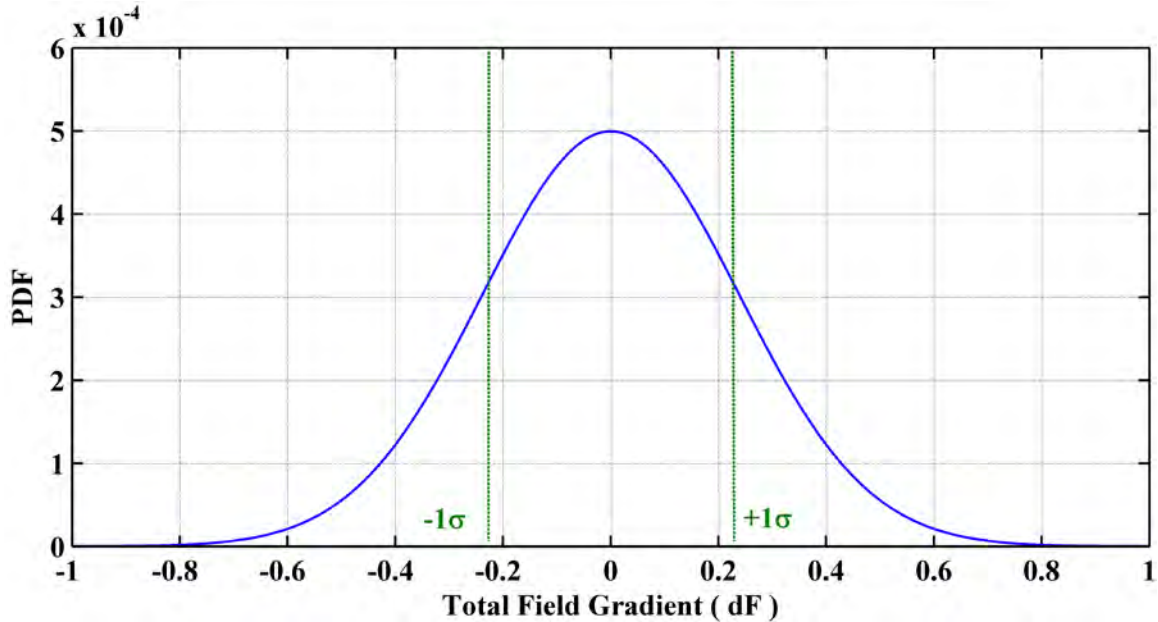


Figure 5-4: PDF of total field gradient during constant field periods.

5.9.2.2 Threshold and Window Size Selection Using Receiver Operating Characteristics

The Receiver Operating Characteristics (ROC) curve allows one to select the test statistics acceptance threshold based on the required probability of detection P_d and the acceptable probability of false alarm P_f . Figure 5-5 shows the ROC for the QSF detector for different sample window sizes. The sensor sampling rate is 0.04 s, which gives a minimum window size of 0.12 s and a maximum of 0.32 s in this case. It can be observed that the ROC tends to flatten out after $P_d = 0.8$. Thus selecting a P_d any larger than this value will cause more false alarms. Hence a P_d of approximately 0.8 is selected for this detector. The effect of the window size on the detector's performance is negligible at the selected P_d . Therefore a window size of three samples is selected to reduce the processing

burden. It is worth mentioning here that the statistical analysis of the QSF detector is carried out by utilizing magnetic field data collected in numerous pedestrian navigation environments. Thus the tuning parameters can be considered as global for the entire pedestrian navigation environment. Table 5-1 summarizes the parameters selected for the QSF detector.

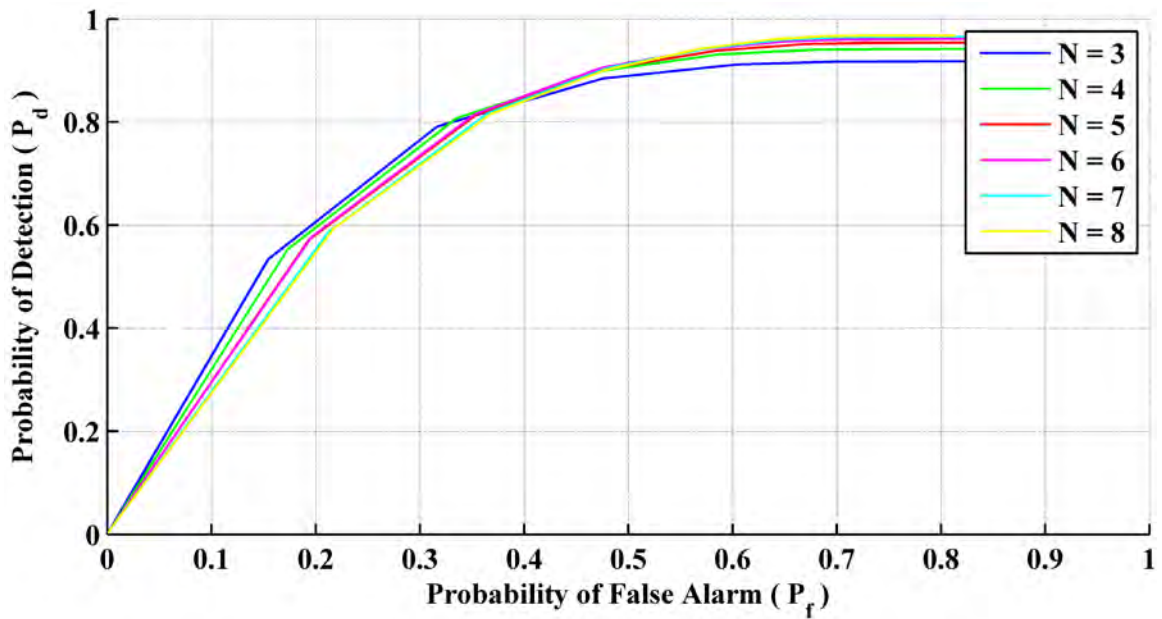


Figure 5-5: ROC for different window sizes.

Table 5-1: Parameters selected for the QSF detector.

Parameter	Value
Window Size (N)	3
Probability of detection (P_d)	0.82
Probability of false alarm (P_f)	0.30
Threshold (γ)	0.14

5.9.2.3 QSF Periods' Analysis in Pedestrian Navigation Environments

Figure 5-6 summarizes the QSF detection periods and their respective durations for all of the pedestrian navigation environments. Most of the detection periods are of 120 ms to 300 ms duration. Figure 5-7 depicts the shortest and longest gaps between two consecutive QSF periods and their percentages of occurrence respectively. The minimum gap, i.e. 240 ms, occurs more frequently as compared with the maximum gap of 480 ms. Therefore it can be concluded that the QSF periods are encountered frequently and hence may allow for estimation of angular rate errors. This analysis justifies the use of QSF periods for estimating errors associated with rate gyroscopes. It is worth mentioning here that unlike some pedestrian navigation applications where Zero Velocity Updates (ZUPT) occur frequently during a pedestrian's walk (e.g. shoe mounted sensors), when the sensor block is in the hand or in a pocket or purse, these may not be encountered at all. In such scenarios, QSF periods can still be used effectively for providing regular measurements for sensor error estimation.

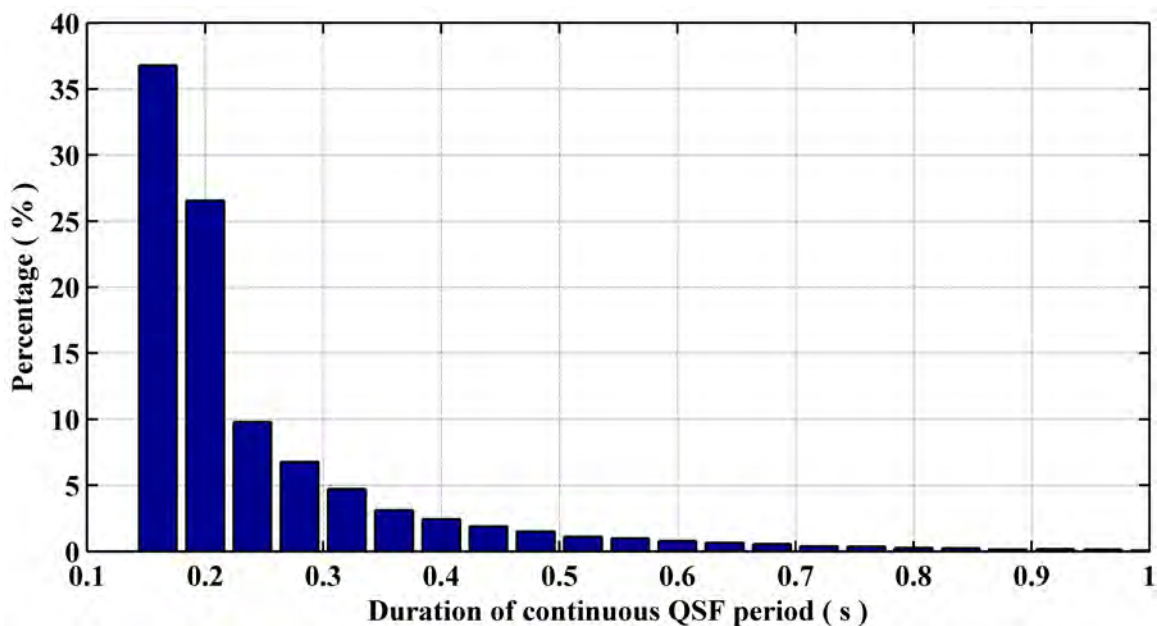


Figure 5-6: Continuous QSF periods and their occurrence.

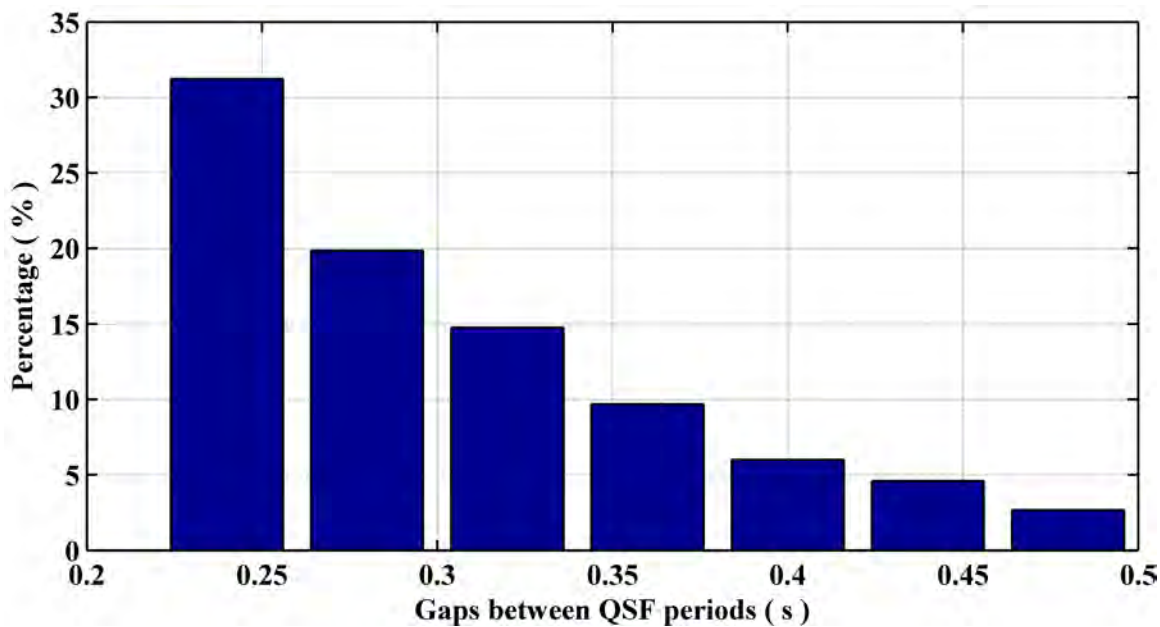


Figure 5-7: Duration of gaps between QSF periods.

5.9.3 Use of QSF Detected Periods for Attitude and Gyroscope Error Estimation

Once the QSF periods are detected during pedestrian motion, the next step is to utilize the magnetic field information during such periods for estimation of attitude and gyroscope

errors. This can be achieved by developing a measurement error model to be used with the EKF developed in Section 5.6.

5.9.4 QSF Measurement Error Model

Let the magnetic field measurement in the sensor frame at the start of quasi-static field period be given by

$$\mathbf{B}_{QSF}^s = \begin{bmatrix} B_{QSF_x}^s & B_{QSF_y}^s & B_{QSF_z}^s \end{bmatrix}^T. \quad (5.57)$$

Considering the attitude at the start of quasi-static period as the reference for this measurement model, the magnetic field measurement can be transformed using

$$\mathbf{B}_{QSF}^n = \hat{\mathbf{C}}_s^n \mathbf{B}_{QSF}^s. \quad (5.58)$$

For the quasi-static field periods, \mathbf{B}_{QSF}^n is considered as a measurement. That is the magnetic field information available from the CGRF model is not considered as a measurement of truth rather the field \mathbf{B}_{QSF}^n is considered as reference over the QSF period. As the inaccuracies in the sensor will cause errors in the estimated attitude, the transformations of proceeding magnetic field measurements from body to navigation frame using the updated $\hat{\mathbf{C}}_s^n$ would be different from \mathbf{B}_{QSF}^n hence causing the measurement error. This gives the relationship for the first measurement error model.

$$\delta \mathbf{B}_{QSF}^n = \mathbf{B}_{QSF}^n - \hat{\mathbf{C}}_s^n \mathbf{B}_{QSF}^s \quad (5.59)$$

Equation (5.59) would equate to zero as \mathbf{B}_{QSF}^n is obtained using $\hat{\mathbf{C}}_s^n \mathbf{B}_{QSF}^s$. Thus the magnetic field information from the proceeding epoch along with new attitude estimate for $\hat{\mathbf{C}}_s^n$ are needed. Let \mathbf{B}_{QSF+1}^s be the next magnetic field measurement obtained from the

magnetometer while the QSF period still exists. Substituting the new magnetic field measurement in Equation (5.59), one obtains

$$\delta \mathbf{B}_{QSF}^n = \mathbf{B}_{QSF}^n - \hat{\mathbf{C}}_s^n \mathbf{B}_{QSF+1}^s. \quad (5.60)$$

Ideally, as the magnetic field during QSF period is locally static (magnetic field vector not changing its magnitude or direction), Equation (5.60) should also equate to zero. But due to errors in rate gyroscope measurements, which are used for estimating the rotation matrix, the following perturbed model is obtained:

$$\delta \mathbf{B}_{QSF}^n = \mathbf{B}_{QSF}^n - (\mathbf{I} - \mathbf{E}) \mathbf{C}_s^n (\mathbf{B}_{QSF}^s + \boldsymbol{\varepsilon}_B) \quad (5.61)$$

where $\boldsymbol{\varepsilon}_B$ is the measurement noise of the magnetometers.

Simplifying (5.61) to get a relationship between measurements and states, one obtains

$$\begin{aligned} \delta \mathbf{B}_{QSF}^n &= \mathbf{B}_{QSF}^n - (\mathbf{C}_s^n - \mathbf{E} \mathbf{C}_s^n) (\mathbf{B}_{QSF+1}^s + \boldsymbol{\varepsilon}_B) \\ \delta \mathbf{B}_{QSF}^n &= \mathbf{B}_{QSF}^n - \mathbf{B}_{QSF}^n - \mathbf{C}_s^n \boldsymbol{\varepsilon}_B + \mathbf{E} \mathbf{C}_s^n \mathbf{B}_{QSF+1}^s + \mathbf{E} \mathbf{C}_s^n \boldsymbol{\varepsilon}_B. \end{aligned} \quad (5.62)$$

Because the last term in Equation (5.62) is of the second order in errors, neglecting it results in

$$\begin{aligned} \delta \mathbf{B}_{QSF}^n &= \mathbf{E} \mathbf{B}_{QSF}^n - \mathbf{C}_s^n \boldsymbol{\varepsilon}_B \\ \delta \mathbf{B}_{QSF}^n &= -[\mathbf{B}_{QSF}^n \times] \boldsymbol{\rho} - \mathbf{C}_s^n \boldsymbol{\varepsilon}_B, \end{aligned} \quad (5.63)$$

where $[\mathbf{B}_{QSF}^n \times] = \begin{bmatrix} 0 & -B_{QSF_z}^n & B_{QSF_y}^n \\ B_{QSF_z}^n & 0 & -B_{QSF_x}^n \\ -B_{QSF_y}^n & B_{QSF_x}^n & 0 \end{bmatrix}$ is the skew symmetric matrix of vector \mathbf{B}_{QSF}^n .

From Equation (5.63), the first QSF measurement error model becomes

$$\delta \mathbf{B}_{QSF}^n = \begin{bmatrix} -[\mathbf{B}_{QSF}^n \times] & \mathbf{0}_{1 \times 3} \end{bmatrix} \begin{bmatrix} \boldsymbol{\rho} \\ \delta \mathbf{x}_\omega \end{bmatrix} - \begin{bmatrix} \mathbf{C}_s^n & 0 \\ 0 & 0 \end{bmatrix} \begin{bmatrix} \boldsymbol{\varepsilon}_B \\ 0 \end{bmatrix}. \quad (5.64)$$

During the quasi-static field periods, the rate of change of the reference magnetic field is zero. Using this information as a measurement, one gets

$$\begin{aligned} \mathbf{B}_{QSF}^n &= \hat{\mathbf{C}}_s^n \mathbf{B}_{QSF}^s \\ \hat{\mathbf{C}}_n^s \mathbf{B}_{QSF}^n &= \mathbf{B}_{QSF}^s \end{aligned} \quad (5.65)$$

Taking the derivative of Equation (5.65) to get the relationship between the rate of change of a vector in two different frames (Natanson et al 1994), one gets

$$\hat{\mathbf{C}}_n^b \dot{\mathbf{B}}_{QSF}^n = \dot{\mathbf{B}}_{QSF}^s + \boldsymbol{\omega}_B^s \times \mathbf{B}_{QSF}^s, \quad (5.66)$$

where $\boldsymbol{\omega}_B^s = [\omega_{B_x} \quad \omega_{B_y} \quad \omega_{B_z}]^T$ is the angular rate vector required for rotating the magnetic field measurements between two epochs in the sensor frame. Because the QSF periods are identified as those where the field vector is not changing its magnitude and orientation, the left hand side of Equation (5.66) equates to zero, reducing to

$$\dot{\mathbf{B}}_{QSF}^s = -\boldsymbol{\omega}_B^s \times \mathbf{B}_{QSF}^s. \quad (5.67)$$

During user motion, the magnetic field components in the body frame will encounter changes, which can be modeled by Equation (5.67). But due to errors in gyroscopes, the predicted changes in magnetic field will be different from the measured ones given by

$$\delta \dot{\mathbf{B}}_{QSF}^s = \dot{\mathbf{B}}_{QSF+1}^s - \hat{\dot{\mathbf{B}}}_{QSF+1}^s, \quad (5.68)$$

where $\dot{\mathbf{B}}_{QSF+1}^s = \frac{\mathbf{B}_{QSF+1}^s - \mathbf{B}_{QSF}^s}{\Delta t}$ and Δt is the time period between two consecutive epochs. Expanding Equation (5.68) and substituting from Equation (5.67) results in

$$\delta \dot{\mathbf{B}}_{QSF}^s = \dot{\mathbf{B}}_{QSF+1}^s + \hat{\boldsymbol{\omega}}_B^s \times (\mathbf{B}_{QSF+1}^s + \boldsymbol{\varepsilon}_B)$$

$$\begin{aligned}\delta \dot{\mathbf{B}}_{QSF}^s &= \dot{\mathbf{B}}_{QSF+1}^s + (\boldsymbol{\omega}_B^s + \delta \boldsymbol{\omega}_B^s) \times (\mathbf{B}_{QSF+1}^s + \boldsymbol{\varepsilon}_B) \\ \delta \dot{\mathbf{B}}_{QSF}^s &= \dot{\mathbf{B}}_{QSF+1}^s + \boldsymbol{\omega}_B^s \times \mathbf{B}_{QSF+1}^s + \delta \boldsymbol{\omega}_B^s \times \mathbf{B}_{QSF+1}^s + \hat{\boldsymbol{\omega}}_B^s \times \boldsymbol{\varepsilon}_B.\end{aligned}\quad (5.69)$$

The first two terms give the rate of change of the reference magnetic field, which, during QSF periods, is zero. Thus Equation (5.69) reduces to

$$\delta \dot{\mathbf{B}}_{QSF}^s = \delta \boldsymbol{\omega}_B^s \times \mathbf{B}_{QSF+1}^s + \hat{\boldsymbol{\omega}}_B^s \times \boldsymbol{\varepsilon}_B, \quad (5.70)$$

which can be rewritten as

$$\delta \dot{\mathbf{B}}_{QSF}^s = -[\mathbf{B}_{QSF+1}^s \times] \delta \boldsymbol{\omega}_B^s + [\hat{\boldsymbol{\omega}}_B^s \times] \boldsymbol{\varepsilon}_B, \quad (5.71)$$

giving the following measurement model:

$$\delta \dot{\mathbf{B}}_{QSF}^s = \begin{bmatrix} \mathbf{0}_{3 \times 3} & -[\dot{\mathbf{B}}_{QSF+1}^s \times] \end{bmatrix} \begin{bmatrix} \boldsymbol{\rho} \\ \delta \mathbf{x}_\omega \end{bmatrix} + \begin{bmatrix} \mathbf{0}_{1 \times 3} & \mathbf{0}_{1 \times 3} \\ \mathbf{0}_{1 \times 3} & [\hat{\boldsymbol{\omega}}_B^s \times] \end{bmatrix} \begin{bmatrix} \mathbf{0}_{3 \times 1} \\ \boldsymbol{\varepsilon}_B \end{bmatrix}. \quad (5.72)$$

Combining Equations (5.64) and (5.72), the complete measurement error model using QSF is given by

$$\underbrace{\begin{bmatrix} \delta \mathbf{B}_{QSF}^n \\ \delta \dot{\mathbf{B}}_{QSF}^s \end{bmatrix}}_{\delta \mathbf{z}} = \underbrace{\begin{bmatrix} -[\mathbf{B}_{QSF}^n \times] & \mathbf{0}_{3 \times 3} \\ \mathbf{0}_{3 \times 3} & -[\dot{\mathbf{B}}_{QSF+1}^s \times] \end{bmatrix}}_{\mathbf{H}_{QSF}} \underbrace{\begin{bmatrix} \boldsymbol{\rho} \\ \delta \mathbf{x}_\omega \end{bmatrix}}_{\delta \mathbf{x}} + \begin{bmatrix} -\mathbf{C}_s^n \\ [\hat{\boldsymbol{\omega}}_B^s \times] \end{bmatrix} \boldsymbol{\varepsilon}_B, \quad (5.73)$$

which can be utilized for constraining the error growth in attitude angles and estimating the rate gyroscope errors.

5.10 Overall Scheme for the Proposed Attitude Estimator

To summarize the overall development of the attitude estimator for pedestrian navigation applications, a schematic is presented in Figure 5-8. All of the information generators as well as the flow of information through the proposed estimator are identified here.

In the next chapter, the estimator will be tested in two perturbed environments, namely an urban canyon and inside a shopping mall, to demonstrate its effectiveness.

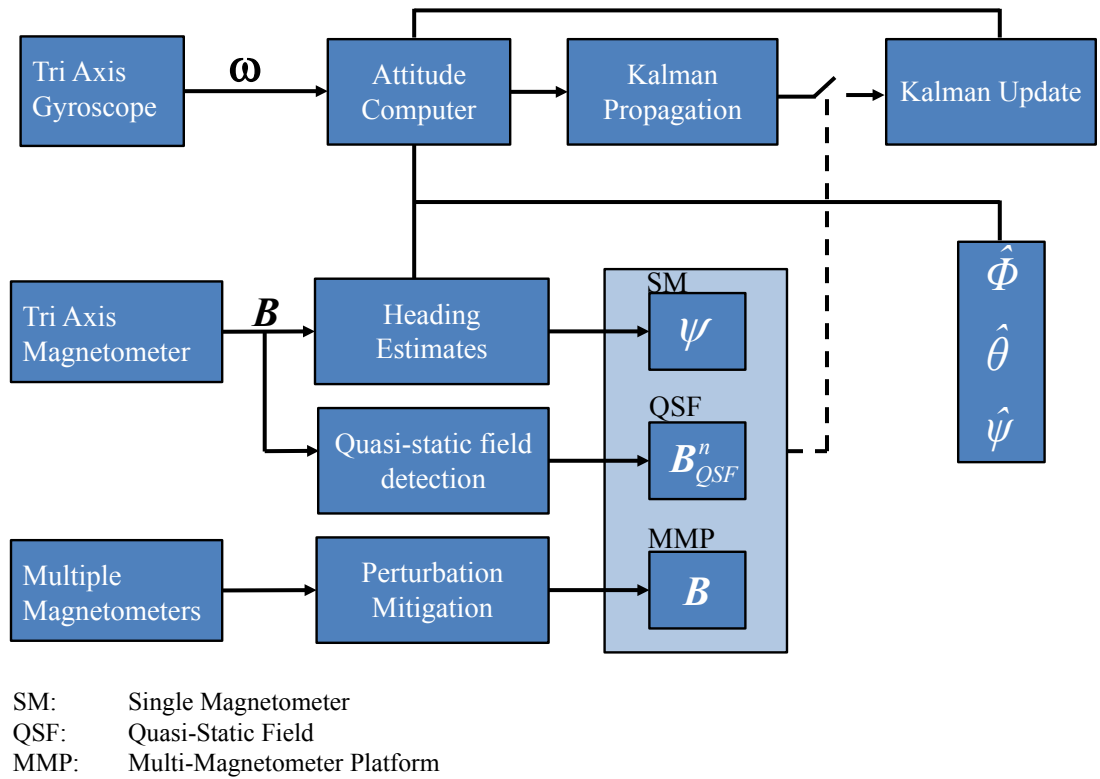


Figure 5-8: Attitude estimator using gyroscopes and magnetometers.

Chapter Six: **Experimental Assessment of the Proposed Algorithms**

Following a detailed theoretical analysis of the magnetic field perturbations and proposing various techniques for mitigating these so as to obtain better estimates of attitude in pedestrian navigation environments, the next step is to thoroughly assess the impact of the proposed algorithms. For this purpose, test data is collected in different environments, and the algorithms developed in Chapter 4 and Chapter 5 are utilized for attitude estimation. This chapter first describes the data collection setup followed by a detailed description of the assessment criterion and test environments selected for the analysis. The results obtained using different techniques for perturbation mitigation as well as gyroscope error estimation are then described. Finally the impact of different measurements for attitude and gyroscope error estimation in a combined fashion is discussed.

6.1 Test Setup

The test setup used for analyzing the impact of the proposed algorithms on attitude estimation comprised MSP, MMP and the optical wheel encoder. All of these modules/sub-systems are described in Chapter 3 and Chapter 4. The wheel encoder is used here for measuring the pedestrian's walking speed so as to bring the outcome of the proposed algorithms from attitude domain to the position domain, which provides better insight into the performance of the system. This wheel encoder is capable of computing the pedestrian's walking speed with an accuracy of $\pm 4 \times 10^{-3}$ m/s. The walking speed is later resolved into North and East components using the estimated attitude to compute the

position. As this research focuses only on attitude estimation, the wheel encoder provides accurate speed measurements, which are necessary for de-correlating the velocity error budget from the attitude one, allowing the assessment of attitude accuracies alone. In an actual portable device such as a smart-phone, the walking speed would be measured by accelerometers. Researchers have utilized shoe mounted consumer grade accelerometers for stride length and speed estimation with reported accuracies of 7% (Stirling et al 2005). This computes to an error of $\pm 100 \times 10^{-3}$ m/s for normal walking speed of 1.4 m/s as encountered herein. Although smart phones of today are equipped with accelerometers of better quality than this, resulting in errors of approximately $\pm 7 \times 10^{-3}$ m/s (Bosch-Sensortec 2008), performing gait analysis with a handheld device would be a challenging task and constitutes a research topic in itself. Thus with the use of wheel encoder, the experimental assessments of the proposed attitude estimator in the position domain as described herein, can be considered free of errors contributed from speed sensors (accelerometers), providing a better insight into attitude accuracy. Indeed in real world situation, all of the factors affecting the position error budget need to be considered while developing a pedestrian navigation system. The MSP developed for this research is hosting the accelerometers, which can be used in future for investigating different methods to estimate stride length and speed, thus implementing a complete pedestrian navigation system. The MSP and MMP are rigidly mounted on a plastic plate, which can be easily carried in a hand. The wheel encoder is mounted on a pole that can be held by a pedestrian and pushed along the ground for measuring the walking speed. Figure 6-1(a) shows the handheld arrangement of the sensor modules (MSP and MMP) used for the test data collection. Here the body and sensor frames are also identified to clarify in which

frame (sensor frame) the attitude is estimated. Figure 6-1(b) shows the overall test data collection setup including the wheel encoder being used in one of the test environments.

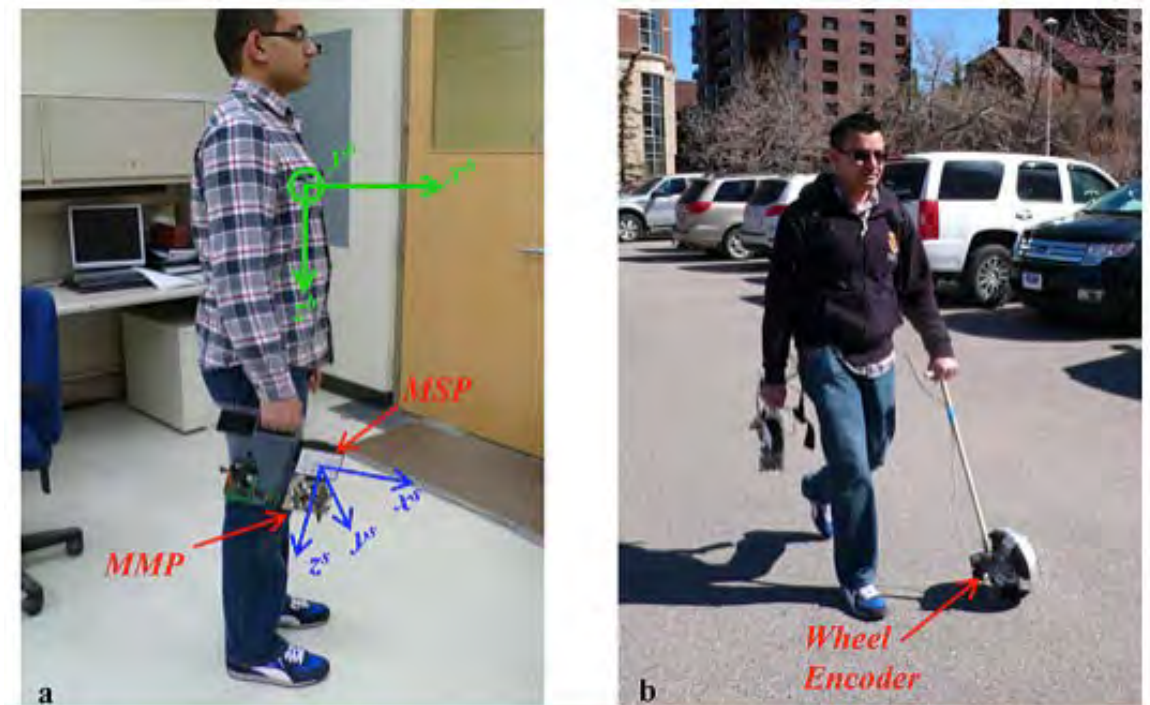


Figure 6-1: Test data collection setup by author.

6.2 Assessment Criterion

In order to assess the impact of the proposed methods on attitude estimation for pedestrian navigation, the solution repeatability criterion is chosen, in the absence of a reference trajectory. Multiple paths of the same trajectory are followed in different environments keeping the same starting and ending points to assess the repeatability criteria. The paths are traversed in such a way so as to keep the separation between them to within 1 m if possible. This is achieved by following prominent patterns on the ground (tiles boundaries, pavement markings/ intersections etc.).

6.3 Selection of the Test Environments

In order to assess the impact of the proposed algorithms on attitude estimation for pedestrian applications, two environments are selected based on their importance from pedestrian navigation's perspective. These are:

1. Urban canyons
2. Shopping malls

6.3.1 Urban Canyons

Urban canyons can be considered as one of the regions where pedestrian navigation applications have a lot of commercial significance. Also before moving indoor, one often ends up being in an urban canyon for some time. Hence detailed analysis of the proposed algorithms in this environment is very important. For this reason, downtown Calgary is chosen as one of the environments for the assessment of attitude estimation schemes proposed herein. Figure 6-2 gives the bird's eye view of the region selected in downtown Calgary for the assessment. The block selected is newly constructed with a walkway filled with ferrous infrastructure all around including phone booths, newspaper dispensers, street light poles and manholes. The walking trajectory around this block was approximately 370 metres and was traversed thrice for repeatability testing.



Figure 6-2: Downtown Calgary data collection environment (Google Maps).

Figure 6-3(a) shows the starting and ending point for each loop around the block with a traffic signal control panel right beside it, which is made out of metal hence contributing to the magnetic field perturbations in this region. Figure 6-3(b) shows one of the paths traversed in the selected region with high rise buildings and metallic infrastructure all around. Indeed this environment includes numerous magnetic field perturbation sources and hence can be considered a good test area for the assessment of attitude estimation algorithms developed herein.



Figure 6-3: Data collection in downtown Calgary.

6.3.2 Shopping Malls

For assessment of the proposed algorithms in an indoor environment, a typical North American shopping mall is selected. The Market Mall in North West Calgary was selected for an indoor environment as it is close to the University of Calgary. Market Mall has a fair combination of shops for clothes, electronics, sports goods etc. The corridors are hosting sitting areas and booths most of which are related to cell phones and jewellery shops. Figure 6-4 gives a bird's eye view of the shopping mall selected for indoor data collection. The trajectory traversed indoor is highlighted in red. As this shopping mall has already been used for assessment of magnetic field perturbations described in Chapter 4, the indoor corridor with the strongest perturbations was identified from the magnetic field surveys and is selected for the final assessment of the proposed attitude estimation techniques.

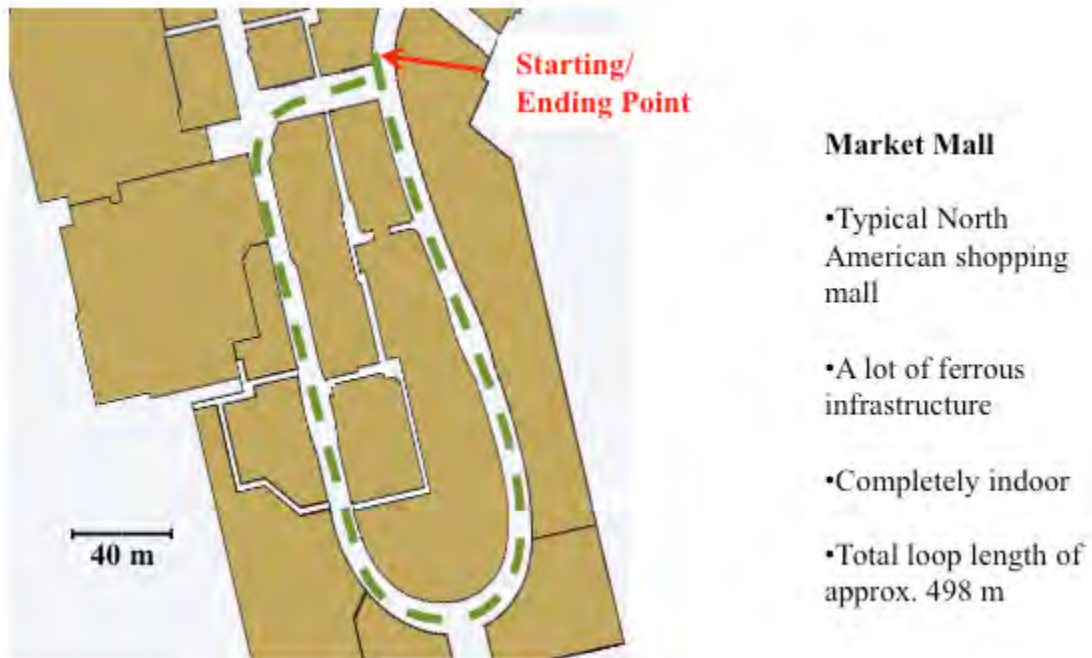


Figure 6-4: Market Mall Calgary data collection environment (Google Maps).

Figure 6-5(a) shows the pedestrian at the starting/ ending point inside the shopping mall. The trajectory traversed indoor was approximately 498 metres and was repeated twice for the repeatability analysis. Figure 6-5(b) shows one of the indoor corridors of the mall with the centre booths and sitting areas clearly visible in the middle of the corridor.

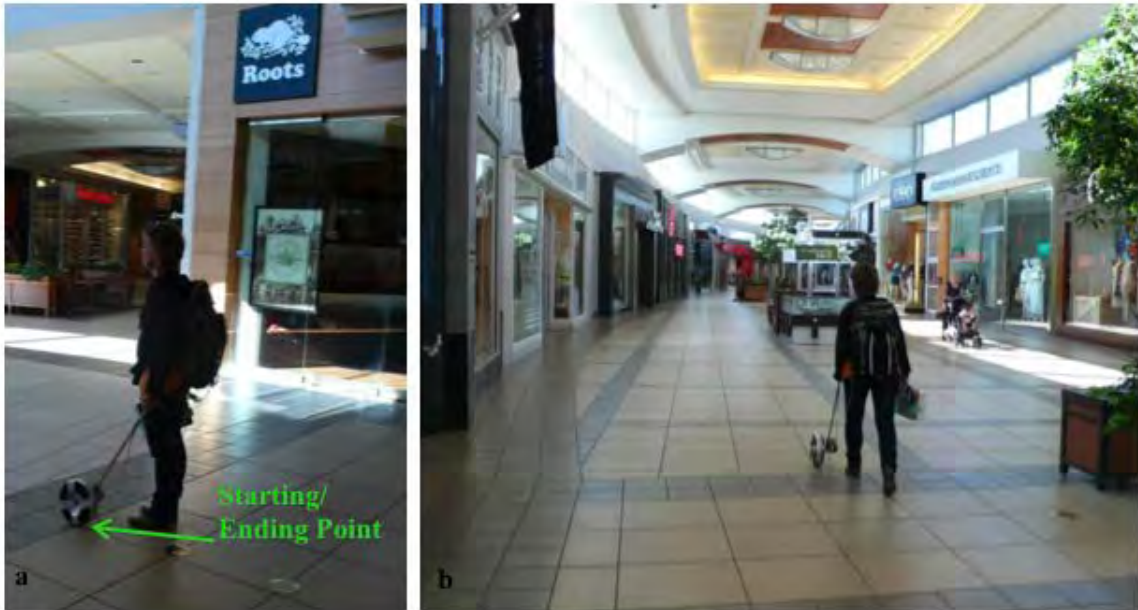


Figure 6-5: Data collection in Market Mall Calgary.

6.4 Single Magnetometer based Heading Estimator

6.4.1 Urban Canyon Environment

The heading estimates available from the perturbation detection and mitigation technique using a Single Magnetometer (SM) can be utilized for correcting the errors associated with the orientation parameter as described in Section 5.8. Figure 6-6 shows the trajectory obtained for the first loop in urban area. The availability of SM measurements is identified in green. Although the SM heading estimator is capable of providing heading estimates along with their respective accuracies at every epoch, only those estimates with standard deviation of 2° or better are used herein, as discussed in Chapter 4. This leads to one good SM measurement every 3 m based on a pedestrian's average speed of approximately 1.4 m/s in this case. The SM measurements are then propagated in time using the rate gyroscopes identified in red, which are referred to here as raw. In between

the SM measurements, it can be seen that the position errors are growing randomly. This is because the SM measurements are unable to completely observe the errors associated with the rate gyroscopes, which is evident from Equation (5.53). Further, in the presence of a strong perturbation source as is identified in Figure 6-6, the position errors tend to grow unbounded because of the unavailability of SM measurements. This is because the pedestrian's orientation is the primary means of resolving the speed into East and North velocity components, and any errors in this parameter are directly reflected in the position domain.

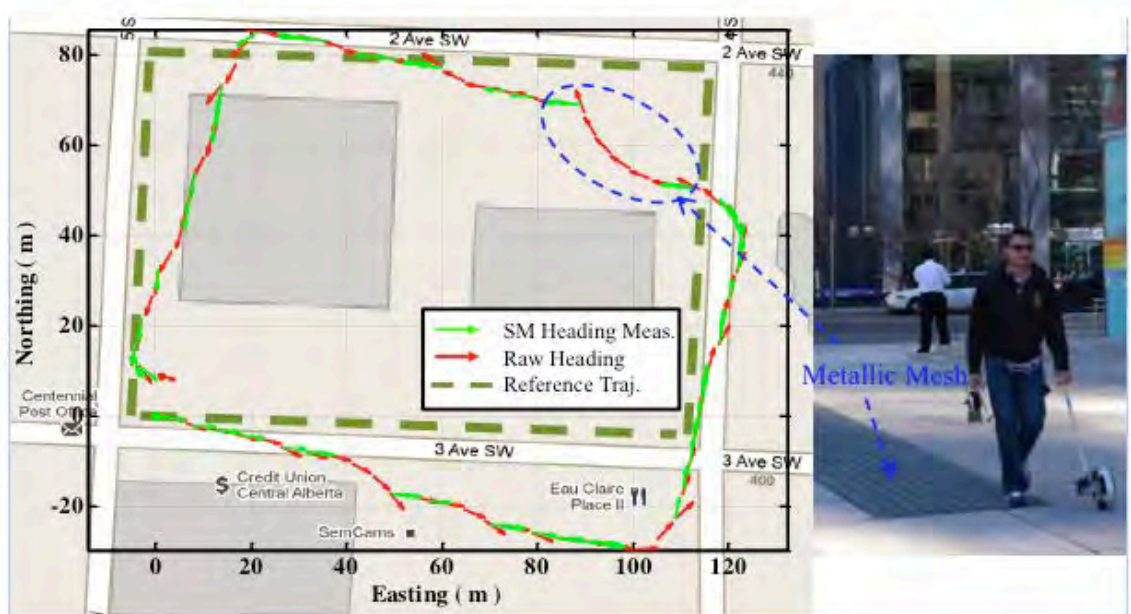


Figure 6-6: First urban canyon loop with a strong perturbation source – SM.

Figure 6-7 shows the third loop of the selected urban canyon. The starting and ending points are kept the same for these tests, as described in Section 6.2, but due to errors in the estimated orientation, these points are no longer at the same location. It can be observed in Figure 6-6 and Figure 6-7 that the SM measurements are available at almost

the same locations. This is because the loops around the block were replicated to within 1 m of one another most of the time, leading to similar SM measurements.

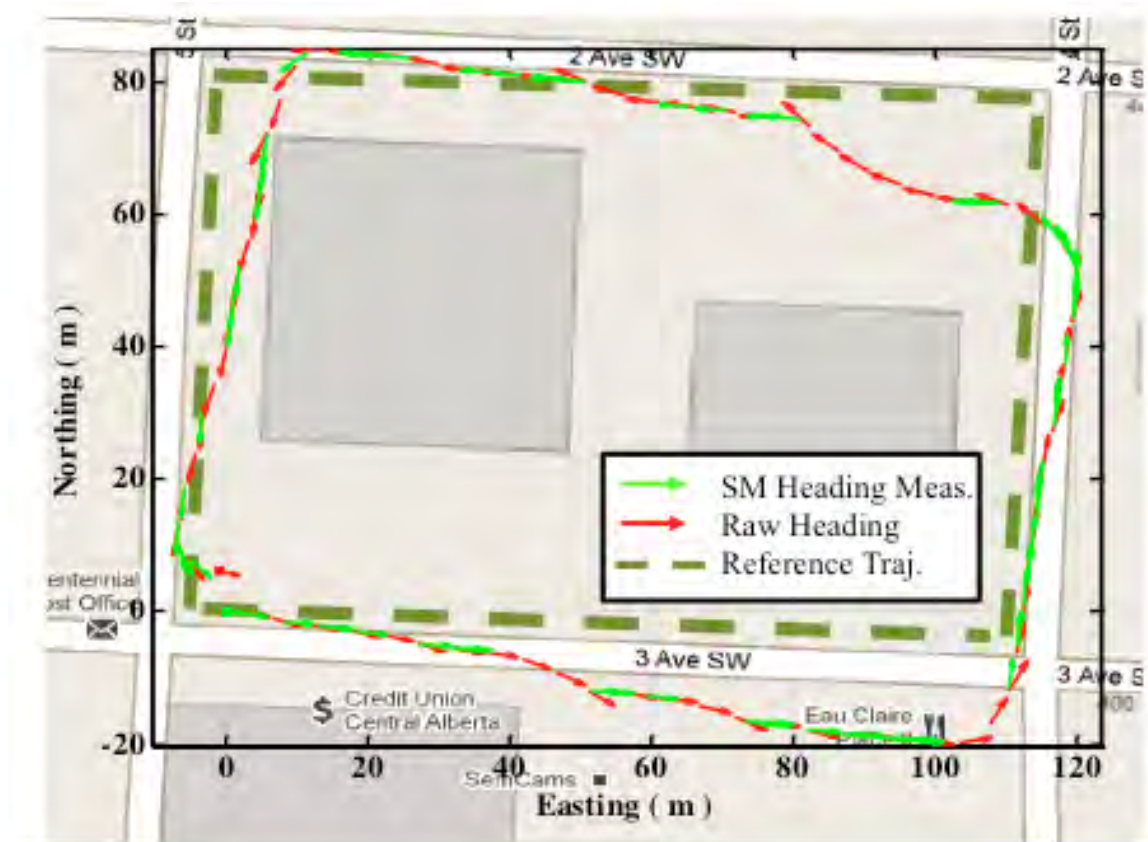


Figure 6-7: Trajectory for the third loop of urban canyon.

Figure 6-8 shows the three trajectories obtained using SM measurements for error estimation. These trajectories are considered independent of each other to analyze their repeatability. It can be observed that these are different from one another by up to 30 m. These differences are due to changing biases associated with the rate gyroscopes. As these errors are random in nature, their corresponding effects in the position domain are also random. It is worth mentioning here that the SM measurements have in fact corrected the overall trajectories to a great extent reducing the overall position errors by approximately 91% as is shown in Figure 6-9.

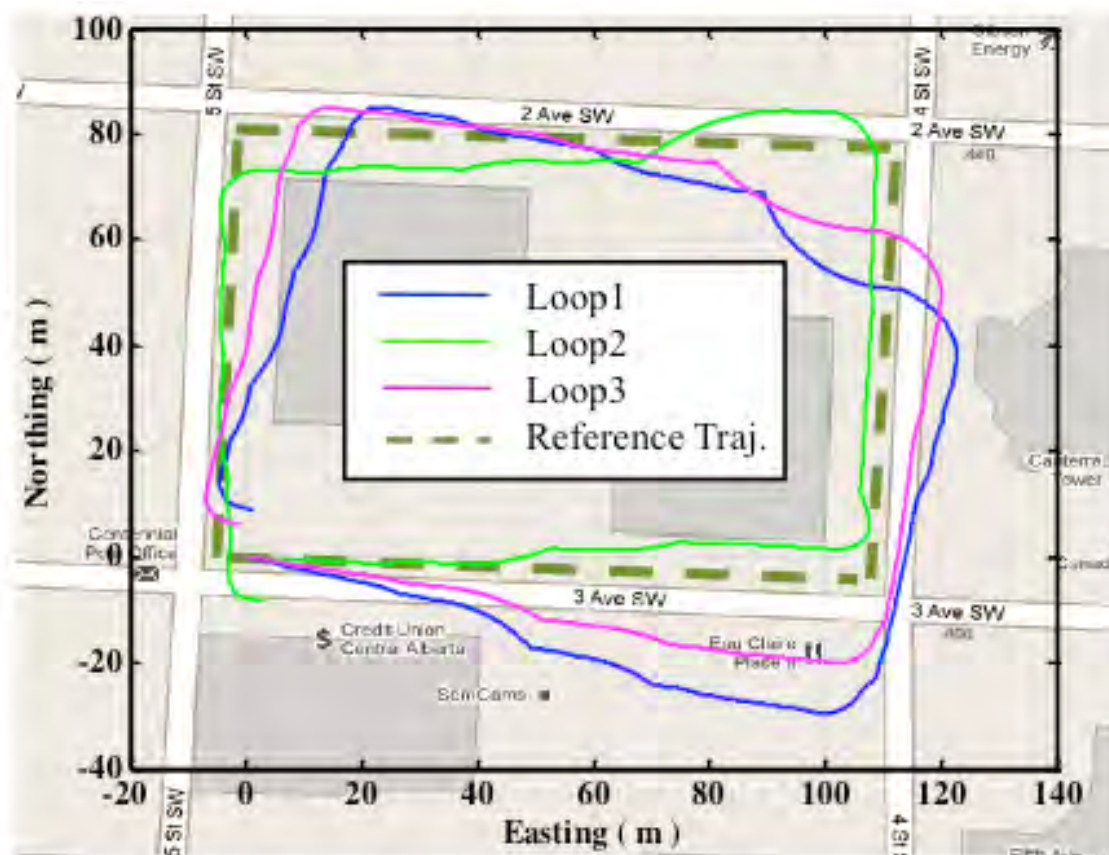


Figure 6-8: Trajectories obtained using SM measurements for error estimation.

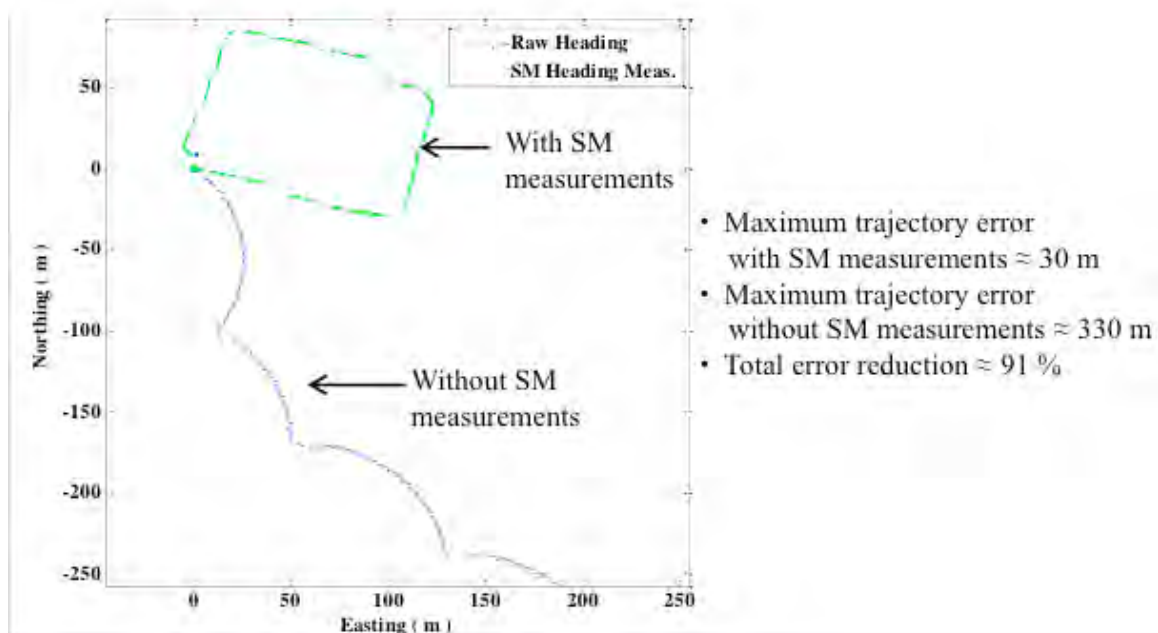


Figure 6-9: Impact of SM measurements on computed trajectory.

Figure 6-10 shows the continuous trajectory obtained for the three loops. Here the starting point for each loop is not reset to the actual one as was done for the above repeatability analysis. This shows that although the SM measurements are providing reliable estimates of the heading, they are not a reliable source (as the only measurement) for pedestrian attitude estimation in general and orientation estimation in particular, because they are unable to completely observe the errors associated with rate gyroscopes.

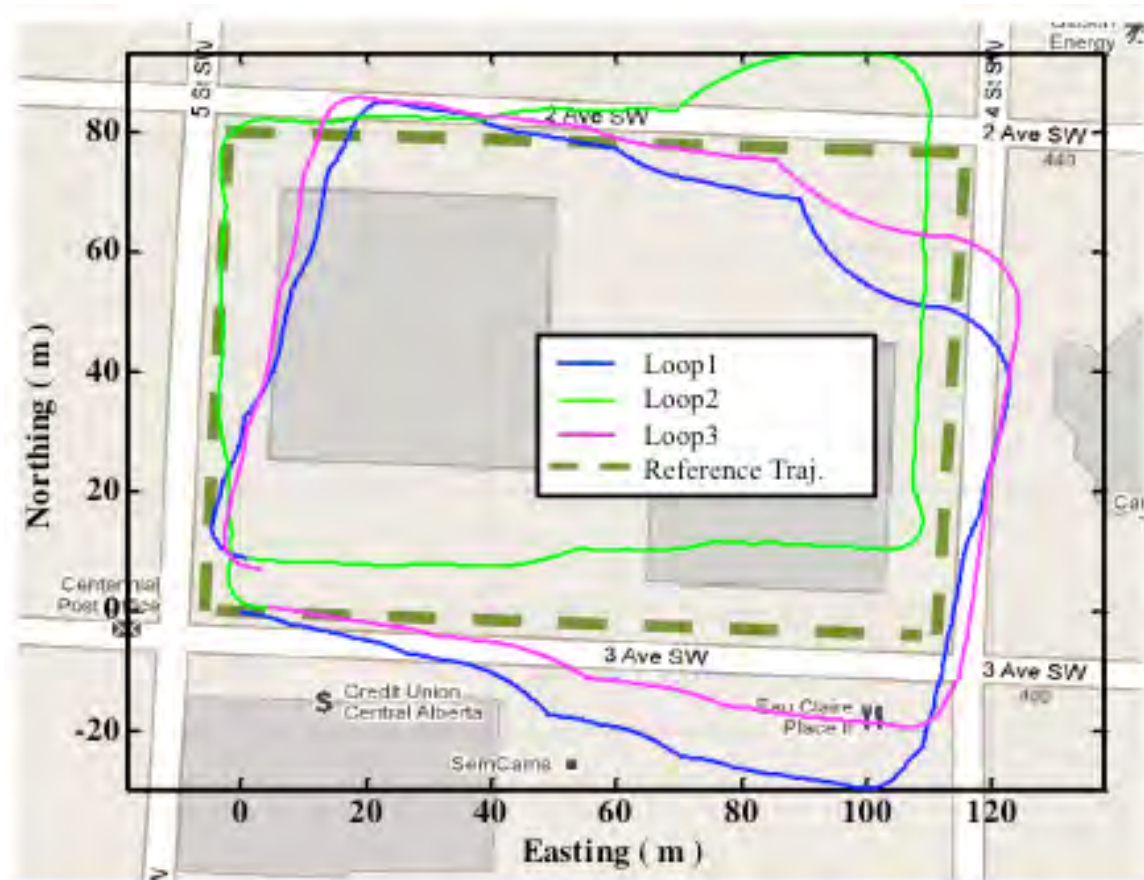


Figure 6-10: Continuous trajectory for the urban canyon using SM measurements.

6.4.2 Indoor Shopping Mall

Figure 6-11 shows the trajectory of the first loop in the shopping mall using SM measurements only. The average walking speed of the pedestrian in this case is 1.4 m/s. It can be observed that the frequency of occurrence of SM measurements (with standard

deviation of 2° or less) is far less than that of the urban canyon case and has reduced from one measurement every three metres (for urban canyon) to one measurement every 20 m. This results in less frequent heading initializations, and hence larger trajectory errors. Although the frequency of SM measurements available for the updates has reduced, it can be observed from Figure 6-11 that these measurements indeed have accuracies of the order of 2° or better (the orientation of the SM heading measurements is in agreement with the loop's orientation) suggesting proper operation of the SM based heading estimator in this environment. Figure 6-12 shows the trajectory obtained for the second loop using SM measurements for the attitude estimation with similar results. The occurrence of good SM measurements is different in this case from the first loop because of the inability of the pedestrian to walk the same paths with an accuracy of 1 m as was done for the urban canyon. The maximum errors between the estimated and nominal trajectories in both cases are of the order of 70 m while the error between starting and ending points are 17 m and 6 m, respectively.

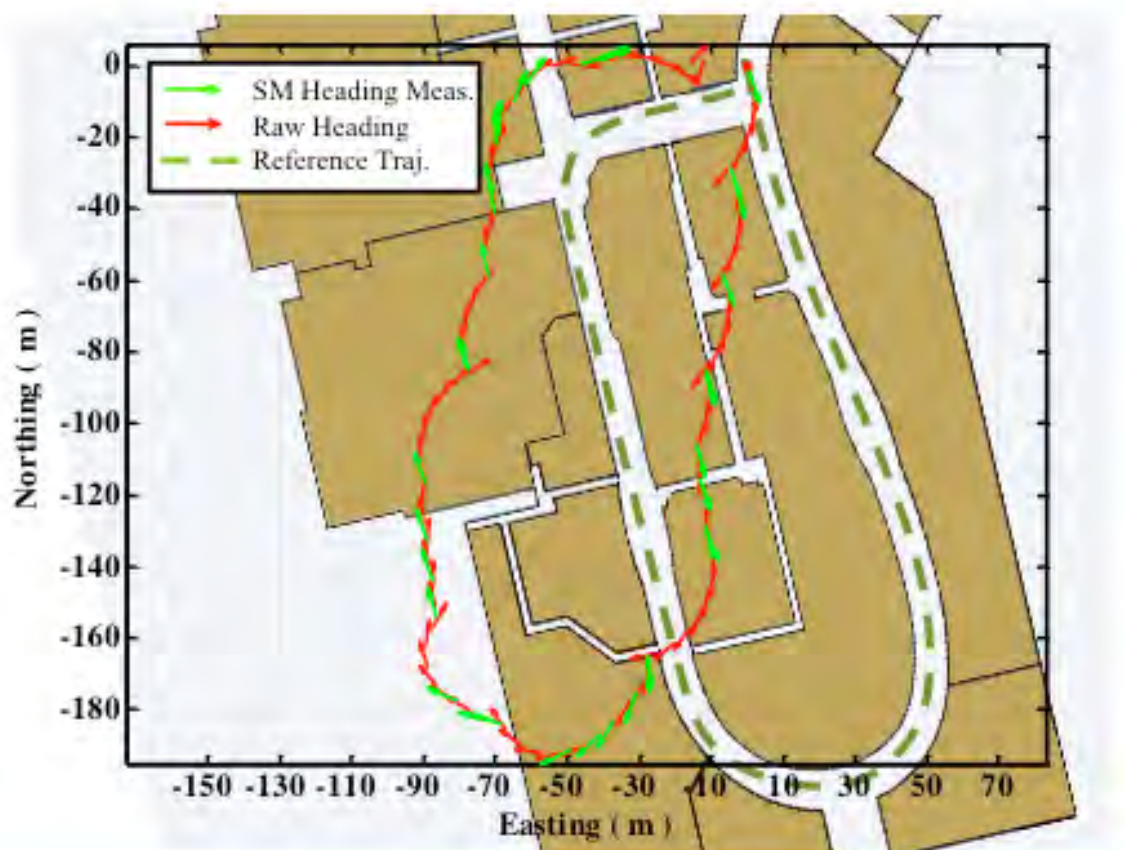


Figure 6-11: Trajectory of first loop in shopping mall.

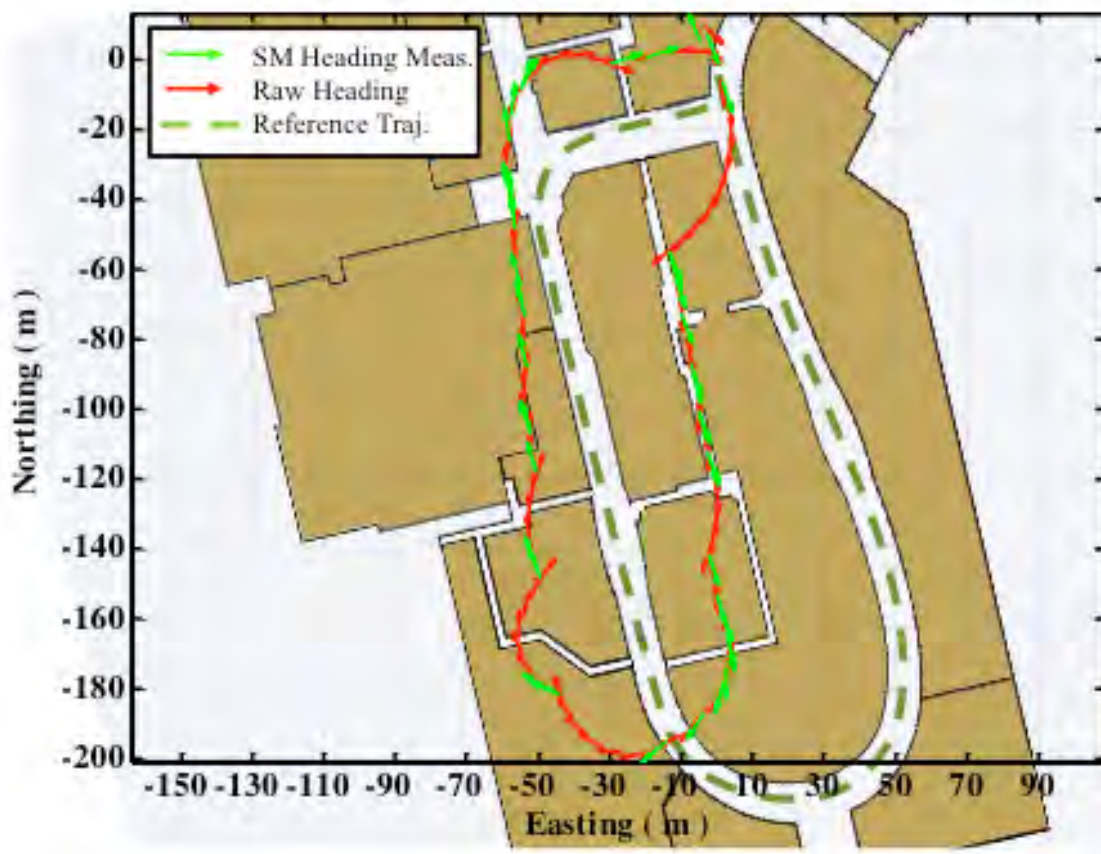


Figure 6-12: Trajectory of second loop in shopping mall.

Figure 6-13 shows the trajectories estimated using the two loops. Here the orientation as well as position are not initialized before the start of the second loop, which results in a total position error of 20 m between the starting and final ending point. Although this error seems small as compared with the total distance traveled, which is approximately 1 km, it does not convey properly the overall accuracy of the estimated trajectory, which is worse as observed in the figure. The maximum error in estimated trajectory has now increased to approximately 87 m, which shows that the SM approach is not reliable for attitude estimation in this type of indoor environment.

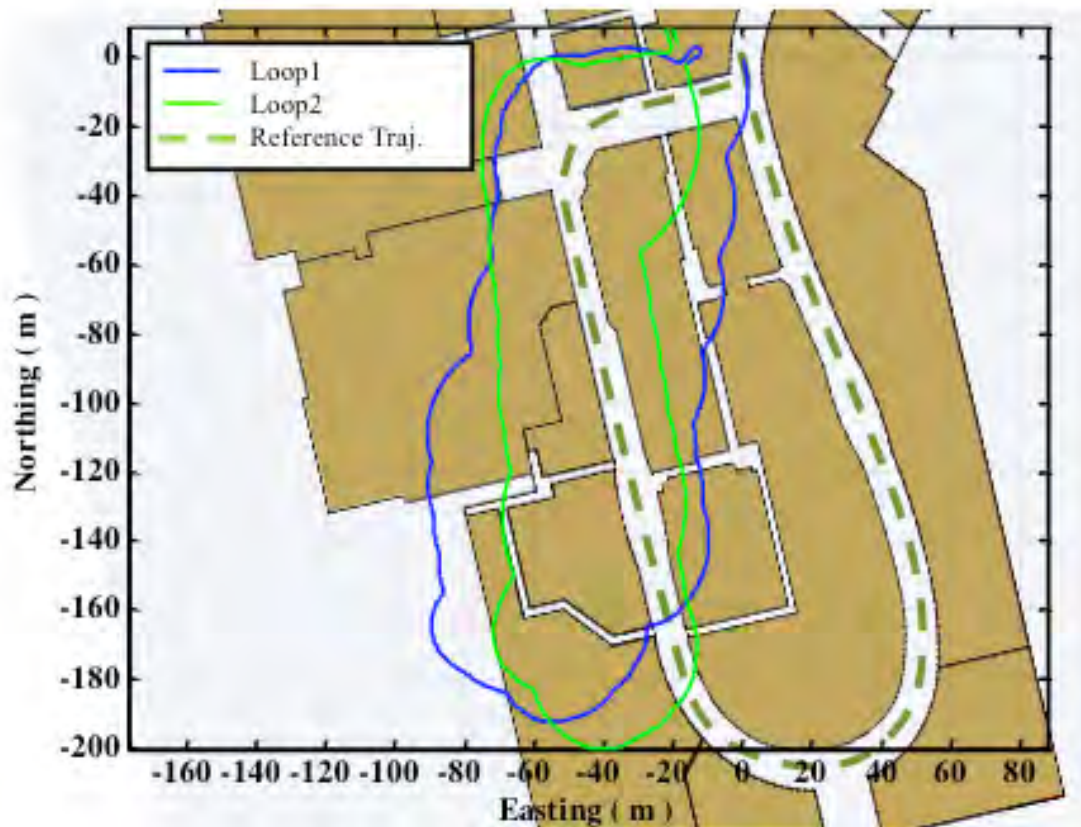


Figure 6-13: Combined trajectory for the two loops in shopping mall.

6.5 Quasi-Static Field based Attitude and Rate Gyroscope Error Estimator

The Quasi-Static Field (QSF) based measurement error model described in Section 5.9.4 can be used for estimating the errors associated with the rate gyroscopes as well as constraining the error growth of attitude estimates.

6.5.1 Urban Canyon Environment

6.5.1.1 QSF Detections

Figure 6-14 shows the total field observed in the urban canyon environment along with the QSF detections. It can be observed that the overall signatures of the total field as well

as the detection of QSF periods are very similar for temporally different paths. This is because the paths traversed were kept within 1 m of one another for assessing the repeatability of the results.

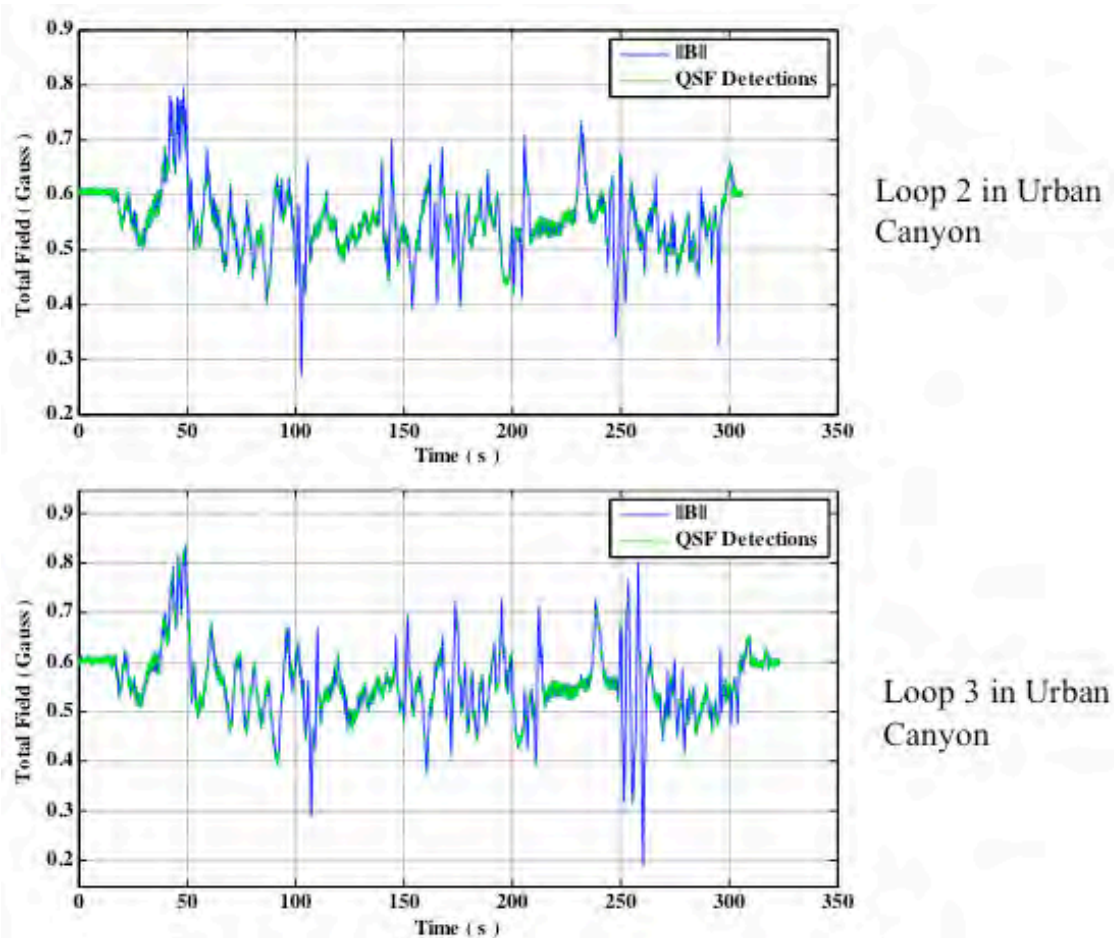


Figure 6-14: Total field and QSF detections for similar paths in urban canyon.

6.5.1.2 Trajectories Obtained using QSF measurements

Figure 6-15 portrays the trajectory obtained for the first path around the test environment in an urban canyon. It can be seen that the start and end points are very close to one another with a difference of only 1.7 m in this case. Also the trajectory estimated using the attitude estimator with QSF measurements shows a rectangular profile, which is the

pattern followed by the pedestrian here. This shows that the QSF measurements available all around the traversed path were enough for observing the errors associated with the rate gyroscopes.

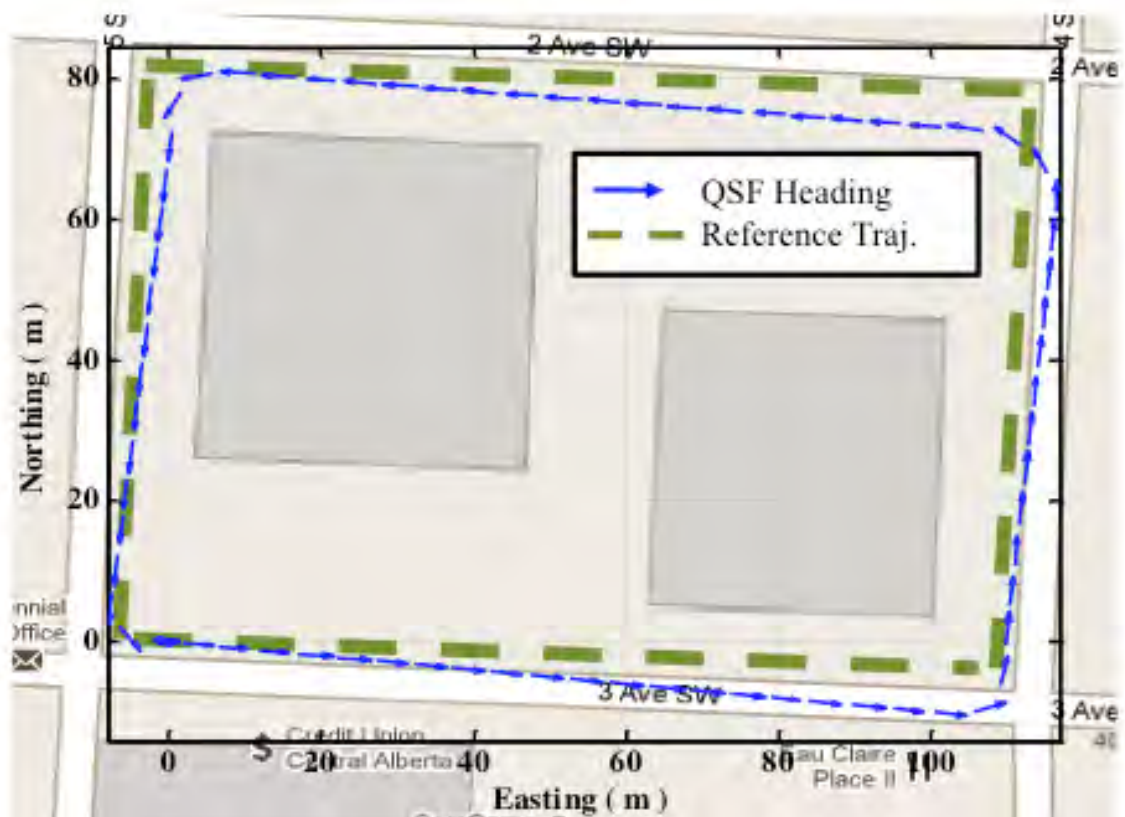


Figure 6-15: Trajectory obtained using QSF measurements in urban canyon.

Figure 6-16 shows the three trajectories obtained using QSF measurements in the urban canyon. These trajectories are obtained by initializing the starting position and orientation for each loop. The first observation is the consistency of the ending locations. These are within 2 m of one another showing the effectiveness of QSF in estimating the rate gyroscope errors. The other observation is the more random skewing of the three trajectories with respect to one another, as compared to that of the SM approach. This is

because the QSF measurements can completely observe the rate gyroscope errors, but are not capable of observing the actual attitude errors. The attitude error growth is constrained using QSF measurements as is evident from Equation (5.73). As the rate gyroscope errors are randomly varying, these cause random errors in the attitude at the beginning of each path while the gyroscope errors are being estimated, which results in a random orientation error. Once the rate gyroscope errors are completely estimated, the attitude error growth is constrained. Thus the accuracy of the estimated trajectory is improved through the use of the QSF detections. The maximum error in trajectories obtained using QSF measurements is approximately 5 m, resulting in an overall improvement of over 95% as compared with the trajectories obtained using unaided rate gyroscopes for attitude estimation.

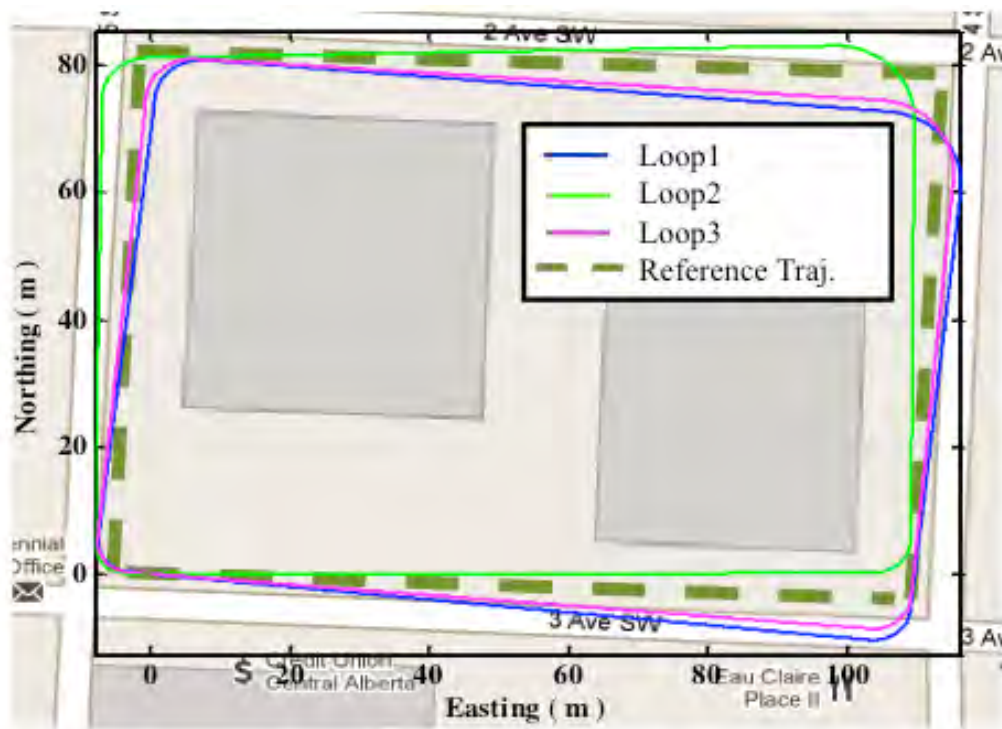


Figure 6-16: Trajectories obtained using QSF in urban canyon.

Figure 6-17 shows the trajectory obtained using the three loops in a continuous fashion. It is quite evident that Loop2 and Loop3 are very similar in this case. This is because the rate gyroscope errors have been properly estimated resulting in trajectories with a steady skew, which means that the orientation errors are now effectively constrained.

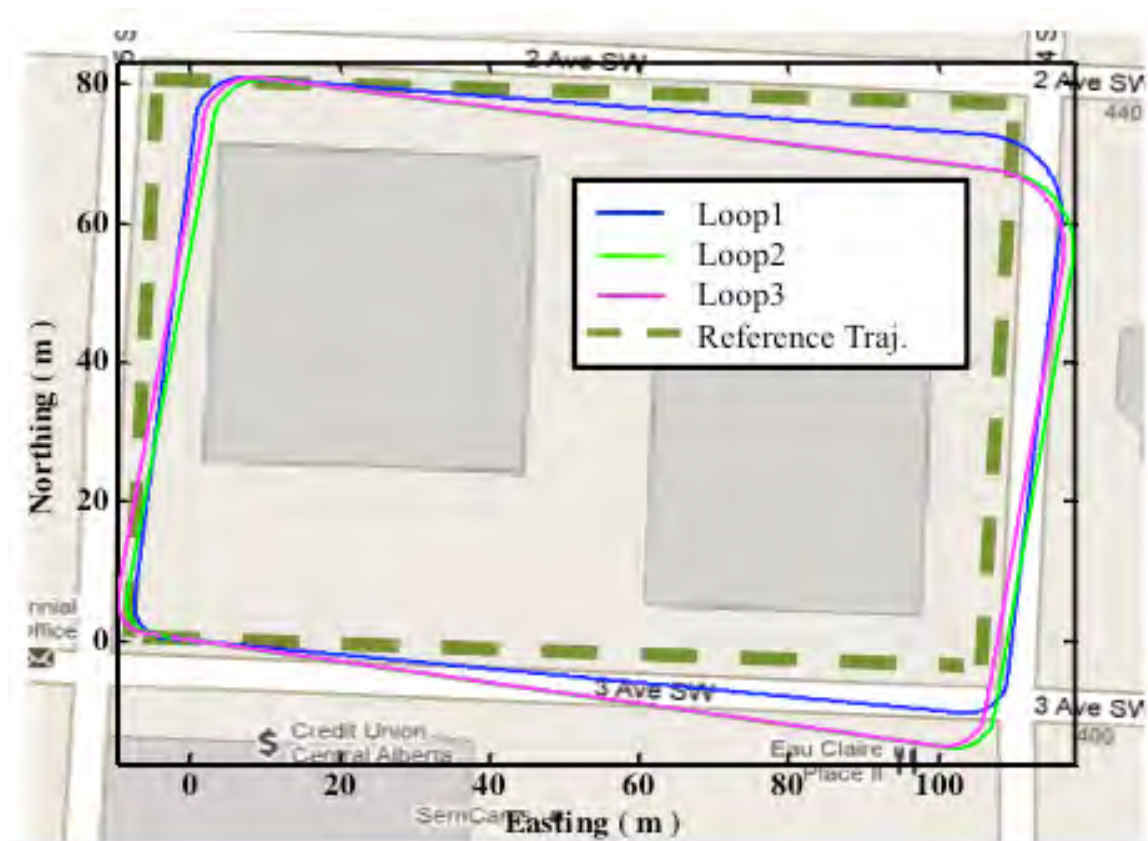


Figure 6-17: Continuous trajectory in urban canyon using QSF.

6.5.2 Indoor Shopping Mall

6.5.2.1 QSF Detections

Figure 6-18 shows the total field and QSF detector's results in the shopping mall. Comparing these with Figure 6-14, it can be observed that the duration of QSF periods is reduced. The frequency of QSF detections is still high with approximately three

detections every second. The total field profiles obtained are similar to one another, resulting from traversing similar paths. Relative to Figure 6-14, it can be observed that the perturbations measured in the mall are at least twice as strong as the ones encountered in the urban canyon. This is another reason for the SM approach to perform less efficiently in a shopping mall, as was described in Section 6.4.2.

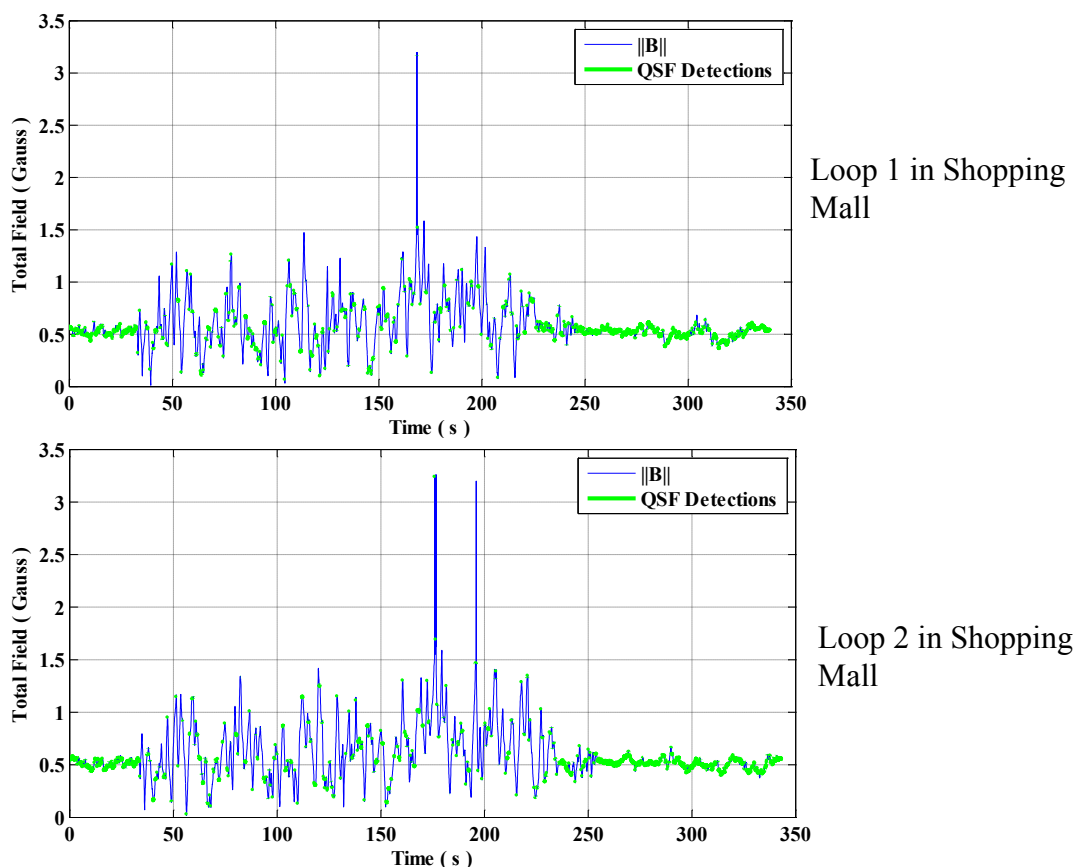


Figure 6-18: Total field and QSF detections for similar paths in shopping mall.

6.5.2.2 Trajectories Obtained using QSF measurements

Figure 6-19 shows the trajectory obtained for the first loop in shopping mall using QSF measurements. Although the overall pattern of the estimated trajectory is comparable to the nominal one, the initial errors associated with rate gyroscopes cause a large error

accumulation in estimated attitude, which cannot be compensated for using QSF measurements. The maximum error in estimated trajectory is approximately 110 m and the error between the starting and ending position is 6 m in this case.

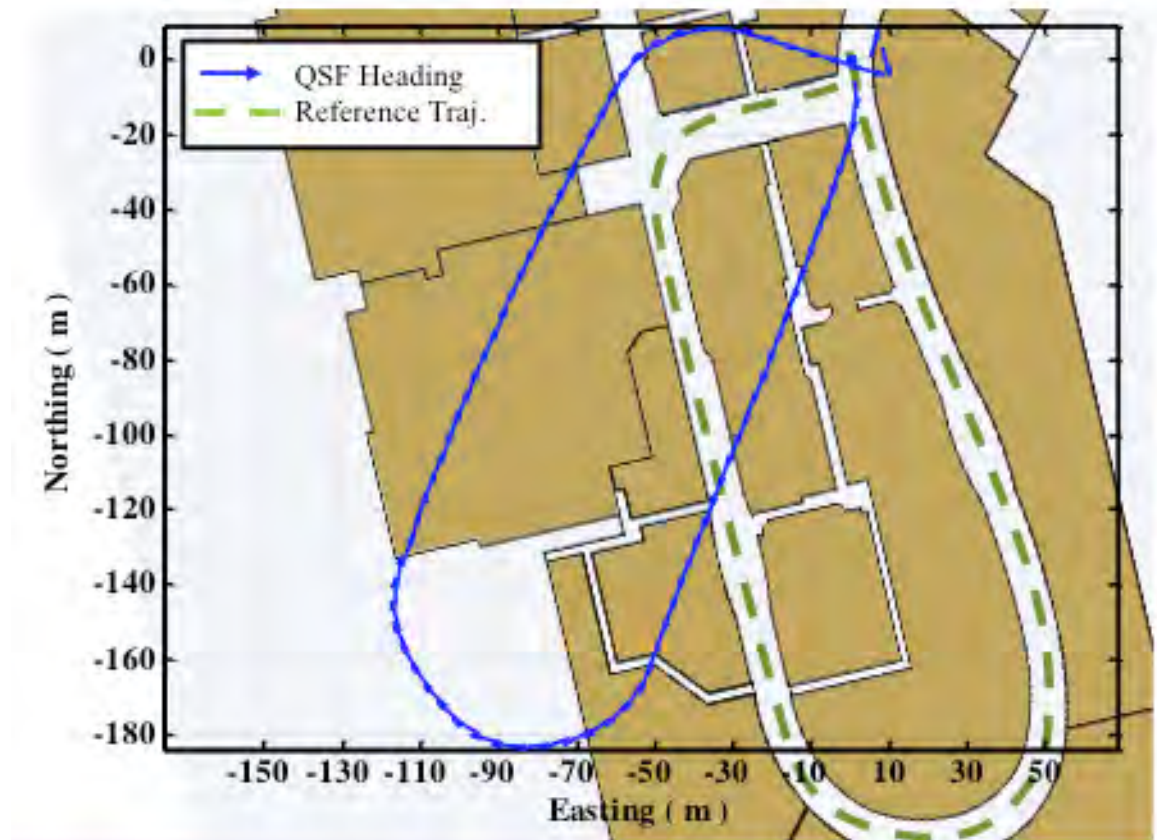


Figure 6-19: Trajectory obtained using QSF measurements in shopping mall.

Figure 6-20 shows the continuous trajectory obtained using the two loops. It can be observed that the second loop becomes further skewed due to the accumulation of attitude errors. It is worth mentioning however that the difference between the starting and ending point for the second loop is less than 1 m, which suggests proper estimation of the rate gyroscope errors.

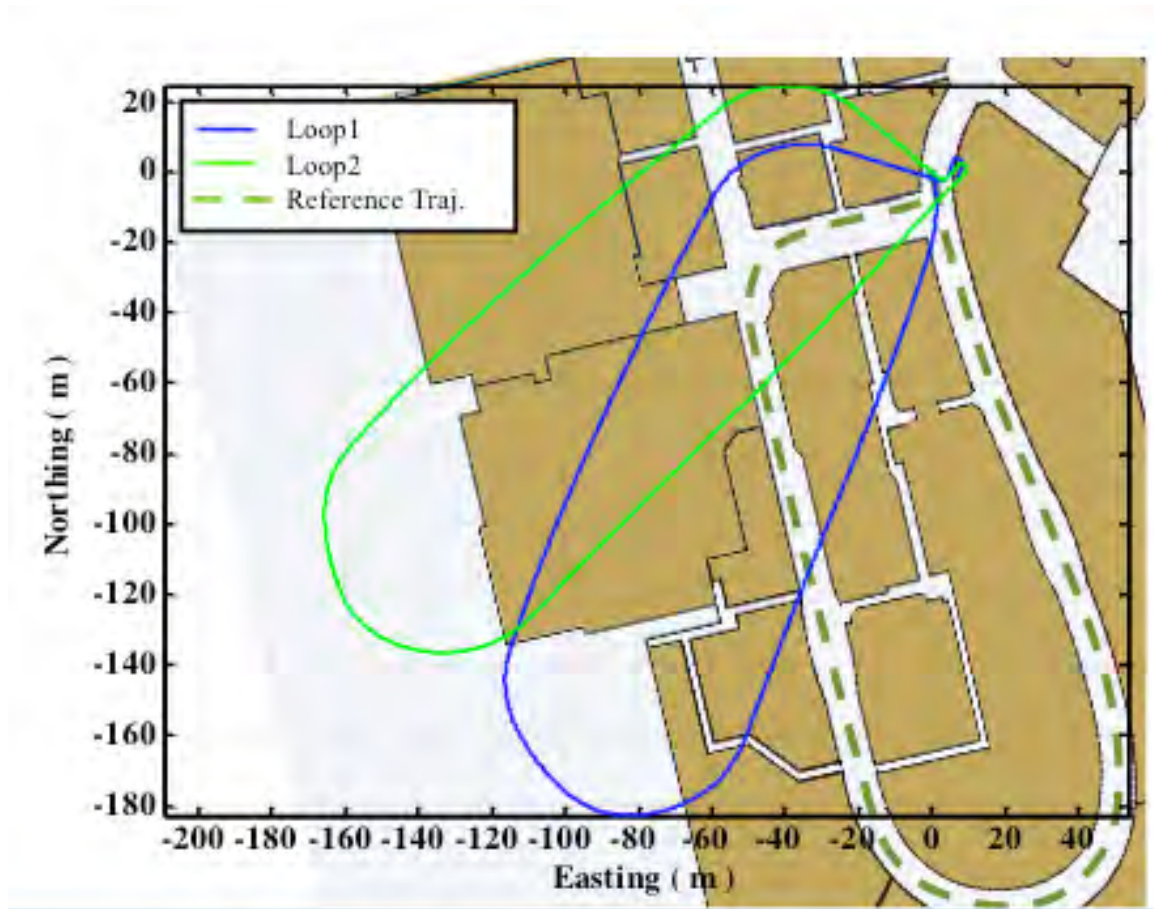


Figure 6-20: Combined trajectory obtained using QSF in shopping mall.

6.6 Combined SM and QSF based Attitude Estimator

It is quite evident from Figure 6-20 that the QSF based measurements on their own are not capable of completely observing the errors associated with attitude. On the other hand, the results obtained using SM measurements show that these are capable of providing good heading estimates. Thus by combining these two measurement error models, one can eliminate the bottleneck of QSF measurements to a great extent.

6.6.1 Urban Canyon Environment

Figure 6-21 shows the trajectories estimated for the same path followed in the urban canyon using QSF alone and QSF+SM as measurements. It can be seen that the skew in the estimated trajectories due to the attitude error observability issues of the QSF method have been rectified by using SM measurements.

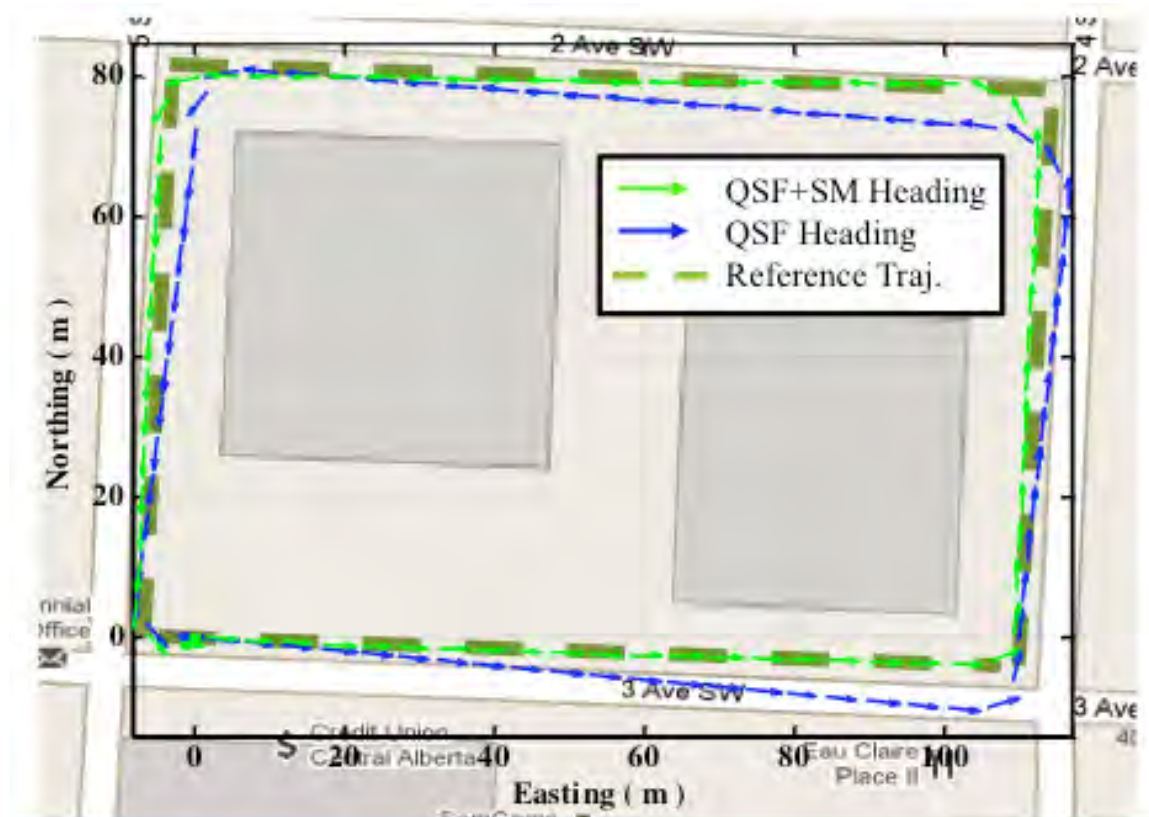


Figure 6-21: Comparison of QSF and QSF+SM measurements.

Figure 6-22 shows the continuous trajectory obtained using QSF+SM measurements in the urban canyon environment. All of the three loops are consistent in terms of orientation errors, which should be the case as the paths were traversed within 1 m of one another, resulting in similar SM measurements. Thus the repeatability criterion is successfully met by combining the QSF and SM measurement models. The difference

between the starting and ending points is approximately 5 m. It is worth mentioning that the repeatability of the three paths traversed was possible only because of the frequent availability of QSF and SM measurements in the test environment. The results show a different picture when one of the measurements is unavailable for some time as illustrated in Figure 6-23 where the SM measurements are not considered for the first 110 metres of each loop traversed. This results in the unobservability of orientation errors resulting in three skewed trajectories.

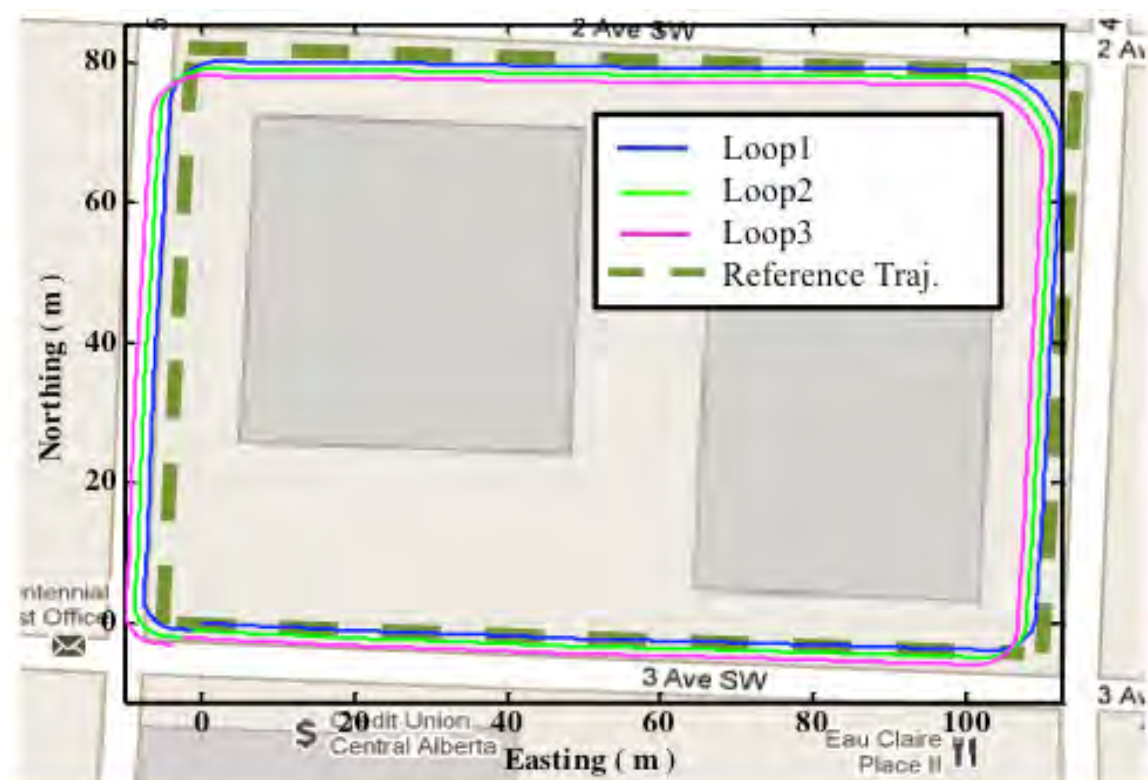


Figure 6-22: Continuous trajectory obtained using QSF+SM in urban canyon.

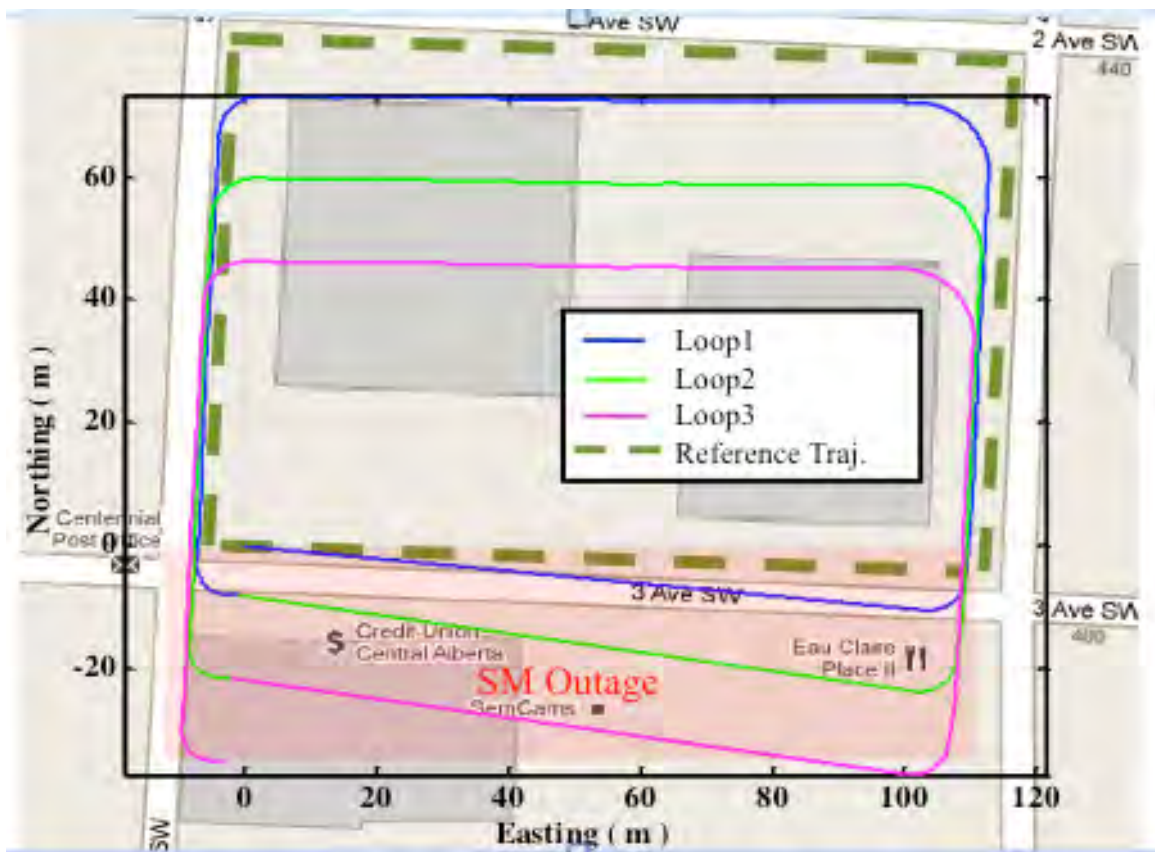


Figure 6-23: Simulated outage of SM measurements for QSF+SM in urban canyon.

6.6.2 Indoor Shopping Mall

Figure 6-24 shows the estimated trajectory in the shopping mall using QSF and SM measurements for the attitude and rate gyroscope error estimation. It is quite evident that the only orientation errors encountered were at the beginning of the path. Afterwards, with the availability of SM measurements, the errors in orientation were successfully observed and compensated for. The maximum error in the estimated trajectory with respect to the nominal one was approximately 10 m and the difference between the starting and ending point also came out to be approximately 10 m in this case.

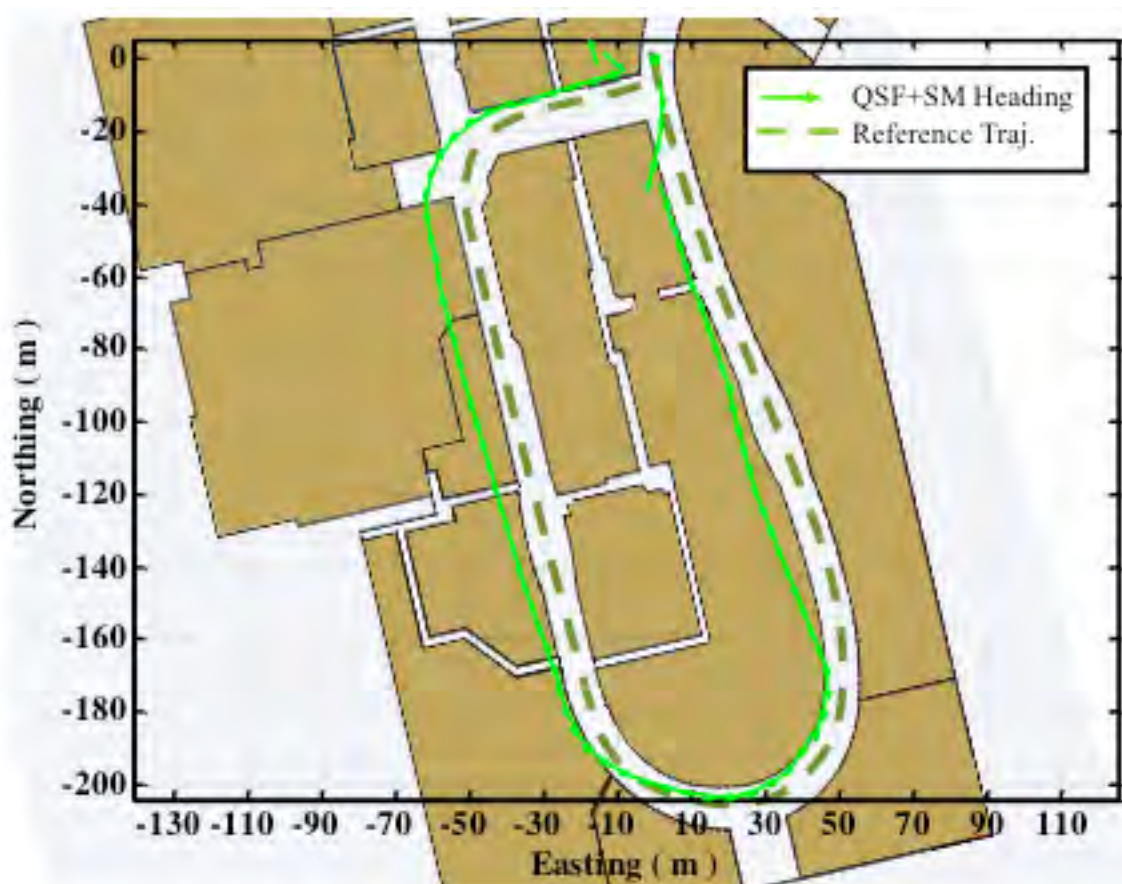


Figure 6-24: Trajectory estimated in shopping mall using QSF+SM.

Figure 6-25 shows the continuous trajectory obtained using QSF and SM measurements. It can be observed that the errors accumulated in orientation estimates are successfully compensated for using SM measurements. The difference between the loops is within 5 m, which can be caused due to slight changes in pedestrian's trajectory. Thus the repeatability criterion is met with combined QSF and SM measurements. The shift of approximately 10 m (Easting) in the estimated trajectory is caused by the accumulation of attitude errors at the beginning of Loop1. Once the rate gyroscope errors are estimated, this error is constrained and does not grow with time or distance traveled.

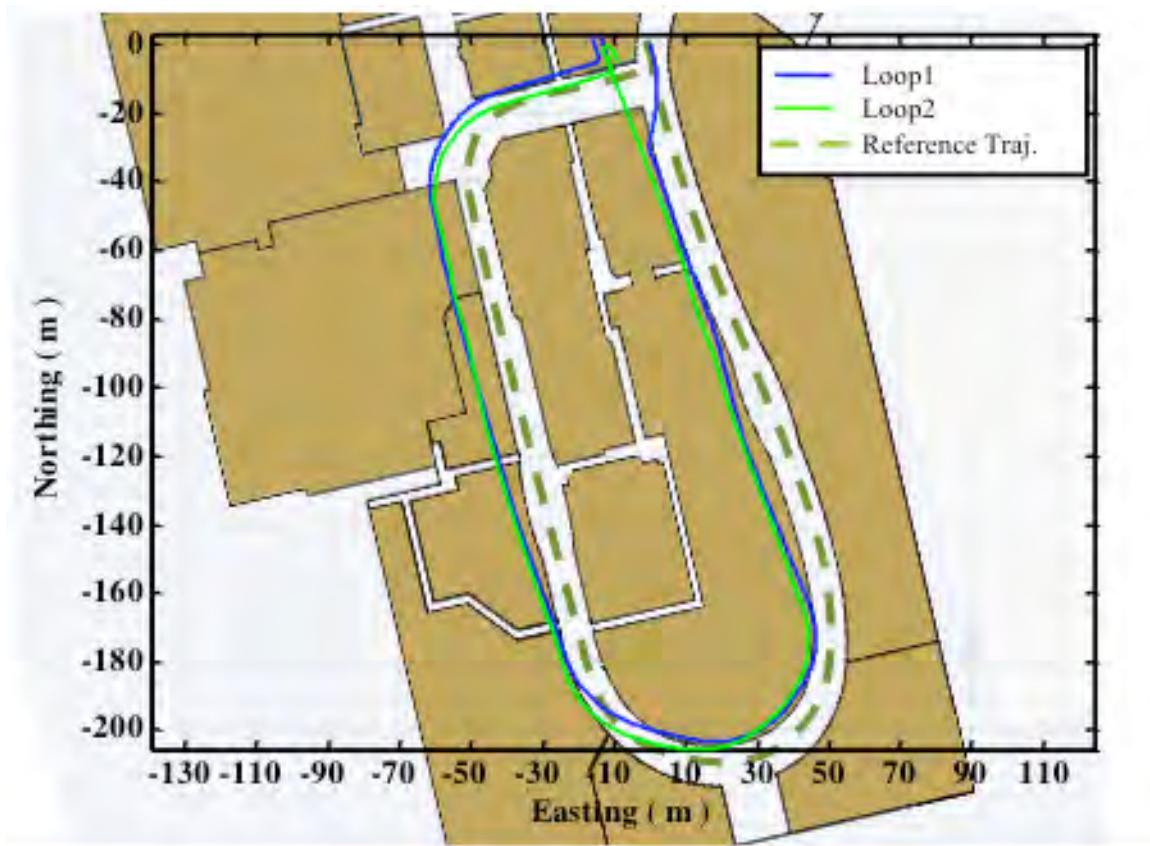


Figure 6-25: Combined trajectory estimates for the two loops using QSF+SM in Shopping Mall.

6.7 Multi-Magnetometer Platform based Magnetic Field Measurements

The Multi-Magnetometer Platform (MMP) based perturbation detection and mitigation scheme described in Section 4.4 can be used for reducing the affects of perturbations on magnetic field components, which can be utilized for attitude and rate gyroscope error estimation.

6.7.1 Urban Canyon Environment

Figure 6-26 shows the trajectory obtained using MMP measurements for estimating attitude and rate gyroscope errors. Comparing it with the trajectory obtained using SM

measurements as depicted in Figure 6-6, the maximum errors in estimated trajectory have reduced from 30 m to approximately 20 m. The main reason for this error reduction is continuous availability of the measurements from MMP, which provide error estimates for attitude and rate gyroscopes on regular basis. As the MMP approach mitigates the affects of perturbation on local magnetic field, the final outcome depends solely on how well the mitigation process performed. The perturbation mitigation technique used with MMP estimator as described in Section 4.4 depends on the observability of perturbation sources as well as the magnetic field information available from the previous epochs. Any errors present in the estimation of magnetic field for previous epochs will impact the present estimates. Thus initialization of the MMP estimator in a clean environment is necessary.

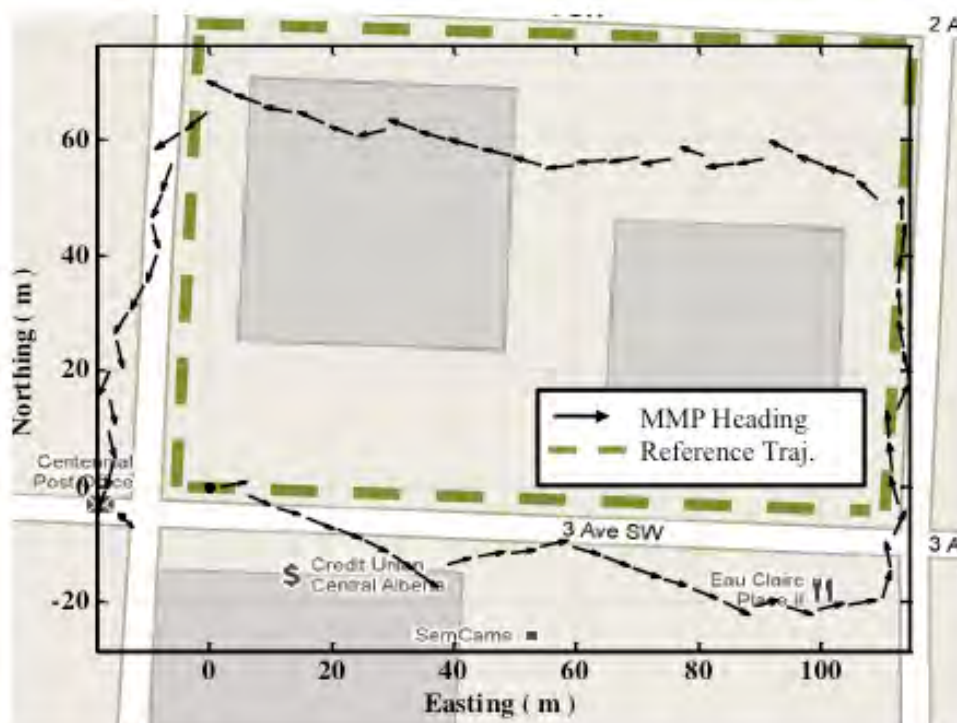


Figure 6-26: Trajectory obtained in urban canyon using MMP measurements.

Figure 6-27 shows the individual trajectories obtained in urban canyon using MMP measurements. Random errors in the estimated trajectories are observed here, which are caused due to inadequate estimation of attitude and rate gyroscope errors. Thus the repeatability criteria cannot be met using MMP alone. Figure 6-28 shows the continuous trajectory obtained in this environment. The errors in estimated position keep accumulating, resulting in a difference of approximately 50 m between starting and ending points.

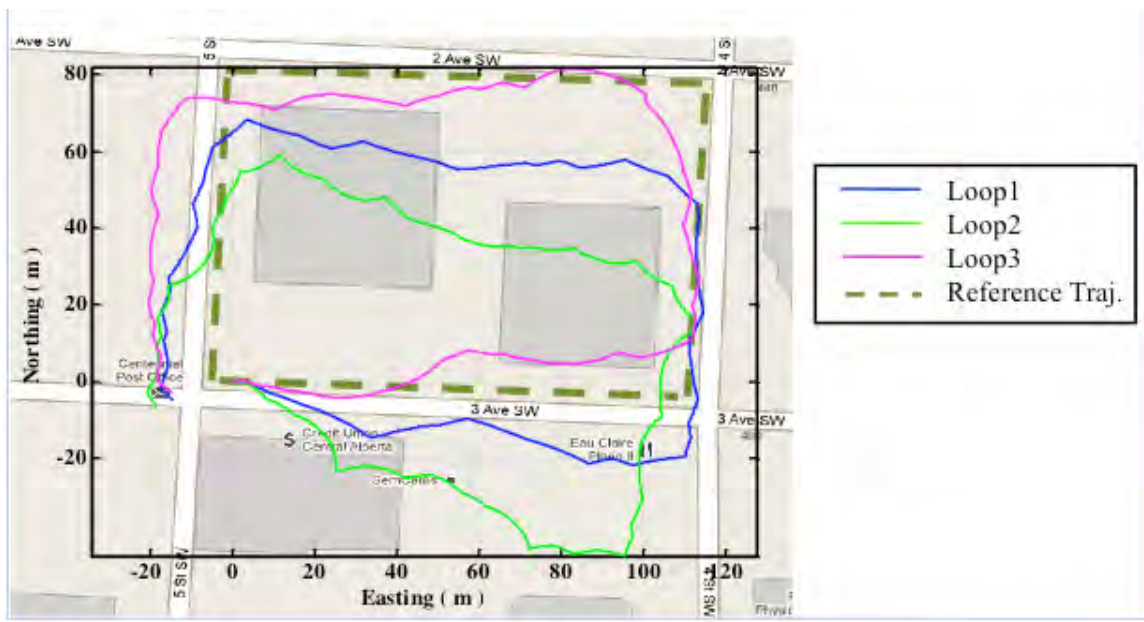


Figure 6-27: Individual trajectories obtained in urban canyon using MMP.

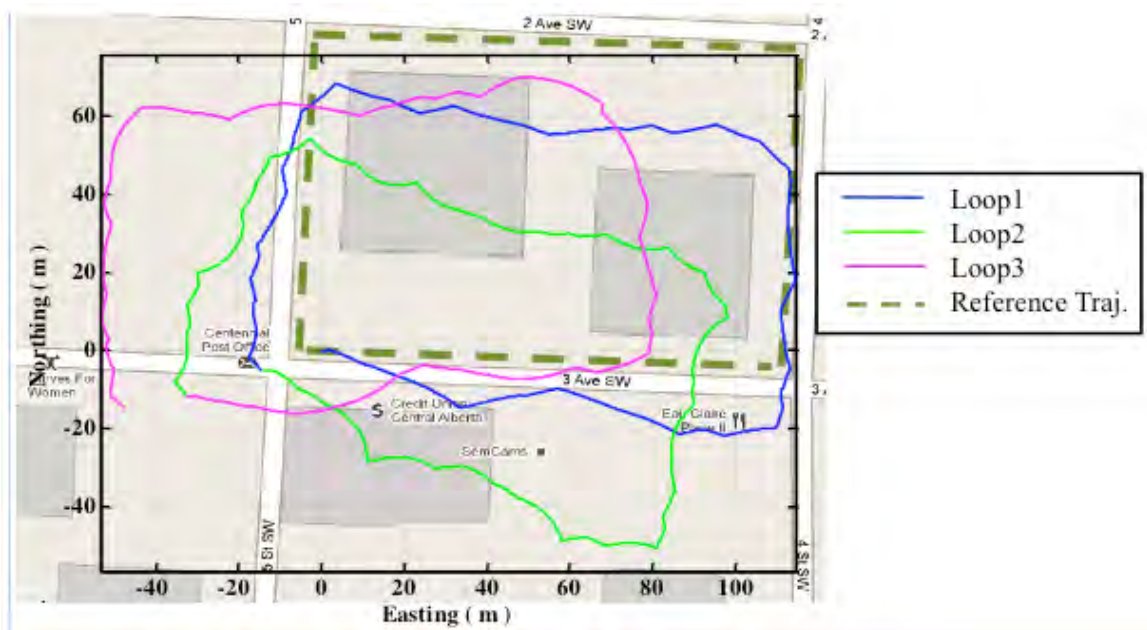


Figure 6-28: Continuous trajectory obtained using MMP in urban canyon.

6.7.2 Indoor Shopping Mall

Figure 6-29 shows the estimated trajectory in shopping mall using MMP measurements. Similar to the urban canyon results, the MMP measurements alone are not able to completely observe the attitude and rate gyroscope errors resulting in a maximum trajectory error of approximately 30 m.

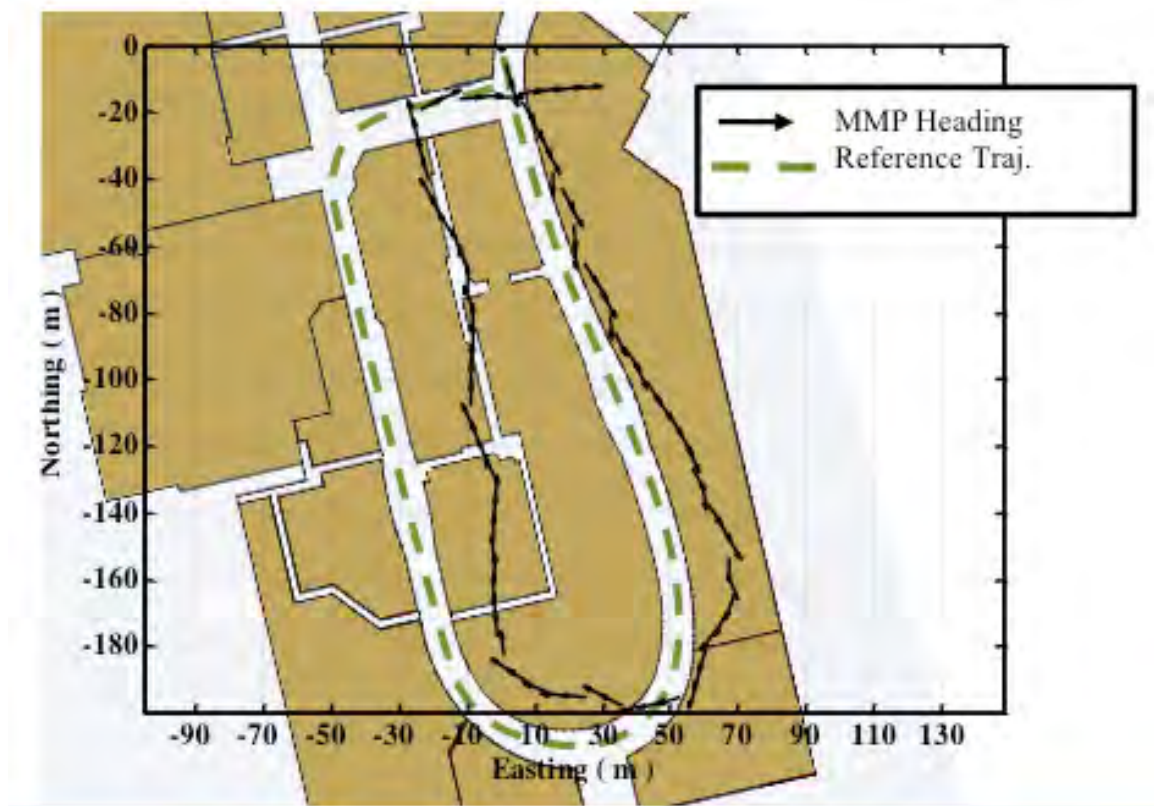


Figure 6-29: Trajectory obtained using MMP measurements in shopping mall.

Figure 6-30 shows the individual trajectories obtained from the two loops traversed with the repeatability criteria not met. The maximum trajectory error of approximately 30 m is obtained for continuous trajectory estimation, which results in a difference of approximately 20 m between starting and ending points as shown in Figure 6-31.

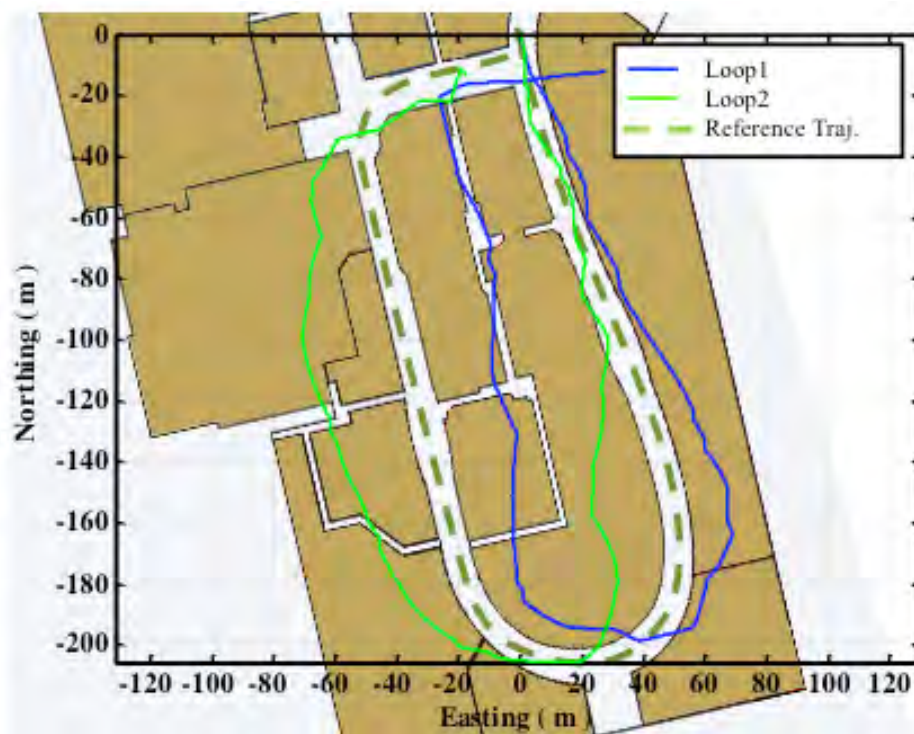


Figure 6-30: Individual trajectories obtained in shopping mall using MMP.

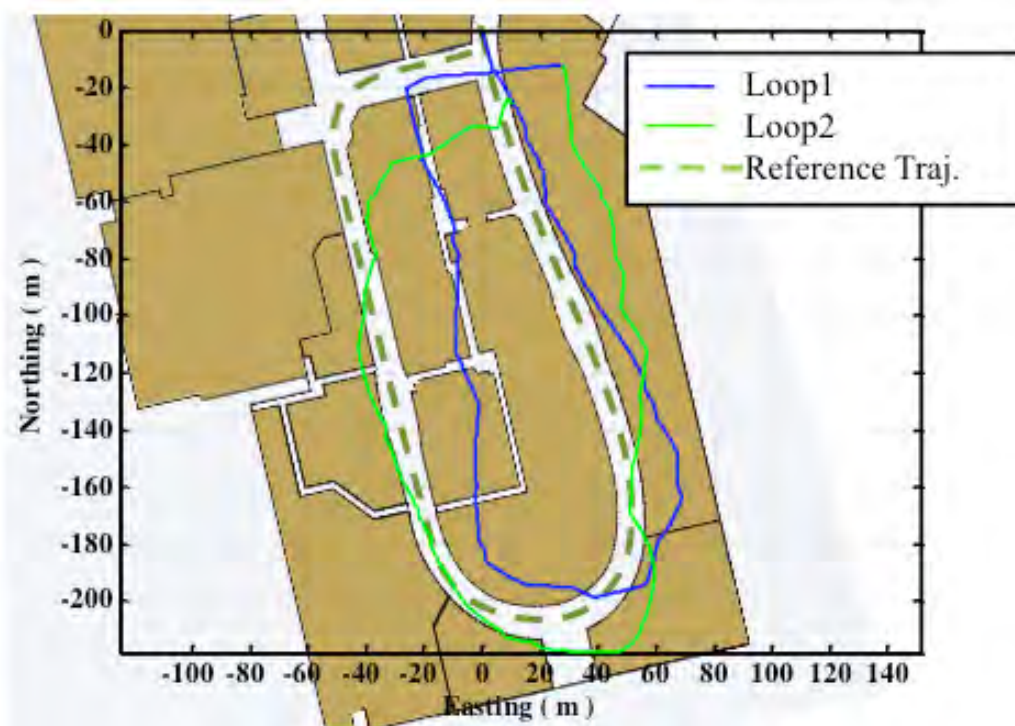


Figure 6-31: Continuous trajectory obtained in shopping mall using MMP.

6.8 Combined MMP and QSF Based Attitude Estimator

Another possible combination of measurement models is between QSF and MMP. As is described earlier in Section 6.5, QSF measurement model lacks the observability of actual attitude errors. The output of MMP based estimator is the local magnetic field vector with reduced impact of perturbations. Combining the two measurement models should solve the observability issues of QSF based estimator. But the final outcome depends on how accurate are the measurements obtained using MMP because any errors in the estimated magnetic field components will result in inaccurate estimation of the attitude errors. Figure 6-32 shows the trajectory obtained by combining the QSF and MMP measurement models. Comparing it with the trajectory obtained using MMP alone as depicted in Figure 6-29, it can be observed that the errors in estimated trajectory have slightly reduced but still are of the order of 25 m. Thus in order to substantially reduce the trajectory errors, the QSF measurement model needs to be aided by a fairly good orientation estimates as was achieved in QSF+SM approach. Similar performance of QSF+MMP is obtained in the urban canyon test environment.

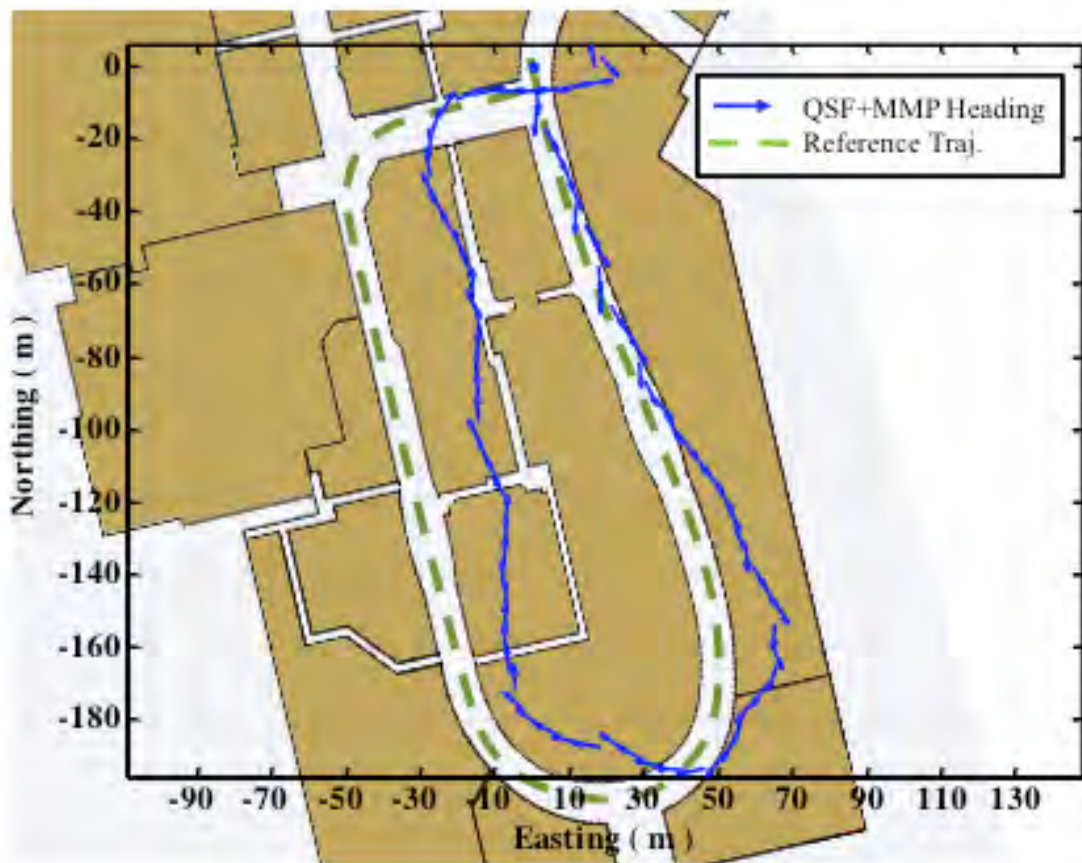


Figure 6-32: Trajectory obtained using QSF+MMP in shopping mall.

6.9 Performance of Attitude Estimator in Different Environments

Figure 6-33 summarises the performance of attitude estimations in a urban canyon using different measurement models for attitude and rate gyroscope error estimation. The best performance achieved is by the combined measurement model of SM and QSF, resulting in a maximum trajectory error of 6 m after traveling a distance of approximately 1 km. The errors with SM measurements alone are steady at 30 m. This is because the loops traversed were kept similar spatially. The QSF only approach comes to a steady state after the first loop as the gyroscope errors have been completely estimated by then. MMP

alone is the worst measurement for attitude and rate gyroscope error estimation in this environment with position errors reaching 50 m.

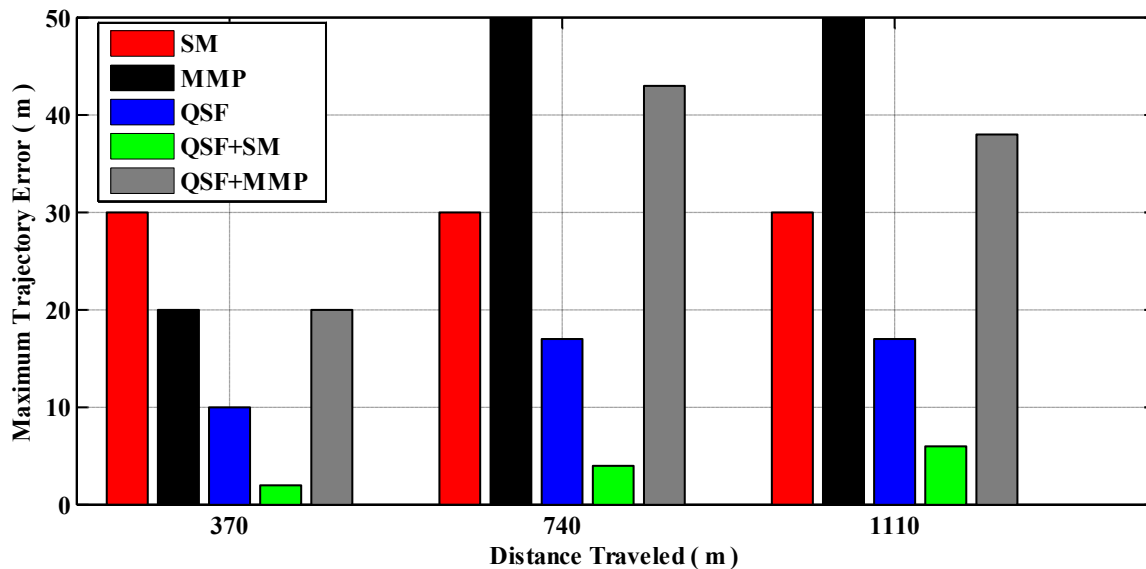


Figure 6-33: Attitude estimation performance in urban canyon.

Figure 6-34 gives an overview of the performance of attitude estimation in a shopping mall using different measurements for attitude and rate gyroscope error estimation. In this case, the best performance achieved is also by the combined measurement model of SM and QSF, resulting in an error of 12 m after traveling a distance of approximately 1 km. The errors with SM measurements alone are lower, as compared with the QSF only approach. This is because the QSF measurements, although able to observe the errors associated with the rate gyroscopes, took a longer time to converge to a solution due to very strong and varying perturbation sources. Contrary to urban canyon, the MMP measurements are providing better estimates of attitude and rate gyroscope errors, constraining the position errors to 30 m for this environment.

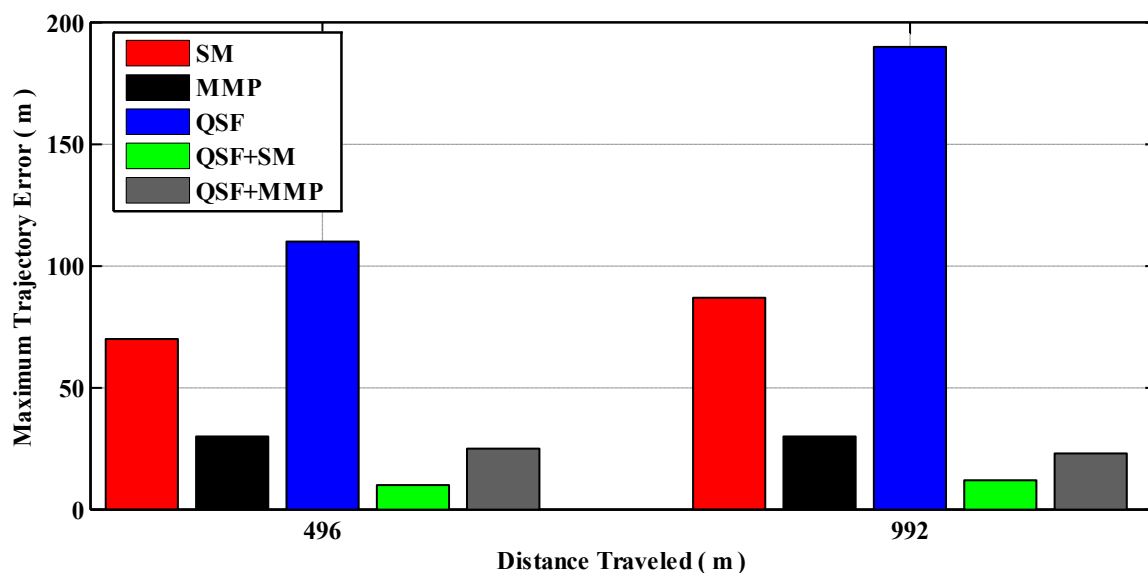


Figure 6-34: Attitude estimation performance in shopping mall.

The results obtained in both environments suggest that the impact of attitude estimates on position error budget for pedestrian navigation can be reduced by 80% in urban canyons and 86% in commercial indoor environments using the novel combined QSF and SM combined measurement models developed in this thesis.

Chapter Seven: **Conclusions and Recommendations**

This thesis investigated the use of handheld devices equipped with low cost consumer grade sensors for pedestrian navigation. As the attitude/orientation errors play a major role in the overall navigation error budget, the research focused on improving the attitude estimates in environments where GPS is denied. For this purpose, the use of the Earth's magnetic field as a measurement source for estimating the errors associated with low cost inertial sensors was investigated. This final chapter presents conclusions emerging from these investigations. Recommendations for future work based on the use of this research for the development of a complete pedestrian navigation system are made.

7.1 Conclusions

Given the theoretical research and test results presented in the previous chapters, the following conclusions arise:

1. While investigating the use of Earth's magnetic field for estimating rate gyroscope errors in pedestrian navigation environments thus providing a seamless attitude/orientation estimation, it was found that magnetic field measurements are severely degraded due to presence of perturbations caused by man-made infrastructure. The literature review suggested that the Earth's magnetic field is rather useless for gyroscope error estimation indoor.
2. A detailed theoretical background was found necessary to model the affects of perturbations on the Earth's magnetic field if one requires its effective use as measurement input in all pedestrian navigation environments. For this purpose,

detailed mathematical models of magnetic fields in general and the effects of perturbation sources on the Earth's magnetic field in particular were developed. This model can be used for simulating multiple perturbation sources, thus representing indoor environments.

3. The portable platform developed for hosting all of the sensors/sub-systems necessary for pedestrian navigation as well as data logging and online processing was found to be effective to collect the data necessary to support the theoretical developments presented in the thesis. As such a platform was not available off-the-shelf, a custom hardware platform was designed and developed by the author, which not only met the requirements set forth by this research, but also hosted the sensors necessary for implementing a complete pedestrian navigation system in the future. All of the sensors selected for this platform are similar grades as those found in today's smart-phones.
4. In view of the fact that the sensors selected for this research were of consumer grade, the calibration of these sensors for their deterministic errors and stochastic modeling of the time varying errors was found necessary. Rate gyroscopes and accelerometers were calibrated using six position tests and rate tests, which are commonly used for lab calibration. Most of the work done for calibrating the magnetic field sensors was found inappropriate for this research as assumptions were made by other researchers to simplify the error models associated with them. Hence the complete calibration technique developed herein that took into account detailed error modelling performed better than the calibration techniques discussed in the literature.

5. Characterization of the magnetic field perturbations found in various pedestrian navigation environments through a detailed survey was found effective to provide a detailed insight into the strength, occurrence as well as the distribution of perturbations and became the foundation for investigating different perturbation detection and mitigation schemes.
6. Using the mathematical model developed for magnetic field perturbations and the actual survey of these perturbations in pedestrian navigation environments, the detection scheme developed utilizing multiple magnetometers was found effective to detect and mitigate perturbations by estimating local magnetic field components and providing perturbation free measurements for gyroscope error estimation. A Multiple-Magnetometer Platform (MMP) was also developed to experimentally assess this detection scheme.
7. Given that most portable devices such as smart-phones are equipped with only one magnetometer triad, investigations into the detection and mitigation of perturbations using a Single Magnetometer (SM) were found necessary. A heading estimator was developed that utilized the information regarding total field, inclination angle, horizontal and vertical field components to assess the quality of the estimated heading.
8. The novel method developed to utilize the perturbed magnetic field for gyroscope error estimation proved to deliver a high level of performance. This method detected the Quasi-Static Field (QSF) periods during pedestrian's motion and related the changes in the magnetic field components during these periods with

the angular rates of the sensor block, thus providing measurements for directly assessing the errors associated with the rate gyroscopes.

9. Development of an Extended Kalman Filter (EKF) for modeling the attitude and gyroscope errors as well as relating these to the magnetic field measurements individually and collaboratively gave an insight into the interdependence of different parameters, which proved beneficial in identifying the limitations of each model.
10. Selection of an urban canyon (disturbed field outdoor) and a shopping mall (disturbed field indoor) for the experimental assessments provided contrasting data sets for a realistic and detailed analysis of the proposed algorithms. Analysing the results in the position domain with the sensor platform carried in a hand gave direct insight into the impact of the attitude estimator on the position error budget. A high accuracy wheel encoder made it possible to isolate the attitude errors from the position ones.
11. The use of SM measurements for identifying good orientation estimates using magnetic field alone in both environments proved feasible. The limitation of these measurements to completely observe the gyroscope errors caused random drifts in the estimated position resulting in errors up to 30 m outdoor and 50 m indoor in the environments tested. The availability of less frequent SM measurements indoor led to the conclusion of their dependence on environmental conditions.
12. The use of unaided QSF measurements to successfully estimate the gyroscope errors in both test environments resulted in constant orientation errors, proving this scheme to be unable to observe the attitude errors completely as was

identified by the mathematical model. This resulted in position errors reaching 17 m outdoor and 190 m indoor. Infrequent indoor QSF periods due to fluctuations in the magnetic field resulted in longer convergence time for gyroscope error estimation, leading to large position errors.

13. The ability of MMP measurements to observe both attitude as well as gyroscope errors constrained the position errors to 50 m outdoor and 30 m indoor. Failure to completely detect and mitigate the perturbations resulted in large attitude and gyroscope errors, which could not be resolved until a magnetically clean environment was encountered.
14. Benefitting from the complementary nature of QSF and SM, the combined QSF+SM measurement model gave the best performance and reduced the errors to 6 m outdoor and 12 m indoor for a traveled distance of approximately 1 km. However, the combined QSF+MMP model suffered from the cons of MMP measurements and did not perform to initial expectations, resulting in errors of 38 m outdoor and 23 m indoor for the same spanned distance.
15. The combined QSF+SM approach was found to be capable of reducing the position error budget for pedestrian navigation by 80% and 86%, respectively, in the urban canyons and commercial indoor environments tested.

7.2 Recommendations

Following the conclusions made above, these recommendations are in order:

1. The MMP based perturbation detection and estimation scheme did not perform as expected. Its performance may be improved by modifying the detection stage and

incorporating QSF rectified gyroscope measurements. Theoretically, this would lead to the detection of perturbations causing the local magnetic field to change its orientation only, thus improving its robustness.

2. The use of accelerometers and pressure sensors for estimating pedestrian's position as well as speed is necessary to completely assess the impact of this research in real world navigation scenarios. Both of these sensors are already incorporated in the MSP developed for this research and will form the basis for the above suggested research.
3. Research into the resolution of the ambiguity between sensor and body frames, which was constrained to be zero for the experiments, is needed. This can be achieved by using the accelerometers, but requires detailed modeling of the pedestrian's walk related to arm swing or hip joint motion.
4. The algorithms proposed herein are assessed for normal walking speeds on level ground. Proper assessment of these algorithms during running, walking on stairs and moving in and out of a vehicle is necessary for a complete investigation of pedestrian navigation. Such motions will have an adverse affect on QSF as its duration will be reduced, hence providing less frequent measurements.
5. The algorithms developed herein are self-contained and assumed a fully denied GNSS environment. However, GNSS is partly available in urban canyons and in numerous indoor environments. Hence research into the integration of the two approaches to maximize availability and accuracy is in order.

References

- Afzal, M. H., V. Renaudin, and G. Lachapelle (2010) "Assessment of Indoor Magnetic Field Anomalies using Multiple Magnetometers," in *ION GNSS10*, 21-24 Sep, Portland, Oregon, pp. 9, The Institute of Navigation
- Aggarwal, P., Z. Syed, X. Niu, and N. El-Sheimy (2006) "Cost-effective Testing and Calibration of Low Cost MEMS Sensors for Integrated Positioning," in *Navigation and Mapping Systems XXIII International FIG Congress*, October 8-13, Munich, Germany, pp. 11
- Aggarwal, P., Z. Syed, X. Niu, and N. El-Sheimy (2007) "Thermal Calibration of Low Cost MEMS Sensors for Integrated Positioning Navigation Systems," in *The Institute of Navigation National Technical Meeting*, January 22-24, San Diego, California, pp. 11, ION
- AKM (2010) *Electronic Compass using Hall Effect Sensors*, http://www.akemd-eu.com/smart_sensor_system/e_compass/index.html, last accessed 26 April, 2010
- Allan, D. W. (1987) "Time and Frequency (Time-Domain) Characterization, Estimation, and Prediction of Precision Clocks and Oscillators," in *IEEE Transactions on Ultrasonics, Ferroelectronics, and Frequency Control*, pp., pp. 647-654, IEEE
- Alonso, J. M., M. Ocana, M. A. Sotelo, L. M. Bergasa, and L. Magdalena. (2009) "WiFi Localization System Using Fuzzy Rule-Based Classification," in *Computer Aided Systems Theory - Eurocast 2009*, MorenoDiaz, R., F. Pichler, and A. QuesadaArencibia, eds., Springer-Verlag Berlin, Berlin, pp. 383-390
- Analog, D. (2010) *Tri-axis accelerometer*, http://www.analog.com/static/imported-files/data_sheets/ADXL335.pdf, last accessed August, 2010
- Bachmann, E. R., X. P. Yun, and R. B. McGhee (2003) "Sourceless Tracking of Human Posture using Small Inertial/ Magnetic Sensors," *2003 IEEE International Symposium on Computational Intelligence in Robotics and Automation, Vols 1-3, Proceedings*, pp. 822-829
- Bachmann, E. R., X. P. Yun, C. W. Peterson, and Ieee. (2004) "An Investigation of the Effects of Magnetic Variations on Inertial/ Magnetic Orientation Sensors," in *2004 IEEE International Conference on Robotics and Automation, Vols 1- 5, Proceedings*, IEEE, New York, pp. 1115-1122
- Bak, T. (1999) *Spacecraft Attitude Determination- a Magnetometer Approach*, Department of Control Engineering, Aalborg University, Aalborg

- Bekir, E. (2007) *Introduction to Modern Navigation Systems*, World Scientific, Hackensack, N.J.,
- Bosch-Sensortec (2008) *BMA150 Digital, Tri-axial Acceleration Sensor*, <http://www.bosch-sensortec.com/content/language4/downloads/BST-BMA150-DS000-06.pdf>, last accessed 22 May, 2011
- Bowditch, N. (1977) *American Practical Navigator : An Epitome of Navigation*, 1977 Ed., Defense Mapping Agency Hydrographic Center, Washington,
- Britting, K. R. (1971) *Inertial Navigation Systems Analysis*, Wiley-Interscience, New York,
- Brown, R. G., and P. Y. C. Hwang (1997) *Introduction to Random Signals and Applied Kalman Filtering*, 3rd Ed., John Wiley & Sons, New York, Chichester, Brisbane, Toronto, Singapore, Weinheim,
- Campbell, W. H. (2001) *Earth Magnetism : A Guided Tour Through Magnetic Fields*, Harcourt/Academic Press, San Diego,
- Caruso, M. J. (1997) "Application of Magneto Resistive Sensors in Navigation Systems," in *SAE Transaction*, , pp. 1092-1098
- Caruso, M. J., and C. H. Smith (2007) *A New Perspective on Magnetic Field Sensing*, www.ssec.honeywell.com/magnetic/datasheets/new_pers.pdf, last accessed April, 2010
- Cheng, C., and J. W. Van Ness (1999) *Statistical Regression With Measurement Error*, Kendall's Library of Statistics 6, London,
- Cheung, S. Y., S. Coleri, B. Dunder, S. Ganesh, C. W. Tan, P. Varaiya, and Trb. (2005) "Traffic Measurement and Vehicle Classification with Single Magnetic Sensor," in *Data Initiatives*, Transportation Research Board Natl Research Council, Washington, pp. 173-181
- Cohen, C. E. (1992) *Attitude Determination using GPS*, Dept. of Aeronautics and Astronautics, Stanford University, Stanford, CA
- Davidson, P., M. A. Vazquez, and R. Piche (2009) "Uninterrupted Portable Car Navigation System Using GPS, Map and Inertial Sensors Data," *ISCE: 2009 IEEE 13th International Symposium on Consumer Electronics, Vols 1 and 2*, pp. 189-193
- Diaz-Michelena, M. (2009) "Small Magnetic Sensors for Space Applications," *Sensors*, vol 9, no 4, Apr, pp. 2271-2288

- Farrell, J. (2008) *Aided Navigation : GPS with High Rate Sensors*, McGraw-Hill, New York,
- Farrell, J., and M. Barth (1999) *The Global Positioning System and Inertial Navigation*, McGraw-Hill, New York ; London,
- Faulkner, W. T., R. Alwood, D. W. A. Taylor, and J. Bohlin (2010) "GPS-Denied Pedestrian Tracking in Indoor Environments Using an IMU and Magnetic Compass," in *Proceedings of the 2010 International Technical Meeting of the Institute of Navigation - ITM 2010*, 21-25 Jan, Washington, pp. 198-204, Institute of Navigation
- Fitzgibbon, A., M. Pilu, and R. B. Fisher (1999) "Direct Least Square Fitting of Ellipses," *IEEE Transaction on Pattern Analysis and Machine Intelligence*, vol 21, pp. 476-480
- Gebre-Egziabher, D., G. H. Elkaim, J. D. Powel, and B. W. Parkinson (2006) "Calibration of Strapdown Magnetometers in Magnetic Field Domain," *J. Aerosp. Eng.*, vol 19, no 2, Apr 2006, pp. 87-102
- Goldenberg, F. (2006) "Geomagnetic Navigation Beyond the Magnetic Compass," in *2006 IEEE/ION Position, Location and Navigation Symposium, Vols 1-3*, IEEE, New York, pp. 684-694
- Grewal, M. S., L. R. Weill, and A. P. Andrews (2001) *Global Positioning Systems, Inertial Navigation, and Integration*, John Wiley & Sons, Inc.
- Grubin, C. (1970) "Derivation of Quaternion Scheme via Euler Axis and Angle," *J. Spacecr. Rockets*, vol 7, no 10, pp. 1261
- Haines, G. V., and L. R. Newitt (1997) "The Canadian Geomagnetic Reference Field 1995," *J. Geomagn. Geoelectr.*, vol 49, no 2-3, pp. 317-336
- Hamani, S., M. Oussalah, P. Hall, and E. Int Assoc. (2007) "Combination of GSM and GPS Signals for Mobile Positioning and Location Service using Kalman Filter," in *World Congress on Engineering 2007, Vols 1 and 2*, Int Assoc Engineers-Iaeng, Hong Kong, pp. 1524-1529
- Haverinen, J., and A. Kemppainen (2009) "Global Indoor Self-localization based on the Ambient Magnetic Field," *Robotics and Autonomous Systems*, vol 57, no 10, Oct 2009, pp. 1028-1035
- Hippenstiel, R. D. (2002) *Detection Theory Applications and Digital Signal Processing*, 1st Ed., CRC Press

Honeywell (2010a) *AN212 Handling of Sensor Bridge Offset*, <http://www.honeywell.com/sites/portal?smap=aerospace&page=Literature&theme=T5>, last accessed April, 2010

Honeywell (2010b) *HMC5843 Data Sheet*, <http://www.honeywell.com/sites/servlet/com.merx.npoint.servlets.DocumentServlet?docid=DA9ACFE3C-F7C0-9998-6085-D9D84941499D>, last accessed August, 2010

Inoue, Y., A. Sashima, and K. Kurumatani (2009) "Indoor Positioning System Using Beacon Devices for Practical Pedestrian Navigation on Mobile Phone," *Ubiquitous Intelligence and Computing, Proceedings*, vol 5585, pp. 251-265

Jimenez, A. R., F. Seco, C. Prieto, and J. Guevara (2009) "A Comparison of Pedestrian Dead-Reckoning Algorithms using a Low-Cost MEMS IMU," in *WISP 2009: Proceedings of the 6th IEEE International Symposium on Intelligent Signal Processing*, 26-28 Aug, New York, pp. 37-42, IEEE

Karunanayake, M. D., M. E. Cannon, G. Lachapelle, and G. Cox (2004) "Evaluation of Assisted GPS (AGPS) in Weak Signal Environments Using a Hardware Simulator " in *ION GNSS 2004*, 21-24 September, Long Beach, California, pp. 11, Institute of Navigation

Kaufman, A. A., R. O. Hansen, and R. L. K. Kleinberg (2009) *Principles of the Magnetic Methods in Geophysics*, 1st Ed., Elsevier, Amsterdam,

Knoepfel, H. (2000) *Magnetic Fields : A Comprehensive Theoretical Treatise for Practical Use*, Wiley, New York,

Ladetto, Q., and B. Merminod (2002) "Digital Magnetic Compass and Gyroscope Integration for Pedestrian Navigation," in *9th Saint Petersburg International Conference on Integrated Navigation Systems*, 2002, Saint Petersburg, Russia, pp. 10

Ladetto, Q., B. Merminod, P. Terrier, and Y. Schutz (2000) "On Foot Navigation: When GPS Alone is Not Enough," *Journal of Navigation*, vol 53, no 2, pp. 279-285

Lassahn, M. P., and G. Trenkler (1995) "Vectorial Calibration of 3D Magnetic Field Sensor Arrays," *IEEE Transactions on Instrumentation and Measurement*, vol 44, no 2, pp. 360-362

Lawrence, A. (1993) *Modern Inertial Technology : Navigation, Guidance, and Control*, Springer, New York,

Li, D., R. J. Landry, and P. Lavoie (2008) "Low-cost MEMS Sensor-based Attitude Determination System by Integration of Magnetometers and GPS: A Real-data Test and

Performance Evaluation," *2008 IEEE/ION Position, Location and Navigation Symposium, Vols 1-3*, pp. 342-350

Li, Q., and J. G. Griffiths (2004) "Least Squares Ellipsoid Specific Fitting," in *Geometric Modeling and Processing*, Beijing, pp. 335-340

Luimula, M., K. Saaskilahti, T. Partala, S. Pieska, and J. Alaspaa (2010) "Remote Navigation of a Mobile Robot in an RFID-augmented Environment," *Pers. Ubiquitous Comput.*, vol 14, no 2, Feb 2010, pp. 125-136

Luinge, H. J., and P. H. Veltink (2005) "Measuring Orientation of Human Body Segments using Miniature Gyroscopes and Accelerometers," *Medical; Biological Engineering; Computing*, vol 43, no 2, pp. 273-282

Markovsky, I., A. Kukush, and S. V. Huffel (2004) "Consistent Least Squares Fitting Ellipsoids," *Numerische Mathematik*, vol 98, pp. 177-194

Masson, G., D. Frachon, T. Dorge, Y. Ronnat, and R. Arlot (2009) "A New Generation of Contactless Magnetic Position Sensors," *Sens. Lett.*, vol 7, no 3, Jun, pp. 451-455

Milsom, J. (2003) *Field Geophysics*, 3rd Ed., J. Wiley, Chichester, England ; Hoboken, N.J.,

Moafipoor, S., D. A. Grejner-Brzezinska, and C. K. Toth. (2008) "Multi-sensor Personal Navigator Supported by Adaptive Knowledge based System: Performance Assessment," in *2008 IEEE/ION Position, Location and Navigation Symposium, Vols 1-3*, IEEE, New York, pp. 716-727

Natanson, G. A., M. S. Challa, J. Deutschmann, and D. F. Baker (1994) "Magnetometer-only Attitude and Rate Determination for a Gyro-less Spacecraft," in *Third International Symposium on Space Mission Operations and Ground Data Systems*, Greenbelt, MD, pp. 791-798

Pahadia, A. (2010) *GPS/ INS Integration Aided with Gyroscope-Free IMU for Pedestrian Applications*, Department of Geomatics Engineering, University of Calgary, Calgary

Park, M., and Y. Gao (2008) "Error and Performance Analysis of MEMS-based Inertial Sensors with a Low-cost GPS Receiver," *Sensors*, vol 8, no 4, Apr 2008, pp. 2240-2261

Petrucha, V., P. Kaspar, P. Ripka, and J. M. G. Merayo (2009) "Automated System for the Calibration of Magnetometers," *J. Appl. Phys.*, vol 105, no 7, Apr 2009, pp. 3

Ramalingam, R., G. Anitha, and J. Shanmugam (2009) "Microelectromechanical Systems Inertial Measurement Unit Error Modelling and Error Analysis for Low-cost Strapdown Inertial Navigation System," *Def. Sci. J.*, vol 59, no 6, Nov 2009, pp. 650-658

Renaudin, V., H. Afzal, and G. Lachapelle (2010) "Complete Tri-axis Magnetometer Calibration in the Magnetic Field Domain," *Journal of Sensors, Hindawi*, vol 2010, pp. 10

Renaudin, V., O. Yalak, P. Tome, and B. Merminod (2007) "Indoor Navigation of Emergency Agents," *European Journal of Navigation*, vol 5, no 3, July 2007, pp. 36-45

Riehle, T. H., P. Lichter, and N. A. Giudice (2008) "An Indoor Navigation System to Support the Visually Impaired," *2008 30th Annual International Conference of the IEEE Engineering in Medicine and Biology Society, Vols 1-8*, pp. 4435-4438

Ripka, P. (2001) *Magnetic Sensors and Magnetometers*, Artech House, Boston,

Roetenberg, D., H. Luinge, and P. Veltink (2003) "Inertial and Magnetic Sensing of Human Movement Near Ferromagnetic Materials," in *Proceedings of the Second IEEE and ACM International Symposium on Mixed and Augmented Reality (ISMAR '03)*, 23 Oct 2003, Los Alamitos, pp. 268-269, IEEE Computer Society

Saber-Sheikh, K., E. C. Bryant, C. Glazzard, A. Hamel, and R. Y. W. Lee (2009) "Feasibility of Using Inertial Sensors to Assess Human Movement," *Manual Therapy*, vol 15, no 1, May 2009, pp. 122-125

Sheinker, A., L. Frumkis, B. Ginzburg, N. Salomonski, and B. Z. Kalpan (2009) "Magnetic Anomaly Detection Using a Three-Axis Magnetometer," *IEEE Transactions on Magnetics*, vol 45, no 1, Jan, pp. 160-167

Shen, G. W., R. Zetik, O. Hirsch, and R. S. Thoma (2010) "Range-Based Localization for UWB Sensor Networks in Realistic Environments," *EURASIP J. Wirel. Commun. Netw.*, pp. 9

Shuster, M. D., and O. S.D (1981) "Three-axis Attitude Determination from Vector Observations," *Journal of Guidance and Control*, vol 4, Jan-Feb 1981, pp. 70-77

Skvortzov, V. Y., H. K. Lee, S. W. Bang, and Y. B. Lee. (2007) "Application of Electronic Compass for Mobile Robot in an Indoor Environment," in *Proceedings of the 2007 IEEE International Conference on Robotics and Automation, Vols 1-10*, IEEE, New York, pp. 2963-2970

SkyTraq (2010) *Single Chip HSGPS*, http://www.skytraq.com.tw/download/Venus634LPx_PB_v3.pdf, last accessed August, 2010

Sohne, W., O. Heinze, and E. Groten. (1994) "Integrated INS GPS System for High-Precision Navigation Applications," in *IEEE 1994 Position Location and Navigation Symposium*, IEEE, New York, pp. 310-313

Sonoda, Y. (1995) "Applications of Magnetometer Sensors to Observing Bio-mechanical Movements," *IEEE Transactions on Magnetics*, vol 31, no 2, pp. 1283-1290

ST, M. (2010a) *Dual-axis MEMS Gyroscope for Roll and Pitch Rates*, <http://www.st.com/stonline/books/pdf/docs/15812.pdf>, last accessed August, 2010

ST, M. (2010b) *Single-axis MEMS Gyroscope for Yaw Rates*, <http://www.st.com/stonline/products/families/sensors/datasheets/ly530alh.pdf>, last accessed August, 2010

Steele, K. E. (2003) "Pitch-roll Buoy Mean Wave Directions from Heave Acceleration, Bow Magnetism, and Starboard Magnetism," *Ocean Eng.*, vol 30, no 17, Dec 2003, pp. 2179-2199

Steiner, C., and A. Wittneben (2010) "Low Complexity Location Fingerprinting With Generalized UWB Energy Detection Receivers," *IEEE Trans. Signal Process.*, vol 58, no 3, Mar 2010, pp. 1756-1767

Steinhoff, U., and B. Schiele (2010) "Dead Reckoning from the Pocket - An Experimental Study," in *2010 IEEE International Conference on Pervasive Computing and Communications (PerCom)*, 29 Mar 2010, pp. 162-170

Sternberg, H., and M. Fessele (2009) "Indoor Navigation with Low-Cost Inertial Navigation Systems," *WPNC: 2009 6th Workshop on Positioning, Navigation and Communication, Proceedings*, pp. 1-4

Stirling, R., K. Fyfe, and G. Lachapelle (2005) "Evaluation of a New Method of Heading Estimation for Pedestrian Dead Reckoning using Shoe Mounted Sensors," *Journal of Navigation*, vol 58, no 1, pp. 31-45

Storms, W. F., and J. F. Raquet (2009) "Magnetic Field Aided Vehicle Tracking," in *Proceedings of the 22nd International Technical Meeting of the Satellite Division of Institute of Navigation (ION GNSS 2009)*, September 2009, Savannah, GA, pp. 1767-1774

Su, J., and Y. X. Jin. (2007) "Indoors Location Technology Research based on WLAN," in *6th WSEAS Int Conf on Instrumentation, Measurement, Circuits & Systems/7th WSEAS Int Conf on Robotics, Control and Manufacturing Technology, Proceedings*, Xu, A., H. Zhu, S. Y. Chen, B. Yan, Q. Meng, D. Miao, and Y. Fang, eds., World Scientific and Engineering Acad. and Soc., Athens, pp. 109-114

Suh, Y. S., and S. Park. (2009) "Pedestrian Inertial Navigation with Gait Phase Detection Assisted Zero Velocity Updating," in *Proceedings of the Fourth International Conference on Autonomous Robots and Agents*, Gupta, G. S. and S. C. Mukhopadhyay, eds., IEEE, New York, pp. 505-510

Tang, W., G. Howell, and Y. H. Tsai (2005) "Barometric Altimeter Short-term Accuracy Analysis," *IEEE Aerosp. Electron. Syst. Mag.*, vol 20, no 12, Dec 2005, pp. 24-26

Tarrio, P., A. M. Bernardos, J. A. Besada, and J. R. Caser. (2008) "A New Positioning Technique for RSS-Based Localization based on a Weighted Least Squares Estimator," in *2008 IEEE International Symposium on Wireless Communication Systems*, IEEE, New York, pp. 358-362

Titterton, D. H., and J. L. Weston (2004) *Strapdown Inertial Navigation Technology*, 2nd Ed., Institution of Electrical Engineers, Stevenage,

Vasconcelols, J. F., G. Elkaim, C. Silvester, P. Oliviera, and B. Cardeira (2008) "A Geometric Approach to Strapdown Magnetometer Calibration in Sensor Frame," in *IFAC Workshop on Navigation, Guidance and Control of Underwater Vehicles*, April 2008, Killaloe, Ireland

VTI, T. (2010) *MEMS Pressure and Temperature Sensor*, http://www.vti.fi/midcom-serveattachmentguid-9cbae6a382efd245cb62354a54ff62c7/scp1000-d01_-d11_pressure_sensor_datasheet_28-08-2007.pdf, last accessed August, 2010

Wahba, G. (1965) "Problem 65-1: A Least Squares Estimate of Spacecraft Attitude," *SIAM Review*, vol 7, no 3, July 1965, pp. 409

Wang, J., J. Liu, B. G. Cai, and I. C. Soc. (2008) "Study on Information Fusion Algorithm in Embedded Integrated Navigation System," in *International Conference on Intelligent Computation Technology and Automation, Vol 2, Proceedings*, IEEE Computer Soc, Los Alamitos, pp. 1007-1010

Wertz, J. R. (1978) *Spacecraft Attitude Determination and Control*, Kluwer Academic Publishers, Dordrecht ; Boston ; Reidel,

Wertz, J. R. (1990) *Space Attitude Determination and Control*, Kluwer Academic Publishers

Wiegert, R., K. Lee, and J. Oeschger. (2008) "Improved Magnetic STAR Methods for Real-Time, Point-by-Point Localization of Unexploded Ordnance and Buried Mines," in *Oceans 2008, Vols 1-4*, IEEE, New York, pp. 1847-1853

Xing, Z. Q., and D. Gebre-Egziabher. (2008) "Modeling and Bounding Low Cost Inertial Sensor Errors," in *2008 IEEE/ION Position, Location and Navigation Symposium, Vols 1-3*, IEEE, New York, pp. 274-284

Xue, L., W. Z. Yuan, H. L. Chang, and C. Y. Jiang (2009) "MEMS-based Multi-sensor Integrated Attitude Estimation Technology For MAV Applications," *2009 4th IEEE*

International Conference on Nano/Micro Engineered and Molecular Systems, Vols 1 and 2, pp. 1031-1035

Zhiqiang, X., and D. Gebre-Egziabher (2008) "Modeling and Bounding Low Cost Inertial Sensor Errors," in *Position, Location and Navigation Symposium, 2008 IEEE/ION*, 5-8 May 2008, pp. 1122-1132

Zhou, J. Y., J. Shi, and X. L. Qu (2010) "Statistical Characteristics of Landmark-based Localization Performance," *Int. J. Adv. Manuf. Technol.*, vol 46, no 9-12, Feb 2010, pp. 1215-1227

Appendix A: **Detection of Good Magnetic Field Using Total Field Measurements**

A detector using an individual magnetic field parameter, namely the total magnetic field F , is developed here. Similar detectors for detecting good magnetic field measurements using the remaining individual magnetic field test parameters can be developed using the derivation documented herein.

A.1 **Total Magnetic Field based Detector**

For a window size of N samples, let the test parameter for a total field detector be given by

$$\{F_k\}_{k=n}^{n+N-1} = \{F_M - F_R\}_{k=n}^{n+N-1} \quad (\text{A.1})$$

where the subscripts M and R stand for the measurements (ideal) and reference, respectively. In reality, the measurements will be contaminated by white Gaussian noise, which leads to the following observation model:

$$y_k^F = F_k + v_k^F \quad (\text{A.2})$$

where y_k^F are the actual total field measurements and v_k^F the measurement noise.

Let H_0 be the hypothesis for bad and H_1 for good magnetic field measurements. In case of a good field measurement, the total field parameter F_k will be completely known whereas in case of a bad field measurement, this parameter will be contaminated by unknown perturbations. Therefore in case of H_0 , the Probability Density Function (PDF) is given by

$$f(y_k^F; F, H_0) = \prod_{k=n}^{n+N-1} \frac{1}{(2\pi\sigma_F^2)^{1/2}} \exp\left(\frac{-1}{2\sigma_F^2}(y_k^F - F_k)^2\right) \quad (\text{A.3})$$

Using the Maximum Likelihood Estimates (MLE) for the unknown parameter F_k in Equation (A.3), one can replace it by its mean over the sample window of size N (Hippenstiel 2002). This leads to the following PDF for H_0 :

$$f(y_k^F; \hat{F}, H_0) = \prod_{k=n}^{n+N-1} \frac{1}{(2\pi\sigma_F^2)^{1/2}} \exp\left(\frac{-1}{2\sigma_F^2}(y_k^F - \hat{F})^2\right) \quad (\text{A.4})$$

$$\hat{F} = \frac{1}{N} \sum_{k=n}^{n+N-1} y_k^F$$

In case of H_1 , the total magnetic field is known. This leads to the following PDF:

$$f(y_k^F; H_1) = \prod_{k=n}^{n+N-1} \frac{1}{(2\pi\sigma_F^2)^{1/2}} \exp\left(\frac{-1}{2\sigma_F^2}(y_k^F)^2\right). \quad (\text{A.5})$$

The GLRT for detecting good total magnetic field measurements is then given by

$$\Lambda(y_k^F) = \frac{f(y_k^F; \hat{F}, H_0)}{f(y_k^F; H_1)} < \lambda. \quad (\text{A.6})$$

Substituting for the PDFs in Equation (A.6) and simplifying yields

$$\Lambda(\mathbf{y}) = \frac{\prod_{k=n}^{n+N-1} \frac{1}{(2\pi\sigma_F^2)^{1/2}} \exp\left(\frac{-1}{2\sigma_F^2}(y_k^F - \hat{F})^2\right)}{\prod_{k=n}^{n+N-1} \frac{1}{(2\pi\sigma_F^2)^{1/2}} \exp\left(\frac{-1}{2\sigma_F^2}(y_k^F)^2\right)} < \lambda \quad (\text{A.7})$$

$$\Lambda(\mathbf{y}) = \prod_{k=n}^{n+N-1} \exp\left(\frac{1}{2\sigma_F^2}(y_k^F)^2 - \frac{1}{2\sigma_F^2}(y_k^F - \hat{F})^2\right) < \lambda \quad (\text{A.8})$$

$$\wedge(\mathbf{y}) = \prod_{k=n}^{n+N-1} \exp\left(\frac{1}{2\sigma_F^2}(y_k^F)^2 - \frac{1}{2\sigma_F^2}(y_k^F)^2 + \frac{2}{2\sigma_F^2}y_k^F\hat{F} - \frac{1}{2\sigma_F^2}\hat{F}^2\right) < \lambda \quad (\text{A.9})$$

$$\wedge(\mathbf{y}) = \prod_{k=n}^{n+N-1} \exp\left(\frac{2}{2\sigma_F^2}y_k^F\hat{F} - \frac{1}{2\sigma_F^2}\hat{F}^2\right) < \lambda \quad (\text{A.10})$$

Taking the natural log on both sides yields

$$\sum_{k=n}^{n+N-1} \left(\frac{2}{2\sigma_F^2}y_k^F\hat{F} - \frac{1}{2\sigma_F^2}\hat{F}^2\right) < \ln(\lambda) \quad (\text{A.11})$$

$$\sum_{k=n}^{n+N-1} (2y_k^F\hat{F} - \hat{F}^2) < 2\sigma_F^2\ln(\lambda) \quad (\text{A.12})$$

$$\left(2 \sum_{k=n}^{n+N-1} y_k^F\hat{F} - \sum_{k=n}^{n+N-1} \hat{F}^2\right) < 2\sigma_F^2\ln(\lambda) \quad (\text{A.13})$$

$$\left\{2 \sum_{k=n}^{n+N-1} y_k^F \frac{1}{N} \sum_{k=n}^{n+N-1} y_k^F - N \left(\frac{1}{N} \sum_{k=n}^{n+N-1} y_k^F\right)^2\right\} < 2\sigma_F^2\ln(\lambda) \quad (\text{A.14})$$

$$\left\{\frac{2}{N} \left(\sum_{k=n}^{n+N-1} y_k^F\right)^2 - \frac{1}{N} \left(\sum_{k=n}^{n+N-1} y_k^F\right)^2\right\} < 2\sigma_F^2\ln(\lambda) \quad (\text{A.15})$$

which gives the following test statistics for the total field detector:

$$\frac{1}{\sqrt{N}} \left(\sum_{k=n}^{n+N-1} y_k^F\right) < \gamma_F. \quad (\text{A.16})$$

γ_F is the test statistics threshold given by

$$\gamma_F = \sqrt{2\sigma_F^2\ln(\lambda)}. \quad (\text{A.17})$$

Equation (A.16) constitutes the total field based detector for detecting good magnetic field measurements.

Appendix B: Attitude Determination Using Gyroscopes

The first step in mechanizing an attitude estimator using angular rates (from gyroscopes) is to select the representation of the transformation matrix, which directly (Euler angles) or indirectly (direction cosines, quaternion) gives the three dimensional attitude. It was concluded in Section 5.2.3 that quaternions are the most efficient way of representing the rotation between two frames. Therefore a derivative of quaternion relating the rotations between frame a and b with the angular rates is derived. The properties of quaternions utilized for the developments that follow are described in numerous books on navigation (Farrell 2008, Lawrence 1993, Titterton & Weston 2004).

B.1 Derivative of a Quaternion

Let \mathbf{v}^a be a vector in frame a . Now one needs to represent this vector in frame b using the transformation matrix \mathbf{C}_a^b given by

$$\mathbf{v}^b = \mathbf{C}_a^b \mathbf{v}^a . \quad (\text{B.1})$$

Let $\boldsymbol{\omega}_{ba}^a$ be the angular velocity of frame a with respect to frame b represented in frame a .

The rate of change of vector \mathbf{v}^b is given by

$$\dot{\mathbf{v}}^b = \boldsymbol{\omega}_{ba}^a \times \mathbf{v}^a . \quad (\text{B.2})$$

The angular velocity in Equation (B.2) can be replaced by its skew symmetric matrix given by

$$\left[\boldsymbol{\omega}_{ba}^a \times \right] = \boldsymbol{\Omega}_{ba}^a = \begin{bmatrix} 0 & -\omega_z^a & \omega_y^a \\ \omega_z^a & 0 & -\omega_x^a \\ -\omega_y^a & \omega_x^a & 0 \end{bmatrix}, \quad (\text{B.3})$$

where ω_x^a, ω_y^a and ω_z^a are the angular rates obtained from the rate gyroscopes in the a frame.

Substituting Equations (B.3) and (B.1) in Equation (B.2) one obtains

$$\dot{\mathbf{v}}^b = \boldsymbol{\Omega}_{ba}^a \mathbf{C}_a^b \mathbf{v}^a. \quad (\text{B.4})$$

Let \mathbf{q} be the quaternion representing the rotation from frame a to frame b , i.e. the quaternion equivalent of \mathbf{C}_a^b . Representing the vectors \mathbf{v}^a and \mathbf{v}^b by their respective quaternion vectors, the transformation of vector \mathbf{v}^a to \mathbf{v}^b can now be achieved using

$$\mathbf{q}_v^b = \mathbf{q} \circ \mathbf{q}_v^a \circ \bar{\mathbf{q}}. \quad (\text{B.5})$$

The derivative of the quaternion \mathbf{q}_v^b is given by

$$\dot{\mathbf{q}}_v^b = \dot{\mathbf{q}} \circ \mathbf{q}_v^a \circ \bar{\mathbf{q}} + \mathbf{q} \circ \dot{\mathbf{q}}_v^a \circ \bar{\mathbf{q}}. \quad (\text{B.6})$$

The quaternion vector \mathbf{q}_v^a in Equation (B.6) can be replaced by its transformation to \mathbf{q}_v^b given by

$$\mathbf{q}_v^a = \bar{\mathbf{q}} \circ \mathbf{q}_v^b \circ \mathbf{q}. \quad (\text{B.7})$$

Substituting Equation (B.7) in Equation (B.6), it becomes

$$\dot{\mathbf{q}}_v^b = \dot{\mathbf{q}} \circ \bar{\mathbf{q}} \circ \mathbf{q}_v^b \circ \mathbf{q} \circ \bar{\mathbf{q}} + \mathbf{q} \circ \bar{\mathbf{q}} \circ \dot{\mathbf{q}}_v^b \circ \mathbf{q} \circ \bar{\mathbf{q}}. \quad (\text{B.8})$$

A quaternion multiplied by its conjugate is an identity quaternion, which represents no transformation. Using this property, Equation (B.8) reduces to

$$\dot{\mathbf{q}}_v^b = \dot{\mathbf{q}} \circ \bar{\mathbf{q}} \circ \mathbf{q}_v^b + \mathbf{q}_v^b \circ \mathbf{q} \circ \dot{\bar{\mathbf{q}}}. \quad (\text{B.9})$$

It can be shown that both products $\dot{\mathbf{q}} \circ \bar{\mathbf{q}}$ and $\mathbf{q} \circ \dot{\bar{\mathbf{q}}}$ have their scalar components equal to zero. This means that the final outcome of Equation (B.9) will have a zero scalar component, which is true because \mathbf{q}_v^b is a quaternion vector. Also the two quaternion products $\dot{\mathbf{q}} \circ \bar{\mathbf{q}}$ and $\mathbf{q} \circ \dot{\bar{\mathbf{q}}}$ have the same magnitudes but opposite directions. Let these quaternion products be given by

$$\dot{\mathbf{q}} \circ \bar{\mathbf{q}} = [0 \quad \mathbf{u}]^T, \mathbf{q} \circ \dot{\bar{\mathbf{q}}} = [0 \quad -\mathbf{u}]^T. \quad (\text{B.10})$$

Substituting Equation (B.10) in Equation (B.9) gives

$$\begin{bmatrix} 0 \\ \dot{\mathbf{v}}^b \end{bmatrix} = \begin{bmatrix} 0 \\ \mathbf{u} \end{bmatrix} \circ \begin{bmatrix} 0 \\ \mathbf{v}^b \end{bmatrix} + \begin{bmatrix} 0 \\ \mathbf{v}^b \end{bmatrix} \circ \begin{bmatrix} 0 \\ -\mathbf{u} \end{bmatrix}. \quad (\text{B.11})$$

Using the conjugate of $\mathbf{q} \circ \dot{\bar{\mathbf{q}}}$, Equation (B.11) can be rewritten as

$$\begin{bmatrix} 0 \\ \dot{\mathbf{v}}^b \end{bmatrix} = \begin{bmatrix} 0 \\ \mathbf{u} \end{bmatrix} \circ \begin{bmatrix} 0 \\ \mathbf{v}^b \end{bmatrix} + \begin{bmatrix} 0 \\ \mathbf{u} \end{bmatrix} \circ \begin{bmatrix} 0 \\ \mathbf{v}^b \end{bmatrix}, \quad (\text{B.12})$$

which in vector form becomes

$$\dot{\mathbf{v}}^b = 2\mathbf{u} \times \mathbf{v}^b. \quad (\text{B.13})$$

Comparing Equation (B.13) and Equation (B.2), it can be observed that

$$\boldsymbol{\omega}_{ba}^a = 2\mathbf{u}. \quad (\text{B.14})$$

Substituting \mathbf{u} from Equation (B.10) and rewriting Equation (B.14) in quaternion form yields

$$\mathbf{q}_{\omega_{ba}^a} = 2\dot{\mathbf{q}} \circ \bar{\mathbf{q}}, \quad (\text{B.15})$$

where $\mathbf{q}_{\omega_{ba}^a} = [0 \quad \boldsymbol{\omega}_{ba}^a]^T$.

Rearranging Equation (B.15), it is possible to establish the differential equation in $\dot{\mathbf{q}}$:

$$\dot{\mathbf{q}} = \frac{1}{2} \mathbf{q}_{\omega_{dc}^c} \circ \mathbf{q}. \quad (\text{B.16})$$

Using the matrix representation of a quaternion, Equation (B.16) can be rewritten as

$$\dot{\mathbf{q}} = \frac{1}{2} \mathbf{Q}_{\omega_{ba}^a} \mathbf{q} = \frac{1}{2} \bar{\mathbf{Q}}_q \boldsymbol{\omega}_{ba}^a. \quad (\text{B.17})$$

As the scalar component of $\mathbf{q}_{\omega_{ba}^a}$ is zero, Equation (B.17) can be reduced to

$$\dot{\mathbf{q}} = \frac{1}{2} \begin{bmatrix} -q_2 & -q_3 & -q_4 \\ q_1 & q_4 & -q_3 \\ -q_4 & q_1 & q_2 \\ q_3 & -q_2 & q_1 \end{bmatrix} \begin{bmatrix} \omega_x^a \\ \omega_y^a \\ \omega_z^a \end{bmatrix}. \quad (\text{B.18})$$

Equation (B.18) is the governing equation for the derivative of the rotation vector represented by a quaternion.

B.2 Quaternion Derivative from Sensor to Navigation Frame

The attitude of the sensor block is represented in the navigation frame. Consequently Equation (B.18) needs to be modified to compensate for the rotation of the navigation frame with respect to the inertial one. Indeed the angular rates measured by the gyroscopes are expressed in the sensor frame with respect to the inertial frame. The angular rate vector for the sensor frame with respect to the navigation frame represented in the sensor frame is given by

$$\boldsymbol{\omega}_{sn}^s = \boldsymbol{\omega}_{in}^s - \boldsymbol{\omega}_{is}^s. \quad (\text{B.19})$$

Here, the term $\boldsymbol{\omega}_{in}^s$ is the angular rate vector of the navigation frame with respect to the inertial frame represented in the sensor frame. For computing this rotation vector, information regarding the position and velocity of the sensor block is necessary. As

position and velocity estimation of the sensor block are not targeted in this research, this term cannot be computed in this case. This leads to two possible solutions:

1. Model ω_{in}^s as a white noise in attitude estimator. This is usually done in case of large displacements between two consecutive measurements as are encountered with aircraft.
2. In case of pedestrian navigation, as the subject is not moving with substantial speeds that can be compared with the Earth's rotation, this term can be neglected.

The second solution is selected herein, leading to the following angular rate measurements for quaternion derivative:

$$\omega_{sn}^s = -\omega_{is}^s, \quad (\text{B.20})$$

where $\omega_{is}^s = [\omega_x^s \ \omega_y^s \ \omega_z^s]^T$ is the angular rate vector obtained using the rate gyroscopes. Substituting the a frame with the sensor frame s and b frame with the navigation frame n in Equation (B.18), the governing equation for the quaternion derivative of the rotation vector from sensor to navigation frame becomes

$$\dot{\mathbf{q}} = \frac{1}{2} \begin{bmatrix} -q_2 & -q_3 & -q_4 \\ q_1 & q_4 & -q_3 \\ -q_4 & q_1 & q_2 \\ q_3 & -q_2 & q_1 \end{bmatrix} \begin{bmatrix} -\omega_x^s \\ -\omega_y^s \\ -\omega_z^s \end{bmatrix}. \quad (\text{B.21})$$

Appendix C: Multiple Magnetometer Platform (MMP) based Local Magnetic Field Estimator

An Extended Kalman Filter based local magnetic field estimator is developed that utilizes the less perturbed magnetic field components as identified by MMP based detector and estimates the remaining components using magnetic field vector information from previous estimates. The state vector, dynamics model and measurement error models are derived below.

C.1 Perturbed State Vector

The state vector is composed of the three local magnetic field components in the sensor frame, which leads to the following perturbed state vector:

$$\boldsymbol{\varepsilon}_{B^s} = \begin{bmatrix} \varepsilon_{B_x^s} & \varepsilon_{B_y^s} & \varepsilon_{B_z^s} \end{bmatrix}^T. \quad (\text{C.1})$$

C.2 Dynamics Model

For Equation (C.1), the error state dynamics model is given by

$$\underbrace{\begin{bmatrix} \dot{\varepsilon}_{B_x^s} \\ \dot{\varepsilon}_{B_y^s} \\ \dot{\varepsilon}_{B_z^s} \end{bmatrix}}_{\delta \dot{\mathbf{x}}} = \underbrace{\begin{bmatrix} 0 & 0 & 0 \\ 0 & 0 & 0 \\ 0 & 0 & 0 \end{bmatrix}}_F \underbrace{\begin{bmatrix} \varepsilon_{B_x^s} \\ \varepsilon_{B_y^s} \\ \varepsilon_{B_z^s} \end{bmatrix}}_{\delta \mathbf{x}} + \underbrace{\begin{bmatrix} 1 & 0 & 0 \\ 0 & 1 & 0 \\ 0 & 0 & 1 \end{bmatrix}}_G \underbrace{\begin{bmatrix} w_{B_x^s} \\ w_{B_y^s} \\ w_{B_z^s} \end{bmatrix}}_w. \quad (\text{C.2})$$

The noise vector \boldsymbol{w} is composed of the uncertainties in each of the three magnetic field components as obtained by sensor error modeling. The state covariance matrix is obtained using the prediction and update equations described in Chapter 5. For the MMP estimator, this matrix is represented by \boldsymbol{R}_{MMP} .

C.3 Measurement Error Model

The observations required for the measurement error model are obtained by utilizing the less perturbed magnetic field component and information regarding the magnetic field vector from previous estimates. Assuming the X axis component is detected as the least perturbed, the remaining two components are estimated as

$$\begin{aligned} B_y^s &= \sqrt{\mathbf{B}_h^2 - (B_x^s)^2} \\ B_z^s &= \sqrt{\mathbf{B}^2 - (B_x^s)^2} \sqrt{\frac{(B_y^s)^2}{\mathbf{B}^2}} \end{aligned} \quad (\text{C.3})$$

Here \mathbf{B}_h is the horizontal field component and \mathbf{B} is the total field, obtained from the last estimates of the local field. The measurement variances for the two observations estimated in Equation (C.3) are obtained as follows:

$$\sigma_{B_y^s}^2 = \frac{4}{(\mathbf{B}^2 + B_x^2)} \left(\mathbf{B}^2 \sigma_B^2 + (B_x^s)^2 \sigma_{B_x^s}^2 \right). \quad (\text{C.4})$$

$$\sigma_{B_z^s}^2 = \frac{4}{(\mathbf{B}^2 + \mathbf{B}_h^2)} \left(\mathbf{B}^2 \sigma_B^2 + \mathbf{B}_h^2 \sigma_{B_h}^2 \right). \quad (\text{C.5})$$

The variance for the total magnetic field \mathbf{B} and the horizontal magnetic field \mathbf{B}_h are obtained from the last estimate. The measurement error model now becomes

$$\underbrace{\begin{bmatrix} B_s^x \\ B_s^y \\ B_s^z \end{bmatrix}}_{\delta z} - \underbrace{\begin{bmatrix} \hat{B}_s^x \\ \hat{B}_s^y \\ \hat{B}_s^z \end{bmatrix}}_{\mathbf{H}} = \underbrace{\begin{bmatrix} 1 & 0 & 0 \\ 0 & 1 & 0 \\ 0 & 0 & 1 \end{bmatrix}}_{\delta x} \underbrace{\begin{bmatrix} \varepsilon_{B_x^s} \\ \varepsilon_{B_y^s} \\ \varepsilon_{B_z^s} \end{bmatrix}}_{\delta x} + \underbrace{\begin{bmatrix} \sigma_{B_x^s}^2 \\ \sigma_{B_y^s}^2 \\ \sigma_{B_z^s}^2 \end{bmatrix}}_{\boldsymbol{\eta}}, \quad (\text{C.6})$$

where the circumflex accent identifies states compensated for the errors obtained from the last update and $\boldsymbol{\eta}$ is the measurement noise uncertainty matrix.

Appendix D: Quasi Static Field Detector

In order to utilize the magnetic field measurements for estimating errors associated with gyroscopes, a detector is required for identifying the magnetic field periods that, although perturbed, are static enough (for that period) to be used for estimating the user angular rate dynamics. The magnetic field that can be used for estimating the said errors is hereby called Quasi Static Field (QSF) and the statistical detector for identifying it is derived herein.

D.1 QSF Detector Derivation

The information to be considered for detecting a QSF is the rate of change of total magnetic field $\|\dot{\mathbf{F}}_k\|$. Therefore for a window of size N , a QSF detector will detect static field if

$$\left\{ \|\dot{\mathbf{F}}_k\| \right\}_{k=n}^{n+N-1} \approx 0. \quad (\text{D.1})$$

Let the hypothesis for a non-static field be H_0 and that for a quasi-static field be H_1 respectively. The Probability Density Functions (PDFs) associated with these two hypotheses are

$$\begin{aligned} & f(\|\dot{\mathbf{F}}_k\|; H_0) \\ & f(\|\dot{\mathbf{F}}_k\|; H_1) \end{aligned} \quad (\text{D.2})$$

The rate of change of the total magnetic field is also contaminated by white Gaussian noise v_k , which, when modeled with the measurements, gives

$$y_k = \|\dot{\mathbf{F}}_k\| + v_k, \quad (\text{D.3})$$

where y_k is the information to be tested for H_0 or H_1 . $\|\dot{\mathbf{F}}_k\|$ is the unknown parameter (for H_0) required to describe the signal completely. Therefore, for the two hypothesis, $\|\dot{\mathbf{F}}_k\|$ is defined as

$$\begin{aligned} H_0 : \exists k \in \Omega_n \text{ s.t. } \|\dot{\mathbf{F}}_k\| \neq 0 \\ H_1 : \forall k \in \Omega_n \text{ then } \|\dot{\mathbf{F}}_k\| = 0 \end{aligned} \quad (\text{D.4})$$

where $\Omega_n = \{\mathbb{R}\}$.

As the complete knowledge about $\|\dot{\mathbf{F}}_k\|$ is unknown for H_0 , the PDF in this case is given by

$$f(\mathbf{y}; \|\dot{\mathbf{F}}_k\|, H_0) = \prod_{k=n}^{n+N-1} \frac{1}{(2\pi\sigma_{\|\dot{\mathbf{F}}_k\|}^2)^{1/2}} \exp\left(\frac{-1}{2\sigma_{\|\dot{\mathbf{F}}_k\|}^2} (y_k - \|\dot{\mathbf{F}}_k\|)^2\right). \quad (\text{D.5})$$

Let the Maximum Likelihood Estimator (MLE) for the unknown parameter in case of H_0 be $\|\hat{\mathbf{F}}_k\|$, which is given by the mean of the signal as

$$\|\hat{\mathbf{F}}_k\| = \frac{1}{N} \sum_{k=n}^{n+N-1} y_k. \quad (\text{D.6})$$

Now the PDF for H_0 becomes

$$f(\mathbf{y}; \|\hat{\mathbf{F}}_k\|, H_0) = \prod_{k=n}^{n+N-1} \frac{1}{(2\pi\sigma_{\|\hat{\mathbf{F}}_k\|}^2)^{1/2}} \exp\left(\frac{-1}{2\sigma_{\|\hat{\mathbf{F}}_k\|}^2} (y_k - \|\hat{\mathbf{F}}_k\|)^2\right). \quad (\text{D.7})$$

For hypothesis H_1 , the rate of change of the total magnetic field is known (it will be zero), therefore the PDF in this case becomes

$$f(\mathbf{y}; H_1) = \prod_{k=n}^{n+N-1} \frac{1}{(2\pi\sigma_{\|\dot{\mathbf{F}}_k\|}^2)^{1/2}} \exp\left(\frac{-1}{2\sigma_{\|\dot{\mathbf{F}}_k\|}^2} y_k^2\right). \quad (\text{D.8})$$

The Generalized Likelihood Ratio Test (GLRT) for detecting a quasi-static field is given by

$$\Lambda(\mathbf{y}) = \frac{f(\mathbf{y}; \|\hat{\mathbf{F}}_k\|, H_0)}{f(\mathbf{y}; H_1)} < \lambda. \quad (\text{D.9})$$

Substituting for the PDFs in Equation (D.9) and simplifying

$$\Lambda(\mathbf{y}) = \frac{\prod_{k=n}^{n+N-1} \frac{1}{(2\pi\sigma_{\|\hat{\mathbf{F}}_k\|}^2)^{1/2}} \exp\left(\frac{-1}{2\sigma_{\|\hat{\mathbf{F}}_k\|}^2} (y_k - \|\hat{\mathbf{F}}_k\|)^2\right)}{\prod_{k=n}^{n+N-1} \frac{1}{(2\pi\sigma_{\|\hat{\mathbf{F}}_k\|}^2)^{1/2}} \exp\left(\frac{-1}{2\sigma_{\|\hat{\mathbf{F}}_k\|}^2} y_k^2\right)} < \lambda, \quad (\text{D.10})$$

$$\Lambda(\mathbf{y}) = \prod_{k=n}^{n+N-1} \exp\left(\frac{1}{2\sigma_{\|\hat{\mathbf{F}}_k\|}^2} y_k^2 - \frac{1}{2\sigma_{\|\hat{\mathbf{F}}_k\|}^2} (y_k - \|\hat{\mathbf{F}}_k\|)^2\right) < \lambda, \quad (\text{D.11})$$

$$\Lambda(\mathbf{y}) = \prod_{k=n}^{n+N-1} \exp\left(\frac{1}{2\sigma_{\|\hat{\mathbf{F}}_k\|}^2} y_k^2 - \frac{1}{2\sigma_{\|\hat{\mathbf{F}}_k\|}^2} y_k^2 + \frac{2}{2\sigma_{\|\hat{\mathbf{F}}_k\|}^2} y_k \|\hat{\mathbf{F}}_k\| - \frac{1}{2\sigma_{\|\hat{\mathbf{F}}_k\|}^2} \|\hat{\mathbf{F}}_k\|^2\right) < \lambda, \quad (\text{D.12})$$

$$\Lambda(\mathbf{y}) = \prod_{k=n}^{n+N-1} \exp\left(\frac{2}{2\sigma_{\|\hat{\mathbf{F}}_k\|}^2} y_k \|\hat{\mathbf{F}}_k\| - \frac{1}{2\sigma_{\|\hat{\mathbf{F}}_k\|}^2} \|\hat{\mathbf{F}}_k\|^2\right) < \lambda. \quad (\text{D.13})$$

Taking the natural log on both sides yields

$$\sum_{k=n}^{n+N-1} \left(\frac{2}{2\sigma_{\|\hat{\mathbf{F}}_k\|}^2} y_k \|\hat{\mathbf{F}}_k\| - \frac{1}{2\sigma_{\|\hat{\mathbf{F}}_k\|}^2} \|\hat{\mathbf{F}}_k\|^2\right) < \ln(\lambda), \quad (\text{D.14})$$

$$\sum_{k=n}^{n+N-1} \left(2y_k \|\hat{\mathbf{F}}_k\| - \|\hat{\mathbf{F}}_k\|^2\right) < 2\sigma_{\|\hat{\mathbf{F}}_k\|}^2 \ln(\lambda), \quad (\text{D.15})$$

$$\left(2 \sum_{k=n}^{n+N-1} y_k \left\| \hat{\mathbf{F}}_k \right\| - \sum_{k=n}^{n+N-1} \left\| \hat{\mathbf{F}}_k \right\|^2 \right) < 2\sigma_{\|\hat{\mathbf{F}}_k\|}^2 \ln(\lambda), \quad (\text{D.16})$$

$$\left\{ 2 \sum_{k=n}^{n+N-1} y_k \frac{1}{N} \sum_{k=n}^{n+N-1} y_k - N \left(\frac{1}{N} \sum_{k=n}^{n+N-1} y_k \right)^2 \right\} < 2\sigma_{\|\hat{\mathbf{F}}_k\|}^2 \ln(\lambda), \quad (\text{D.17})$$

$$\left\{ \frac{2}{N} \left(\sum_{k=n}^{n+N-1} y_k \right)^2 - \frac{1}{N} \left(\sum_{k=n}^{n+N-1} y_k \right)^2 \right\} < 2\sigma_{\|\hat{\mathbf{F}}_k\|}^2 \ln(\lambda), \quad (\text{D.18})$$

$$\left| \frac{1}{\sqrt{N}} \left(\sum_{k=n}^{n+N-1} y_k \right) \right| < \gamma_{\|\hat{\mathbf{F}}_k\|}, \quad (\text{D.19})$$

where $\gamma_{\|\hat{\mathbf{F}}_k\|} = \sqrt{2\sigma_{\|\hat{\mathbf{F}}_k\|}^2 \ln(\lambda)}$.

Equation (D.19) constitutes the detector for identifying a quasi-static total magnetic field in all pedestrian environments.